NORTHWESTERN UNIVERSITY

Tuning Non-Covalent Interactions to Optimize Supramolecular Biomaterials

A DISSERTATION

SUBMITTED TO THE GRADUATE SCHOOL
IN PARTIAL FULFILLMENT OF THE REQUIREMENTS

for the degree

DOCTOR OF PHILOSOPHY

Field of Materials Science and Engineering

By

Charlotte Hui Chen

EVANSTON, ILLINOIS

September 2019

ABSTRACT

Tuning Non-Covalent Interactions to Optimize Supramolecular Biomaterials

Charlotte Hui Chen

Built from non-covalent interactions, supramolecular biomaterials are highly dynamic and tunable, and recent work has shown that they are uniquely capable of mimicking functional biological structures. In this work, supramolecular biomaterials built from self-assembling peptide amphiphiles (PA) were investigated with the goal of precisely tuning their cohesive interactions to optimize biological function. First, this work examined self-sorting versus co-assembly in a multicomponent PA system, where fluorescent PAs conjugated to either fluorescein isothiocyanate (FITC) or carboxytetramethylrhodamine (TAMRA) fluorophores were mixed with non-fluorescent diluent PA. The diluent PA self-assembled into a matrix of negatively charged nanofibers, which FITC-conjugated PA did not co-assemble with but TAMRA-conjugated PA did since the FITC fluorophore is negatively charged while the TAMRA fluorohpore is zwitterionic. This caused the FITC- and TAMRA-conjugated PA to undergo "matrix-mediated" self-sorting, which was suppressed when Na^+ counterions were added to screen the negative charge of FITC residues. In another part of this work the cytotoxicity of cationic PAs was systematically altered, by changing the way the molecule's alkyl segment was conjugated to its peptide chain. When the alkyl tail was conjugated to the peptide's N-terminus, the PA assemblies exerted a rapid cytotoxic

effect by physically disrupting the cell membrane. Conversely, when the alkyl tail was conjugated to the peptide's C-terminus, the PA supramolecular assemblies exerted a slower cytotoxic effect by sequestering cholesterol from the cell membrane, which initiated programmed cell death. In the PA causing slower cytotoxicity, switching the orientation of the lysine linker between the alkyl tail and peptide chain hindered cholesterol sequestration and rescued cell viability. Next, this work examined the damage and self-repair of infinitely long PA nanofibers in response to freezing or freeze drying stress, which are important processes for the clinical translation of the biomaterials investigated. Freezing or freeze drying was found to physically break long nanofibers into shorter ones, which are not optimal for supporting cell adhesion, but thermal energy was found to re-elongate them and rescue their biological function. The long nanofibers are a thermodynamically preferred state that the system can return to but kinetic traps may impede this "repair" process. Furthermore, freeze drying can increase the charge density on the PA molecules, introducing charge repulsion that shifts the thermodynamic minimum to shorter nanofibers, which interferes with self-repair. Finally, this work presented a possible off-the-shelf PA formulation for clinical use for specific application in spinal fusion surgeries. In this formulation the PA is stored as a dried powder to improve its stability, and rehydrated immediately prior to use. The rehydrated PA solution contained short metastable nanofibers that successfully reduced the therapeutic bone morphogenetic protein-2 (BMP-2) protein dose by a factor of 100 in a rat spinal fusion model without requiring thermal elongation of the nanofibers. This suggests that nanofiber length is not a critical property for promoting successful bone growth, and that nanoscale supramolecular interactions may be more crucial to achieving

this desired biological function. In conclusion, this work has shown that that while non-covalent interactions can lead to complex self-assembly behaviors in supramolecular biomaterials, with sufficient mechanistic knowledge, they can be precisely tuned and controlled to produce clinically viable therapies.

ACKNOWLEDGEMENTS

After working at two biotechnology startups, I came back to graduate school because I recognized the importance of basic science knowledge to the successful clinical translation of biomaterials. I wanted a PhD project with potential for clinical translation, but that would also provide me with training in conducting basic science research. I could not have asked for a better project to meet these criteria, and for that, I thank my advisor Prof. Samuel Stupp. He has given me ample freedom to design my project as an independent researcher, and has provided a well-funded, collaborative, and inter-disciplinary environment to support my work. He has also given me opportunities to attend national conferences and participate in professional development activities. I would like to thank my thesis committee members for their help during my PhD. Prof. Kenneth Shull provided helpful feedback on the materials characterization aspects of my work, and I also had the pleasure of being a Teaching Assistant for his MSE 332 class. Not having an undergraduate materials science background, I learned a lot myself from the class, and I learned how to be an effective communicator and teacher. I want to thank Prof. Monica Olvera de la Cruz, who was a crucial collaborator on the original work where PA self-assembly energy landscapes were characterized. I was not involved in that project, and at that time, I had no idea how much it would eventually influence my work. I would also like to thank Prof. Ramille Shah, for providing suggestions on the biological aspects of my work. At the time, I was focused on the materials science aspects of my project, and this encouraged me to think more about my biological experiments. Also on

my committee is Prof. Erin Hsu, who is a wonderful collaborator on my research (more on that below).

I would like to thank Prof. Liam Palmer, for always providing valuable scientific input, both in his own field of study, which is chemistry, as well as other fields, such as materials science and biology. His knowledge of science in fields beyond his own is inspiring, and has pushed me to gain awareness of work outside of my field. When I started writing my first manuscript, the task seemed so daunting and I am grateful that he was there to help. I have already said that I think basic science is important to clinical translation, and indeed, I spent the majority of my PhD pursuing basic science work before I applied my knowledge to a clinical application. During this time, I am grateful to have had the guidance of Dr. Hiroaki Sai, a postdoc whose knowledge of materials science is highly extensive. I won the lottery when he was assigned to the desk next to mine in Cook 3046. Although I am a materials scientist, I have the skills to do basic biological experiments, and for that I have Prof. Shantanu Sur to thank. I caught him in his final postdoc days, right before he left to start his own lab at Clarkson University, and he taught me how to culture cells, encapsulate them into 3D scaffolds, and image them with microscopy. He also introduced me to Evernote, which I now swear by to keep my projects organized. Now, he is my mentor-turned-collaborator, and I have had the opportunity to work on an exciting project with him, described in Chapter 3. For that project, I thank his graduate students, Darren Sipes and Arielle Stoian, for generating a lot of the *in-vitro* data. Also, they were amazing hosts when I gave an invited talk at Clarkson University. I also acknowledge Dr. Feng Chen for giving me and helping me culture C2C12 cells, and giving me multiple protocols for biological assays. Of course,

for translational work, you eventually have to move beyond cells and into animal models, and it was Dr. Sungsoo Seth Lee who first introduced me to the *in-vivo* work I would end up doing. He taught me what spinal fusion was, what peptide amphiphiles could do for it, and how to conduct a successful *in-vivo* study (in collaboration with the Hsu Lab). He was also the first person to show me how to dissolve $V_3A_3E_3$ PA, which I used throughout my entire PhD. After Seth left, Dr. Mark McClendon conducted a lot of *in-vivo* studies (also in collaboration with the Hsu Lab), and he generated data that was extremely helpful to my research, specifically, Chapter 5 of this thesis. I would also like to thank Dr. Faifan Tantakitti and Dr. Christina Newcomb, who were senior graduate students when I was just beginning my PhD journey. They were both always approachable when I had questions, and even after they both left the lab, they were easily reachable by email. I would also like to thank Miranda So, who was a great labmate, classmate, and friend who made the beginning of graduate school much more enjoyable. I would also like to thank the staff who keep the lab running, which include Maura Walsh, Laura Fields, Todd Linton, Anastasiia Wedding, Daniel Allar, Matthew Irwin, and Daniel Carstensen. I also acknowledge Mark Seniw for creating beautiful Cinema 4D graphics that bring to life the scientific concepts we dream up, but can't quite express visually with limited artistic skills.

With a highly interdisciplinary research project like mine, it is unlikely that one lab could handle all its parts. I could not have completed this work without the Hsu Lab, lead by Profs. Erin Hsu and Wellington Hsu. I have always been impressed by how efficiently Prof. Erin Hsu runs her lab, as well as her extensive knowledge in experimental design and bone biology. Dr. Wellington Hsu is a brilliant orthopedic

surgeon who was willing to take time out of his busy schedule to talk to me about the bone scaffolds I was developing, and how I could make my materials clinically feasible. I would also like to thank Prof. Chawon Yun, for being such an amazing collaborator from the Hsu Lab. He was always willing to help me with biological experiments, and also always willing to eat the results of my cooking and baking experiments (not conducted in the lab). I also want to thank Soyeon "Sophia" Jeong, for always being willing to answer questions and greeting me when I entered the Hsu Lab. I would have no *in-vivo* data at all if it weren't for Allison Greene, Jonathan Yamaguchi, Mitchell Hallman, and David Ellenbogen, who are Hsu Lab fellows currently in medical school, as well as Vivek Shah, a volunteer researcher in the Hsu Lab. We have recently started a new exciting collaboration with the Hsu Lab, for which we are very lucky to have Dr. Silvia Minardi. She is extremely knowledgeable in working with biomaterials, and in the short time that she's been here, I've learned a lot from talking to her.

Getting a PhD in Materials Science and Engineering requires having materials to work on, and I would have had none without the Peptide Core at the Simpson Querrey Institute. For that, I acknowledge Dr. Mark Karver, the director of the Peptide Core. In addition to running the core facility that has made several grams of peptide amphiphiles for me, he is a great collaborator on a project I'm working on now, related to the scale-up manufacturing of these materials. Self-assembly is complicated, and I'm glad to be working with someone who is knowledgeable in chemistry and also patient with all the issues non-covalent interactions can cause. I want to thank the people in the Peptide Core who have made countless molecules for me, including Dr. Suvendu Biswas, Emily Testa, and Charles "Chuck" Bressan. I also want to thank Christopher Tarczynski, the Peptide

Core staff member who conducted countless mass spectroscopy experiments for me. I was extremely honored to have ordered the last batch of $V_3A_3E_3$ PA he made, before he left to pursue his dreams of becoming a nurse. We took a picture to commemorate his last $V_3A_3E_3$ PA batch, and it is still hanging on the SQI kitchen bulletin board.

I could not have completed this work without the numerous core facilities at Northwestern University. My work has involved a lot of microscopy, and I would have no microscopy skills if it were not for Charlene Wilke and Dr. Jessica Hornick of the Biological Imaging Facility, as well as Dr. Constadina Arvanitis, Dr. Joshua Rappoport, and Dr. Wensheng Wilson Liu of the Center for Advanced Microscopy. For more spectroscopic techniques, I acknowledge Theint Aung, David Bettinardi, Patrick Brechka, and Dr. Arabela Grigorescu of Keck Biophysics Facility. Theint was the first person to discover that the NanoSight could be used to image nanofibers floating around in solution, which was a highly exciting moment for the both of us. For me, it was also the experiment that set off my first successful project, and what would become Chapter 4 in this thesis. She left to pursue a PhD at the University of Chicago, and while I missed being able to ask her for help with random equipment, I'm sure she is doing wonderful research. I would like to thank Dr. Carla Shute for maintaining the rheometer in the Materials Characterization and Imaging Facility, because it was really through viscosity measurements that I first got to know my material. I also want to acknowledge Karl Hagglund and Eric Miller of the NUANCE center for their help with SEM. Without them, I could never have corrected the stigmation enough to observe nanoscale features. Later, after I got decent at SEM, Tirzah Abbott joined NUANCE and has been extremely helpful when I run into random problems or forget things after not doing SEM for a

while. I would like to acknowledge Eric Roth and Reiner Bleher of the NUANCE BioCryo Facility, for all their help with sample preparation for electron microscopy. Eric taught me how to use the critical point dryer and glow discharger, without which I would have no samples for SEM or TEM. Although it didn't work out for my project, they also showed me the fancy STEM microscope. I would also like to thank Dr. Steven Weigand of DND-CAT at Argonne National Lab, who taught me how to shoot X-rays at solutions. Once when he was on-call, I called him around 2am in the morning to ask how to take the hard drive out of the computer, which he patiently walked me through. I am grateful to Alexandra Kolot of ANTEC for always keeping the freeze dryers up and running. Anyone who knows anything about my research will know why that was important to my work.

I have said that it was my experience in industry that inspired me to get a PhD. I want to acknowledge my coworkers at Relypsa, which include my boss, Deidre Madson, as well as Victor Ramiro, Dr. Inez Lees, Dr. Xinnan Zhang, Dr. Dale Waters, Dr. Faleh Salaymeh, Hector Nuño, Dr. Eric Connor, Betsy Goka, and Anita Mistry. They were extremely supportive when I was taking the GRE and writing my personal statements, and they shared their own PhD experiences with me as I prepared to embark on my own. I also acknowledge Dr. Martin Ng and Ashish Mitra of Endoluminal Sciences, who gave me a rare opportunity to be involved in all aspects of an early stage startup company.

Having the support of friends is vital to success in graduate school, and it's even better when they have insight into your work. Dr. Tina Chen is a wonderful best friend and brilliant doctor, who helped me understand how patients come to get spinal fusion surgery and how it fits into a patient's overall medical care. Because of her, the

application for my work was not just some abstract concept, but felt like a real medical procedure that my work might impact. It is very easy to get caught up in the stresses of graduate school and forget the ultimate purpose of biomaterials research, which is to help patients. Fortunately for me, Tina provides a constant reminder of this, because the time and effort she puts into providing world-class medical care is phenomenal. Carle Foundation Hospital is very lucky to have her. I also want to thank my family – parents and extended family – who built the foundation that allowed me to reach this point. My father completed his PhD in Chemistry, so I guess the apple did not fall far from the tree. I remember being so excited to see myself in the acknowledgements of his PhD thesis, and now the roles will hopefully be reversed!

LIST OF ABBREVIATIONS

1D	1-dimensional
2D	2-dimensional
3D	3-dimensional
αMEM	Alpha minimum essential media
ACS	Absorbable collagen sponge
ALP	Alkaline phosphatase
ATP	Adenosine triphosphate
a.u.	Arbitrary units
BCA	Bicinchoninic acid (assay)
BMP-2	Bone morphogenetic protein-2
BSA	Bovine serum albumin
CD	Circular dichroism
CryoTEM	Cryogenic transmission electron microscopy
DBM	Demineralized bone matrix
DCM	Dichloromethane
ddH_2O	Double distilled water
DIEA	*N*,*N*-Diisopropylethylamine
DiI	1,1'-Dioctadecyl-3,3,3',3'-tetramethylindocarbocyanine perchlorate
DiO	3,3'-Dioctadecyloxacarbocyanine perchlorate
DMF	Dimethylformamide
DI (water)	Deionized
DLS	Dynamic light scattering
DMEM	Dulbecco's modified essential media
DNA	Deoxyribonucleic acid
ECM	Extracellular matrix
EDTA	Ethylenediaminetetraacetic acid
ELISA	Enzyme-linked immunosorbent assay
EPR	Electron paramagnetic resonance (spectroscopy)

equiv	Equivalents (molar)
ESI	Electrospray ionization
EthD-1	Ethidium homodimer-1
EtOH	Ethanol
FBS	Fetal bovine serum
FDA	Food and Drug Administration (of the United States)
FITC	Fluorescein isothiocyanate
Fmoc	Fluorenylmethyloxycarbonyl
FRAP	Fluorescence recovery after photobleaching
FRET	Förster resonance energy transfer
FTIR	Fourier-transform infrared spectroscopy
HBSS	Hank's balanced salt solution
HBTU	*O*-Benzotriazole-*N*, *N*, *N*′, *N*′-tetramethyluronium hexafluorophosphate
HFIP	Hexafluoroisopropanol
hMSC	Human mesenchymal stem cell
HOBt	Hydroxybenzotriazole
HPLC	High performance liquid chromatography
KSFM	Keratinocyte serum free media
LC-MS	Liquid chromatography-mass spectroscopy
MβCD	Methyl-β-cyclodextrin
MBHA	4-Methylbenzhydrylamine
MTS	3-(4,5-Dimethylthiazol-2-yl)-5-(3-carboxymethoxyphenyl)-2-(4-sulfophenyl)-2H-tetrazolium)
MTT	MTT 3-(4,5-dimethylthiazol-2-yl)-2,5-diphenyltetrazolium bromide
Mtt	4-Methyltrityl
NBD (cholesterol)	22-(*N*-(7-Nitrobenz-2-oxa-1,3-diazol-4-yl)amino)-23,24-bisnor-5-cholen-3β-Ol
NTA	Nanoparticle tracking analysis
PA	Peptide amphiphile
PBS	Phosphate buffered saline

PDL	Poly-D-lysine
PEEK	Polyether ether ketone
PEG	Polyethylene glycol
PFA	Paraformaldehyde
PI	Propidium iodide
PMMA	Polymethyl methacrylate
PyBOP	Benzotriazol-1-yl-oxytripyrrolidinophosphonium hexafluorophosphate
rlu	Relative luminescence unit
rcf	Relative centrifugal force
rpm	Revolutions per minute
ROI	Region of interest
RT	Room temperature
SAXS	Small angle x-ray scattering
SEM	Scanning electron microscopy
TAMRA	5-Carboxytetramethylrhodamine
TCA	Trichloroacetic acid
TEM	Transmission electron microscopy
TFA	Trifluoroacetic acid
ThT	Thioflavin T
TIPS	Triisopropylsilane
Tris	Tris(hydroxymethyl)aminomethane
UV	Ultraviolet
UV-Vis	Ultraviolet-visible (spectroscopy)
v/v	Volume/volume (%)
wt%	Weight percent

Dedicated to my family

and in loving memory of my

grandfather and grandmother

TABLE OF CONTENTS

LIST OF FIGURES

1 INTRODUCTION

1.1 SUPRAMOLECULAR BIOMATERIALS

A *biomaterial* is defined as a substance that is not a food or drug and that is in contact with biological tissue or fluid, for therapeutic or diagnostic purposes.[1, 2] The study of biomaterials is an emerging field, with significant growth in the past few decades. In 1975, there were 12 biomedical engineering departments with around 3000 students in the United States, and by 2005 there were 75 biomedical engineering departments with over 16,000 students.[3] Traditionally, biomaterials were comprised of synthetic substances such as metals, ceramics, or polymers.[2] In these cases, the material is generally intended to provide a structural replacement for missing or diseased tissue, as opposed to mimicking or promoting biological functions. For example, 316L stainless steel was used to make the first generation of cardiovascular stents, because its high compressive strength allows it to physically open blocked vessels and successfully maintain a conduit (Palmaz-Schatz™, Johnson & Johnson). Hydroxyapatite and β-tricalcium phosphate granules can physically fill bone defects (Mastergraft®, Medtronic), and while these minerals do exist in natural bone, this synthetic bone filler is not osteoinductive. Polymethyl methacrylate (PMMA) and polyether ether ketone (PEEK) are used to create implants for craniofacial defects, because their mechanical properties allow a customized fit to each patient's anatomy as well as the rigidity needed to maintain structural integrity (PMMA Customized Implant, PEEK Customized Implant, Stryker CMF). These synthetic materials, held together by ionic and covalent bonds, are mechanically robust and thus highly capable of providing structural support. However,

due to their static nature, they generally cannot interact with native tissue to promote a desired biological response.

Therapeutic products created from biology's own materials can offer improved biocompatibility and biodegradability, an advantage over synthetic materials that are foreign to living organisms. Furthermore, natural biological substances may be recognizable by cells, allowing them to promote certain cellular behaviors. Collagen, a natural protein found in the mammalian extracellular matrix (ECM), has been sourced from bovine and used to create scaffolds for surgical wound healing (Helistat®, Integra LifeSciences). A natural ECM protein, collagen can promote cell adhesion such that the patient's own cells infiltrate the scaffold, degrade it, and eventually heal the wound. Collagen is known to promote binding of integrin receptors,[4] which facilitate cell adhesion,[4] mediate several signaling pathways,[5] and are important in wound repair.[6] Natural polysaccharides have been used to create biodegradable wound dressings, such as algae-derived alginate films (Tegaderm™, 3M) and bacteria-derived cellulose films (Nanoderm™, Axcelon Biopolymers Corporation). Demineralized bone matrix (DBM), of which there are several commercial suppliers, is bone harvested from human cadavers and processed to remove inorganic components. The remaining organic component contains several osteoinductive growth factors, and can be implanted into bone defects to promote healing. Although processing natural biological substances into therapeutic materials is a logical and attractive strategy, the use of synthetic materials would expand diversity in biomaterials design. Thus, the creation of synthetic materials *using biology as inspiration* can be a productive approach to the development of new biomaterials.

Supramolecular chemistry is defined as "chemistry beyond the molecule," and deals with supramolecular structures comprised of several molecules interacting with each other.[2, 7] These interactions are *non-covalent* in nature, and include hydrogen bonding, hydrophobic interactions, π-π interactions, metal chelation, and van der Waals interactions.[2, 7] Biology exploits supramolecular self-assembly to create highly functional structures that are essential to cell function. For example, the DNA double helix is held together by hydrogen bonds between complementary base pairs, and microtubule polymerization occurs through non-covalent self-assembly of tubulin subunits. Phospholipids arrange themselves into bilayers through hydrophobic interactions, forming the architecture of cell membranes. This natural phenomenon has inspired research in creating *synthetic supramolecular biomaterials*, which offer several advantages for therapeutic applications. Compared to the ionic and covalent bonds in metals, ceramics, or polymers, non-covalent bonds are dynamic and highly tunable,[8-11] allowing the rational design of structures that are reversible and responsive to environmental cues.[2, 9, 12-16] Furthermore, non-covalent self-assembly of molecules into supramolecular structures allows *modularity* in the design of supramolecular biomaterials, because the individual molecules can be adjusted to affect the final material.[2, 17-19] Due to these characteristics, supramolecular biomaterials are uniquely qualified to mimic the complex and dynamic nature of biology, and to interact with dynamic biological systems to promote a desired therapeutic response.

To build supramolecular biomaterials, biocompatible molecules containing non-covalent bonding moieties must be used. Through the formation of intermolecular, non-covalent bonds, these molecules self-assemble into functional supramolecular structures

that can exert therapeutic effects. Discovered in the early 1960s, liposomes are spherical vesicles containing at least one lipid bilayer, which surround a hydrophilic core.[20-22] Amphiphilic lipids assume this configuration due to hydrophobic forces, so the liposome is constructed from non-covalent interactions. Around 30 years later in 1995, Doxil® became the first FDA-approved supramolecular "nano-drug," consisting of the chemotherapeutic agent doxorubicin encapsulated within PEG (polyethylene glycol)-based liposomes.[23] While liposomes can be rationally designed for biological applications,[24-27] they are largely a natural occurrence, formed through the same mechanism as cell membrane lipid bilayers. Currently, there is great interest in the synthesis of *bio-inspired* molecules with rationally designed non-covalent bonding motifs, which may self-assemble in ways not found in biology. To that end, one versatile platform for the design of supramolecular structures is *self-assembling peptides*, comprised of amino acids with varying capacities for hydrogen bonding and degrees of hydrophobicity.[13, 15, 28-37] In addition, the peptide chains may be modified by lipids[31, 38, 39] or aromatic groups,[40-43] which allow for additional hydrophobic or π-π stacking interactions. Another peptide-based strategy is to produce engineered *recombinant proteins*, containing segments that can participate in non-covalent interactions.[44-46] While peptide-based approaches exploit the hydrogen bonding capacity of amino acids, small molecules with hydrogen bonding moieties can also serve as the basis for supramolecular structures.[16, 47-53] Other non-covalent motifs that have been used to create synthetic supramolecular systems include the host-guest[54-59] and metal-ligand interactions.[60-62] The great diversity in these approaches – from synthetic small molecules to much larger recombinant proteins – demonstrate that many sources of non-covalent interactions can

be exploited to create supramolecular biomaterials. This thesis focuses on supramolecular biomaterials built from a *self-assembling peptide* platform, comprised of short peptide chains modified with alkyl tails. While this thesis focuses on materials within this specific platform, the results can be applicable to other supramolecular biomaterials.

1.2 PEPTIDE AMPHIPHILES AS SUPRAMOLECULAR BIOMATERIALS

1.2.1 Self-Assembly Across Multiple Scales

Peptide amphiphiles (PA) are a class of self-assembling molecules, comprised of a peptide segment (hydrophilic) conjugated to an alkyl tail (hydrophobic).[31, 32] In canonical form, PAs contain an alkyl tail to induce hydrophobic collapse, a β-sheet forming peptide segment to allow hydrogen bonding, and charged peptide residues to promote solubility in aqueous media (Figure 1-1).[31, 32, 63] This gives rise to a versatile self-assembly platform, which has created a variety of nanostructures including micelles, fibers, and ribbons (Figure 1-1).[63, 64] The fibrous assemblies are particularly useful for biological applications, because they mimic the fibrillar morphology of the natural extracellular matrix (ECM).[31, 64, 65] PA nanostructures can also interact with each other to form hierarchical structures such as closed sacs or aligned fibers, which are generally on the order of microns or larger (Figure 1-1).[63]

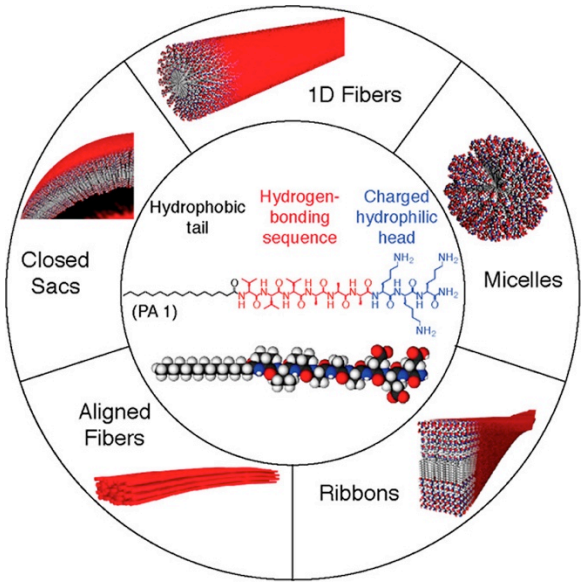

Figure 1-1: The general molecular structure of peptide amphiphile molecules, and the variety of supramolecular structures that can result from their self-assembly. Figure from Hendricks et al., 2017.[63]

The formation of macroscale structures from nanoscale assemblies is particularly interesting to the design of biomaterials, because eukaryotic cells are micron-sized entities that can sense nanoscale cues.[66-69] The hierarchical structures formed by PAs ultimately originate from the nanoscale, where non-covalent interactions between individual PA molecules occur. This allows the "bottom-up" design of supramolecular biomaterials from PAs, in which nanoscale interactions may be tweaked to either directly affect cell behavior or to tune the larger scale structures that interact with cells (Figure 1-2). When cells come into contact with hierarchical structures of PA nanofibers, the individual nanofibers may provide nanoscale cues, while the hierarchical structures interact with cells on a larger length scale (Figure 1-2).

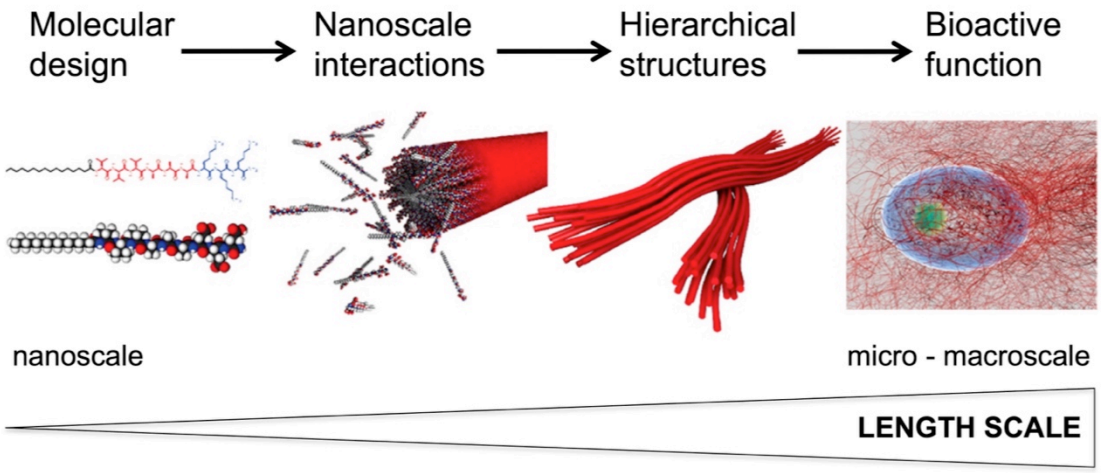

Figure 1-2: A "bottom-up" design strategy for supramolecular biomaterials, starting with nanoscale molecular design and self-assembly. Figure adapted from Hendricks et al, 2017.[63]

Over the past two decades, there have been several reports of hierarchical structures formed by PAs. In 2002, one of the earliest reports of PA nanofibers described birefringent PA gels, indicating alignment over tens of microns.[32] A few years later, the Stupp laboratory began to report the intentional creation of hierarchical structures. A 2008 report showed that when PAs come into contact with a high molecular weight polymer of opposite charge, closed sacs and membranes form due to a diffusion barrier between the two solutions.[70] The PA nanofibers self-assemble perpendicular to the membrane, such that the closed sacs become filled with PA nanofibers.[70] These sacs are on the order of millimeters, and can successfully encapsulate human mesenchymal stem cells (hMSCs) and differentiate them towards a chondrogenic lineage.[70] In another example from 2010, long PA nanofibers were aligned by manual extrusion through a pipet tip, which subjects them to shear forces (Figure 1-3a).[71] The nanofibers were "fixed" in this aligned configuration using salty media, resulting in PA "strings" up to

several centimeters long (Figure 1-3a-b).[71] Cells encapsulated within these structures showed macroscopic alignment, mimicking aligned biological structures such as the spinal cord or muscle (Figure 1-3c-d).[71] Specifically, cardiomyocytes encapsulated within these structures were able to propagate an electrical signal along the string's long axis.[71]

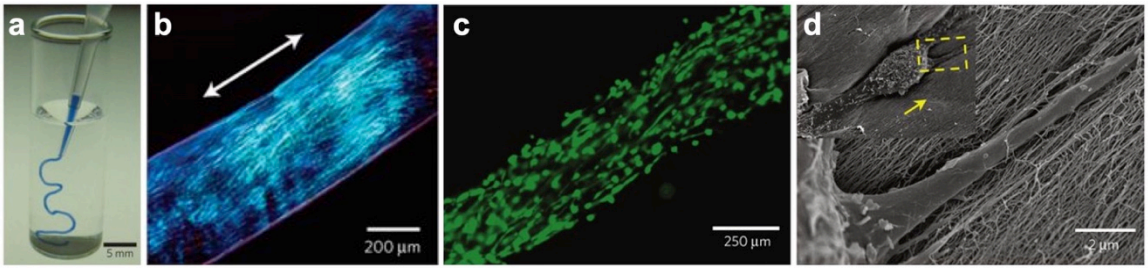

Figure 1-3: PA "strings" containing macroscopically-aligned PA. (a) Photograph showing the creation of aligned PA strings. A PA solution containing trypan blue for visualization is pipetted into PBS. (b) Polarized light micrograph of a PA string, showing a birefringent monodomain arising from nanofiber alignment. (c) Human mesenchymal stem cells (hMSCs) encapsulated within PA strings, visualized with calcein. (d) SEM micrograph of a single cell within an aligned PA string. Figure adapted from Zhang et al., 2010.[71]

Another 2010 report found that, at sufficiently high concentrations of PA, electrostatically charged PA nanofibers spontaneously arranged into a crystalline hexagonal lattice.[72] The nanofibers assumed this configuration to minimize inter-fiber charge repulsion, resulting in a self-assembled system with long range order.[72] More recently in 2018, superstructures of entwined PA nanofibers bearing a short oligonucleotide sequence were reported.[73] Through Watson-Crick pairing, nanofibers bearing complementary oligonucleotides crosslinked with each other to form large

bundles.[73] The formation of these bundles changed the mechanical properties of the PA, which changed the phenotype of neural cells in contact with the material.[73] In all of these examples, the final large scale structures ultimately originate from nanoscale self-assembly. Therefore, a fundamental understanding of nanoscale interactions is crucial to the development of PA structures that serve as biomaterials.

While hierarchical structures should be appreciated, this thesis focuses on tuning the nanoscale non-covalent interactions in PA assemblies. Since the first report of ECM-like PA nanofibers in 2001[31], the Stupp laboratory has continued to study the factors that govern PA self-assembly. In the last five years, significant progress has been made in understanding the internal dynamics and cohesion within PA assemblies. In 2014, conformational dynamics through a PA nanofiber's cross-section were probed using electron paramagnetic resonance spectroscopy (EPR).[74] That work found that the β-sheet forming segment of PA nanofibers exhibited solid-like behavior, while the hydrophobic core and charged headgroups showed more liquid-like dynamics (Figure 1-4).[74] If the PA's hydrogen bonding segment was altered to weaken β-sheet formation, the PA nanofiber exhibited more liquid-like conformation throughout its cross-section (Figure 1-4).[74]

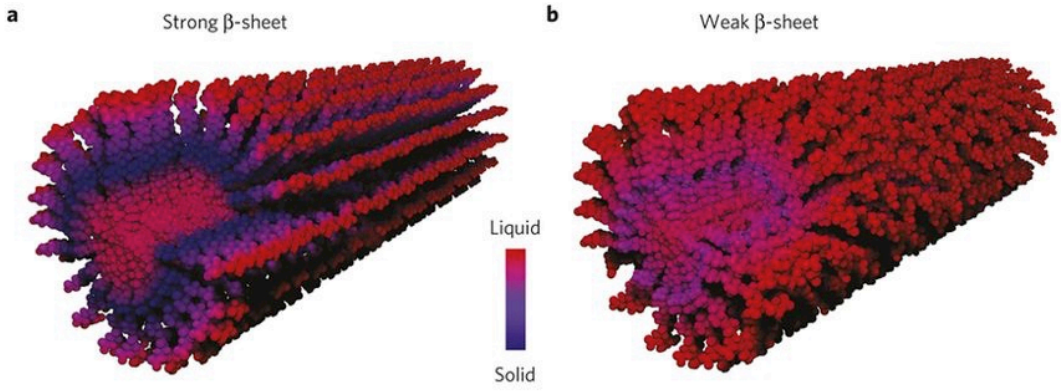

Figure 1-4: Internal conformational dynamics of supramolecular nanofibers, measured by EPR. Figure from Ortony et al. 2014.[74]

The internal dynamics of supramolecular structures should affect how they interact with cells, and indeed, another 2014 report linked nanofiber cohesion to their cytotoxic properties.[75] Cationic species are known to disrupt negatively charged cell membranes, potentially causing cell death,[76-79] so it was not surprising that positively charged PA coatings are cytotoxic (Figure 1-5a-b).[75] However, cell viability was rescued if the PA contained a strong β-sheet forming segment, which enabled self-assembly of highly cohesive nanofibers (Figure 1-5a-b).[75] These cohesive structures promote strong association between cationic PA molecules, which are then less likely to associate with cell membranes.[75] Membrane interactions with cationic species do not always result in cytotoxicity, and in 2016, cationic PA was reported to enhance growth factor signaling in cells (Figure 1-5c-d).[80] Weakly cohesive cationic PA assemblies interacted with the cell membrane to increase lipid raft mobility, which increases the efficiency of receptor activation.[80] Strongly cohesive assemblies at the same concentration did not amplify growth factor signaling (Figure 1-5c-d).[80]

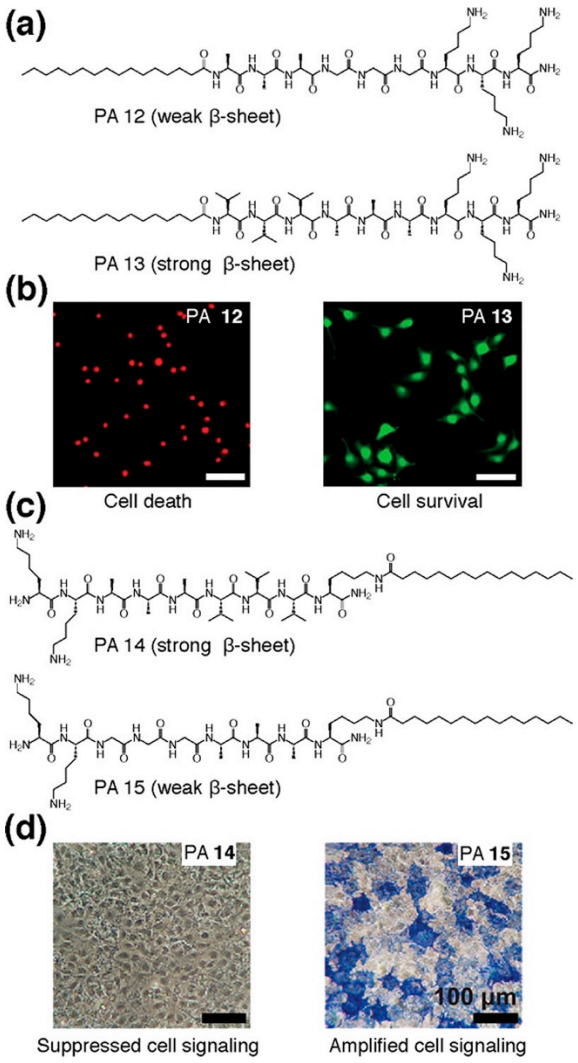

Figure 1-5: Supramolecular cohesion of PA affects biological response. (a,c) Cationic PAs with different propensities for β-sheet formation, due to amino acids in the hydrogen bonding portion. (b) Fluorescence images of live (green, calcein) or dead (red, EthD-1) MC3T3 cells cultured on indicated PA surfaces. Scale bars: 100 μm (d) Fast-blue staining for alkaline phosphatase activity in C2C12 cells, treated with the indicated PAs along with a sub-efficacious dose of recombinant bone morphogenetic protein - 2. Figure from Hendricks et al., 2017,[63] adapted from original images in Newcomb et al., 2014[75] and Newcomb et al., 2016.[80]

In 2016, researchers used super-resolution microscopy to examine molecular exchange between nanofibers.[81] They found that hydrogen bonding interactions along the nanofiber are heterogeneous, such that the nanofibers contain a variety of substructures.[81] Some substructures may be more "active" than others, and thus more inclined to engage in exchange.[81] When PA molecules exchange between nanofibers, they appear to exchange as members of "active" substructures as opposed to individual monomers.[81] This structural diversity within PA nanofibers is likely to be important for their interactions with biological systems, just as nanofiber cohesion was shown to be important for cytotoxicity and growth factor signaling. Following from these recent works, this thesis further probes non-covalent interactions within PA assemblies, with a specific focus on characteristics important to the design and clinical translation of biomaterials.

1.2.2 Advantages of Non-Covalent Nature

Self-assembled PA structures hold many advantages that are characteristic of supramolecular systems, which were discussed in Chapter 1.1. The hydrogen bonds among PA molecules are highly tunable, reversible, and modular, which has allowed the creation of biomimetic structures.

Highly Tunable

PA nanofibers are reminiscent of natural extracellular matrix (ECM),[31, 64] and are capable of forming self-supporting gels through ionic crosslinking of charged

headgroups. These PA gels can serve as artificial scaffolds that support cells, which are known to be sensitive to mechanical cues.[82-85] The mechanical properties of these gels can be tuned by making small adjustments to the PA's amino acid sequence. In one report, researchers systematically varied the number and position of valine and alanine residues in the PA's β-sheet forming segment, which changed the storage modulus of PA gels.[86] Valines tended to increase the stiffness of the PA gel, but the order of valines and alanines was also important.[86] These mechanical differences were attributed to intra-fiber hydrogen bonds, with some peptide sequences promoting a "twisted" β-sheet configuration that weakened the gels.[86] Interestingly, all PAs in this work self-assembled into high-aspect-ratio nanofibers, which were morphologically similar even as the hydrogen bonding configuration and mechanical properties changed.[86]

The ability to vary PA mechanical properties through manipulating the hydrogen bonding sequence was later exploited to design scaffolds for muscle regeneration. In that work, three different PAs were found to create gels of varying stiffness (Figure 1-6a), despite all self-assembling into similar long nanofibers that produced similar birefringent features (Figure 1-6b).[87] Aligned PA strings containing encapsulated muscle stem cells were created using a previously described technique (Figure 1-3),[71] mimicking the alignment of muscle fibers. These PA strings containing cells were implanted into muscles, with the PA's alignment matched to the muscle's fiber alignment.[87] Quantitative analysis of encapsulated cells showed increased directionality in stiffer PA strings, demonstrating that higher PA stiffness promoted cellular alignment (Figure 1-6c-d).[87] These differences in cellular alignment were caused by changes to the PA's amino

acid sequence (Figure 1-6a), demonstrating that the material can be tuned at the nanoscale to create a desired biological behavior.

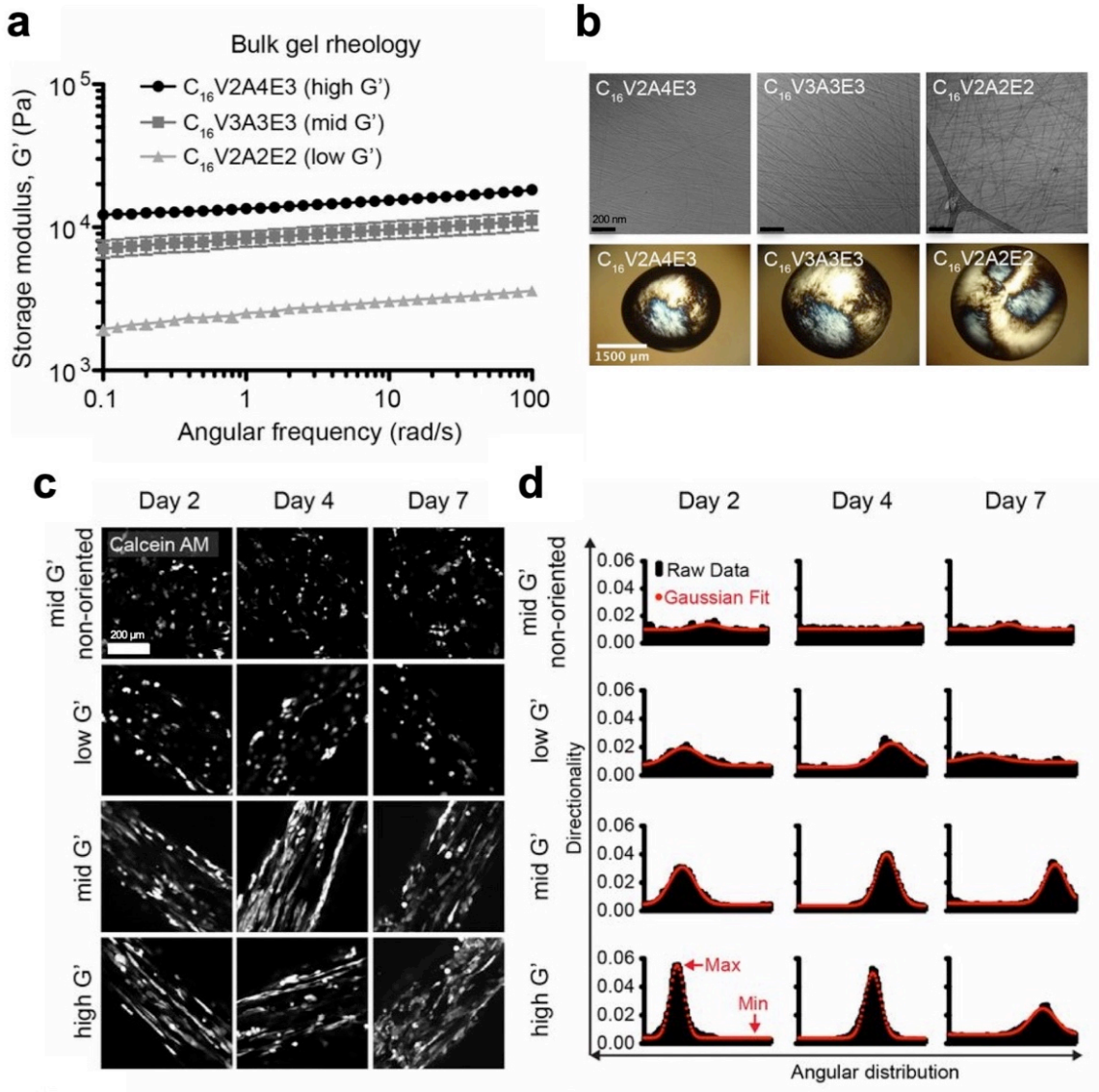

Figure 1-6: Tunable PA scaffolds for muscle regeneration. (a) Storage modulus of PA gels with different peptide sequences. (b) Cryogenic transmissin electron (top) and polarized light (bottom) micrographs of PAs analyzed in panel *a*. These micrographs are of PA solutions and not gels. (c) Confocal micrographs of calcein-stained C2C12 cells within PA strings, created with

PAs analyzed in panel *a*. (d) Directonality analysis from the images in panel *c*. Figure adapted from Sleep et al, 2017.[87]

Reversible

Due to their non-covalent nature, PA assemblies can exhibit reversibility in self-assembly. In the first report of PA nanofibers in 2001, the nanofibers contained thiol groups that could be reversibly crosslinked through oxidation and reduction.[31] More recently, a covalent-supramolecular hybrid polymer was created using PAs as the supramolecular component, and the PA component could be reversibly extracted and re-formed to affect the overall hybrid structure.[88] In another recent report, PA nanofibers bearing complementary DNA strands reversibly formed bundled superstructures (Figure 1-7).[73] Hybridization of the complementary DNA sequences allowed the nanofibers to entwine and form large-scale bundles, which could be dissolved using an invader oligonucleotide to disrupt the Watson-Crick interactions (Figure 1-7).[73] When no superstructured bundles were present, astrocytes cultured on the PA nanofibers adopted a naïve phenotype (Figure 1-7).[73] The formation of bundles increased the storage modulus of the PA surface, which caused astrocytes to exhibit a reactive phenotype (Figure 1-7).[73] When the bundles were dissolved, once again decreasing the storage modulus of the PA, previously reactive astrocytes switched to a naïve morphology (Figure 1-7).[73] Through the use of non-covalent interactions, reversible structures can be created and destroyed, which can be used to control biological outcomes.

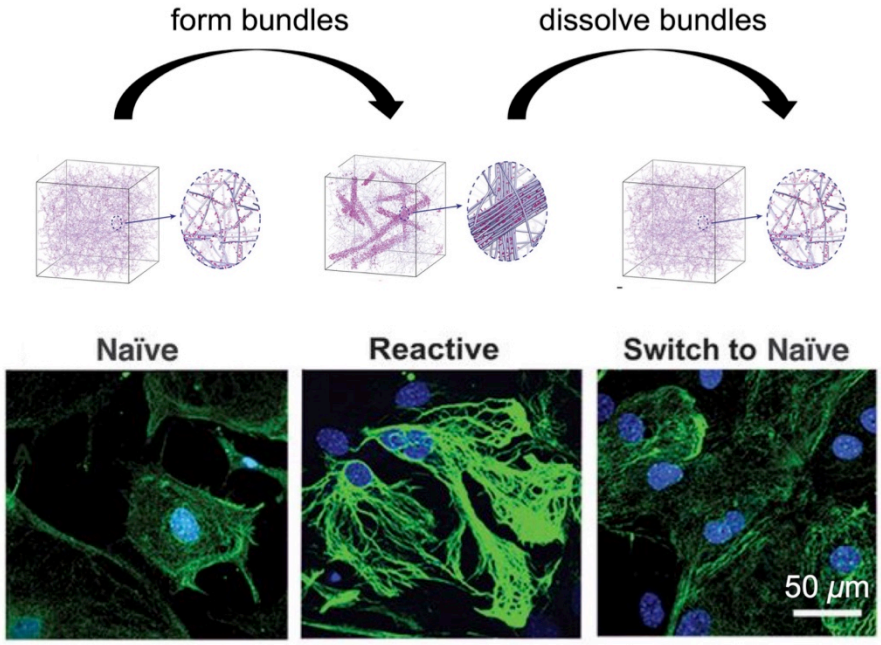

Figure 1-7: Reversible PA bundles direct astrocyte phenotype. Bundle formation promotes a reactive phenotype in astrocytes. Bundle formation can be reversed, which causes the astrocytes to revert to a naïve phenotype. Figure adapted from Freeman et al., 2018.[73]

Modular

The building block for PA assemblies is individual PA molecules, which engage in non-covalent interactions to form the resultant self-assembled structures. Thus, the individual PA molecules in the system can be tuned to affect the structures, allowing for a modular "bottom-up" creation of PA materials. To create an artificial scaffold for neural regeneration, researchers synthesized PA molecules bearing the laminin-mimetic epitope IKVAV (isoleucine-lysine-valine-alanine-valine).[89] Only PA molecules bearing IKVAV were used, which created nanofibers presenting a high density of bioactive signal at their surface (Figure 1-8).[89] The PA nanofibers presented IKVAV at a much higher density than native laminin, which amplified differentiation signals to cells.[89] In other

applications, maximal ligand loading may not be necessary, and precise tuning of ligand density and presentation may be preferred. RGDS (arginine-glycine-aspartic acid-serine), a fibronectin-derived cell adhesion motif, functions with some lateral spacing between the ligands, and the ligand density can also be tuned to affect cell behavior.[90-97] On PA nanofibers, the RGDS density can be modulated by introducing diluent PA molecules bearing no epitope,[98-100] or by synthesizing branched PA molecules that lower packing efficiency.[99] The RGDS signal may be further optimized by adding a linker between the PA and RGDS sequence, such that the RGDS is further away from the nanofiber surface.[98] Longer linkers were associated with increased cell area, improved actin fiber formation, and enhanced β1 integrin signaling in fibroblats.[98] In both the IKVAV and RGDS PA scaffolds, individual PA molecules were tuned to achieve the final epitope topography at the nanofibers' surface. The composition of PA molecules (i.e. diluent versus epitope-bearing PA) could be tweaked to control epitope density, or the PA's molecular design (i.e. branching, linker) could also be adjusted to control epitope spacing and presentation. This demonstrates the possibility for a modular "bottom-up" design strategy in PA assemblies.

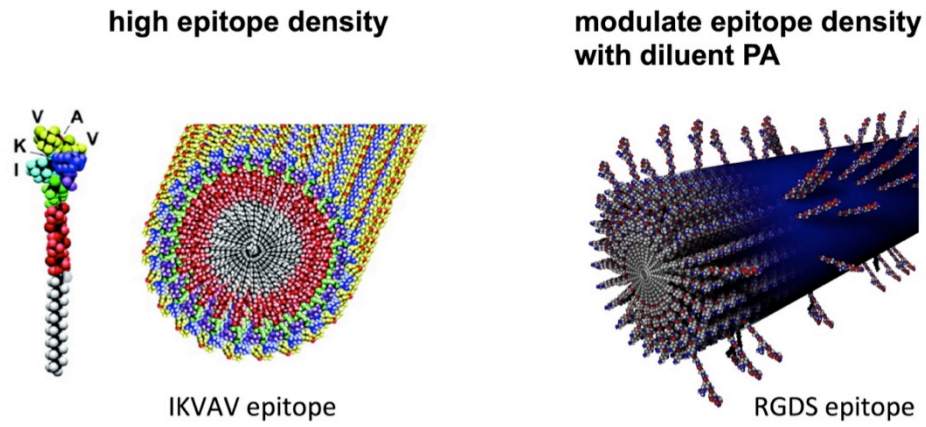

Figure 1-8: Altering epitope density at the surface of PA nanofibers. Figure adapated from Silva et al., 2004[89] and Sur et al., 2015.[98]

1.2.3 Challenges Posed by Pathway Dependence

As discussed in Chapter 1.2.2, the non-covalent nature of PA assemblies provides many advantages in the design of biomaterials. However, they can also give rise to complex pathway dependence behavior, because non-covalent self-assembly can be highly sensitive to pathway selection.[101-103] One major cause of pathway dependence is the formation of kinetic traps, which prevent self-assembly into thermodynamic structures. Thus, if PA molecules are rationally designed to create certain structures under thermodynamic conditions, the desired material may not be achieved. Conversely, the opposite situation can occur, where kinetically trapped products are more functional and bioactive. In this case, the self-assembly pathway would need to be carefully optimized to promote the formation of kinetic structures. From a functional standpoint, high sensitivity to processing conditions can present difficulties in obtaining "correct" PA assemblies with the desired therapeutic function.

In a 2014 report, researchers found that PA assemblies did not form in the presence of hexafluoroisopropanol (HFIP), a "good" solvent that molecularly dissolves the PA molecules.[102] When PAs were dissolved in HFIP/water mixtures, 21% HFIP was the critical fraction above which PA's could not nucleate β-sheets.[102] However, if the PA was first exposed to a lower HFIP content, such that β-sheet formation occurred, the β-sheets did not readily disassemble upon addition of HFIP.[102] Thus, PA assemblies that had already formed did not disappear immediately when transferred to destabilizing conditions, and instead remained kinetically trapped.[102] Two years later in 2016, the link between kinetic traps and pathway-dependent self-assembly was further explored, and attributed to the existence of *energy landscapes*.[103] Specifically, this work examined electrostatically charged PA under conditions of low and high ionic screening, and found that high charge screening reduced intermolecular charge repulsion to allow β-sheet formation.[103] Therefore, long nanofibers with β-sheet character were the thermodynamic configuration under conditions of high charge screening, while shorter nanofibers with random coil character were preferred in conditions of low charge screening (Figure 1-9).[103] However, if long nanofibers formed and were then transferred to conditions favoring shorter fibers, they did not disassemble right away.[103] In fact, there is an energy barrier to equilibrate kinetic structures to their thermodynamic minimum (171 kJ/mole, Figure 1-9).[103] Long nanofibers were more effective at supporting cell adhesion than their shorter counterparts, demonstrating that energy landscape position is vital to biological function.[103] Furthermore, this work found that freshly dissolved PA solutions contain metastable nanostructures, which can be equilibrated to their global minimum by overcoming an energy barrier (Figure 1-9).[103] These results suggest that PA energy

landscapes can contain a variety of local minima, and different pathways can bring the system to different positions along its energy landscape. Drawing an analogy to protein folding, incorrect pathways can lead to mis-folded proteins, which are considered non-functional positions in their energy landscapes.[104] To deal with this problem, biology has evolved molecular chaperones that direct proteins towards the correct supramolecular folding events.[105, 106] In the absence of chaperones for synthetic surpamolecular systems, optimizing self-assembly conditions becomes much more crucial. For any specific PA system, the desired bioactive structures may lie in one particular local or global minimum, which perhaps can only be achieved with a select few self-assembly pathways. Practically, this can make it difficult to achieve the "correct" structures, particularly when certain processing steps are necessary during clinical translation.

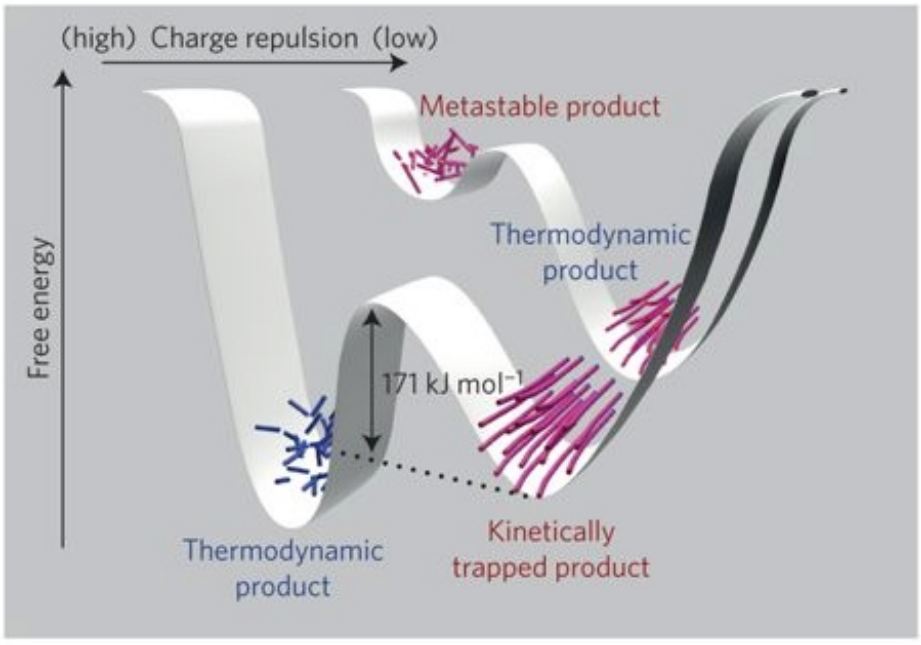

Figure 1-9: Example of a PA energy landscape. Figure from Tantakitti et al, 2016.[103]

1.2.4 Considerations for Clinical Translation

Biomaterials comprised of self-assembling PAs have shown promise in preclinical models for a variety of applications. Supramolecular scaffolds comprised of PA nanofibers have demonstrated the ability to regenerate bone,[107-110] cartilage,[111] muscle,[87] blood vessels,[112] neurons,[89, 113] spinal cord,[114] and peripheral nerves.[115] Furthermore, PA assemblies have been used to develop drug delivery systems,[116-119] anti-cancer therapies,[118, 120, 121] and a treatment for trauma-induced hemorrhage.[122] While these successes in preclinical models support efforts to pursue clinical translation, our understanding of PA non-covalent self-assembly is incomplete. In this thesis, Chapters 2 and 3 will discuss previously unknown factors influencing PA self-assembly, as well as implications for cell-material interactions. Furthermore, the challenges posed by pathway dependent self-assembly must be anticipated during clinical translation. This topic will be addressed in Chapters 4 and 5 of this thesis. The creation of clinically feasible products requires large-scale manufacturing, long-term storage, transportation to end users, and material preparation by end users. These tasks may require certain processing steps, which may not be compatible with stringent requirements for careful selection of self-assembly pathways.

This thesis will discuss in detail one particular processing step that is pervasive in the large-scale distribution of organic materials. *Freeze drying* is often used to preserve organic structures such as proteins,[123] nanoparticles,[124] and liposomes,[125] and cells[126] which can be structurally damaged by ice nucleation, the use of extreme temperatures, and dehydration.[123-126] Due to their non-covalent nature, PA nanostructures in solution are dynamic, so they are typically freeze dried and stored as dry powders. The stable

dried powders can then be rehydrated immediately prior to use in biological applications. Indeed, many pharmaceutical products, particularly protein drugs that are unstable, are supplied as freeze dried powders.[127] One specific clinical application that PAs have shown promise for is *spinal fusion*,[107, 108], a surgical procedure where adjacent spinal vertebrae are fused by growing bone between them. For surgeries such as spinal fusion, an off-the-shelf product that is ready to use with minimal preparation is required, because long preparation times are not permitted in the operating room. Furthermore, the material should have a shelf life on the order of a few years. Thus, the PA must be stored as a freeze dried powder that is ready to use upon rehydration in the operating room. Building on previous knowledge that PAs are highly sensitive to processing pathways, this thesis treats freeze drying as a self-assembly pathway and examines its affects on PA structures.

1.3 THESIS OVERVIEW

Supramolecular interactions bring many advantages to the design of biomaterials, but they can also be challenging to control due to their dynamic nature. If non-covalent interactions in supramolecular biomaterials are thoroughly understood, they can be exploited to harness the advantages while the challenges are successfully managed. The work in this thesis provides methods for tuning the non-covalent interactions in one class of supramolecular biomaterials, built from a self-assembling PA platform. It is organized from general to specific, beginning with a basic science study on PA self-assembly (Chapter 2), then moving on to more applied works that focus on PA-based biomaterials

(Chapter 3 and 4). Finally, it culminates with a report of a PA bone graft for spinal fusion, a very specific clinical application (Chapter 5).

In Chapter 2, a multicomponent PA system comprised of three distinct PA molecules is examined. This system consists of a diluent PA bearing no fluorophore, a PA bearing a FITC fluorophore, and a PA bearing a TAMRA fluorophore, with the diluent PA being in molar excess of the fluorescent PAs. The fluorescent PAs were found to self-sort in solvents of relatively low ionic strength. When salt is added to increase the ionic strength, the fluorescent PAs showed more mixing. By systematically examining the two fluorescent PAs separately, a likely mechanism for the self-sorting is identified. Under conditions of low ionic strength, PAs bearing negatively charged FITC fluorophores cannot associate with negatively charged diluent PA nanofibers, while PAs bearing zwitterionic TAMRA fluorophores can. At higher ionic strengths than screen electrostatic charges, both FITC- and TAMRA-conjugated PAs can associate with the diluent PA matrix, where they "mix."

The rest of this thesis focuses on single component PA systems, which are simpler and thus easier to control. In Chapter 3, non-covalent interactions in cationic PA nanofibers are tuned by changing the alkyl tail position relative to the peptide portion, the hydrogen bonding sequence, and the polarity of a lysine linker. These small molecular changes were found to have a significant effect on the cytotoxicity of PAs. Some PAs were found to induce oncotic cell death by sequestering cholesterol from the cell membrane, a different mechanism from the cell death caused by disruption of the lipid bilayer of the plasma membrane. Whether the PA would sequester cholesterol or not was

linked to the internal structure of PA assemblies, which was varied by small molecular details.

Due to the potential cytotoxic effects of cationic PA, anionic PAs are generally used for regenerative medicine applications. Chapter 4 focuses on one particularly promising anionic PA molecule, and examines how its self-assembled nanostructures change when subjected to freezing or freeze drying cycles. These processing steps are highly relevant to long-term storage and large-scale manufacturing, which are important for clinical translation. Several materials characterization techniques show that structural damage occurs during freezing and freeze drying, with long nanofibers breaking into shorter ones, but this damage can be repaired. The repair is possible because the long nanofibers are a thermodynamically preferred configuration, so the system can be re-equilibrated to this global minimum. The repair pathway can be complicated by the presence of kinetic traps, caused by strong hydrogen bonds that do not dissociate easily to allow rearrangement into longer nanofibers. Certain freeze drying conditions can also shift the global minimum, by increasing the electrostatic charge on the PA molecules. This frustrates self-assembly by introducing charge repulsion, which shifts the thermodynamic minimum towards shorter nanofibers.

Using insights gained in Chapter 4, Chapter 5 presents a freeze dried PA formulation for a specific clinical application, where PAs are used as bone grafts for spinal fusion. Although Chapter 4 demonstrates the capacity of short, freeze dried nanofibers to “repair” into longer ones, the elongation process is kinetically limited and requires an energy barrier to be overcome. Practically, this requires a lengthy preparation procedure after the PA is rehydrated, which is not permissible in the surgical setting.

Thus, thermodynamic long nanofibers will not be attainable, which is concerning because long nanofibers are superior to shorter ones for supporting cell adhesion. However, this thesis identifies a freeze drying pathway that preserves *in-vivo* efficacy in a rat spinal fusion model, despite the obviously shorter nanofibers after freeze drying. A different freeze drying pathway did not product a therapeutic material, demonstrating that not all short, metastable nanofibers are functionally identical.

Chapter 6 concludes by summarizing the insights gained in Chapters 2-5, and providing future outlook for both the PA platform as well as other supramolecular biomaterials.

2 SELF-SORTING IN SUPRAMOLECULAR ASSEMBLIES

2.1 OBJECTIVES AND SIGNIFICANCE

Supramolecular self-assembly enables living organisms to form highly functional hierarchical structures, comprised of individual components that self-organize across multiple length scales. This natural phenomenon has inspired the design of synthetic supramolecular materials, which can contain one or more distinct self-assembling components. The use of multiple components allows greater diversity in material design, but the factors that drive particular monomers to self-sort or co-assemble when mixed together are not fully understood. For example, in the design of PA-based biomaterials, sometimes PAs with biological epitopes are mixed with diluent PAs that do not contain the epitope.[98, 108, 111] In this work, we create a supramolecular matrix comprised of self-assembling peptide amphiphile (PA) nanofibers, to which we introduce a small mole percentage of PA molecules bearing a pendant fluorophore. The fluorescent PAs were conjugated to either fluorescein isothiocyanate (FITC) or tetramethylrhodamine (TAMRA) through a lysine linker, but were otherwise identical to the PA molecules in the rest of the matrix. We found that a pendant FITC significantly interferes with the fluorescent PA's ability to associate with the non-fluorescent PA matrix, while a pendant TAMRA causes no such interference. This difference in interaction strength of FITC- and TAMRA-labeled PA with the supramolecular matrix causes them to "self-sort" in the presence of this matrix, through a phenomenon that is fundamentally different from self-sorting mediated by molecular recognition events.

2.2 BACKGROUND

Living organisms maintain a high degree of self-organization by exploiting non-covalent self-assembly, which has inspired significant research activity on synthetic supramolecular materials over the past decade.[128] In the design of synthetic supramolecular materials, two or more components can be mixed to achieve properties not attainable with only a single molecule. When different molecules are mixed and allowed to self-assemble together, they may self-sort or co-assemble, and the factors that promote one versus the other are not completely understood. Previous work has shown that molecular recognition events, such as hydrogen bonding complementarity,[51, 129] chirality,[130] or sterics,[131] can mediate self-sorting in supramolecular systems. More recently, kinetic control of self-assembly has been used to achieve self-sorting; specifically, the pH can be gradually altered to sequentially induce self-assembly of two different molecules, resulting in a segregated system.[132, 133]

Our laboratory has developed peptide amphiphiles (PA), a class of molecules that self-assembles into a wide range of nanostructures, enabled by hydrophobic collapse and hydrogen bonding.[31, 32] Using this platform, we have developed a variety of biomaterials, many of which are multicomponent systems combining different PA molecules.[98, 107, 108, 110, 111] Although this design strategy has shown promise, the factors that influence whether different PA molecules will self-sort or co-assemble are still poorly understood. Our laboratory and others have shown that supramolecular assemblies are dynamic and can exchange monomers over time, as non-covalent interactions allow individual molecules to leave one assembled nanostructure and join a different one.[81, 134] We hypothesized that stronger cohesive forces within supramolecular assemblies would

decrease the rate of this exchange, thus trapping the system in a phase separated state. In the case of PAs, our laboratory previously showed that counterion screening of charged PAs increases their propensity for hydrogen bonding, thus increasing cohesion within the nanofiber.[103] Thus, we hypothesized that the addition of salt would hinder molecular exchange of PAs among nanostructures, resulting in a phase separated system

2.3 RESULTS AND DISCUSSION

2.3.1 Self-Sorting of Two Peptide Amphiphile Molecules

Our laboratory has worked extensively with PA containing the peptide sequence $V_3A_3E_3$, which promotes self-assembly into highly anisotropic nanofibers.[71, 103, 135] For this work, we synthesized fluorescent analogs of this PA with the goal of examining molecular exchange between the PA nanofibers. We first prepared separate 2 wt% (17.32 mM) aqueous solutions of $V_3A_3E_3$ PA (diluent PA, Figure 2-1), $V_3A_3E_3$ PA conjugated to fluorescein isothiocyanate (FITC PA, Figure 2-1), and $V_3A_3E_3$ PA conjugated to carboxytetramethylrhodamine (TAMRA PA, Figure 2-1). In both fluorescent PAs, the fluorophore is pendant to the PA molecule and does not interrupt the $V_3A_3E_3$ peptide sequence responsible for self-assembly (Figure 2-1). All three PAs were dissolved with 30 mM NaOH to deprotonate the acidic residues and improve solubility. Fluorescent PA solutions (either FITC or TAMRA PA) were then mixed with diluent PA at 1% (v/v). These 2 wt% PA mixtures (diluent PA with either FITC or TAMRA PA) were then diluted with equal volume of pure water or NaCl, such that the resultant solutions contained 1 wt% (8.66 mM) PA and 0, 26, or 150 mM NaCl. At each NaCl

concentration, PA solutions containing diluent and FITC PA were mixed in equal volume with PA solutions containing diluent and TAMRA PA. Thus, the final composition in the PA mixture was 0.99 wt% diluent PA, 0.005 wt% FITC PA, and 0.005 wt% TAMRA PA, and the solution contained either 0, 26, or 150 mM NaCl (Figure 2-1). Previous work from our laboratory has shown that electrostatic screening of charged PAs can promote more cohesive assemblies,[103] and in the current work, NaCl provides Na^+ ions to screen the PA's negatively charged glutamic acids. At 8.66 mM of PA molecules that bear three glutamic acids, 26 mM provides equal charge balance to the PA. In the 150 mM NaCl sample, the salt is in excess of the PA and this condition is also physiological ionic strength. Our laboratory has shown that PA assemblies are dynamic and can exchange monomers over time,[81] and we presumed that NaCl would slow this exchange by charge screening PA molecules and allowing closer associations between them.

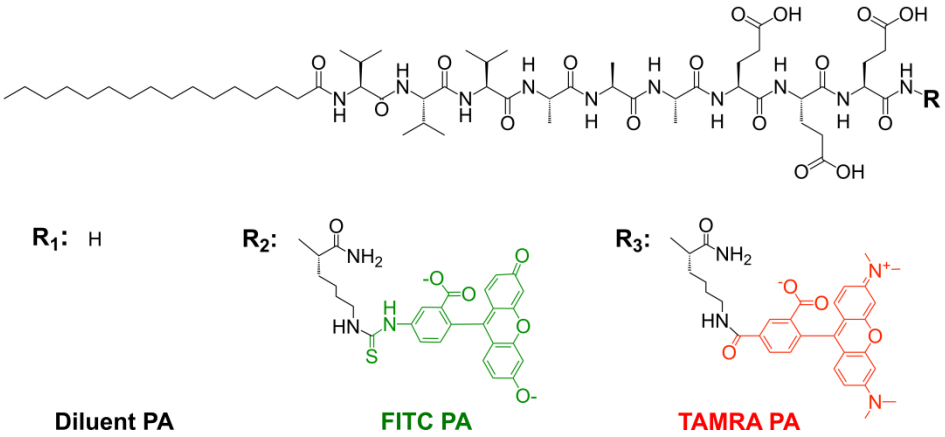

Figure 2-1: Chemical structures of diluent and fluorescent PA molecules. The base PA has a palmitic acid tail conjugated to the peptide sequence $V_3A_3E_3$, and fluorophores are attached to the C terminus via a lysine linker.

To access the spatial proximity of the two fluorescent PAs, we first examined the PA mixtures described in Figure 2-1 by conducting Förster resonance energy transfer (FRET) experiments on the bulk solutions. Since FITC can act as a FRET donor for TAMRA, we irradiated the sample at 450 nm to directly excite FITC (excitation maximum: 490 nm, emission maximum: 525 nm) but not TAMRA (excitation maximum: 555 nm, emission maximum: 585 nm). TAMRA, the FRET acceptor, will emit only if it receives energy from FITC, which can only occur if the two fluorophores are within a few nanometers of each other. If this energy transfer occurs, donor (FITC PA) emission is quenched while acceptor (TAMRA PA) emission increases. When the PA samples are analyzed while freshly dissolved, immediately after they are created, the emission spectra show a TAMRA emission peak in samples with and without NaCl (Figure 2-2 left).

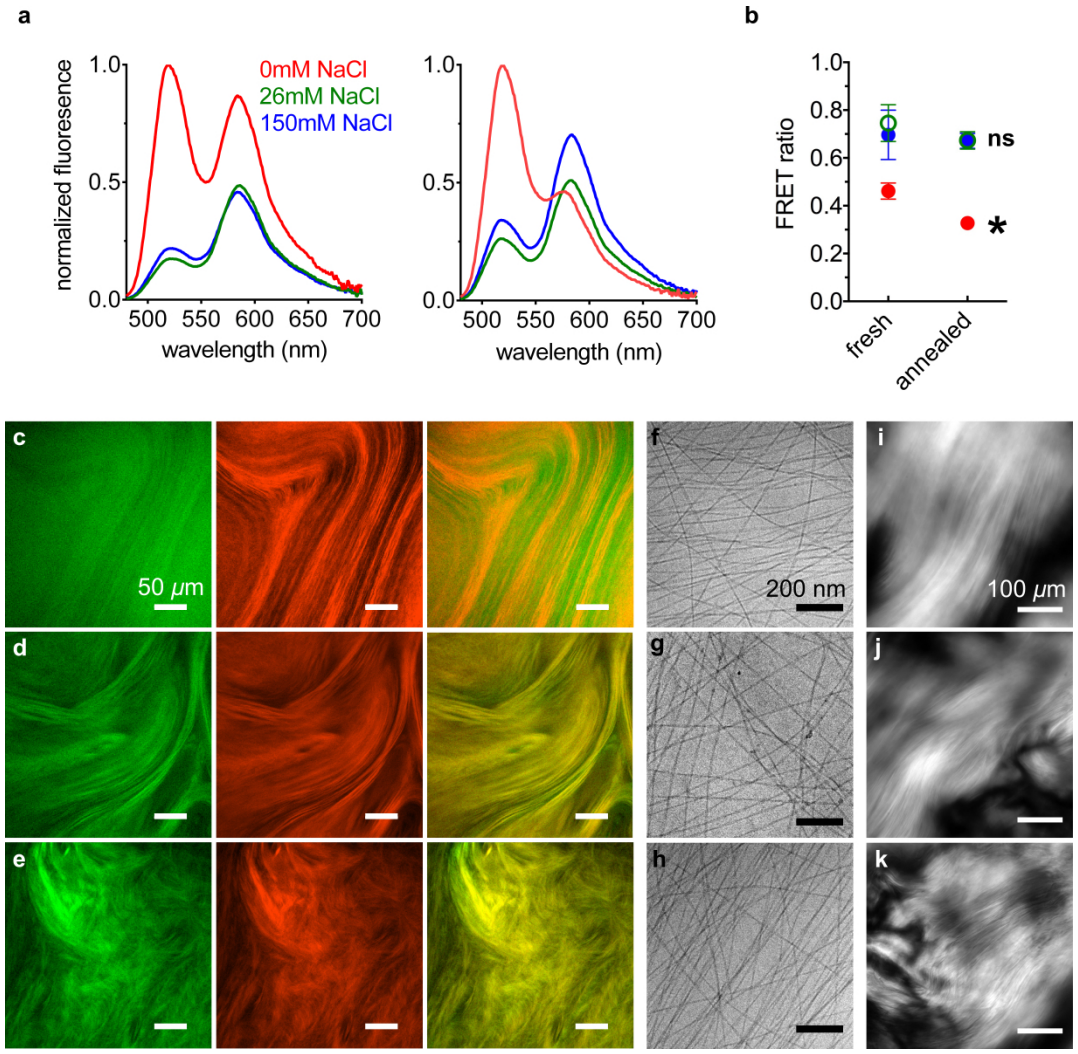

Figure 2-2: PA mixtures containing diluent, FITC, and TAMRA PA. (a) Fluorescence emission spectra of PA mixtures excited at 450 nm, while freshly dissolved (left) and after annealing (right), at the indicated NaCl concentrations. (b) Förster resonance energy transfer (FRET) ratios of fluorescence emission spectra shown in panel *a*. Error bars represent the standard deviation. Confocal micrographs of annealed PA mixtures containing (c) 0, (d) 26, and (e) 150 mM NaCl (left - FITC channel, middle – TAMRA channel, right – merge). Cryogenic transmission electron micrographs (cryoTEM) of PA mixtures containing (f) 0, (g) 26, and (h) 150 mM NaCl. Cross polarized light micrographs of PA mixtures containing (i) 0, (j) 26, and (k) 150 mM NaCl. (*FRET ratio of annealed 0 mM NaCl sample is significantly different than the freshly dissolved 0 mM NaCl sample, paired t-test, $p < 0.05$; ns: FRET ratio of annealed 26 and 150 mM NaCl samples are not significantly different than their corresponding freshly dissolved samples)

We note that the overall fluorescent signal is lower when NaCl is present, which is likely due to FITC self-quenching. When FITC PA is mixed with diluent PA alone, with no TAMRA PA, salt-dependent quenching is observed (Figure 2-3). Fluorescein is known to self-quench when two molecules come within a few nanometers of each other,[136] and our laboratory previously showed that salt counterions allow charged PA molecules to pack closer together by screening their charges.[103] Thus, we hypothesize that the fluorescence quenching is due to PA molecules packing more closely within the nanofiber, which allows for more self-quenching events. This would reduce the amount of FITC fluorophores that can potentially interact with TAMRA, but the shape of the emission spectra still shows a TAMRA peak, indicating that FITC and TAMRA are engaging in FRET interactions when NaCl is present.

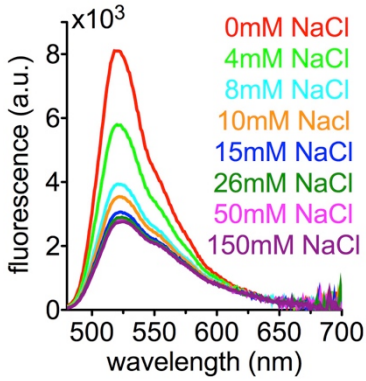

Figure 2-3: Fluorescence spectra of freshly dissolved PA mixtures containing FITC PA and diluent PA, at indicated NaCl concentrations.

Next, the PA mixtures were subjected to a thermal annealing cycle (80°C for 30 minutes, slow cool overnight), which was previously reported to induce PA self-assembly

into long nanofibers.[71, 103] We have previously shown that PA nanofibers are highly dynamic and can thus exchange monomers over time,[81] and that this exchange is likely to be important for nanofiber elongation.[135] Since the FITC and TAMRA PA are mixed before the annealing cycle, when nanofiber elongation occurs, we expected annealing to promote mixing of the fluorescent PAs. Instead, we were surprised to find that the emission spectrum shifts to show noticeably less donor quenching and less acceptor excitation in the absence of NaCl (Figure 2-2a right). In samples containing either 26 or 150 mM NaCl, the spectra do not show significant changes in FRET upon annealing (Figure 2-2a right). Similar to the results with freshly dissolved PA (Figure 2-3), the overall fluorescent signal is lower when NaCl is present, which is likely due to FITC self-quenching (Figure 2-4).

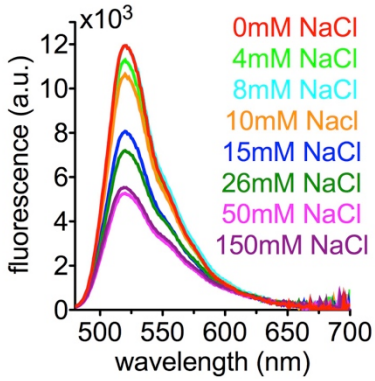

Figure 2-4: Fluorescence spectra of annealed PA mixtures containing FITC PA and diluent PA, at indicated NaCl concentrations.

We quantified the FRET behavior in Figure 2-2a by calculating a FRET ratio for each sample (Figure 2-2b). As suggested by the emission spectra, PA mixtures

containing 0 mM NaCl have a lower FRET ratio than PA mixtures containing 26 or 150 mM NaCl, both before and after annealing. Furthermore, the annealing procedure causes a statistically significant decrease in the FRET ratio of the 0 mM NaCl sample, while the FRET ratios of the 26 and 150 mM NaCl samples remain unchanged. Counterintuitively, these data suggest that NaCl enables more mixing between FITC and TAMRA PA, and also prevents the annealing-induced separation observed in the 0 mM NaCl sample. Interestingly, when no NaCl is present, shorter heating times also sufficient to induce the separation observed by FRET (Figure 2-5) and this separation also occurs at lower PA concentrations (Figure 2-6). When NaCl is added to an already annealed, salt-free, separated system, it appears to induce mixing almost immediately (Figure 2-7).

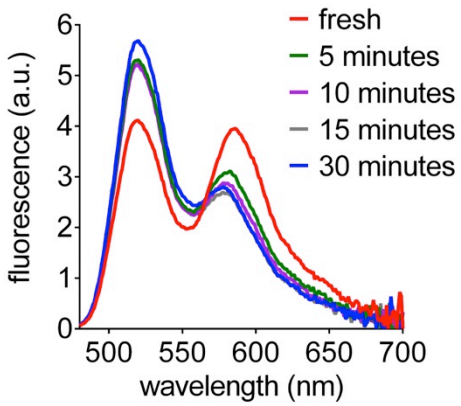

Figure 2-5: FRET spectra of PA mixtures containing 0 mM NaCl, heated at 80°C for the indicated times. Excitation: 450 nm.

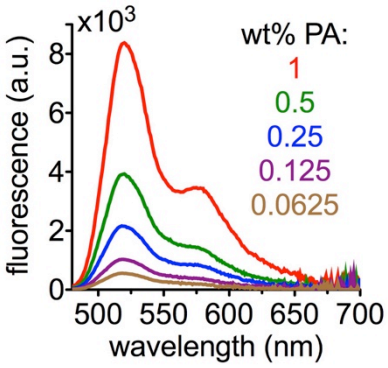

Figure 2-6: FRET spectra of PA mixtures at indicated PA concentrations, in 0 mM NaCl. Excitation: 450 nm.

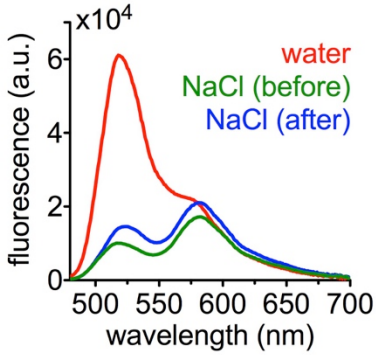

Figure 2-7: FRET spectra of annealed PA mixtures containing NaCl, added before or after annealing. For comparison, annealed PA containing no NaCl is shown. Excitation: 450 nm.

Since NaCl should allow more cohesive nanofibers by charge screening the PAs,[103] we expected less PA exchange between nanofibers in samples containing NaCl. Furthermore, we did not expect the annealing procedure to cause an apparent separation between the fluorescent PAs, because they were mixed before annealing and allowed to self-assemble together during annealing. Since the annealing procedure thermally equilibrates the self-assembling system to its energy minimum,[103] we hypothesized that a

phase-separated system may be more stable under salt-free conditions. Thus, we proceeded to further examine the annealed PA mixtures.

Because FRET efficiency can also be affected by the relative orientation of the fluorophore dipoles,[137] we wanted to examine the spatial distribution of dyes using another technique. We imaged the annealed PA mixtures using confocal microscopy, which examines the samples at the micron-scale. Conversely, since FRET interactions can only occur if fluorophores are within a few nanometers of each other, those experiments report on nanoscale features of the samples. In annealed PA mixtures containing no NaCl, the FITC and TAMRA channels appear different and the merged image shows poor overlap (Figure 2-2c). Conversely, PA mixtures containing either 26 or 150 mM NaCl show similar features in the FITC and TAMRA channels, and the merged image shows more overlap (Figure 2-2d-e). Interestingly, the FITC channel shows qualitatively weaker features than the TAMRA channel when no NaCl is present. When NaCl is added, the FITC channels exhibits stronger micron-scale features, which also match the micron-scale features of the TAMRA channel. Thus, the FRET and confocal microscopy data are consistent, with both showing self-sorting of FITC and TAMRA PA when NaCl is absent and mixing when NaCl is present.

Next, we wanted to further investigate how NaCl affects PA self-assembly, in order to gain insight on how it enables mixing of the fluorescent PAs. We imaged the annealed PA mixtures using cryogenic transmission electron microscopy (cryoTEM), which can reveal the individual PA nanofibers in their hydrated state, avoiding drying effects associated with drop casting the sample. We also imaged the samples using polarized light microscopy, which can reveal organized micron-scale features formed by

the nanoscale assemblies. While FRET and confocal microscopy can only interrogate the fluorescently labeled PAs, these techniques can access the entire PA sample, including the 99% of diluent PA in the mixture. CryoTEM reveals long nanofibers in all samples (Figure 2-2f-h), which are expected to form after the thermal annealing procedure.[71, 103] These long nanofibers are expected to form liquid crystalline domains,[71] and indeed polarized light microscopy shows the presence of birefringent features (Figure 2-2i-k). The cryoTEM and polarized light microscopy data show that NaCl causes no obvious differences in the supramolecular assemblies' morphology, and small angle x-ray scattering (SAXS) experiments also show little change with NaCl (Figure 2-8).

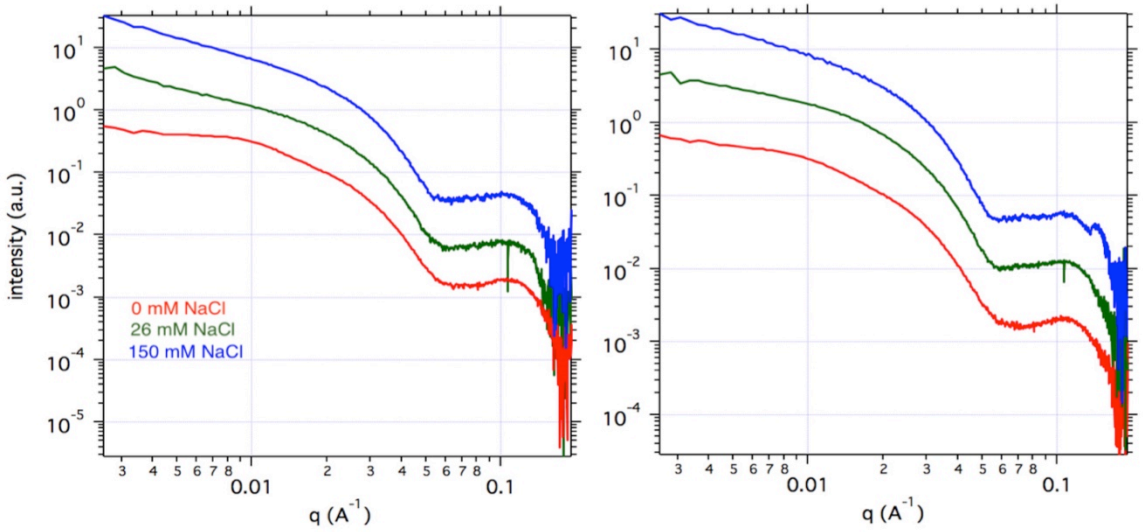

Figure 2-8: SAXS spectra of annealed PA mixtures with indicated NaCl amounts. Two separate experiments are shown.

Thus, morphology cannot explain how NaCl encourages mixing of the fluorescent PAs, but morphology alone does not report on molecular packing arrangement within the

nanofibers. Charge screening by salts is known to promote closer association between PA by decreasing repulsive forces between them,[103] but may not necessarily change the nanofibrous structure. Indeed, we probed the β-sheet content of diluent PA at different NaCl concentrations using Thioflavin T (ThT) dye, and found that it increased with NaCl (Figure 2-9).

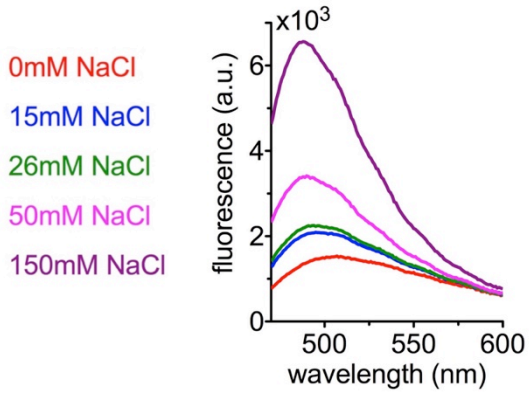

Figure 2-9: ThT fluorescence spectra with freshly dissolved diluent PA, at indicated NaCl concentrations.

We note that the FITC fluorophore attached to the PA bears two negative charges, while the TAMRA fluorophore is zwitterionic and bears zero net charge (Figure 2-1). Thus, it is plausible that charge screening by NaCl affects these two PAs differently, which may change how they interact with the matrix of negatively charged diluent PA nanofibers. Therefore, we wanted to examine the two fluorescent PAs separately, while mixed with diluent PA but not with each other.

2.3.2 Effect of Counterions on Self-Assembly

To study how it interacts with diluent PA assemblies, we mixed FITC PA with diluent PA at range of salt concentrations. First, 2 wt% (17.32 mM) diluent PA and 2 wt% FITC PA solutions were prepared by dissolving PA with 30 mM NaOH, and then FITC PA was mixed with diluent PA at a volume ratio of 1:100. This 2 wt% PA mixture, containing both diluent PA and FITC PA, was then diluted to 1 wt% PA with either pure water or NaCl, such that the final PA solution contained 0.99 wt% diluent PA, 0.1 wt% FITC PA, and 0, 26, or 150 mM NaCl. We used confocal microscopy to image these solutions while freshly dissolved, and found no discernable micron-scale features regardless of NaCl amount (Figure 2-10a-c). After thermal annealing, the PA mixture containing 0 mM NaCl remains featureless, while the 26 and 150 mM NaCl samples exhibit micron-scale hierarchical structures (Figure 2-10d-f). These micron-scale features are stable enough to image while the sample is a bulk solution, which led to us to believe that FITC PA molecules may be less mobile when NaCl is present and these micron-scale structures appear. Therefore, we performed fluorescence recovery after photobleaching (FRAP) experiments to measure the diffusion of FITC PA. We photobleached 10 μm diameter circles and monitored fluorescence intensity recovery, which only occurs from diffusion of unbleached FITC PA into the bleached spot, because photobleaching is irreversible. We monitored fluorescence recovery at short time points after photobleaching (<2 seconds), during which the recovery profile should be dominated by the fastest diffusing species, which is likely to be individual PA molecules as opposed to entire nanofibers. In both freshly dissolved and annealed PA solutions, the presence of NaCl slows diffusion of FITC PA, indicated by the decreased fluorescence

recovery after ~1.8 seconds (Figure 2-10g). Intriguingly, although the 0, 26, and 150 mM NaCl freshly dissolved samples look identical by confocal microscopy, their FRAP signatures are extremely different (Figure 2-10g left). Upon annealing, the mobility of FITC PA in 150 mM NaCl is further decreased and completely immobile, while the mobility of FITC PA in 0 mM and 26 mM NaCl remains similar (Figure 2-10g right). Although the confocal microscopy and FRAP experiments reveal information on the dynamics of FITC PA, we cannot make any conclusions about the non-fluorescent diluent PA. Since confocal microscopy and FRAP can only interrogate FITC PA and not diluent PA, we interpret these data to be the behavior of FITC PA *as it interacts with the diluent PA matrix*.

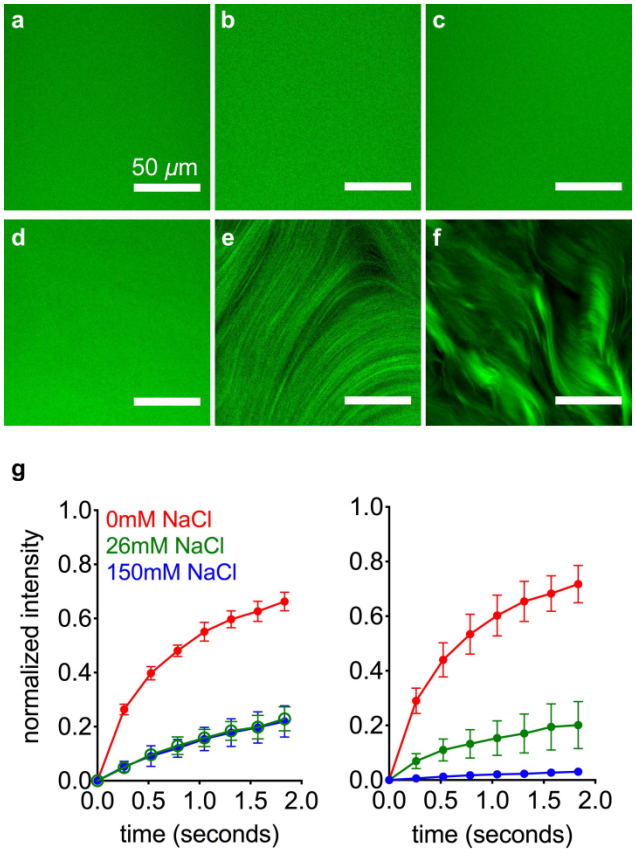

Figure 2-10: Characterization of FITC PA. Confocal micrographs of freshly dissolved FITC PA mixed with diluent PA, containing (a) 0, (b) 26, and (c) 150 mM NaCl. Confocal micrographs of annealed FITC PA mixed with diluent PA, containing (d) 0, (e) 26, and (f) 150 mM NaCl. (g) Fluorescence recovery after photobleaching (FRAP) experiments on freshly dissolved (left) and annealed (right) FITC PA mixed with diluent PA, at indicated NaCl concentrations. Error bars represent the standard deviation.

Next, we repeated the confocal microscopy and FRAP experiments for TAMRA PA, to determine if it behaved differently than FITC PA in the presence of a diluent PA matrix. Using the same procedure as described for FITC PA mixtures, we prepared PA mixtures containing 0.99 wt % diluent PA and 0.01 wt % TAMRA PA and 0, 26, or 150 mM NaCl. Similar to FITC PA mixtures, when the PA samples were freshly dissolved, confocal micrographs show no micron-scale features regardless of NaCl amount (Figure

2-11a-c). After annealing, micron-scale features appear in all these samples, whether they contain 0, 26, or 150 mM NaCl (Figure 2-11d-f). Thus, all confocal micrographs of TAMRA PA are similar to their FITC PA counterparts (Figure 2-11a-f versus Figure 2-10a-f), except for the sample that was annealed without NaCl. In this condition, TAMRA PA exhibits micron-scale features (Figure 2-11d) but FITC PA does not (Figure 2-10d). This was the condition where an apparent separation between the two fluorescent PAs occurred (Figure 2-2c), and that confocal micrograph showed qualitatively weaker micron-scale features in the FITC channel. This is congruous with the confocal micrographs of the two fluorescent PAs alone, where FITC PA (Figure 2-10d) shows no micron-scale features while TAMRA PA does (Figure 2-11d).

We performed FRAP experiments on TAMRA PA, to determine if its diffusion rate was different than FITC PA. In both experiments, the diluent PA matrix is exactly the same, and the differing fluorescent PA is only 1% of all PA in the system. While freshly dissolved, the 0 mM NaCl TAMRA PA sample appears slightly less mobile than its corresponding FITC PA sample, with ~40% (TAMRA PA) versus ~60% (FITC PA) recovery at ~1.8 seconds (Figure 2-10g left versus Figure 2-11g left). Upon annealing, this difference becomes far more drastic, as the TAMRA PA becomes almost completely immobile (Figure 2-10g right versus Figure 2-11g right). In the presence of either 26 or 150 mM NaCl, the FRAP curves of FITC and TAMRA PA are similar, although the annealed 26 mM NaCl FITC PA sample is slightly more mobile than its TAMRA PA counterpart (Figure 2-10g right versus Figure 2-11g right). Thus, the most drastic difference between FITC and TAMRA PA is in the 0 mM NaCl annealed condition, where FITC PA was highly mobile while the TAMRA PA was almost completely

immobile. Again, this is the condition under which apparent separation between the two fluorescent PAs occurred (Figure 2-2c).

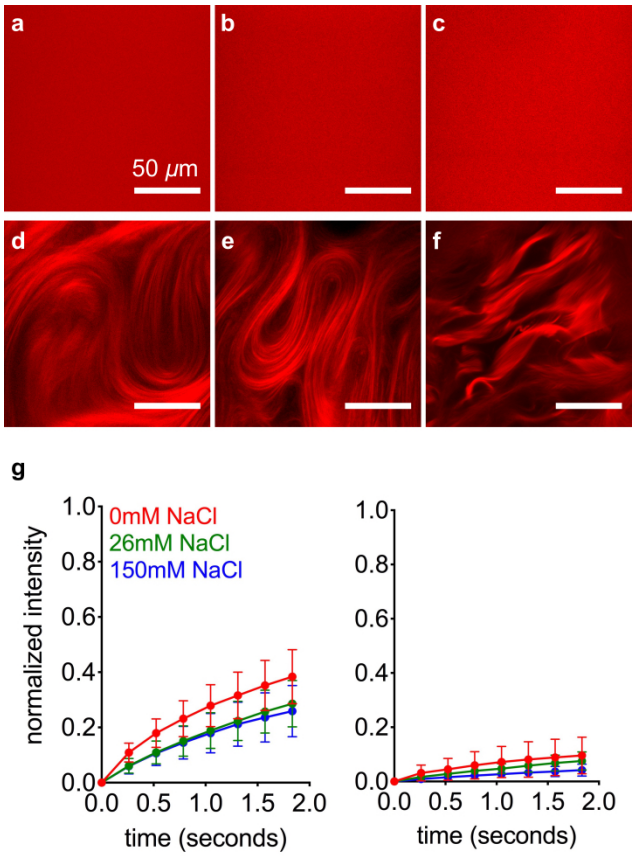

Figure 2-11: Characterization of TAMRA PA. Confocal micrographs of freshly dissolved TAMRA PA mixed with diluent PA, containing (a) 0, (b) 26, and (c) 150 mM NaCl. Confocal micrographs of annealed TAMRA PA mixed with diluent PA, containing (d) 0, (e) 26, and (f) 150 mM NaCl. g. Fluorescence recovery after photobleaching (FRAP) experiments on freshly dissolved (left) and annealed (right) TAMRA PA mixed with diluent PA, with different concentrations of NaCl. Error bars represent the standard deviation.

2.3.3 Proposed Mechanism of Self-Sorting

Based on these data, we hypothesize that FITC PA interacts weakly with the diluent PA nanofibers while TAMRA PA interacts strongly, leading to the apparent separation when they are in the same solution. Since the FITC fluorophore bears two negative charges, it is plausible that charge repulsion prevents the FITC PA from interacting strongly with the negatively charged diluent PA. When NaCl is added, the FITC's negative charges are screened, which enables the FITC PA to associate more closely with the diluent PA assemblies. On the other hand, the TAMRA fluorophore is zwitterionic and overall neutral, so NaCl is not necessary for its association with the diluent PA matrix. Thus, under conditions of low charge screening at 0 mM NaCl, the FITC PA remains in solution around the diluent PA nanofibers whereas the TAMRA PA closely associates with the diluent PA matrix. This leads to spatial separation between the two fluorescent PAs.

To further explore this hypothesis, we modeled the FRAP data using a single exponential model:

$$y = y_0(1 - e^{-t/\tau}) \quad (1)$$

where y is the normalized fluorescence intensity (on a scale of 0 to 1, 0 indicates no recovery after photobleaching and 1 indicates full recovery) and t is the time after photobleaching. By fitting the experimental data, we can determine the constants in the model: y_0, the mobile fraction (thus, $1 - y_0$ is the immobile fraction), and τ, the characteristic diffusion time of the mobile species. Using this model, we analyzed the

FRAP data for FITC PA when it is mixed with diluent PA. In freshly dissolved samples, approximately 30% of FITC PA is immobile if no NaCl is present, and this immobile fraction increases to 70% if either 26 or 150 mM NaCl is added (Figure 2-12a). After annealing, the immobile fraction remains similar to the freshly dissolved state in the 0 and 26 mM NaCl samples, but increases from 70% to 97% in the 150 mM NaCl sample (Figure 2-12a). To further probe the nature of the diffusing species, we used the Soumpasis approximation to estimate their diffusion coefficient from the FRAP data. The diffusion coefficient can give some indication of the diffusing species' size, although other factors can also affect it (i.e. supramolecular interactions with each other or with diluent PA nanofibers). We plotted the diffusion coefficients for FITC PA in various NaCl conditions, along with the hypothetical diffusion coefficient for PA micelles and 200 nm short nanofibers (Figure 2-12b). These hypothetical values are based on the Stokes-Einstein equation, which assumes non-interacting spherical objects. Therefore, this model cannot precisely predict the behavior of all PA nanostructures, but these estimates can help place the diffusing species' size within an order of magnitude. We found that regardless of *how much* FITC PA is mobile and participating in diffusion (i.e. the mobile fraction), the FITC PA that *is mobile* exists in structures of sizes expected for micelles or short nanofibers (Figure 2-12b). We note that the immobile PA, which likely exists in longer nanofibers, creates a hindrance to diffusion that is not reflected by the Stokes-Einstein equation. In the absence of this hindrance, the diffusion coefficients should be higher, which would place the diffusing species much less than 200 nm and closer to micelles (Figure 2-12b). Since our model is not extremely precise, another possible source of diffusion is FITC PA molecules that are exchanging between micelles

or nanofibers. Unimer exchange between micelles has been described in block copolymer micelles.[138, 139] However, the hydrophobicity of the C_{16} alkyl tail should favor hydrophobic collapse into self-assembled structures, so the amount of single FITC PA molecules in solution is likely to be extremely small.

These calculations suggest that the FITC PA mobile fraction is comprised of structures much smaller than 200 nm, so we presume that all longer nanofibers (>200 nm) are immobile in the timeframe of our experiments ($t < 2\ seconds$). Annealed diluent PA nanofibers are significantly over 200 nm, and while they are shorter in freshly dissolved samples, they are still likely to be at least or greater than 200 nm.[103, 135] Therefore, we interpret the immobile fraction to be a rough estimate of the amount of FITC PA molecules that are associated with diluent PA nanofibers, and this interpretation helps explain the confocal micrographs of FITC PA mixed with diluent PA. In annealed solutions, the long diluent PA nanofibers form liquid crystalline structures by aligning with each other. FITC PA that is associated with the long nanofibers will reflect these hierarchical structures in confocal microscopy, which appear in the presence of 26 or 150 mM NaCl (Figure 2-10e-f). When no salt is present, the diluent PA still forms these hierarchical structures, which are visible by polarized light microscopy (Figure 2-2i), but most of the FITC PA (approximately 75%) is not associated with the diluent PA (Figure 2-12a). Instead, the featureless confocal micrograph reflects FITC PA that is diffusing around the diluent PA nanofibers, which likely exists as micelles. Conversely, the relatively shorter diluent PA nanofibers in freshly dissolved solutions do not form hierarchical structures, so no micron-scale structures are visible regardless of whether FITC PA is associated with diluent PA nanofibers or not (Figure 2-10a versus Figure

2-10b-c). In both freshly dissolved and annealed samples with no NaCl, the majority of FITC PA (70 - 75%) does not associate with the diluent PA nanofibers. The FITC fluorophore's -2 charge likely creates charge repulsion between the FITC PA and the negatively charged diluent PA assemblies. When NaCl is added, the FITC's -2 charge is screened, allowing the PA to associate with the negatively charged diluent PA matrix.

For comparison, we performed the same analysis for TAMRA PA mixed with diluent PA, from the FRAP data shown in Figure 2-11g. In freshly dissolved samples, the immobile fraction is around 50% when either 0 or 26 mM NaCl is present, and increases to approximately 65% when 150 mM NaCl is added (Figure 2-12c). Upon annealing, the immobile fraction increases to around 80% in both the 0 and 26 mM NaCl samples, and around 95% in the 150 mM NaCl sample. Compared to FITC PA (Figure 2-12a versus Figure 2-12c), the immobile fraction of TAMRA PA shows much less dependence on NaCl amount and much more dependence on whether or not the sample is annealed. After annealing, the majority of TAMRA PA associates with the diluent PA nanofibers regardless of how much NaCl is present, because the zwitterionic TAMRA fluorophore will not cause electrostatic repulsion between TAMRA and diluent PA. In freshly dissolved samples, when the TAMRA and diluent PA solution have just been physically mixed, the TAMRA PA has perhaps not had time to incorporate into the diluent PA matrix. Similar to mobile FITC PA, mobile TAMRA PA likely exists in small structures on the order of micelles (Figure 2-12d), regardless of how much TAMRA PA is mobile.

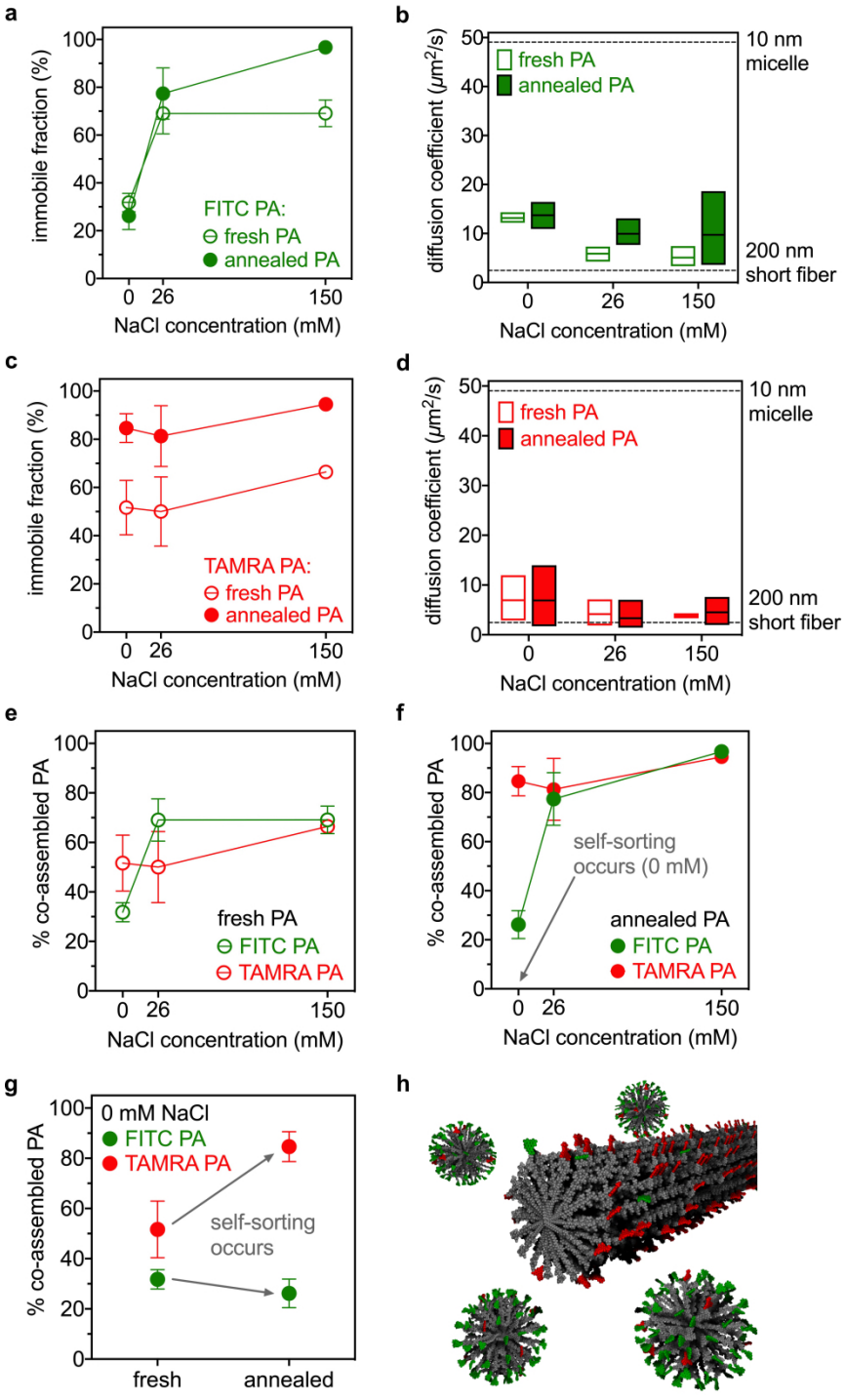

Figure 2-12: Proposed mechanism for self-sorting. (a) Immobile fraction of FITC PA when mixed with diluent PA and (b) diffusion coefficient of mobile FITC PA, at indicated conditions. The dashed lines are hypothetical values. (c)

Immobile fraction of TAMRA PA when mixed with diluent PA and (d) diffusion coefficient of mobile TAMRA PA, at indicated conditions. The dashed lines are hypothetical values. Percentage of FITC and TAMRA PA that is co-assembled with the diluent PA nanofibers when the PA solutions are (e) fresh and (f) annealed, at indicated conditions. (g) The affect of annealing on the amount of co-assembled FITC and TAMRA PA, at 0 mM NaCl. (h) Schematic depicting the system at 0 mM NaCl after annealing. The relative amounts of the fluorescent PAs are not drawn to scale and are exaggerated for clarity. In all graphs with error bars, the error bars are the standard deviation. In all box plots, the line inside the box is at the mean of the data and the box spans the minimum to the maximum.

Due to the noticeable dependence of FITC PA behavior on NaCl amount, we performed FRAP experiments and calculations for additional NaCl concentrations, on annealed samples containing diluent and FITC PA (same ratio as experiments in Figure 2-10g). FRAP data on FITC PA behavior at additional NaCl concentrations show that NaCl decreases FITC PA diffusion in a concentration-dependent matter (Figure 2-13) over the range of 0 – 150 mM NaCl. For comparison, we created a physical PA gel by introducing divalent counterions (Ca^{2+} from $CaCl_2$) that ionically crosslink the PA's negatively charged glutamic acids. These $CaCl_2$ gels contained no NaCl. As expected, FITC PA in this physical gel was mostly immobile. We note that in the 500 mM NaCl sample, the sample is a liquid solution while freshly dissolved by becomes a gel upon annealing.

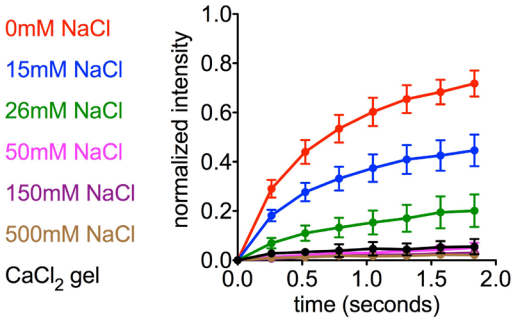

Figure 2-13: FRAP at additional NaCl concentrations for FITC PA, mixed with diluent PA.

We also took confocal micrographs of the samples analyzed in Figure 2-13, and observed the development of micron-scale features as NaCl was added. Interestingly, $CaCl_2$ gels have similar features to liquid solutions of PA containing around 15-50 mM NaCl.

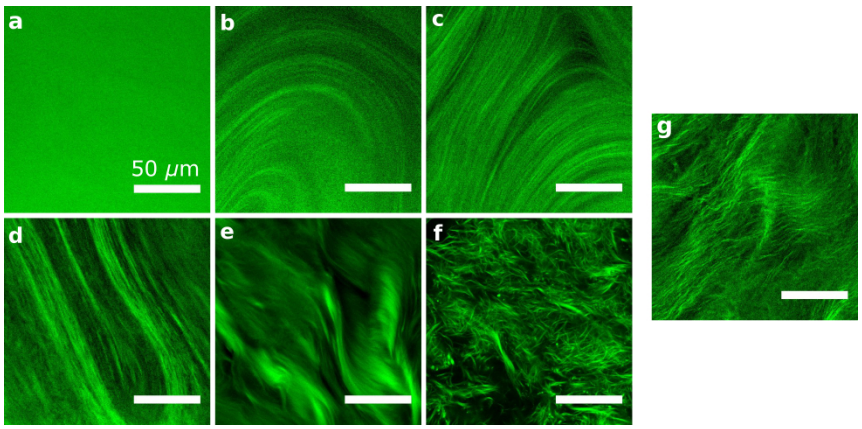

Figure 2-14: Confocal micrographs at additional NaCl concentrations for FITC PA, mixed with diluent PA. (a) 0 mM, (b) 15 mM, (c) 26 mM, (d) 50 mM, (e) 150 mM, (f) 500 mM, (g) $CaCl_2$ gel.

We also conducted a FRAP experiment where *free fluorescein dye* was mixed with PA, as opposed to PA conjugated to fluorescein (Figure 2-15). The presence of NaCl did not affect the mobility of free fluorescein dye that was simply physically mixed with PA, suggesting the PA-mediated self-assembly is responsible for the affect of NaCl on FITC PA diffusion.

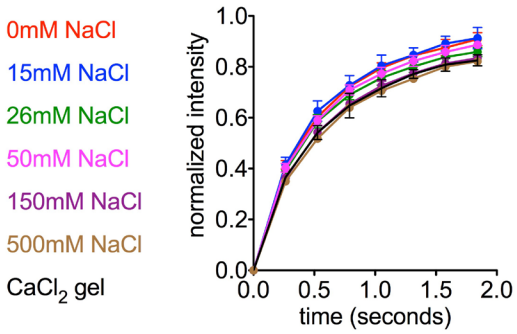

Figure 2-15: FRAP on free fluorescein dye mixed with diluent PA, at indicated NaCl concentrations.

From these FRAP data at additional NaCl concentrations, we calculated the immobile fraction and diffusion coefficient of FITC PA and free fluorescein dye, both of which were mixed with annealed diluent PA (Figure 2-16). The data shows that 0 – 150 mM NaCl is a critical range over which the FITC PA behavior changes drastically. We conclude that, over this range, NaCl significantly affects whether or not FITC PA will interact with the diluent PA matrix, likely by screening the -2 charge on the FITC fluorophores. Furthermore, we note that fluorescein dye is a small molecule around 1 nm, so its diffusion coefficient is much slower than expected from the model. This may

be due to interactions with long diluent PA nanofibers, which the model does not account for, and likely applies to all other calculations.

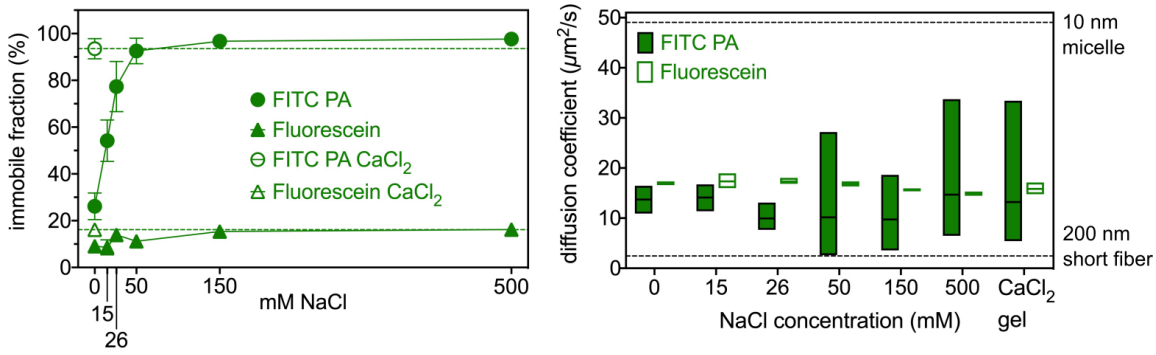

Figure 2-16: Diffusion of FITC PA. Left: Immobile fraction of FITC PA or fluorescein dye when mixed with diluent PA, at indicated conditions. The error bars represent the standard deviation. Right: Diffusion coefficient of mobile FITC PA or fluorescein dye, at indicated conditions. The line inside the box is at the mean of the data and the box spans the minimum to the maximum.

After modeling the FRAP data for both FITC PA and TAMRA PA, we wanted to relate the calculations to the observed self-sorting (Figure 2-2). We interpret the immobile fraction of fluorescent PA to be a rough estimate of the fraction that is incorporated into diluent PA nanofibers, which should be immobile within the FRAP experiment's timeframe (Figure 2-12b, d). The exact nature by which fluorescent PA interacts with and incorporates into diluent PA nanofibers is difficult to probe directly, since fluorescent PA may simply be adsorbed to the surface of the nanofibers, or it may be co-assembled into the nanofibers. We performed cryoTEM on FITC and TAMRA PA alone, without any diluent PA, and found that both were capable of forming nanofibers by themselves (Figure 2-17). Thus, we speculate that the fluorescent PAs co-assemble with the diluent PA nanofibers *if* they interact with the nanofibers at all, so the immobile

fraction can be interpreted as the fraction of fluorescent PA that is co-assembled with the diluent PA matrix. Within this interpretation, we plotted the percentage of co-assembled FITC and TAMRA PA under various conditions, in freshly dissolved and annealed solutions, which contained various amounts of NaCl (Figure 2-12e-f). At the 0 mM NaCl annealed condition where self-sorting was observed (Figure 2-2), we found a substantial difference between the percentage of co-assembled FITC PA and co-assembled TAMRA PA (~25% versus ~85%). Therefore, we conclude that, in 0 mM NaCl annealed samples, the majority of FITC PA is not co-assembled with the diluent PA and instead exists in smaller, less ordered states while the majority of TAMRA PA is co-assembled with the diluent PA nanofibers. This is consistent with the confocal micrographs of FITC and TAMRA PA in different solutions, where FITC PA shows no micron-scale features (Figure 2-10d) but TAMRA PA does (Figure 2-11d). When FITC and TAMRA PA were mixed in the same solution and self-sorting occurred, confocal micrographs qualitatively showed stronger micron-scale features in the TAMRA PA channel (Figure 2-2c). The presence of NaCl charge screens the FITC PA, allowing it to co-assemble into the diluent PA matrix and mix with the TAMRA PA. Indeed, confocal micrographs showed the formation of micron-scale features by FITC PA when salt was added (Figure 2-10e-f).

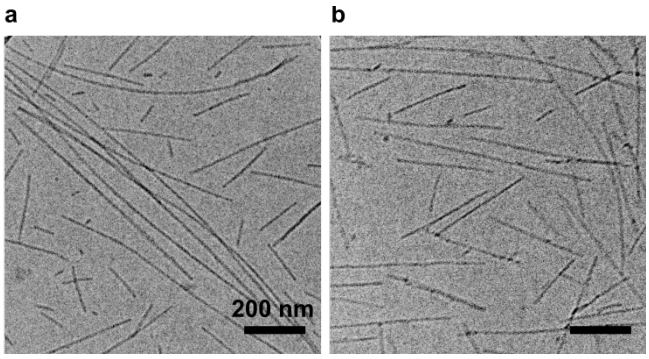

Figure 2-17: CryoTEM of annealed fluorescent PAs alone. (a) FITC PA and (b) TAMRA PA, with no diluent PA.

We note that, in the 0 mM NaCl condition, the annealing procedure *enhanced* the observed self-sorting, indicated by the decrease in FRET behavior (Figure 2-2a-b). The decrease is FRET signal is accompanied by a greater difference in amount of co-assembled FITC PA and co-assembled TAMRA PA (Figure 2-12g), suggesting that differential co-assembled amount is responsible for the annealing-induced self-sorting. The self-sorted system at 0 mM NaCl, after annealing, is depicted in Figure 2-12h. As illustrated, the majority of TAMRA PA is co-assembled into the diluent PA nanofiber, with a small amount existing in smaller structures such as micelles. Conversely, FITC PA exhibits the opposite trend. Thus, the self-sorting between FITC and TAMRA PA at 0 mM NaCl is mediated by their differential ability to interact with the diluent PA nanofiber matrix, which is determined by the strength of repulsive forces exerted by the pendant fluorophores.

Interestingly, physical disruption of the diluent PA matrix using pure mechanical force does not compromise the observed self-sorting, suggesting that the effect is more related to chemical properties. We mechanically fractured the PA nanofibers using two

methods. We subjected annealed PA nanofibers to a freeze-thaw cycle, where the ice crystals are known to break long nanofibers (Chapter 4). In addition to freeze-thawing, we also vortexed annealed PA solutions. We found that vortexting causes a decrease in viscosity, suggesting breakage of the nanofibers from mechanical perturbation (Figure 2-18).

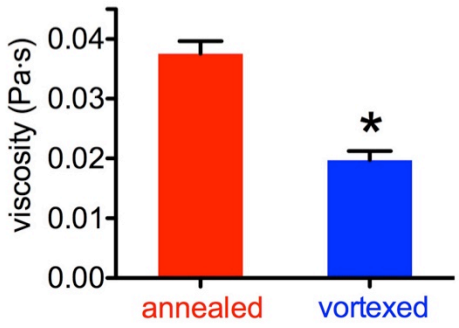

Figure 2-18: Viscosity of annealed PA before and after vortexing (*p<0.05).

Annealed PA mixtures, containing diluent PA, FITC PA, and TAMRA PA were subjected to either freeze-thawing or vortexing, and their FRET spectra were measured. We found that the FRET spectra do not change upon freeze-thawing or vortexing, suggesting that mechanical perturbation of the nanofibers did not disturb the self-sorted configuration (Figure 2-19). Freshly dissolved PA solutions, which contain short nanofibers that have not had time to elongate, exhibit more FRET activity than annealed PA solutions (Figure 2-2a-b). However, since freeze-thawing or vortexing decrease the length of the PA nanofibers without compromising self-sorting, we note that length cannot be solely responsible for the self-sorting.

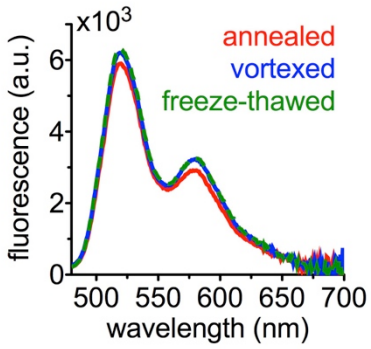

Figure 2-19: FRET spectra PA mixtures after mechanical perturbation, by vortexing or freeze-thawing. An intact annealed PA is included for comparison. Excitation: 450nm.

Previous work from our laboratory suggests that PA nanofiber assemblies are not homogenous, but instead contain "active" and "inactive" clusters, with "active" clusters being more likely to break off a nanofiber and exchange to another one.[81] In the current work, it is plausible that FITC PA form "active" clusters that exchange easily, due to its extra two negative charges, while TAMRA PA exists in more "inactive" clusters, due to its net neutral charge. When NaCl is added to charge screen the FITC PA, it exists in more "inactive" clusters, or perhaps the entire nanofiber becomes more "inactive" as the negatively charged diluent PA is also screened. Although we cannot definitively prove that either fluorescent PA is co-assembling with the diluent PA matrix, the data demonstrates that, under certain conditions, they have different affinities for interacting with this matrix. This difference was linked to an apparent separation between the fluorescent PAs, which are identical in the portion of their peptide sequences responsible for self-assembly and differ only in their pendant fluorophores.

2.3.4 Effect of Diluent PA Matrix on Self-Sorting

Although this work focuses mainly on the effect of the pendant fluorophores, we briefly examined the effects of changing the diluent PA matrix's chemical identity. Instead of having a diluent PA matrix comprised of solely $V_3A_3E_3$ PA ("strong PA"), we introduced an $A_3G_3E_3$ PA molecule ("weak PA," Figure 2-20), which has a weaker propensity for hydrogen bonding. Both PAs have identical hydrophobic tails (C_{16}, palmitic acid) and charged headgroups (E_3, glutamic acids), but the peptide sequence A_3G_3 has much weaker propensity for β-sheet formation than V_3A_3. We also synthesized a fluorescent analog of $A_3G_3E_3$ PA, which bears a pendant FITC fluorophore (Figure 2-20).

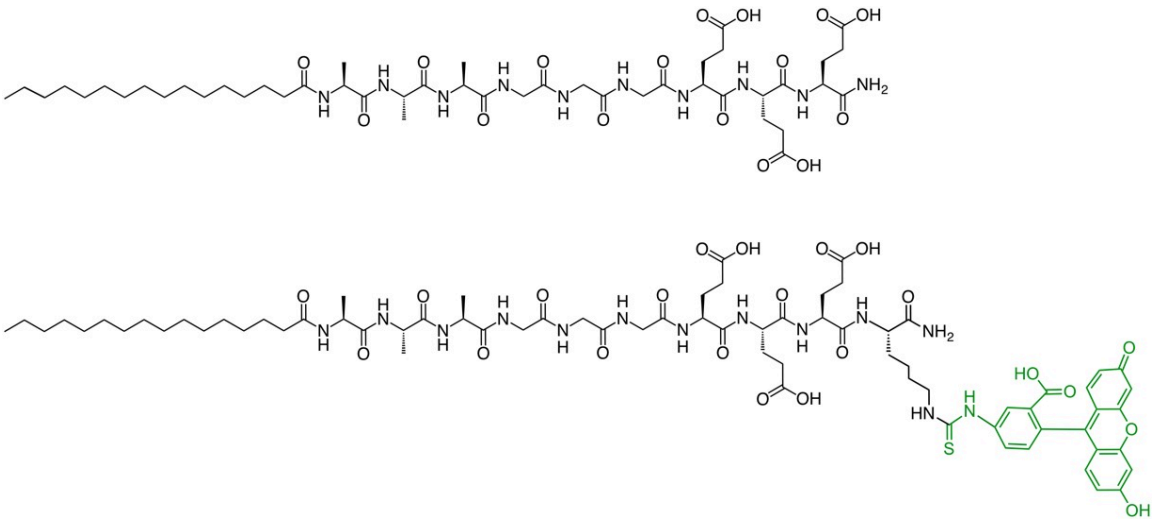

Figure 2-20: Chemical structure of $A_3G_3E_3$ and $A_3G_3E_3$K-FITC (weak diluent PA and weak FITC PA, respectively).

Our laboratory previously showed that similar weak PA molecules self-assemble into less cohesive nanostructures than strong PA,[75, 80] which we confirmed in the current

work with other techniques. A Thioflavin T (ThT) assay to detect β-sheet content showed substantially less ThT fluorescence in weak PA compared to strong PA (Figure 2-21a). Furthermore, the presence of NaCl had no effect on the ThT fluorescence, in contrast to strong PA, where ThT fluorescence increased with NaCl amount (Figure 2-9). Circular dichroism (CD) experiments are consistent with the ThT results, showing a β-sheet signature in strong PA and a random coil signature in weak PA (Figure 2-21b). Furthermore, similar to the ThT experiments, the CD signature of strong PA changes upon addition of NaCl while the CD signature of weak PA does not. Also, while strong FITC PA mixed with strong diluent PA showed fluorescence quenching in the presence of NaCl (Figure 2-3), which was attributed to closer association due to charge screening, weak FITC PA mixed with weak diluent PA does not show changes in fluorescence intensity with NaCl (Figure 2-21c). Taken together, the ThT, CD, and fluorescence data demonstrate that weak PA has a decreased propensity for hydrogen bonding, which is consistent with previous work in our laboratory.[75, 80] We also note the NaCl does not appear to alter the self-assembly behavior of weak PA, in contrast to the behavior of strong PA. In the case of strong PA, screening the negatively charged glutamic acids with positively charged sodium ions allows closer associations between PA molecules, and thus stronger hydrogen bonding between them. Conversely, in the case of weak PA, the same negatively charged glutamic acids can be screened by the sodium ions. However, even if this charge repulsion is screened to allow closer association between the PA molecules, the PA molecules do not have the capacity to form strong β-sheet interactions with each other.

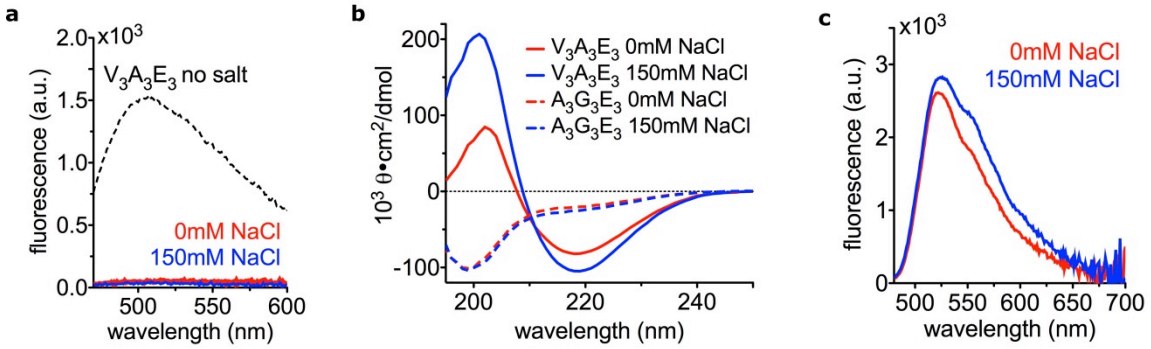

Figure 2-21: Characterization of weak PA. (a) Thioflavin T (ThT) fluorescence in weak PA solutions, with and without NaCl as indicated. The ThT fluorescence in a strong PA solution with no salt is plotted for comparison (black dotted line). (b) Circular dichroism spectra of strong and weak PA solutions, with and without NaCl as indicated. (c) Fluorescence spectra of weak FITC PA, with and without NaCl as indicated. Excitation 450 nm.

We made PA solutions containing weak FITC PA (Figure 2-20) and strong TAMRA PA (Figure 2-1), with diluent weak PA and diluent strong PA also mixed in. The amount of fluorescent PAs were kept constant, while the ratio of the diluent PAs changed, as illustrated in Figure 2-22. Thus, the diluent PA "matrix" is changing as the ratio of strong to weak diluent PA changes, but the amount of PAs with pendant fluorophores is not. These mixtures all contain no NaCl.

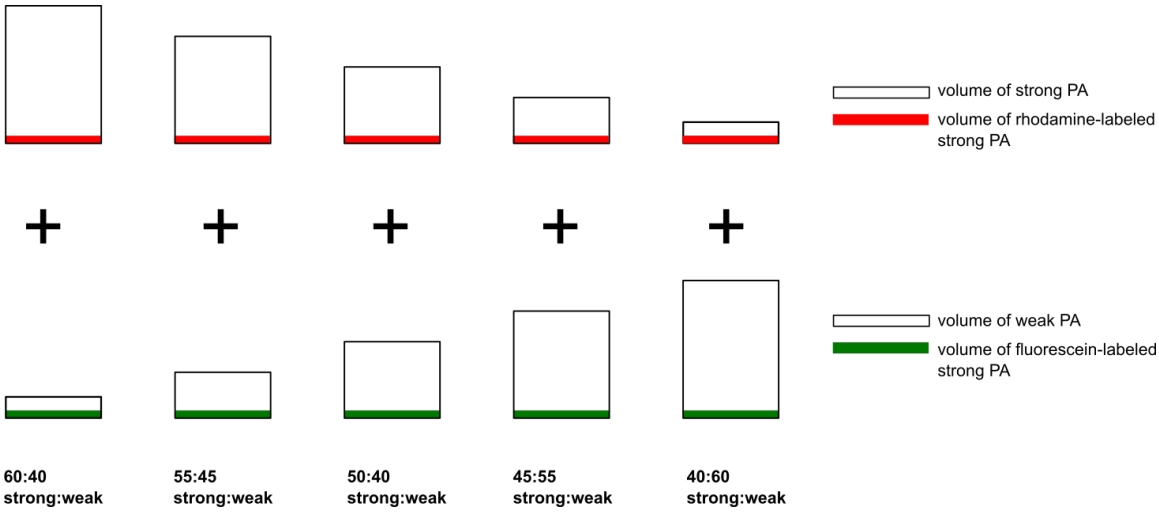

Figure 2-22: Schematic illustrating preparation of strong and weak PA mixtures. All illustrated solutions contained the same PA molar concentration. As indicated, solutions were mixed to give mixtures with different molar ratios of strong:weak diluent PA, but the same amount of fluorescent PA. Volumes are not drawn to scale, and are exaggerated for clarity.

We thermally annealed the strong and weak PA mixtures, and measured their FRET spectra (Figure 2-23). We found that when strong:weak diluent PA is at a molar ratio of 60%:40%, the FRET spectrum shows similar self-sorting to the sample with only strong PA (Figure 2-2). As the amount of weak PA is increased, the FRET spectrum shifts to suggest more mixing, becoming qualitatively more similar to strong PA samples containing NaCl (Figure 2-2). In the 60%:40% strong:weak sample where self-sorting was still observed, we found that the presence of NaCl suppresses the self-sorting (Figure 2-24), similar to data with strong PA alone (Figure 2-2).

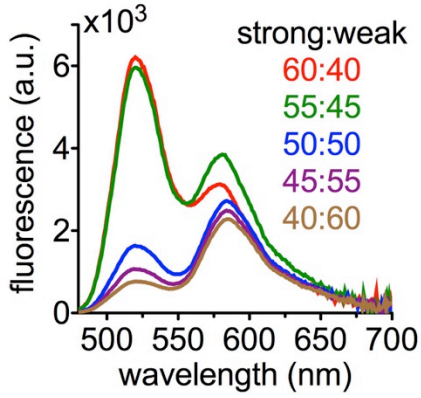

Figure 2-23: FRET spectra of annealed PA containing weak and strong PA at indicated molar ratios. All samples contained no added NaCl. Excitation: 450 nm.

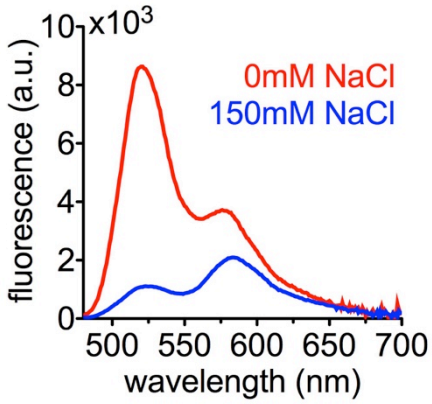

Figure 2-24: FRET spectra of PA mixture with 60:40 strong:weak PA molar ratio, after annealing and at indicated concentration of NaCl. Excitation: 450 nm.

We imaged the nanostructures of 60:40 (self-sorted) and 40:60 (mixed) strong:weak PA mixtures in 0 mM NaCl (Figure 2-25a-b), as well as 60:40 strong:weak (mixed) PA mixture in 150 mM NaCl (Figure 2-25c). All samples showed long nanofibers, so morphology cannot explain the FRET data. We hypothesize that, while the nanofibers are similar in morphology, the presence of weak PA causes them to become less cohesive, which allows more exchange of the fluorescent PAs. It is possible

that, as opposed to the case with strong PA alone, weakly cohesive nanofibers will allow more exchange of the TAMRA PA. Thus, instead of being stuck to the diluent PA matrix all the time, TAMRA PA can exchange into solution where it can interact with the FITC PA. This preliminary data shows that the identity of the supramolecular matrix, as determined by the diluent PA's molecular design, can affect self-sorting versus mixing of the minority components (fluorescent PAs).

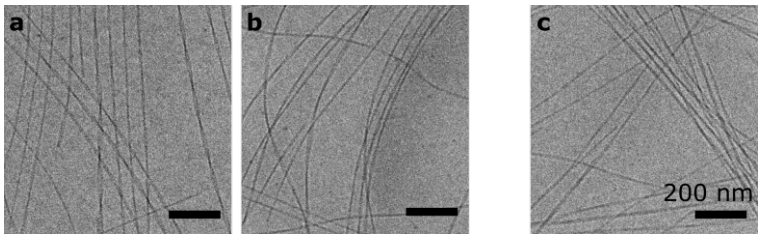

Figure 2-25: CryoTEM images of strong:weak PA mixtures containing a strong:weak PA molar ratio of (a) 60:40, in 0 mM NaCl, (b) 40:60 in 0 mM NaCl, and (c) 60:40 in 150 mM NaCl.

2.4 CONCLUSIONS

Regarding the design of multi-component supramolecular systems, there have been many studies on the factors that drive some molecules to self-sort, which generally focus on identifying molecular features that promote separation. Here we explore a different approach in which the separation is based on variable interaction of the components with a "matrix," which is in molar excess relative to the components. In particular, the diluent PA was in excess of the two fluorescent PAs. Intriguingly, the interactions of FITC and TAMRA PA with the diluent PA matrix appear to be heavily mediated by the pendant fluorophores, as the PA peptides responsible for self-assembly are identical in all PA

molecules. We believe the concepts presented in this work present a new approach to analyzing self-sorting versus co-assembly in multicomponent supramolecular systems.

2.5 MATERIALS AND METHODS

Peptide Synthesis

Peptide amphiphiles (PA) were synthesized as described in Chapter 4, and is copied and pasted below for convenience. This procedure was used to synthesize the C_{16}-$V_3A_3E_3$ PA, C_{16}-$V_3A_3E_3$K-FITC, C_{16}-$V_3A_3E_3$K-TAMRA, C_{16}-$A_3G_3E_3$ PA, and C_{16}-$A_3G_3E_3$K-FITC PA molecules (FITC – fluorescein isothiocyanate; TAMRA – tetramethylrhodamine).

PA molecules were synthesized using fluorenylmethyloxycarbonyl (Fmoc) solid phase peptide synthesis, by coupling Fmoc-protected amino acids (P3 BioSystems, Louiseville, KY, USA) from Rink amide MBHA resin (Novabiochem [EMD Millipore], Billerica, MA, USA). All amino acid couplings were performed in a CEM Liberty microwave-assisted peptide synthesizer (CEM, Matthews, NC, USA), using default microwave settings. Fmoc groups were deprotected using 20% 4-methylpiperidine and 0.1 M hydroxybenzotriazole (HOBt) in dimethylformamide (DMF) at 75 °C for 3–4 min. Amino acids were coupled using 5 molar equivalents (equiv) of protected amino acid, 5 equiv *O*-benzotriazole-*N*, *N*, *N*′, *N*′-tetramethyluronium hexafluorophosphate (HBTU) and 10 equiv *N*,*N*-diisopropylethylamine (DIEA), at 75 °C for 5–10 min. Using this same procedure, palmitic acid (C_{16}) was conjugated to the N-terminus of the peptide. After

each coupling, unreacted amines were capped using 0.5 M acetic anhydride, 0.125 M DIEA and 0.015 M HOBt in DMF, at 65 °C for 2 minutes.

Conjugation of Fluorophores to PA: All fluorophores (FITC or TAMRA) were conjugated to the amine on a lysine side chain, which was Mtt-protected during the peptide synthesis procedure described above. For this purpose, Fmoc-Lys(Mtt)-OH (P3 BioSystems, Louseville, KY, USA) was used. To expose the amine on the side chain, Mtt was deprotected using 1% trifluoroacetic acid, 3% triisopropylsilane in dichloromethane (DCM), for 15 minutes. After Mtt deprotection, either 5(6)-carboxytetramethylrhodamine (TAMRA acid) or fluorescein isothiocyanate (FITC) were coupled. When coupling TAMRA, the reaction was conducted with 1.5 equiv. TAMRA, 1.5 equiv. benzotriazol-1-yl-oxytripyrrolidinophosphonium hexafluorophosphate (PyBOP), in DMF with 8-10 times molar excess of DIEA. When coupling FITC, the same reaction conditions were used except there was no PyBOB. Fluorophore couplings for both dyes were conducted overnight.

Completed PA molecules were cleaved off the resin using a solution of 95:2.5:2.5 trifluoroacetic acid/triisopropylsilane/water for 2–3 h. Volatile solvents were removed with rotary evaporation, and the PA was precipitated with cold diethyl ether and dried using a fritted filter. The PA was then purified by preparatory scale reverse phase high-performance liquid chromatography (HPLC, Varian), using a Phenomenex Gemini column (C18 stationary phase, 5 μm, 100 Å pore size, either 30 × 150 mm or 50 x 250 mm). A mobile phase of acetonitrile and water was used, both containing 0.1% NH_4OH to aid solubility of acidic PA. Pure fractions were identified and collected, using electrospray ionization (ESI) mass spectroscopy. Excess acetonitrile was removed with

rotary evaporation, freeze-dried, and the powders stored at -20°C until use. The purity of PA molecules was confirmed using liquid chromatography-mass spectroscopy (LC-MS), which was performed using an Agilent 6520 QTOF-LCMS with a similar Phenomenex column.

Preparation of PA Mixtures Containing Diluent PA, FITC PA, and TAMRA

$V_3A_3E_3$ (diluent PA), $V_3A_3E_3K$-FITC (FITC PA), and $V_3A_3E_3K$-TAMRA (TAMRA PA) powders were all separately dissolved to 2 wt%. Diluent PA (at 2 wt%) was divided into two aliquots, and 1% (volume/volume) of 2 wt% $V_3A_3E_3K$-FITC PA was added to one aliquot, and 1% (volume/volume) of 2 wt% $V_3A_3E_3K$-TAMRA PA to the other aliquot. These PA solutions containing either FITC- or TAMRA-labeled PA were further split into aliquots, and diluted to 1 wt% PA with an equal volume of pure water or NaCl solution. For example, PA solutions containing 26 mM NaCl were diluted from 2 to 1 wt% PA by adding equal volume 52 mM NaCl. Next, diluent + FITC PA solutions were mixed with diluent + TAMRA PA solutions containing the same NaCl concentration. These PA mixtures were either analyzed immediately (freshly dissolved samples), or after undergoing a heating and cooling cycle (80°C for 30 minutes followed by slow cooling overnight, annealed samples). When samples were annealed, they were subject to heating immediately after the initial mixing.

For the experiment where heating time was varied, the PA mixtures were heated at 80°C for the indicated times. Afterwards, the samples were immediately submerged in room temperature water after heating, so they did not undergo the typical slow cooling step in the annealing procedure. All samples began heating at the same time, and

samples with shorter heating times were stored at room temperature while other samples continued to heat. For example, the 10-minute sample was heated for 10 minutes and then stored at room temperature for 20 minutes while the 30-minute sample continued heating. The unheated sample was simply stored at room temperature for 30 minutes.

For the experiment where PA concentration was varied, freshly dissolved 1 wt% PA mixtures were first prepared. Through serial dilutions in pure water, freshly dissolved mixtures of 0.5, 0.25, 0.125, and 0.0625 wt% PA were prepared, which simultaneously reduces the concentration of diluent, FITC, and TAMRA PA in solution. These diluted solutions were thermally annealed (80°C 30 minutes, slow cool overnight), and their FRET spectra collected as described above.

For the experiment where the order of adding NaCl to PA mixtures was varied, annealed PA mixtures at 1 wt% were first prepared. All samples were then diluted to 0.5 wt% PA for this experiment in three different ways:

1.) 0 mM NaCl salt: PA annealed at 1 wt% in 0 mM NaCl, diluted to 0.5 wt% with pure water
2.) 75 mM NaCl salt (before): PA annealed at 1 wt% in 150 mM NaCl, diluted to 0.5 wt% with pure water
3.) 75 mM NaCl salt (after): PA annealed at 1 wt% in 0 mM NaCl, diluted to 0.5 wt% with 150 mM NaCl

Samples 2 and 3 above contain the same final PA and salt concentration (0.5 wt% PA, 75 mM NaCl), but the NaCl was added at different times during processing. Sample 1 serves as a control with no NaCl.

For experiments where PA mixtures were mechanically perturbed, we used two methods of mechanically disrupting the nanofibers. PA samples were annealed before being subject to mechanical perturbation. Freeze-thawed samples were created by subjecting the annealed PA mixtures to ~30 seconds of submersion in liquid nitrogen, and allowing them to thaw at room temperature. Vortexed samples were created by subjecting the annealed PA mixtures to ~1 minute of vortexing.

Preparation of Diluent + FITC PA and Diluent + TAMRA PA Mixtures

For FITC PA experiments, $V_3A_3E_3$ PA and $V_3A_3E_3K$-FITC PA were first separately dissolved to 2 wt% with 30 mM NaOH. Next, 1% (volume/volume) of $V_3A_3E_3K$-FITC PA solution was added to the $V_3A_3E_3$ PA solution. This solution was then split into different aliquots, which were diluted to 1 wt% PA with equal volume pure water or NaCl solution to achieve the desired NaCl concentration. For example, PA samples containing 26 mM NaCl were diluted from 2 to 1 wt% PA by adding equal volume of 52 mM NaCl. This same procedure was also used to mix TAMRA PA samples, as well as weak diluent PA ($A_3G_3E_3$) with weak FITC PA ($A_3G_3E_3K$-FITC).

Preparation of PA Solutions Containing Only Fluorescent PA

For consistency with diluent PA experiments, FITC PA and TAMRA PA were dissolved to 17.32 mM with 30 mM NaOH, which is the molarity of 2 wt% diluent PA. These PA solutions were then diluted to 8.66 mM (the molarity of 1 wt% diluent PA) with pure water, and thermally annealed (80°C 30 minutes, slow cool overnight).

Preparation of PA Mixtures Containing Strong and Weak PA

Strong ($V_3A_3E_3$) PA was first dissolved to 1 wt% (8.66 mM) with 15 mM NaOH. To keep the molar concentration consistent, weak ($A_3G_3E_3$) PA was first dissolved to 0.89 wt%, which is 8.66 mM. This experiment contains no added NaCl. Fluorescent PAs ($V_3A_3E_3$K-TAMRA, $A_3G_3E_3$K-FITC) were dissolved to the same concentrations as their non-fluorescent counterparts. Before mixing strong and weak PA solutions, fluorescent PAs was added to their respective PA solutions. All mixtures contained the same amount of fluorescent PA, regardless of the molar ratio of strong:weak unlabeled PA (Figure 2-22). The PA solutions (before mixing strong and weak solutions) for the 50:50 molar ratio sample had 1% volume/volume of fluorescent PA, and all other solutions received the same amount. Thus, the volume percentage of fluorescent PA to diluent PA varied from 0.0833 – 1.25% (60:40 vs. 40:60 molar ratio). Samples were thermally annealed for 80°C for 30 minutes, and slow-cooled overnight.

For the experiment where NaCl was added to solutions containing weak PA, strong PAs ($V_3A_3E_3$, $V_3A_3E_3$K-TAMRA) were first separately dissolved to 2 wt%, and weak PAs ($A_3G_3E_3$, $A_3G_3E_3$K-FITC) were first dissolved to 1.78 wt%, to keep the molarity of the diluent PA solutions constant. To keep the amount of fluorescent PA consistent with what it would be in a 50:50 mixture, strong diluent PA solutions received 0.833% (volume/volume) of its fluorescent analog ($V_3A_3E_3$K-TAMRA), while weak diluent PA solutions received 1.25% (volume/volume) of its fluorescent analog ($A_3G_3E_3$K-FITC). These solutions were then diluted with equal volume of either pure water or 300 mM NaCl, resulting in final concentrations of 1 wt% strong PA or 0.89 wt% weak PA (8.66 mM for both), and 0 or 150 mM NaCl. Strong and weak PA solutions,

now containing their respective fluorescent PAs and appropriate NaCl amounts, were then mixed to achieve a 60:40 molar ratio of strong:weak PA. These mixtures were then thermally annealed at 80°C for 30 minutes and slow-cooled overnight.

Förster Resonance Energy Transfer (FRET)

In all experiments in this work, FITC was the FRET donor and TAMRA was the FRET acceptor. PA samples (50 μL) were loaded into a 96-well black plate with a clear bottom, which was analyzed using a Cytation^{TM}3 (BioTek, Winooski, VT, USA). The solutions were excited at 450 nm (direct FITC excitation), and fluorescence spectra collected from 480 – 700 nm, which covers both FITC and TAMRA emission.

For the FRET experiments in Figure 2-2, the fluorescence spectra were normalized to the highest fluorescent intensity detected in the 0 mM NaCl sample. The experiment was repeated four times, and the normalized fluorescence spectra were averaged together and plotted in Figure 2-2a. Each normalized spectra was used to calculate a FRET ratio, and the average FRET ratio is reported in Figure 2-2b. In all other FRET experiments, the fluorescence spectrum shown is one representative experiment.

For the data in Figure 2-2b, the normalized FRET spectra for each sample were deconvoluted using Igor Pro (Wavemetrics, Portland, Oregon, USA). An example of a deconvolution is shown below in Figure 2-26. The FRET ratio was then calculated as:

$$\frac{F_A}{F_A + F_D}$$

where F_A is the intensity of acceptor emission and F_D is the intensity of donor emission. Thus, in the example shown below, we have:

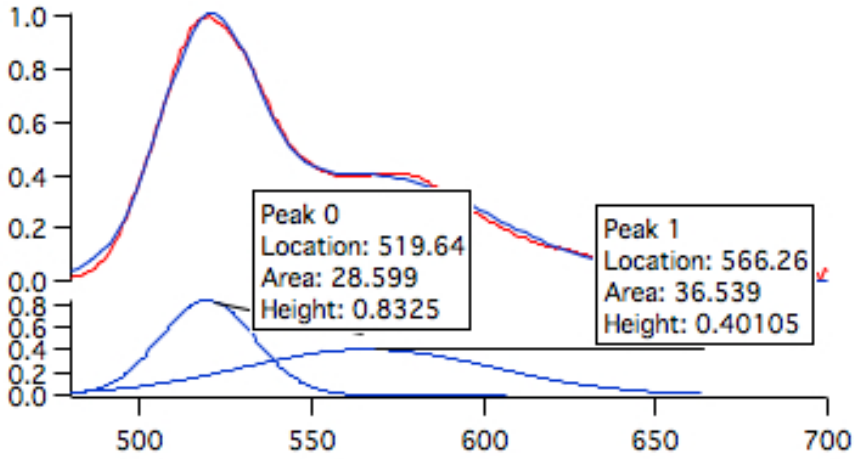

Figure 2-26: Example of fluorescence spectra deconvolution. The x-axis is wavelength in nm and the y-axis is arbitrary fluorescence intensity. Peak 0 is the deconvoluted FITC emission peak and Peak 1 is the deconvoluted TAMRA emission peak.

$$\frac{F_A}{F_A + F_D} = \frac{0.40105}{0.40105 + 0.8325} = 0.325$$

Although this calculation is complicated by the self-quenching behavior of FITC (Figure 2-3, Figure 2-4) and the overlap in emission spectra of FITC and TAMRA, the data still reveals trends between the samples.

Confocal Microscopy Imaging of Diluent + FITC + TAMRA PA Mixtures

PA solutions (50 μL) were pipetted onto a glass cover slip for imaging at 40x on a Nikon A1R microscope, using the 488 and 561 nm laser lines.

Fluorescence Spectra for FITC PA (Strong and Weak PA)

Diluent + FITC PA solutions were prepared as described above, and contained 1 wt% PA (99% diluent, 1% FITC PA) and 0 – 150 mM NaCl. They were analyzed either immediately (freshly dissolved) or after thermal annealing (80°C for 30 minutes, slow cool overnight). PA solutions (50 μL) were loaded into a 96-well black plate with a clear bottom. The plate was read on a Cytation^{TM}3 (BioTek, Winooski, VT, USA), with excitation at 450 nm and emission spectra collected from 480 – 700 nm.

Cryogenic Transmission Electron Microscopy (CryoTEM)

Immediately before preparation for cryoTEM, PA solutions were diluted 1:100 (1 wt% to 0.01 wt%) in pure water, except for the samples containing only FITC PA or only TAMRA PA. When diluent PA was not present, the fluorescent PAs were dissolved to 8.66 mM, which is consistent with 1 wt% of diluent PA. These fluorescent PA-only samples were annealed and prepared without dilution, because they were not as viscous as samples containing diluent PA. All samples (6.5 μL) were deposited onto 300-mesh copper grids with lacey carbon film (Electron Microscopy Sciences, Hatfield, PA, USA) inside a FEI Vitrobot Mark IV (FEI, Hillsboro, OR, USA), which was maintained around 95% humidity. Before use, the copper grids were glow discharged for 30 seconds in a PELCO easiGlow system (Ted Pella, Inc., Redding, CA, USA). The samples were

plunged into liquid ethane, and then transferred to a Gatan 626 cryo-holder (Gatan, Pleasanton, CA, USA) while submerged in liquid nitrogen. Samples were imaged on a JEOL 1230 TEM operating at 100 kV, and micrographs were captured with a bottom-mounted Gatan 832 camera.

Polarized Light Microscopy on PA Mixtures

PA solutions (50 μL) were pipetted onto a glass cover slide, and observed between cross-polarizers set to 90°. All PA samples imaged with this technique were at 1 wt%.

Small Angle X-Ray Scattering (SAXS)

SAXS measurements were taken at the Advanced Photon Source of Argonne National Laboratory, on Beamline 5-ID-D of the DuPont-Northwestern-Dow Collaborative Access Team (DND-CAT). A double crystal monochromator was used to select a beam energy of 17 keV (λ = 0.7293), and the detector was positioned 8.5 cm behind the sample. PA solutions (1 wt%) were loaded into quartz capillaries, with 1.5 mm diameter with 0.1 mm wall thickness (Charles Supper, Natick, MA, USA), and SAXS spectra were collected with an exposure time of 1 second. Two separate experiments were conducted.

Fluorescence Recovery After Photobleaching (FRAP)

Before photobleaching for FRAP analysis, images of the PA solutions were taken on the confocal microscope. PA samples (50 μL) were pipetted onto a glass cover slip.

FITC PA was imaged with the 488 nm laser line while TAMRA PA was imaged with the 561 laser line, both using a 40x objective on a Leica SP5 confocal microscope (Leica, Wetzler, Germany).

After confocal imaging, the same PA samples were subject to photobleaching. For FITC PA samples, circles 10 μm in diameter were photobleached with the 488 nm laser line at 100% power. For TAMRA PA samples, squares that were 10 μm long on each side were photobleached instead. This is because, due to the high rate of photobleaching in TAMRA PA, the FRAP configuration does not allow photobleaching of circles. During photobleaching, the microscope zooms in on a square around the bleach spot, so if the bleach spot is a circle, the area outside the circle will be subject to the lower laser intensity used for imaging as opposed to the higher laser intensity used for photobleaching. In the case of TAMRA PA, this exposure to lower laser intensity causes the area outside the circle to become noticeably lower than the unbleached PA outside the zoom box. However, this area still had a higher fluorescence intensity than the area within the actual bleach circle. To avoid this problem, the entire square was photobleached. FITC PA appears to be less susceptible to photobleaching than TAMRA PA, so circles could be bleached. For both experiments, the microscope scanned a 512 x 512 pixel area at 1000 Hz, allowing an image to be captured approximately every 0.263 seconds. Fluorescence intensity in the photobleached area was normalized to fluorescence intensity in an image area that was not photobleached, in order to account for photobleaching due to imaging. The following equation was used to obtain the final values ($I_{corrected}$):

$$I_{corrected} = I_{measured} * \frac{I^0_{unbleached}}{I_{unbleached}}$$

where the initial unbleached value ($I^0_{unbleached}$) is the average of 5 pre-bleach frames, in the unbleached image area. These corrected intensities ($I_{corrected}$) were then used to obtain a value between 0 and 1 ($I_{normalized}$, where 0 represents no recovery and 1 represents full recovery), and these values were plotted over time. The pre-bleach fluorescence ($I_{prebleach}$) was obtained by averaging the bleach spots fluorescence intensity in the 5 pre-bleach frames, while the post-bleach intensity ($I_{postbleach}$) was obtained by taking the bleach spot's fluorescence intensity immediately after photobleaching. The following equation was used to normalize fluorescence intensity in the bleach spot for all other time points:

$$I_{normalized} = \frac{I_{corrected} - I_{postbleach}}{I_{prebleach} - I_{postbleach}}$$

For FRAP experiments with free fluorescein dye, fluorescein sodium salt (Sigma Aldrich, St. Louis, MO, USA) was dissolved in pure water to 6 mg/mL. This solution was mixed with 1 wt% freshly dissolved PA solution at 1% (volume/volume), for a final concentration of 30 μg/mL fluorescein sodium salt in the PA solution. The PA solution containing fluorescein dye was then annealed at 80°C for 30 minutes and slowly cooled overnight. For $CaCl_2$ gels, 10 μL of PA solution (diluent + FITC PA) was pipetted into 4 μL of 30 mM $CaCl_2$.

Thioflavin T (ThT) Assay

Diluent PA (strong or weak) was first dissolved to 2 wt%, and then split into separate aliquots. These aliquots were then diluted to 1 wt% with equal volume of pure water or NaCl, such at the final PA solution contained 1 wt% PA and either 0, 26, or 150 mM NaCl. These solutions were analyzed while freshly dissolved. It is not possible to use this assay to analyze annealed PA samples, because the bundles created by the long nanofibers interfere with ThT dye diffusion. It is also not possible to conduct this assay with fluorescent PA, because the fluorescence would interfere with the ThT fluorescence. The 1 wt% PA samples were then mixed with a solution of ThT dye dissolved in pure water, such that the final concentrations of PA and ThT dye were 500 μM and 50 μM, respectively. This PA/ThT dye solution (100 μL) was loaded into a 96-well black plate with a clear bottom. The NaCl concentrations on the graph refer to the concentration of NaCl in the original 1 wt% PA solution, and not after dilution for the ThT assay. The plate was read on a Cytation^{TM}3 (BioTek, Winooski, VT, USA), with excitation at 440 nm and emission spectra collected from 470 – 600 nm.

Viscosity Measurements

PA samples (200 μL, 1 wt% PA) were loaded onto the measuring plate (set to 23°C) of a MCR 302 rheometer (Anton Paar, Graz, Austria). Measurements were performed with the CP25-2 fixture (25 mm diameter cone-plate), which increased the shear rate from 1–100 s^{-1} over 240 seconds, and measured the respondent shear stress. The final viscosity at 100 s^{-1} is reported.

Circular Dichroism (CD)

CD experiments were performed on freshly dissolved PA solutions, since the long nanofibers formed during annealing can scatter light and interfere with the signal. Strong and weak diluent PA samples containing no fluorescent PA first dissolved to 2 wt% and 1.78 wt%, respectively, so that the molarities would match (17.32 mM). These solutions were then diluted with equal volume of water or 300 mM NaCl, to get 8.66 mM PA. For analysis by CD, the final 8.66 mM PA solutions were diluted 1:20 in pure water and loaded into a 1 mm path length cuvette. A JASCO J-815 spectrophotometer was used to scan the samples from 190 – 250 nm, with a scan speed of 100 nm/minute. All data is the average of three scans.

Mathematical Modeling of FRAP Data

We modeled individual FRAP curves (averaged together in Figure 2-10g, Figure 2-11g) to describe the diffusion of fluorescent PA using a single exponential:

$$y = y_0(1 - e^{-t/\tau}) \qquad (1)$$

This is a general equation of the form:

$$y = y_0 - Ae^{-\frac{(t-t_0)}{\tau}} \qquad (2)$$

where $y_0 = A$ and $t_0 = 0$. The experimental data (y versus t) is the FRAP data (in Figure 2-10g, Figure 2-11g), and was fitted to equation 2 using the **exp_XOffset** function in Igor Pro 6.3 (WaveMetrics, Portland, OR, USA). In this fitting, t_0 is automatically set to the first data point in the inputted curve, which was always 0 seconds in our FRAP data. In collecting our FRAP data, the first frame after photobleaching ($I_{postbleach}$) was always taken to be $t = 0\ seconds$, where the normalized intensity was set to 0 for 0 recovery. Since our FRAP data only has 8 data points and will therefore not be exactly precise, we did not force $y_0 = A$ in the curve fittings. However, we note that the values for y_0 and A were similar by visual inspection. From these fittings, we obtained the parameters y_0, τ, and A, and the parameter A was not used in further analysis. From τ, the half recovery time ($t_{1/2}$) of the mobile species can be calculated:

$$t_{1/2} = \tau \ln(2) \qquad (3)$$

From this and the parameters of the FRAP experiment, the diffusion coefficient (D) of the mobile species can be calculated using the Soumpasis approximation[140]:

$$D = 0.224 \frac{w^2}{t_{1/2}} \qquad (4)$$

where w is the radius of the bleach area (5 μm). Using the Stokes–Einstein equation, we calculated hypothetical diffusion coefficient for 10 nm PA micelles and 200 nm PA short nanofibers, by setting ($R = 5\ nm, 100\ nm$):

$$D = \frac{k_B T}{6\pi\eta R} \qquad (5)$$

where k_B is Boltzmann's constant, T is temperature, and η is the viscosity of the solution. We used the viscosity of water for η, because the PA is dissolved in water and constitutes 1 wt% of the entire solution. Since the Stokes-Einstein equation assumes spherical objects diffusing through a uniform liquid medium, the size calculations will not accurately reflect anisotropic nanofibers or objects that are diffusing around long PA nanofibers, but we performed this calculation to estimate the size to an order of magnitude.

Since the collected FRAP data has only 8 data points due to constraints with imaging speed, and there are errors associated with fluorescence measurements, the curve fitting sometimes gave grossly and obviously inaccurate results. These fittings were excluded from our analysis. This was more prone to happen in samples with a large immobile fraction, because the amount of fluorescence recovery was small in these cases, so the assumed exponential behavior may not be detected. If the fitted parameters had an error several orders of magnitude greater than the fitted value, the fitting was excluded from our analysis. Also, the fitted parameter y_0 must be a value between 0 and 1 if it is to represent normalized fluorescence, so fittings where y_0 was significantly larger than 1 were excluded from our analysis. Indeed, some of these excluded fittings may have described the absence of diffusion, where the mobile phase $y_0 \to 0$ and characteristic diffusion time $\tau \to \infty$. However, we did not want to arbitrarily exclude some fittings while including others as having a 100% immobile fraction, so we simply excluded these

fittings. Furthermore, we did observe some degree of fluorescence recovery at $t \cong 1.8\ seconds$ in all samples, so we assumed that all samples had some amount of mobile fraction. We note that in one case, the mobile fraction was calculated to be almost exactly 1, which appeared to be an incorrect fitting. This data point was later excluded due to the removal of outliers (described below).

Of the data points that were not excluded due to an obviously incorrect fitting (described above), we systematically removed outliers. Because our FRAP data contains only 8 data points and therefore limited precision, we assumed that outliers in curve fitting parameters (y_0 and τ) were due to inaccuracies in the fitting as opposed to actual variations in the system's behavior. To identify and remove outliers, we employed the ROUT method,[141] which combines Robust regression and Outlier Removal, using GraphPad Prism 8 (GraphPad Software, San Diego, CA, USA). We chose Q = 10% for the ROUT analysis, which is relatively aggressive in detecting outliers, and relatively more likely to detect false outliers. We chose this parameter due to our assumption that most variation in the data was caused by lack of precision in the model, as opposed to variation in the actual system. Since y_0 and τ come from the same fitted equation, if one was excluded for a specific curve, the other parameter for that curve was automatically excluded too.

3 CELL DEATH MEDIATED BY ALKYL TAIL PLACEMENT

3.1 OBJECTIVE AND SIGNIFICANCE

In multicellular organisms, cell death is tightly regulated by signal transduction pathways, with certain pathways leading to programmed cell death. Synthetic materials can induce cell death, by rapidly destroying cellular structures, or by slowly activating the cell's native cell death program. All synthetic materials first interface with cells through their plasma membrane, so understanding material-membrane interactions is crucial to understanding the materials' cytotoxic effects. In this work, we show that subtle differences in the molecular design of self-assembling peptide amphiphiles (PA) can affect their cytotoxicity. PAs are comprised of an alkyl tail conjugated to a short peptide chain, and the placement of the alkyl tail can significantly influence the PA assemblies' cytotoxic effects. When the alkyl tail is placed at the peptide's N-terminus, the cytotoxic effect is rapid, with 100% of cells dead after 2 hours. However, when the alkyl tail is positioned the C-terminus, cell death occurs over a longer time period, taking up to 12 hours for the percentage of dead cells to plateau. While PA-induced rapid cell death occurs through physical rupture of the cell membrane, PA-induced slower cell death likely occurs through an oncotic signaling pathway, initiated by cholesterol sequestration from the cell membrane. In the PA causing slower death, the alkyl tail is connected to the peptide through a lysine linker, and reversing its polarity hindered cholesterol sequestration and rescued cell viability. This work shows that PA alkyl tail position can determine its biological function, which we believe can apply to other supramolecular biomaterials built from amphiphilic self-assembling molecules.

3.2 BACKGROUND

Programmed cell death occurs when cells intentionally orchestrate their own demise, a process that was named *apoptosis* in 1972.[142] Apoptosis plays an important role in normal life-sustaining functions, including embryonic development,[142-145] eliminating self-reactive immune cells,[146-151] and wound healing.[152, 153] Cells that lose the ability to undergo apoptosis can form malignant growths, leading to the development of cancer.[154, 155] In the 1990s, mechanistic studies showed that apoptosis is controlled by signaling cascades, deliberately working to execute a regulated cell death program.[156-162] A less studied cell death mechanism is *oncosis*, which is distinct from apoptosis in many regards.[163-166] Most notably, apoptotic cells shrink before death, while oncontic cells swell and develop giant blebs.[163-166] Traditionally, oncosis was thought to be "accidental" as opposed to "programmed" cell death,[163, 165] but signaling pathways that mediate oncosis have been identified.[167] Thus, oncosis can be considered a form of programmed cell death, resulting from intentional activation of certain signaling cascades. When no signaling pathways are activated to program cell death, cells may still be killed by direct physical rupture of the cell membrane, which can be considered truly "accidental" cell death. This distinction may be important in studying synthetic biomaterials, particularly cationic species that can interact with and disrupt negatively charged cell membranes.[75-79]

In the development of synthetic therapeutic agents, cytotoxicity is an important design parameter. Cytotoxicity can be beneficial in the development of anti-cancer therapies, but would be highly unfavorable for regenerative medicine applications. For nanoscale materials, the factors that influence cytotoxicity have been studied, and are

now known to include size,[168-170] surface chemistry,[171-174] and shape.[175-177] Notably, these are static, bulk properties of nanomaterials, which will interact with highly dynamic and fluid cell membranes. The cell membrane is the barrier between the cell and its environment, and thus serves as the contact point for all cell-material interactions. Comprised of a lipid bilayer held together by non-covalent hydrophobic interactions, the cell membrane is a *supramolecular* structure. Thus, *synthetic supramolecular nanomaterials* may interact with the cell membrane in ways that more static materials do not. Indeed, recent work showed that supramolecular cohesion in self-assembled peptide amphiphile (PA) nanofibers affected their ability to cause cell death.[75] Weakly cohesive nanofibers were able to disrupt the cell membrane and exert a cytotoxic effect, while strongly cohesive nanofibers could not.[75] Both PAs contained positive charges that could potentially compromise negatively charged cell membranes, but only weakly cohesive PA was cytotoxic.[75] In another system, weakly cohesive cationic nanostructures were able to enhance growth factor signaling, which was linked to their ability to increase lipid raft fluidity in cell membranes.[80] The interaction of two supramolecular structures – the cell membrane and the self-assembled nanofibers in this case – may yield phenomenon that are unique to non-covalent synthetic materials.

In this work, we systematically alter the alkyl tail position of PAs and examine the effects on cytotoxicity. The molecules studied in this work follow the canonical form of PAs, which includes an alkyl tail to induce hydrophobic collapse, a β-sheet forming peptide region to promote intermolecular hydrogen bonding, and a charged peptide residue region to promote solubility in water.[31, 32] In all PAs here, the charged peptide residues are cationic, meaning they may disrupt negatively charged cell membranes.[75-79]

First, we alter the PA's polarity by differentially attaching the alkyl tail to either the N- or C-terminus of the peptide sequence. Next, we changed the orientation of a lysine linker between the alkyl tail and peptide portion. Finally, knowing that cell death can be programmed, we probe the mechanism through which different PA assemblies exert their cytotoxic effects. Previous work linking supramolecular cohesion to cytotoxicity focused on the hydrogen bonding segment of the PA,[75] as opposed to the placement of the hydrophobic alkyl tail. The overall goal of this work is to elucidate how alkyl tail position affects the PA assemblies and their interactions with cell membranes, and how this determines the cytotoxic response.

3.3 RESULTS AND DISCUSSION

3.3.1 Differential Cell Viability to Molecular Design

We synthesized **PA1** (Figure 3-1a), which has been previously shown to enhance growth factor potency due to its ability to interact with the cell membrane.[80] In **PA1**, the C_{16} alkyl tail is attached at the peptide's C-terminus, though a lysine linker with the peptide chain attached to the α-amine and the alkyl tail attached to the ε-amine (Figure 3-1a). **PA1** contains a weak hydrogen bonding segment that allows it to associate with cell membranes and increase lipid raft mobility, thus increasing growth factor signaling through membrane-bound receptors.[80] However, the positively charged headgroups of **PA1** may result in cytotoxicity, since cationic species are known to induce cell death by disrupting negatively charged cell membranes.[75-79] **PA1** enhances growth factor in its soluble form, when added to cell media,[80] but **PA1**'s cytotoxicity as a surface coating has

never been studied. Specifically, previous work showed that an analog of **PA1** containing the same set of amino acids, but with the alkyl tail positioned at the peptide's N-terminus instead of the C-terminus, was highly cytotoxic both in solution and as a material coating (**PA2**, Figure 3-1a).[75] In **PA2**, there is no lysine linker between the C_{16} alkyl tail and the peptide, because C_{16} can be directly coupled to the N-terminus. We speculate that the cationic charges of **PA1** allow it to interact with negatively charged cell membranes and increase lipid raft mobility, but this same PA-cell interaction may also pose the risk of cell membrane disruption and thus cell death. Since PA coatings are more relevant for the design of regenerative medicine scaffolds, we wanted to investigate the cytotoxicity of surfaces coated with **PA1**. As a control, we also synthesized **PA3**, an analog of **PA1** containing a strong hydrogen bonding segment, which should reduce its ability to interact with the cell membrane (Figure 3-1a).[75] We observed all three PAs in aqueous solution using cryogenic transmission electron microscopy (cryoTEM), and found that all PAs self-assemble into nanofibrous structures (Figure 3-1b). We note that **PA2** formed shorter nanofibers than **PA1** and **PA3**.

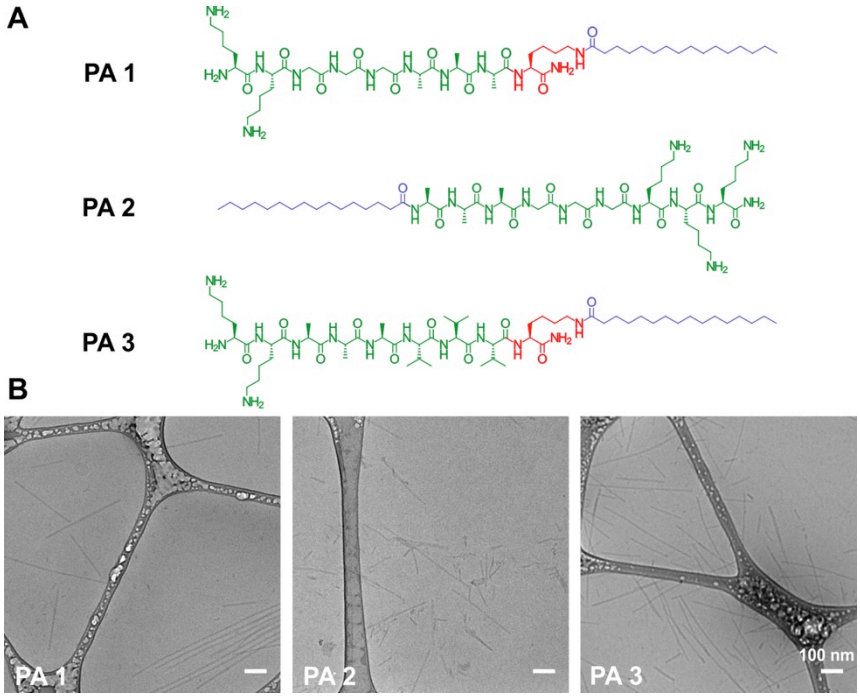

Figure 3-1: Molecular design of cationic PAs and their supramolecular structures. (a) Chemical structure of PA molecules used in this study, all PAs have the same hydrophobic region (alkyl tail, blue); **PA1** contains a weak ß-sheet forming region, **PA2** differs from **PA1** by positioning of the alkyl tail at the N-terminus of the peptide sequence, **PA3** is the same orientation as **PA1** but in β-sheet forming region, valines and alanines replace alanines and glycines, respectively. (b) CryoTEM showing self-assembled PA nanofibers formed by 1% (w/v) PA solutions in water.

To investigate the interactions of the three PAs with cells, we first studied the cytotoxicity of these PAs as nanofiber coated surfaces. We coated 96-well plates with PA and seeded CXT2 cervical cancer cells onto these surfaces, allowing the cells to interact with PA coatings as opposed to soluble PA in the media. After an incubation of 48 hours, we performed a live/dead assay using the fluorescent dyes calcein/ToPro3 and quantified the percentage of dead cells (Figure 3-2a). Similar to results from a previous study,[75] we found that nearly all cells on **PA2** surfaces were dead. On **PA1** surfaces 86±3% of cells were dead, demonstrating that **PA1** has similar cytotoxic properties

to **PA2**. Both **PA1** and **PA2** have cationic headgrounds in combination with weak hydrogen bonding segments, which likely contribute to their cytotoxicity. Conversely, as shown by the decreased cytotoxicity on **PA3** surfaces (6±2% dead), increasing PA hydrogen bonding propensity rescues cell viability. Based on previous work, this is likely due to the decreased ability of more cohesive assemblies to interact with the cell membrane,[75, 80] which decreases the PA's ability to exert a cytotoxic effect. We confirmed the live/dead assay results with an MTT assay, which indicated a significantly higher number of viable cells on **PA3** surfaces (Figure 3-2b). To confirm that the cytotoxic effect of **PA1** was not specific to cancer cell lines, we performed a live/dead assay with non-cancerous cervical epithelial cells, which showed that nearly 84±4% of these cells were dead after 48 hours (Figure 3-2c).

Interestingly, when we performed a series of live/dead experiments at different time points after cell seeding on the PA coatings, the time course showed that the cytotoxicity of **PA2** was much more rapid than that of **PA1**. After 2 hours of exposure, nearly 100% of CXT2 cells on **PA2** surfaces are dead while little cytotoxicity is observed on **PA1** surfaces, where the proportion of dead cells gradually increased and plateaued around 70-80% after 8-12 hours (Figure 3-2d). Since **PA1** and **PA2** contain the same amino acids and differ mainly in alkyl tail position (C-terminus in **PA1** versus N-terminus in **PA2**), we hypothesized that alkyl tail placement could mediate the observed differences in their cytotoxic effects. Indeed, **PA2** has one more positive charge from the side chain of an extra lysine headgroup, which instead serves as non-reactive lysine linker in **PA1**, but the overall surface charge is cationic for both PAs. Furthermore, the different temporal scales of cytotoxicity exerted by **PA1** and **PA2** suggest that the

mechanism of cell death in these two situations may be different. Such differences, if they exist, are likely to be mediated by the internal supramolecular structure of the PA assemblies. Supporting this hypothesis, a previous study showed that small changes in molecular design can have significant changes on the internal dynamics of PA assemblies, although that work focused more on the hydrogen bonding segment as opposed to the alkyl tail of the PA.[74]

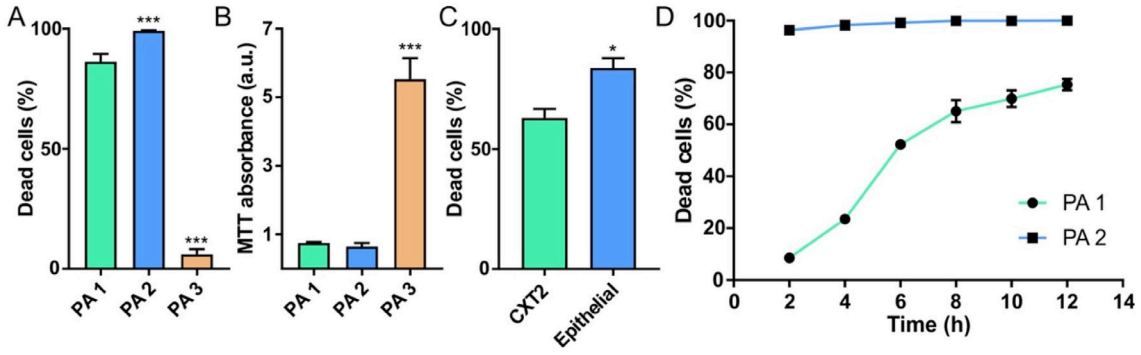

Figure 3-2: Cytotoxicity of cationic PA coatings. CXT2 cells were cultured on PA coated surfaces for 48 hours and viability was assessed by (a) calcein/ToPro3 staining and (b) MTT assay. (c) Viability of CXT2 cells on **PA1** is compared against non-cancerous cervical epithelial cells. (C) Time course of CXT2 cell death on **PA1** and **PA2** coatings. (***$p < 0.001$, *$p<0.05$)

3.3.2 Lysine Linker Polarity Rescues Viability

To investigate if altering alkyl tail placement has an impact on cellular response, we synthesized an analog of **PA1** where the polarity of the lysine linker between the peptide and the alkyl tail is reversed (**PA4**, Figure 3-3a). In **PA1**, the lysine amino acid linking the peptide to the alkyl tail has the peptide attached at the α-amine and the alkyl

tail attached at the ε-amine (Figure 3-1a). Conversely, in **PA4**, the peptide is attached at the ε-amine while the alkyl tail is attached at the α-amine (Figure 3-3a). Thus, **PA1** and **PA4** are completely identical except for the lysine linker's polarity. We examined **PA4** in aqueous solution by cryoTEM (Figure 3-3b), and found that it forms nanofibers similar to those formed by **PA1** (Figure 3-1b). To investigate if alkyl tail position could affect the PA assemblies' internal structure, we took circular dichroism (CD) spectra of **PA1** and **PA4** in aqueous solution, as well as of **PA2** and **PA3** (Figure 3-3c). The CD spectra for **PA1** suggests a random coil conformation, which is expected since previous work showed a low hydrogen bonding propensity in this PA.[80] Interestingly, the CD spectra of **PA4**, which differs from **PA1** only in lysine linker polarity, shows a positive signal between 190 – 200 nm and a negative signal at 218 nm, suggestive of more β-sheet character than **PA1**. **PA2** showed a random coil CD signature while **PA3** showed more β-sheet character, which is expected since PA2 is designed to have a weak hydrogen bonding segment[75] while **PA3** is designed to have a strong hydrogen bonding segment.[80] Thus, the CD data suggest that **PA4** is a more cohesive nanostructure than **PA1**, and that switching the lysine linker polarity can alter the internal supramolecular interactions in PA assemblies. To probe the effect of lysine linker polarity on PA cytotoxicity, we evaluated the cytotoxicity of **PA1** and **PA4** surfaces with multiple cell lines. Surprisingly, for all cell lines studied, we found a significantly lower percentage of dead cells on **PA4** than on **PA1** (Figure 3-3d). The live/dead data demonstrates that **PA4** surfaces are less cytotoxic than **PA1** surfaces, and the CD data suggests that one possible mechanism is through increased cohesion in **PA4** nanostructures. This mechanism is consistent with previous work, which reported that increased supramolecular cohesion in

cationic PA assemblies rescued cell viability.[75] However, further investigation is necessary to determine if this is the only mechanism through which lysine linker polarity rescues cell viability.

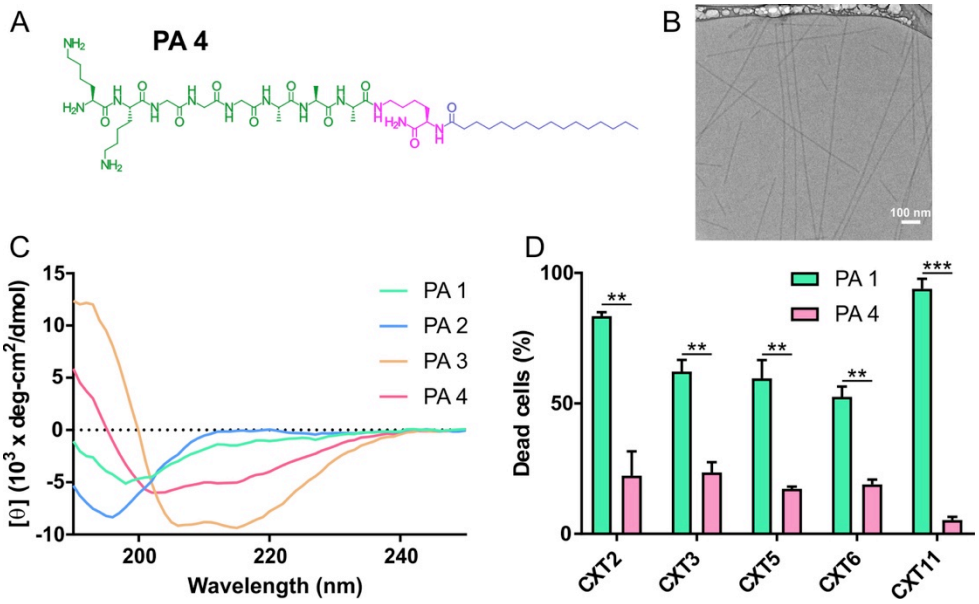

Figure 3-3: Altering lysine linker orientation rescues viability. (a) Structure of **PA4**. (b) CryoTEM image of **PA4**. (c) CD spectra of all PAs used in this study. (d) Cell viability of several cervical cancer cell lines on indicated PA surfaces, measured with Calcein/ToPro3 staining. (***p<0.001, **p<0.01)

3.3.3 PA-Cell Membrane Interactions

Based on the surprising cytotoxicity results, we were motivated to examine how the different PAs interact with the cell membrane. Previous work has shown that **PA2** induces cytotoxicity through disruption of the cell membrane.[75] To visualize the PA and cells, we added a small amount of fluorescently labeled PA analog to PA surfaces and labeled the cells with DiO, a cell membrane intercalating dye. We seeded cells on the PA surfaces and allowed them to incubate for 4 hours, and then fixed the cells, mounted the

samples onto glass slides, and imaged them by confocal microscopy after 1 day (Figure 3-4a). We chose a 4-hour time point because at this time, most cells plated on **PA2** coatings were dead but the majority of cells still remained viable on **PA1** coatings (Figure 3-2d). Consistent with previous work,[75] our results showed **PA2** penetrating and compromising the cell membrane, thus killing the cell (Figure 3-4b). Similar to **PA2**, **PA1** is also cationic and contains a weak hydrogen bonding segment, but doesn't co-localize with the cell membrane (Figure 3-4b). We note that the shorter nanofibers of **PA2** may insert into cell membranes more easily than the longer ones of **PA1**, even though both have a weak hydrogen segment. Surprisingly, at a higher confocal plane above the cell-PA interface, we observed "fan-like" structures extending from the cell membrane in **PA1** samples (Figure 3-4b). This "fan" is highly 2-dimensional, and formed at the interface of the mounting slide and mounting media. This "fan" does not form when the sample is not mounted, and it is formed gradually over the course of one day after mounting. We also did this experiment with **PA3** and **PA4** surfaces, which are less cytotoxic than **PA1** surfaces, and neither PA induced formation of these "fan-like" structures (Figure 3-4b). To determine if these "fan-like" structures are lipid membrane extensions and fluid in nature, we labeled the cells with two different lipophilic dyes (DiI and DiO) to examine mixing between "fans" from different cells (Figure 3-4c). We did not observe the mixture of two "fans" from two different cells; however, we found cells with co-localized dyes, which indicates that close association of two cells can allow exchange of cell membrane lipids. Although we do not observe direct co-localization of **PA1** with the cell membrane, the formation of these "fan-like" structures suggests that

PA1 interacts with and alters the cell membrane structure, resulting in increased membrane fluidity.

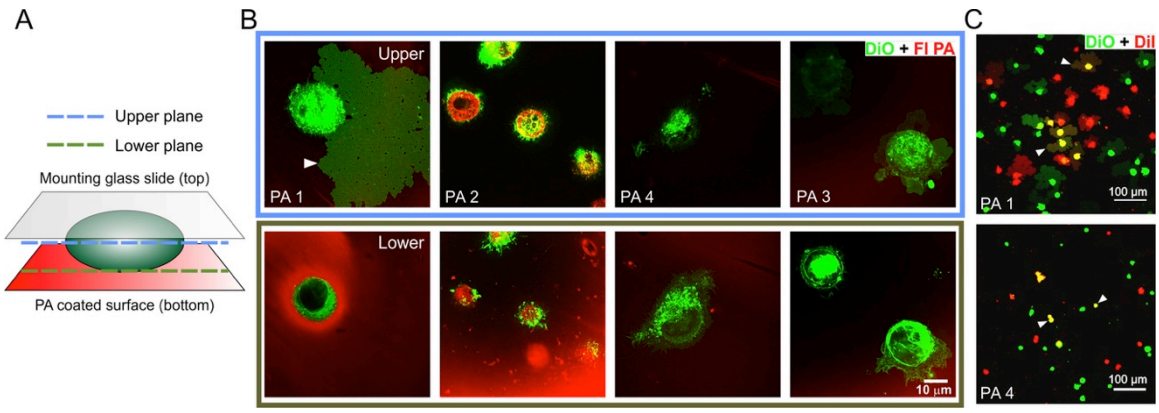

Figure 3-4: Confocal images of cells with cationic PA coatings. (a) Schematic representation of the upper and lower planes that were imaged. (b) Images of CXT2 cells plated on indicated PA surfaces (DiO: green; TAMRA PA: red). The white arrowhead indicates the large "fan-like" cell membrane extensions observed on **PA1** coatings at the upper plane. (c) Confocal images of cells labeled with two different dyes (DiO: green; DiI: red).

3.3.4 Cholesterol Sequestration from Cell Membrane

Cholesterol is an essential structural component of the eukaryotic cell membrane,[178-182] and is involved in regulating membrane fluidity in many tyeps of cells.[183-186] Therefore, one possible mechanism for the "fan" formation is through depletion of cholesterol from the cell membrane by PA. We tried to block cholesterol sequestration by **PA1** using fetal bovine serum (FBS), which contains proteins that can adsorb to the charged PA nanostructures. The resultant protein corona would block the cationic charges of the PA from interacting with the cell membrane, which could prevent

cholesterol transport from the cell membrane to the PA. Furthermore, FBS is known to contain cholesterol, which might compete with membrane cholesterol for interaction with PA and provide a protective effect for cells. We added FBS to **PA1** surfaces, either by pre-incubating the surfaces in cell media containing 10% FBS, or by seeding cells in media containing 10% FBS. As a control, we also seeded cells in serum-free media, onto **PA1** surfaces that had not been treated with FBS. A live/dead assay showed that both pre-incubation of **PA1** surfaces with FBS and the addition of FBS while seeding cells rescued cell viability, although pre-incubation was less effective (Figure 3-5a).

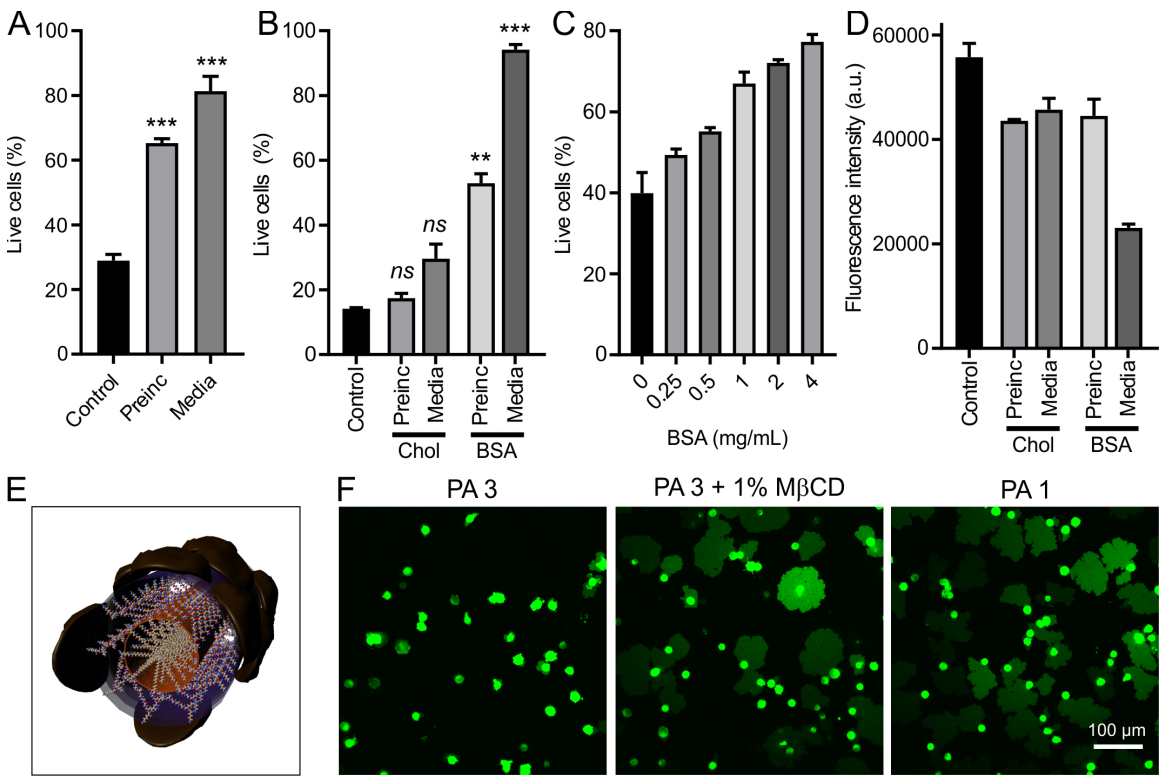

Figure 3-5: FBS and BSA affect cytotoxicity of **PA1** surfaces. (a) Live/dead assay of CXT2 cells on **PA1** surfaces, in serum-free media, media containing 10% FBS or **PA1** coatings that were pre-incubated with cell media containing

10% FBS. (b) Live/dead assay of CXT2 cells on **PA1** surfaces, with BSA or cholesterol either in the cell media or on pre-incubated PA coatings. (c) Live/dead assay of CXT2 cells on **PA1** surfaces, with indicated BSA concentrations in cell media. (d) Fluorescence of LysoSensor™ dye in the presence of PA, after indicated treatments with cholesterol or BSA. (e) Schematic showing proposed mechanism of PA-BSA interactions that block molecular diffusion, preventing sequestration of cholesterol by PA. (f) Cells stained with DiO on **PA3** or **PA1** surfaces, with or without MβCD as indicated. (***$p<0.001$, **$p<0.01$, *ns* $p>0.05$)

To further investigate the mechanism by which FBS rescues cell viability, we examined two of its major components. The main protein component of FBS is bovine serum albumin (BSA), which is a negatively charged protein that should interact with the positively charged PA nanostructures. We incubated **PA1** and **PA3** with BSA and found similar BSA adsorption to both PAs (Figure 3-6), which is not surprising because they both have positive charges. However, in contrast to **PA1**, **PA3** is not cytotoxic even in the absence of serum or BSA (Figure 3-2a-b). We added 4 mg/mL BSA to serum-free cell media, which is similar to the BSA concentration in 10% FBS, and this alone rescued cell viability (Figure 3-5b). Similar to the results with 10% FBS, both pre-incubation of the PA surfaces with BSA and adding BSA to the cell media rescued cell viability, but BSA in the cell media was more protective (Figure 3-5b). Furthermore, we found that the protective effect of BSA is concentration dependent (Figure 3-5c). Conversely, when we added 10 μg/mL cholesterol to serum-free media, we did not observe a significant prevention of cytotoxicity (Figure 3-5b). Pre-incubation of PA coatings with cholesterol also has no protective effect (Figure 3-5b).

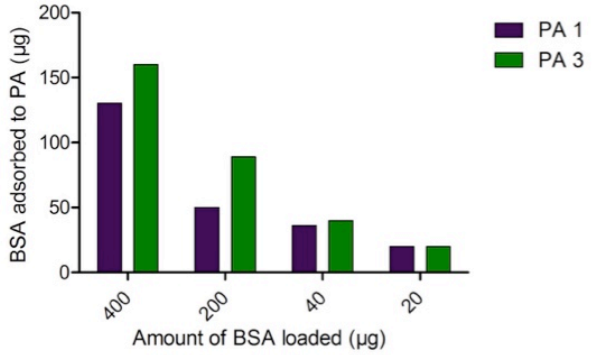

Figure 3-6: BSA adsorbed to **PA1** and **PA3** nanofibers, measured using bicinchoninic acid (BCA assay).

To investigate whether BSA is exerting its protective effect through charge neutralization of positively charged nanofibers, we performed live/dead experiments on **PA2** surfaces with BSA in the cell media. Although **PA2** is also positively charged, BSA did not reverse its cytotoxic effects (Figure 3-7), so charge neutralization alone cannot explain BSA's protective effects. This data, along with the time course cytotoxicity experiment (Figure 2c) and confocal imaging (Figure 4a), suggests that **PA1** exerts its cytotoxic effect through a different mechanism than **PA2**.

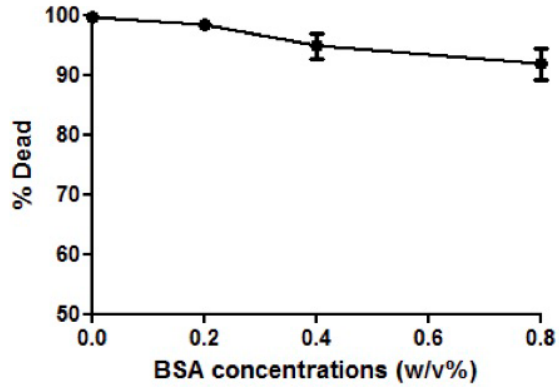

Figure 3-7: Cytotoxicity of **PA2** with indicated BSA concentrations in the cell media.

To explain BSA's rescue of cell viability on **PA1**, we propose that BSA forms a protein corona around **PA1** nanostructures, which impedes the diffusion of small molecules such as cholesterol into the PA's hydrophobic core. Thus, in the presence of BSA, **PA1** would not be able to sequester cholesterol from the cell membrane as efficiently, reducing its ability to kill cells. To further explore this hypothesis, we examined the diffusion of LysoSensor™ Green into **PA1** nanofibers. The LysoSensor™ Green dye is a fluorophore conjugated to a weak base that accumulates in the membrane of acidic organelles after protonation. This dye also shows a strong propensity to accumulate in PA assemblies, resulting in strong fluorescent staining of nanofibers (Figure 3-8).

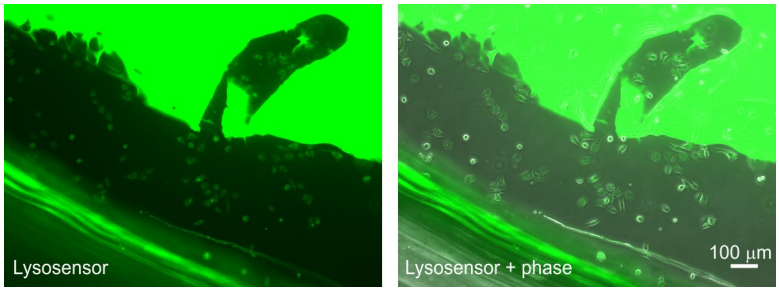

Figure 3-8: LysoSensor™ staining of a **PA1** nanofiber coating. The left image is the LysoSensor™ signal alone, the right image is an overlay of the LysoSensor™ signal and a phase contrast micrograph.

BSA in the media reduces the LysoSensor™ staining intensity (Figure 3-5d), suggesting that a BSA protein corona might prevent the diffusion of weakly polar LysoSensor™ molecules into the PA. We also observed reduction in fluorescence intensity when the dye was incubated with cholesterol, although the effect was less prominent than with BSA in the media (Figure 3-5d). We speculate that cholesterol may compete with

LysoSensor™ molecules for diffusion into **PA1** nanostructures, thus reducing the amount of LysoSensor™ that can be sequestered. Furthermore, we confirmed that PA nanostructures can uptake cholesterol using a NBD cholesterol-binding assay (Figure 3-9).

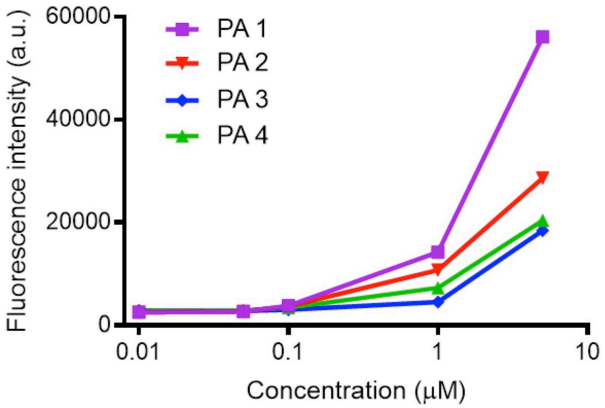

Figure 3-9: Fluorescence of NBD cholesterol in the presence of indicated PAs. The x-axis represents the concentration of NDB cholesterol.

NBD-labeled cholesterol contains a fluorophore that replaces the terminal segment of cholesterol's flexible alkyl tail, and its fluorescence increases when it is within a hydrophobic environment. Interestingly, mixing NBD-cholesterol with **PA1** resulted in a higher fluorescent intensity than **PA2-4**. Although free cholesterol in solution is different from cholesterol within plasma membranes, this data shows that **PA1** is capable of uptaking cholesterol. In light of all these data, we hypothesize that **PA1** exerts its cytotoxic effects by sequestering cholesterol from cell membranes. When BSA adsorbs to **PA1** nanofibers, it forms a protective coating that prevents the nanofibers from depleting the cell membrane of cholesterol (Figure 3-5e).

Previous works have shown that cholesterol depletion from the cell membrane can result in cell death,[187, 188] and we wanted to determine if this applied to our particular system. We tested CXT2 cell viability at different concentrations of a known cholesterol-sequestering agent, methyl-β-cyclodextrin (MβCD). We saw a dose-dependent cytotoxic effect by MβCD, and that 10% FBS reduced this cytotoxicity (Figure 3-10). We introduced MβCD to cells on **PA3** surfaces, which previously did not induce formation of "fan-like" structures (Figure 3-4b) or cause cell death (Figure 3-2a-b). With the addition of 1% MβCD in the cell media, we observed distinct "fan" formation from the cells, similar to **PA1** surfaces with no MβCD (Figure 3-5f). This suggests **PA1** *surface coatings* are exerting a similar effect on cells as MβCD, a known cholesterol-sequestering agent, when MβCD is *dissolved in the cell media*.

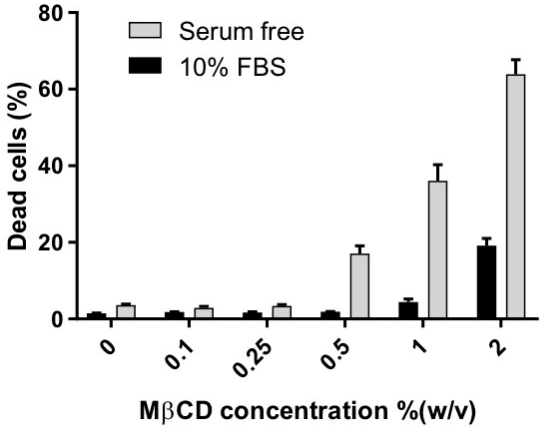

Figure 3-10: Cytotoxicity of MβCD, with and without serum in the cell media.

Taken together, the experiments with FBS, BSA, cholesterol, and LysoSensor™ suggest that **PA1** nanofibers interact with cell membranes to sequester cholesterol, which

results in a cytotoxic effect. Conversely, **PA4** nanofibers cannot deplete the cell membrane of cholesterol, so it is not cytotoxic. These differences are caused by a change in lysine linker polarity (Figure 3-1, Figure 3-3), and are illustrated in Figure 3-11.

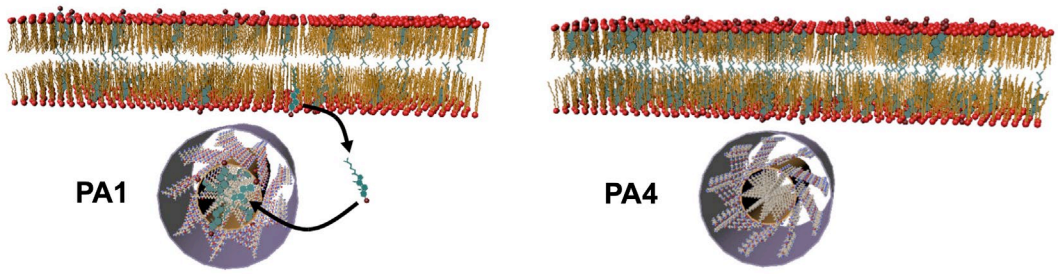

Figure 3-11: Illustration of cholesterol sequestration by **PA1** nanofibers, but not **PA4** nanofibers

3.3.5 Programmed Death is Linked to Oncotic Mechanism

As shown by previous work, cholesterol depletion from the cell membrane can activate signaling cascades that result in apoptosis.[187, 188] In these reports, the ultimate cell death is programmed through activation of apoptotic pathways, as opposed to immediate physical rupture of the cell membrane. We hypothesized that the cytotoxicity of **PA1** is through *programmed cell death*, as opposed to physical disruption of the cell membrane. Conversely, results from the current work (Figure 3-4) and previous work[75] both suggest that **PA2** physically disrupts the cell membrane. To probe the cell death mechanism of **PA1**, we performed time lapse imaging of CXT2 cells on **PA1** surfaces. We observed the formation of giant blebs before cell death (Figure 3-12a), which is characteristic of an oncotic, not apoptotic, mechanism.[163-166] We note that the blebs

observed in this work (Figure 3-12a, white arrows) appear quite similar to blebs observed in other oncotic cells (Figure 1b[165]).

Additionally, cells were labeled with rhodamine 123, which stains mitochondrial membranes in live cells, and propidium iodide (PI) was added to the cell media, which identifies dying cells with permeable membranes. In healthy cells, rhodamine 123 penetrates the plasma membrane and concentrates in intact mitochondrial membranes, causing it to self-quench its fluorescence intensity. When the mitochondria are compromised, the mitochondrial membrane potential drops and rhodamine 123 molecules are released into the cytoplasm, thus increasing fluorescence intensity. During a cell death event, rhodamine 123 intensity increases approximately 1 hour before the uptake of propidium iodide (Figure 3-12b), suggesting that mitochondrial compromise occurs prior to cell death on **PA1** surfaces. Next, we observe an uptake of propidium iodide into the cell, during which rhodamine 123 fluorescence intensity rapidly drops (Figure 3-12b). As the cell membrane breaks down during cell death, rhodamine 123 is no longer contained within the cytoplasm, so its fluorescence intensity decreases. We note that the first giant blebs form during the period of initial increase in rhodamine 123.

The role of mitochondria in coordinating cell death is well established, and compromised mitochondria are early indicators of cell damage.[160, 189-193] The rhodamine 123 experiments suggest that mitochondria damage occurs prior to cell death on **PA1** surfaces, and we further explored this idea by measuring intracellular ATP levels. We performed this experiment after 6 hours of incubation on PA surfaces, when nearly 100% of cells were dead on **PA2** surfaces but only 61% of cells were dead on **PA1** surfaces. Intracellular ATP was not detectable on **PA2** (Figure 3-12c), where 100% of cells are

already dead (Figure 3-2d). On **PA3** and **PA4**, which are not cytotoxic (Figure 3-2a-b, Figure 3-3d), the intracellular ATP level was comparable to that of a control poly-D-lysine surface (Figure 3-12c). However, on **PA1** surfaces, we found a significantly lower intracellular ATP level compared to **PA3** and **PA4** surfaces, but a significantly higher ATP level compared to **PA2** surfaces (Figure 3-12c). Concomitant live/dead assays show that while the percentage of live cells on **PA1** surfaces is only around 30% less than on **PA3** and **PA4**, the ATP level detected on **PA1** surfaces is already around 60% less than on **PA3** and **PA4** surfaces. This suggests that, on **PA1** surfaces, mitochondrial damage occurs some time before ultimate cell death. This result, along with the time course cytotoxicity assay and mechanistic studies with BSA and MβCD, suggest that **PA1** induces *programmed cell death* mediated by signaling cascades. The necessary oncotic signaling pathways may take some time to activate, which is in contrast to the physical cell membrane rupture caused by **PA2**.

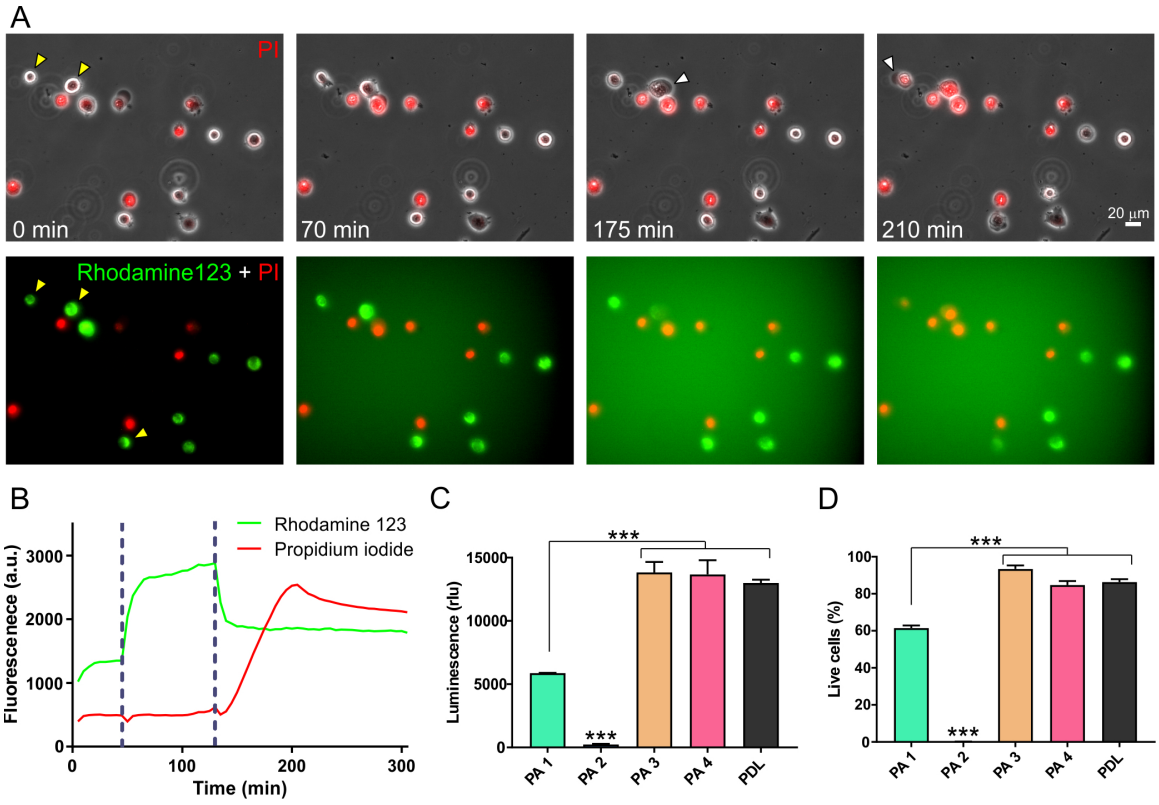

Figure 3-12: Mitochondrial distress precedes cell death on **PA1** surfaces. (a) CXT2 cells on PA surfaces and stained with rhodamine 123 and propidium iodide. Yellow arrowheads indicate cells that die in later frames. White arrowheads indicate giant blebs preceding cell death. (b) Representative time course of rhodamine 123 and propidium iodide fluorescence intensities, in an individual cell. (c) Fluorescence detection of ATP in CXT2 cells, after 6 hours on indicated PA surfaces. (d) Viability of cells on indicated PA coatings after 6 hours. (***p<0.001)

3.4 CONCLUSIONS

In summary, we have shown that subtle changes to PA molecular design, specifically the alkyl tail position, can significantly affect their interactions with the cell membrane and thus their cytotoxic effects. Specifically, placing the alkyl tail at the peptide's N-terminus will result in rapid cytotoxicity, while placing the alkyl tail at the C-terminus results in slower cytotoxicity. The rapid cytotoxic effects were linked to

physical disruption of the cell membrane, caused by the cationic PA inserting itself into the negatively charged lipid bilayer. A slower cytotoxic effect occurred when the PA did not physically enter the cell membrane structure, but instead sequestered membrane cholesterol. This cholesterol sequestration initiated a programmed cell death cascade, which appears to be though oncosis rather than apoptosis. Reversing the polarity of the lysine linker between the alkyl tail and the peptide decreased the PA's ability to sequester cholesterol, which rescued cell viability. When shifting the alkyl tail from the N-terminus to the C-terminus, a lysine linker must be added, and the effect of this subtle difference is not completely understood (**PA1** versus **PA2**). However, in reversing the lysine linker's polarity, both the alkyl tail and peptide portion remain identical (**PA1** versus **PA3**). Our results suggest that subtle changes in molecular design are able to exert significant biological effects due *to supramolecular self-assembly*, since it is the PA *nanostructures* that ultimately interact with cells. We believe the concepts presented here are applicable to other supramolecular biomaterials, specifically those containing amphiphilic species. In particular, these results may be interesting to the development of anti-cancer therapies, where it may be beneficial to selectively induce programmed cell death, as opposed to physically damaging cells with blunt force.

3.5 MATERIALS AND METHODS

Peptide Synthesis

PA molecules were synthesized using standard fluorenylmethyloxycarbonyl (Fmoc) solid phase peptide synthesis, at the Peptide Synthesis Core at the Simpson

Querrey Institute. For PA1, PA3, and PA4, where the alkyl tail is attached at the peptide's C-terminus via a lysine, Fmoc-Lys(Mtt)-OH was first coupled to rink amide resin. For PA1 and PA3, the Mtt-protected ε-amine was deprotected with 3% trifluoroacetic acid (TFA), 5% triisopropylsilane (TIPS) and 93% dichloromethane (DCM). The C_{16} alkyl tail was then coupled to this ε-amine using 5 molar equivalents of C_{16} alkyl tail, 5 equiv *O*-benzotriazole-*N*, *N*, *N*′, *N*′-tetramethyluronium hexafluorophosphate (HBTU) and 10 equiv *N*, *N*-diisopropylethylamine (DIEA), at 75 °C for 5–10 minutes. For PA4, the same procedure was used to attach the C_{16} alkyl tail, except that the C_{16} alkyl tail was coupled to the lysine's α-amine. To do this, the Fmoc-protected α-amine was deprotected with 20% 4-methylpiperidine and 0.1 M hydroxybenzotriazole (HOBt) in dimethylformamide (DMF) at 75 °C for 3–4 minutes, to allow the alkyl tail to be coupled to the α-amine. For PA1 and PA3, the peptide was then synthesized in a CEM Liberty microwave-assisted peptide synthesizer, which performed deprotection of Fmoc groups and amino acid couplings. Fmoc deprotection was performed with 20% 4-methylpiperidine and 0.1 M hydroxybenzotriazole (HOBt) in dimethylformamide (DMF) at 75 °C for 3–4 minutes, and amino acids were coupled using 5 molar equivalents of protected amino acid, 5 equiv *O*-benzotriazole-*N*, *N*, *N*′, *N*′-tetramethyluronium hexafluorophosphate (HBTU) and 10 equiv *N,N*-diisopropylethylamine (DIEA), at 75 °C for 5–10 minutes. For PA4, the Mtt-protected ε-amine was deprotected with 3% trifluoroacetic acid (TFA), 5% triisopropylsilane (TIPS) and 93% dichloromethane (DCM), and the peptide was then synthesized in a CEM Liberty microwave-assisted peptide synthesizer, which performed Fmoc deprotections and amino acid couplings, as described above for PA1 and PA3. For PA2, where the

alkyl tail is attached at the peptide's N-terminus, amino acids were simply coupled to the rink amide resin, using the Fmoc deprotection and amino acid coupling procedures described above. The C_{16} alkyl tail was then coupled to the last amino acid, at the peptide's N-terminus, using the same procedure for coupling amino acids. For PA2, all Fmoc deprotections and amino acid or alkyl tail couplings were performed in a CEM Liberty microwave-assisted peptide synthesizer.

Following synthesis of all PA molecules, they were cleaved from the rink amide resin with 95:2.5:2.5 TFA:TIPS:water for 2-3 hours. Volatile solvents were removed using rotary evaporation, and the PA was precipitated using diethyl ether. The PA was dried using a fritted filter and then purified using reverse phase high performance liquid chromatography. PAs were purified with a mobile phase gradient of acetonitrile and water, containing 0.1% TFA to aid solubility, on a Phenomenex Jupiter Proteo column (C_{12} stationary phase, 10 μm, 90 Å pore size, 150 x 30 mm). HPLC fractions containing PA were identified using ESI mass spectroscopy, and acetonitrile was removed from fractions using rotary evaporation. The pure fractions were then lyophilized to a dry powder, which was stored at -20°C until use. The PA powders were checked for purity using liquid chromatography - mass spectroscopy (LC-MS).

Cryogenic Transmission Electron Microscopy

All PAs were dissolved to 1 wt% in pure water, and cryoTEM samples were prepared immediately after. PA solutions (6.5 uL) were deposited onto 300-mesh copper grids with lacey carbon film (Electron Microscopy Sciences, Hatfield, PA, USA), which had been glow discharged for 30 seconds in a PELCO easiGlow system (Ted Pella, Inc.,

Redding, CA, USA). The samples were automatically blotted and plunged into liquid ethane using a FEI Vitrobot Mark IV (FEI, Hillsboro, OR, USA), maintained around 95% humidity. After vitrification in ethane, samples were transferred to a Gatan 626 cryo-holder (Gatan, Pleasanton, CA, USA). The samples were submerged in liquid nitrogen during the transfer. Finally, the samples were imaged on a JEOL 1230 TEM operating at 100 kV, and micrographs taken with a bottom-mounted Gatan 832 camera.

Peptide Amphiphile (PA) Coatings

To create 2D coatings of PA, a solution of 0.01 wt% poly-D-lysine (PDL) in 0.1 M (pH 8.5) borate buffer was added to completely cover the surface (50 μL per well for 96-well plates or 300 μL per 12 mm glass coverslip). The glass cover slips were placed into 24-well plates for coating, and submerged with 300 μL of PDL solution in the entire well. The surfaces were incubated with the PDL solution for 3 hours at room temperature, and then washed 3x with double distilled water (ddH_2O). Next, a 0.25 wt% alginate solution in ddH2O was added to the surfaces (50 μL per well for 96 well plates or 75 μL per glass coverslip). The glass cover slips were in 24-well plates for coating, but the alginate solution was only added to the glass cover slip. Surfaces were incubated with alginate at room temperature for 2 hours, after which the alginate was gently aspirated leaving a thin layer of coating. The surfaces were then rinsed twice with 10 mM $CaCl_2$ to crosslink the alginate. PA solutions (0.05 wt% in ddH2O) were then added to the surfaces and left overnight at 37°C. PA-coated surfaces were washed twice with Hanks' Balanced Salt Solution (HBSS, GIBCO [Thermo Fisher] Waltham, MA, USA). Glass-bottom dishes (MatTek Corporation, Ashland, MA, USA) were coated using the

same technique, with minor changes in solution volumes, to ensure full coverage of the glass surface.

Cell Culture (Cervical Cancer Cells)

Cervical epithelial cells were isolated from tissue purchased through the Coopertative Human Tissue Network as described previously.[194] Both non-cancerous and cancerous (CXT) cervical epithelial cells were cultured in Keratinocyte Serum Free media (KSFM, GIBCO) at 37°C and 5% CO_2. Cells were passaged at >80% confluency using 0.05% trypsin/EDTA (Life Technologies, Carlsbad, CA, USA). The trypsin was neutralized with KSFM containing 10% FBS (fetal bovine serum), and removed by centrifugation at 600 rcf for 5 minutes. For experiments, cells were resuspended in KSFM and plated at the desired cell numbers. The numbers assigned to the CXT cervical cancer cells (CXT2, CXT3, etc.) designate cells derived from different patients.

Live/Dead Assay

Cells (CXT or normal cervical epithelial cells) were plated at 5,000 cells/well of a 96 well plate containing a PA coating, in 100 μL of KSFM media (GIBCO). After the desired treatment time, cells were incubated with 2 μM calcein-AM and 1 μM ToPro-3 iodide in KSFM for 30 minutes at 37°C. Then cells were imaged using a Spectramax i3x Microplate reader. The images were analyzed by counting the number of calcein positive cells (live) and the number of ToPro-3 positive cells (dead).

MTT Assay

Cells were plated at 5,000 cells/well of a 96 well plate containing a PA coating, in 100 μL of KSFM media (GIBCO). After the desired treatment time, cells were incubated with 100 μL of MTT solution (1 mM MTT in KSFM) for 4 hours. After this incubation, the MTT solution was removed and replaced with 100 μL of DMSO to solubilize the formazan precipitate. The absorbance in each well was measured at 555 nm using a Spectramax i3X Microplate reader.

Circular Dichroism (CD)

As a buffer for PA samples during CD experiments, we diluted Hank's Balanced Salt Solution (HBSS) 25x in pure water. All PAs were dissolved to 1 wt% with pure water, and then PAs were diluted 50x in the diluted HBSS buffer. This PA sample (200 *u*L) was loaded into a 1 mm path length quartz cuvette, and scanned on a JASCO J-815 spectrophotometer from 190 - 250 nm.

Confocal Microscopy (for PA-cell membrane interactions)

CXT2 cells were seeded onto 12 mm glass cover slips containing a PA coating, placed in a 24-well plate. For visualization, the PA solution contained 1 wt% of a fluorescent analog. For PA4, a fluorescent analog was not available, so 1 wt% of fluorescent PA1 was used. Cells were harvested and labeled by incubation with a 1 μM solution of DiO or DiI in KSFM, at 37°C for 30 minutes. After this incubation, cells were washed in KSFM twice, and centrifuged at 600 rcf for 5 minutes to remove the wash solutions. After the washes, cells were resuspended with KSFM to 300 cells/*u*L,

and 50 *u*L of this solution (15,000 cells) was deposited onto the cover slips. To allow cell attachment without disturbance, glass cover slips were incubated with this 50 *u*L cell suspension for 1 hour before more KSFM was added to fill the well. Cells incubated with the PA coatings for a total of 4 hours, and then fixed using 4% paraformaldehyde (PFA) for 15 minutes at room temperature. Following PFA fixation, samples were washed 3x with PBS and the coverslips were mounted onto glass slides. One day after mounting, images were using the 63x objective on a Leica DM18 confocal microscope. Z-stacks were taken to capture the focal planes shown in Figure 3-4a.

Live/Dead Assays Using FBS, BSA, or Cholesterol to Block Nanostructures

FBS, BSA, or cholesterol was added to KSFM media, and PA surfaces were incubated with these solutions for 2 hours prior to cell seeding. For "pre-incubation" samples, these solutions were removed prior to cell seeding, and cells were seeded in KSFM media alone. For "media" samples, cells were seeded in KSFM media still containing FBS, BSA, or cholesterol.

LysoSensor™ Staining

PA coatings in 96-well plates, after overnight incubation with cholesterol or BSA at 37°C, were incubated with 500 nM LysoSensor™ Green (Invitrogen [Thermo Fisher], Carlsbad, CA, USA) in 100 μL PBS for 30 minutes. For "pre-incubation" samples, the PBS did not contain cholesterol or BSA. For "media' samples, the PBS contained cholesterol or BSA. After 30 minutes, the PA coatings were rinsed with fresh PBS, which contained cholesterol or BSA in "media" samples but no cholesterol or BSA in "pre-incubation" samples. Fluorescence measurements of each well (21 spots per well)

were collected using a Spectramax i3X Microplate reader, with an excitation/emission of 488nm/530nm. The fluorescence of the 21 spots was averaged to reduce artifacts due to uneven PA coating. The example shown in Figure 3-8 is a PA1 coating in a glass bottom dish, without any FBS, BSA, or cholesterol.

Methyl-β-Cyclodextrin (MβCD).Experiments

Cells were plated at 5000 cells/well in a 96-well plate and allowed to equilibrate overnight before MβCD exposure. After this overnight incubation, cells were exposed to the indicated concentrations of MβCD in KSFM media, with or without 10% FBS, for 1 hour at 37°C. Following MβCD exposure, cell death was quantified with a live/dead assay, using calcein/ToPro-3 dyes.

Quantification of BSA Adsorbed to PA Gels Using a Bicinchoninic Acid (BCA) Assay

To form PA gels, cationic PAs were first dissolved to 1 wt% with ddH_2O and sonicated. These solutions were gelled by exposing 20 *u*L of PA solutions to ammonia vapors for 30 minutes at room temperature, which should ionically crosslink the cationic lysines. The gels were then incubated overnight with 100 *u*L of PBS containing the indicated BSA amount. After incubation with BSA, the supernatant was collected and analyzed using a BCA kit through the manufacturer's instructions (Pierce™ BCA Protein Assay Kit, Thermo Fisher, Waltham, MA, USA). Briefly, the supernantant was diluted into BCA working reagent (25 *u*L sample + 200 *u*L working BCA reagent) and incubated at 37°C for 30 minutes. Afterward this incubation, the absorbance of the samples and a standard curve at 562 nm were read on a Spectramax i3X Microplate reader. The

concentration of BSA in the supernatant was calculated using the standard curve, and this concentration was subtracted from the initial BSA concentration to calculate the amount of BSA that had adsorbed to PA gels.

NBD-Cholesterol Assay

NBD cholesterol (Life Technologies [Thermo Fisher], Carlsbad, CA, USA) was dissolved in ethanol to make a 2.5 *u*M stock solution, which was stored This stock solution was diluted with PBS to obtain the following concentrations of NBD cholesterol: 2 mM, 1 mM, 200 *u*M, 20 *u*M, 10 *u*M, 2 *u*M. These solutions will be diluted 1:200 with PA solution, so the final NBD cholesterol concentrations in the assay will be: 10 *u*M, 5 *u*M, 1 *u*M, 0.1 *u*M, 0.05 *u*M, 0.01 *u*M. PAs were first dissolved to 1 wt% in pure water, and then further diluted with PBS to obtain a 200 *u*M PA solution. The molecular weights of the PAs are as follows: PA1 – 1025 g/mol, PA2 – 1025 g/mol, PA3 – 1151 g/mol, PA4 – 1025 g/mol. In a 96-well plate, 100 *u*L of the 200 *u*M PA solution was mixed with 0.5 *u*L of the NBD cholesterol solution, at various concentrations of NBD cholesterol. The plate was incubated for 1 hour in the dark at room temperature, and read on a Cytation^{TM}3 (BioTek, Winooski, VT, USA). The samples were excited at 473 nm and the fluorescence emission collected from 500 – 600 nm.

Rhodamine 123 + Propidium Iodide (PI) Time Lapse Imaging

CXT2 cells (7,500 cells in 100 μL of KSFM) were seeded into a glass bottom dish, coated with PAs. The cells were allowed to equilibrate for 1 hour at 37°C before a rhodamine 123 solution (5 μg/mL in KSFM) was added. After 45 minutes at 37°C, the

rhodamine 123 solution was removed, the dishes were gently washed 3x with KSFM before adding a PI solution (1.5 mL of 1 μg/mL PI). Cells were imaged every 5 minutes over 24 hours at 10X magnification, with 12 fields of view for each time point, on a Nikon BioStation IM live imaging microscope.

ATP Assay

CXT2 cells were plated into 96-well plates coated with PA, and incubated on PA coatings for 6 hours. After 6 hours, cells were washed once with PBS, and then incubated with 30 μL 0.5% trichloroacetic acid (TCA) at 4°C for 30 minutes to lyse the cell membranes. After 30 minutes, TCA was neutralized with addition of 180 μL 50 mM tris-acetate buffer (pH 7.75). Samples were mixed well and centrifuged at 1000*g* at 4°C for 5 minutes, and the supernatant was collected and stored at -20°C until analysis. For analysis with an ENLITEN® ATP Assay (Promega, Madison, WI, USA), the supernatant was diluted 10x in tris-acetate buffer. The ATP content was analyzed using the manufacturer's instruction, and plates were read on a Spectramax i3X Microplate reader.

4 SELF-REPAIR OF SUPRAMOLECULAR NANOSTRUCTURES

4.1 OBJECTIVE AND SIGNIFICANCE

Supramolecular nanostructures formed through self-assembly can have energy landscapes, which determine their structures and functions depending on the pathways selected for their synthesis and processing, and on the conditions they are exposed to after their initial formation. We report here on the structural damage that occurs in supramolecular peptide amphiphile nanostructures, during freezing in aqueous media, and the self-repair pathways that restore their functions. We found that freezing converts long supramolecular nanofibers into shorter ones, compromising their ability to support cell adhesion, but a single heating and cooling cycle reverses the damage and rescues their bioactivity. Thermal energy in this cycle enables non-covalent interactions to reconfigure the nanostructures into the thermodynamically preferred long nanofibers, a repair process that is impeded by kinetic traps. In addition, we found that nanofibers disrupted during freeze drying also exhibit the ability to undergo thermal self-repair and recovery of their bioactivity, despite the extra disruption caused by the dehydration step. Following both freezing and freeze drying, which shorten the 1D nanostructures, their self-repair capacity through thermally driven elongation is inhibited by kinetically trapped states, which contain highly stable non-covalent interactions that are difficult to rearrange. These states decrease the extent of thermal nanostructure repair, an observation we hypothesize applies to supramolecular systems in general and is mechanistically linked to suppressed molecular exchange dynamics.

4.2 BACKGROUND

Supramolecular self-assembly directs biological molecules into quaternary protein structures, lipid membranes, and DNA double helices, and is thus essential to cell function. This natural phenomenon has inspired the design of self-assembling biomaterials for a variety of applications including regenerative medicine[31, 63, 89], drug delivery,[195] cancer therapies,[196] and immuno-engineering.[197] Although supramolecular biomaterials show great promise, a recently identified aspect of their structure and function is proper selection of their self-assembly pathway in order to optimize bioactivity.[101-103] In recent work some pathways have been found to result in structures with greater cytotoxicity.[102, 103] Even after the molecules have traversed an undesired self-assembly pathway, it may be possible to "repair" the "damaged" supramolecular structures, since their non-covalent nature provides inherent reversibility.[16, 88, 198] The self-repair ability of supramolecular materials has been previously demonstrated in the context of mechanical defects. For example, supramolecular elastomers spontaneously self-heal when broken pieces are brought into contact, because hydrogen bonds readily reform at the fracture site.[199, 200] Heat[201, 202] or light[203] can induce rearrangement of intermolecular interactions near a fracture site, allowing the network to fill in the defect. While these strategies can mend mechanical defects, they cannot repair defective supramolecular nanostructures that have undergone incorrect self-assembly pathways and reached non-functional positions in their energy landscapes. For example, misfolded protein configurations are considered non-functional positions in their energy landscape.[104] The repair of misfolded proteins has been reported but the processes are

extremely cumbersome, requiring finely tuned mixtures of small molecules and chaperones,[204-206] because the energy landscapes of protein folding are extremely complex.

Our laboratory has developed a broad platform of self-assembling molecules known as peptide amphiphiles (PAs), which in canonical form contain a hydrophobic tail, a β-sheet forming peptide domain to trigger self-assembly into highly one-dimensional fiber-like nanostructures, and charged amino acid headgroups to promote solubility in water.[31, 32] In some cases, the peptide sequence terminates in a bioactive domain designed to interact directly with cell receptors or bind specific signaling proteins such as growth factors.[89, 108, 111, 112] We have demonstrated their functionality in a variety of *in-vivo* pre-clinical models for the regeneration of bone[108], cartilage[111], muscle,[87] blood vessels,[112] as well as spinal cord[114] and peripheral nerves.[115] For regenerative medicine applications, our group has extensively studied the use of PAs with the peptide sequence $V_3A_3E_3$ (Figure 4-1). This PA self-assembles into high-aspect ratio nanofibers that can mimic the architecture of mammalian extracellular matrices, and also forms self-supporting gels when the negatively charged glutamic acids are ionically crosslinked with divalent counterions (usually Ca^{2+}).[71, 86, 207, 208] Since PA nanostructures in solution are dynamic, we typically freeze dry PA solutions and store the dried powders until they are to be used in biological applications. Knowing that self-assembly of PA molecules into nanostructures is sensitive to their preparation pathway,[102, 103] we were motivated to study how the freeze drying process affects the PA nanoscale filaments. Amyloid fibrils, another self-assembling peptide system, can fragment into shorter pieces[209] or undergo liquid crystalline phase transformations[210] when exposed to freeze-thaw cycles. Other

organic nanostructures such as proteins,[123] nanoparticles,[124] and liposomes,[125] as well as cells[126] are often preserved by freezing or freeze drying, and thus sometimes are structurally damaged by ice nucleation, the use of extreme temperatures, and dehydration.[123-126] The objective of this work has been to characterize freezing and freeze drying damage to PA nanostructures and explore mechanisms and strategies to repair their structure and function.

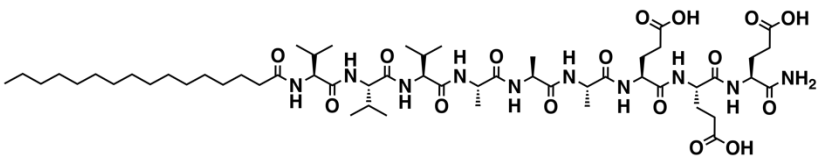

Figure 4-1: Chemical structure of $V_3A_3E_3$ PA.

4.3 RESULTS AND DISCUSSION

4.3.1 Structural Damage to Nanostructures During Flash Freezing

Before freezing and freeze drying $V_3A_3E_3$ PA solutions, we equilibrated the nanostructures at their thermodynamic minimum by applying a previously discovered, thermally activated self-assembly pathway (annealing at 80°C for 30 minutes followed by slow cooling overnight).[71, 103] These solutions contained 1 wt% (8.66 mM) PA dissolved in 15 mM NaOH, conditions that lead to a low charge density on the nanostructures, which in turn favor β-sheet formation and thus formation of long nanofibers.[103] Therefore, the annealing procedure results in formation of highly viscous solutions. When this solution is flash frozen and allowed to thaw at room temperature, its viscosity decreases drastically, suggesting disruption of the nanofiber structure (Figure 4-2a-b).

Using nanoparticle tracking analysis (NTA) to visualize light scattered by nanofibers, we estimated their lengths in annealed and flash frozen solutions, and found that annealed PA nanofibers tend to be well over 10 μm long, while flash frozen nanofibers are generally less than 5 μm (Figure 4-2c). Viewed under cross-polarizers, annealed solutions of PA nanostructures contain large birefringent monodomains (Figure 4-2d), while flash frozen PA contains smaller ones (Figure 4-2e), indicating shorter fibers forming domains with less alignment. These observations are consistent with the lyotropic liquid crystalline nature of aqueous solutions formed by the nanoscale filaments.[71] We examined individual nanofibers by cryogenic transmission electron microscopy (cryoTEM) from both annealed (Figure 4-2f) and flash frozen solutions (Figure 4-2g), confirming the previous observations. Taken together, the viscosity, light scattering, and microscopy data demonstrate that flash freezing long nanofibers in solution fractures them into significantly shorter ones. Although long nanofibers should be thermodynamically favored, we infer that the short freeze-damaged nanofibers are kinetically trapped in a local energy minima and do not spontaneously grow back to their original lengths during our time of observation.

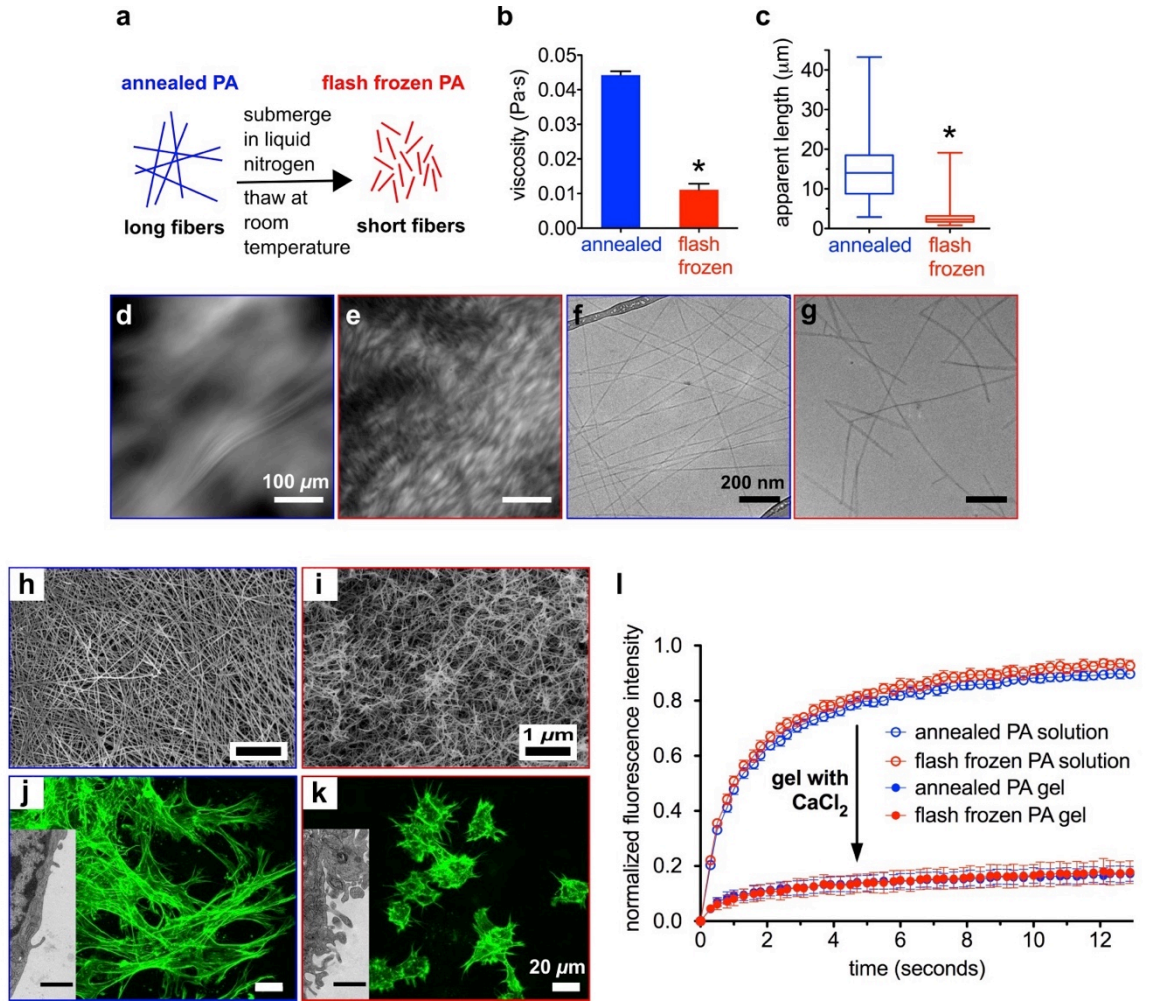

Figure 4-2: Flash freezing PA nanofibers. (a) Schematic representation summarizing the effects of flash freezing annealed PA solutions. (b) Viscosity of annealed and flash frozen PA solutions (*$p < 0.0001$, two-tailed paired t-test; error bars represent standard error of mean). (c) Box-and-whisker plot of apparent nanofiber lengths in annealed and flash frozen PA using nanoparticle tracking analysis (NTA) video frames (*$p < 0.0001$, two-tailed unpaired t-test) (d, e) Cross-polarized light micrograph of annealed and flash frozen PA, respectively. (f, g) CryoTEM of annealed and flash frozen PA, respectively. (h, i) SEM micrographs of annealed and flash frozen PA gels, respectively. (j, k) Confocal micrographs of MC3T3 mouse preosteoblast cells encapsulated inside annealed and flash frozen PA gels, respectively (insets are TEM micrographs of cell cross-sections; scale bar for inset: 1 μm). (l) Fluorescence recovery after photobleaching (FRAP) experiments on FITC-conjugated BSA within annealed and flash frozen PA solutions and gels (error bars are 95% confidence intervals).

Knowing that flash freezing shortens nanofibers in PA solutions, we studied the bioactivity implications for the PA gels made up of these one-dimensional nanostructures. The nanostructures can localize and deliver growth factors and provide a scaffold to support cell infiltration.[108, 111, 211] We prepared PA gels by introducing $CaCl_2$ to annealed and flash frozen PA solutions, which crosslinks negatively charged glutamic acids with positively charged Ca^{2+} ions, and then examined the resultant structure of the gels, as well as cell and protein interactions with the gels. Scanning electron micrographs (SEM) reveal that annealed PA gels contain long nanofibers (Figure 4-2h) while flash frozen PA gels contain shorter nanofibers (Figure 4-2i), which is consistent with our observations in solution. Since cells are sensitive to nanoscale topographical cues,[66-68] we studied whether this difference would affect cellular response to the nanofibers within the PA gels. We encapsulated MC3T3 mouse preosteoblasts in annealed and flash frozen PA gels, allowed the cells to equilibrate for 24 hours, and then imaged the cell morphology using actin staining. Confocal microscopy images show that cells within annealed PA gels spread and elongate (Figure 4-2j), but those within flash frozen PA gels remain more rounded (Figure 4-2k). For a closer view of the interface between cells and PA, we cut thin sections of cells inside PA gels and observed them with transmission electron microscopy (TEM). These thin sections revealed that cells inside the annealed PA gels have a few small protrusions along otherwise smooth plasma membranes (Figure 4-2j, inset), while cells inside the flash frozen PA gels show intense membrane blebbing (Figure 4-2k, inset). Previous work has shown that cell membrane blebbing occurs in the earliest stages of cell spreading, with blebs maturing to adherent lamellipodia in later stages.[212-214] Therefore, we hypothesize that the cell membrane continues blebbing after

unsuccessful attempts to attach to shorter, freeze-damaged fibers. These results are consistent with previous work from our laboratory, which showed that chemically identical PA surfaces support cell adhesion better when fibers are longer.[103] Taken together, these results indicate that freezing damage is detrimental for either encapsulation of cells within PA gels or the recruitment of endogenous cells when they need to infiltrate implanted PA gels.

Since cells are known to be sensitive to matrix mechanical properties (i.e. stiffness), we also performed rheological analysis of the annealed and flash frozen PA gels. We induced gelation of PA solutions with $CaCl_2$, and were surprised to find that the shorter nanofibers of flash frozen PA forms stiffer gels than the longer nanofibers of annealed PA (Figure 4-3a-b). Although the magnitudes of the storage and loss modulus are different, the frequency (Figure 4-3c-d) and strain (Figure 4-3e-f) responses of annealed and flash frozen PA gels are similar. They both become stiffer and show more elastic behavior at higher frequencies, and both break under strain to show more viscous behavior.

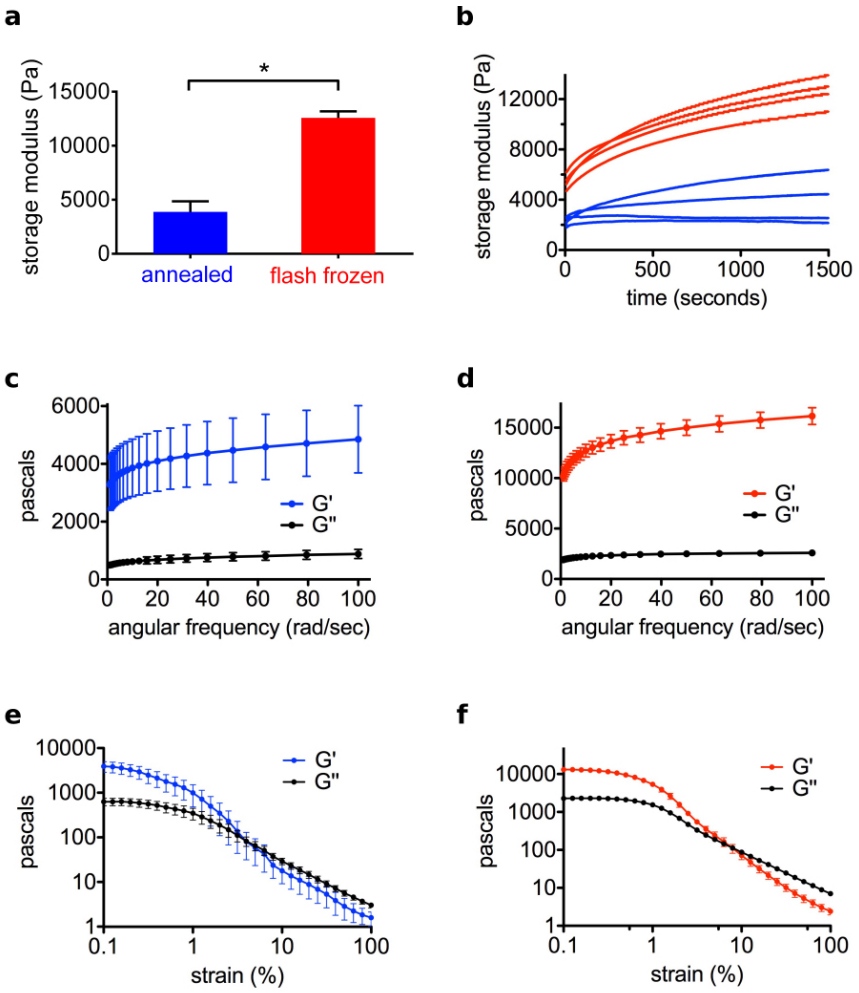

Figure 4-3: Rheology of annealed and flash frozen PA. (a) Storage modulus of annealed and flash frozen PA gels, formed by $CaCl_2$ crosslinking, after an equilibration period. (b) Storage modulus of annealed and flash frozen PA gels, during $CaCl_2$ crosslinking for indicated amounts of time. The storage modulus reported in panel *a* is the final data point in panel *b*. Frequency sweep experiment of (c) annealed and (d) flash frozen PA gels after crosslinking in $CaCl_2$. Strain sweep experiment of (e) annealed and (f) flash frozen PA gels after crosslinking in $CaCl_2$.

Next we investigated protein interactions with annealed and flash frozen PA gels, since PA gels are known to be effective vehicles for growth factor delivery.[108, 111] We examined the effect of flash freezing on the ability of PA nanofibers to bind proteins

using bovine serum albumin (BSA). Although BSA has an overall negative charge, it contains both negatively and positively charged residues, and is known to attach to either positively or negatively charged surfaces.[215] We mixed FITC (fluorescein isothiocyanate)-conjugated BSA into annealed and flash frozen PA solutions, induced gelation with $CaCl_2$, and imaged the gels with confocal microscopy. We performed fluorescence recovery after photobleaching (FRAP) experiments by bleaching 10 μm diameter circles in the gels and monitoring fluorescence recovery. Since photobleaching is irreversible, fluorescence recovery only occurs if unbleached FITC-BSA diffuses into the bleached area. Less or slower recovery indicates less protein mobility, signifying stronger association with the nanofibers. FRAP data shows that annealed and flash frozen PA are equally capable of immobilizing BSA within their gels, with only 10-20% of the initial fluorescence recovered in both cases (Figure 4-2l). This suggests that protein retention by nanofibers derives from surface properties, such as electrostatic forces and is independent of fiber length. Furthermore, BSA diffuses freely through PA solutions and recovers approximately 90% of initial fluorescence (Figure 4-2l), demonstrating that gelation of PA or immobilization of nanofibers into a solid structure is responsible for immobilization of proteins. For applications where PA gels are intended only as growth factor delivery vehicles, freezing damage to the nanostructures does not seem to be harmful. Although interactions with cells are sensitive to nanofiber length, our data indicate that their ability to retain proteins is controlled by their surface properties and therefore the chemical structure of PA molecules.

4.3.2 Self-Repair After Damage From Flash Freezing

Considering the sensitivity of cells to nanofiber length, we proceeded to determine if this effect was reversible. In light of recent work on the energy landscapes of peptide amphiphile self-assembly,[103] we hypothesized that we could restore the thermodynamically preferred long nanofibers by overcoming the activation barrier to reach this energy minimum. To test this hypothesis, we re-annealed the flash frozen PA (Figure 4-4a, left pathway), giving it the same amount of thermal energy used to create the original annealed PA. The viscosity of flash frozen PA was found to increase upon re-annealing (Figure 4-4b), suggesting the formation of long nanofibers again. Although the viscosity does not reach that of the original annealed PA solutions (Figure 4-4b), several techniques show the reappearance of long nanofibers. Cross-polarized light microscopy shows large birefringent monodomains (Figure 4-4c) and cryoTEM reveals long nanofibers (Figure 4-4d), similar to the original annealed PA (Figure 4-2). Most importantly, cells spread and elongate within re-annealed PA gels (Figure 4-4e), demonstrating that flash frozen and re-annealed nanofibers regain the ability to promote cell adhesion. Furthermore, flash frozen and re-annealed nanofibers still retain the ability to bind BSA protein (Figure 4-5). These data demonstrate that, given thermal energy to rearrange supramolecular interactions, freeze-damaged PA nanostructures successfully self-repair.

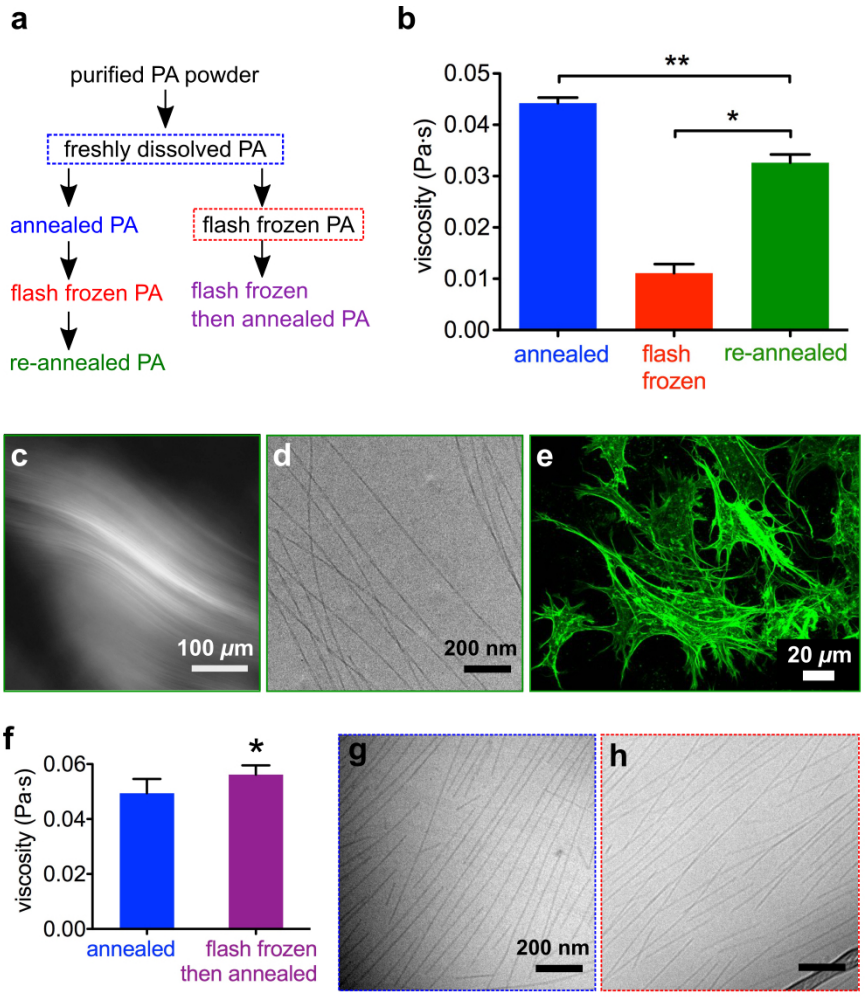

Figure 4-4: Self-repair after damage from flash freezing. (a) Two flash freezing pathways for PA solutions, with (left) and without (right) annealing prior to freezing. (b) Viscosity of annealed, flash frozen, and re-annealed PA (*p = 0.0002 **p = 0.0006, two-tailed paired t-tests; error bars represent standard error of mean). (c) Cross-polarized micrograph of re-annealed PA. (d) CryoTEM of flash frozen and re-annealed PA. (e) Confocal micrograph of MC3T3 mouse preosteoblast cells encapsulated within flash frozen and re-annealed PA gel and visualized by actin staining (green). (f) Viscosity of PA solutions after annealing freshly dissolved material, and after annealing freshly dissolved material that was flash frozen prior to annealing (p = 0.0341, two-tailed paired t-test; error bars represent standard error of mean). (g) CryoTEM of freshly dissolved PA solution. (h) CryoTEM of freshly dissolved PA solution that has been flash frozen (right pathway).

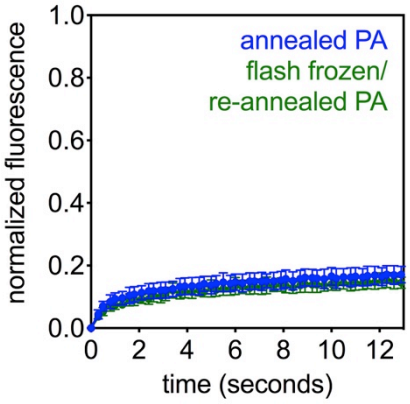

Figure 4-5: Effect of flash freezing on protein interactions with PA. Fluorescence recovery after photobleaching (FRAP) experiments on FITC-conjugated BSA, encapsulated within annealed and flash frozen/re-annealed PA gels (error bars are 95% confidence intervals).

Although re-annealing successfully repairs structural and functional damage, we wanted to understand why the solution viscosity does not return to its original value. We hypothesized that when PA solutions are flash frozen, forces exerted by ice crystals mechanically break the supramolecular nanofibers. However, since they were formed under conditions of high charge screening, the long annealed nanofibers likely contain highly cohesive β-sheets,[103] which become kinetically trapped in the short fibers. We omitted the first annealing step before flash freezing, and instead flash froze *freshly dissolved* PA and immediately annealed it (Figure 4-4a, right pathway). We found that this flash freezing pathway did not result in a reduction of the post-annealing viscosity. In fact, this pathway resulted in a small but statistically significantly increase in viscosity after annealing (Figure 4-4f). CryoTEM images of freshly dissolved PA (Figure 4-4g) and flash frozen freshly dissolved PA (Figure 4-4h) show no obvious differences between the two conditions, in contrast to the drastic change observed after flash freezing

annealed PA (Figure 4-2). Flash freezing annealed PA activates a pathway that results in a metastable state of short fibers with cohesive β-sheets, an energy landscape position that is not reached when flash freezing non-equilibrium nascent nanostructures in freshly dissolved PA. Indeed, circular dichroism (CD) experiments show that flash frozen PA solutions retain a characteristic β-sheet signature (Figure 4-6), in contrast to thermodynamically stable short nanofibers that exhibit a random coil CD signature, reported in previous work from our laboratory.[103] We note that supramolecular assemblies can scatter circularly polarized light, which can interfere with CD experiments, and is likely contributing to the positive peak intensity in the annealed PA. When the annealed PA is flash frozen and the nanofibers break into shorter ones, they scatter less light so the positive peak intensity decreases. Despite these interferences from the supramolecular assemblies, the characteristic β-sheet signature (negative peak around 220 nm, positive peak around 202 nm) is apparent.

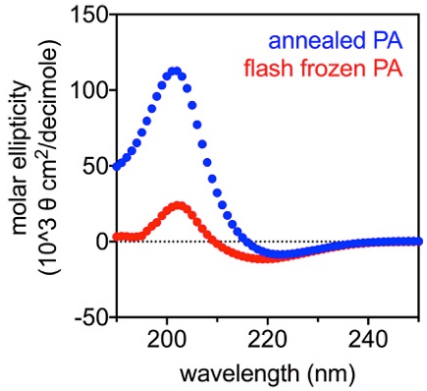

Figure 4-6: Circular dichroism of annealed and flash frozen PA.

Using super-resolution microscopy, our laboratory previously showed that molecular exchange occurs between different nanofibers in solution,[81] and we presume that this exchange is necessary for elongation of nanofibers. We hypothesize that annealed PA nanofibers have slower exchange rates than freshly dissolved metastable assemblies, possibly due to a higher coherence length of β-sheets along the nanofiber. This β-sheet configuration and slower exchange rate persists into the short freeze-damaged nanofibers, making them more resistant to change during re-annealing. In contrast the un-annealed assemblies prior to freezing are in non-equilibrium states which must have shorter β-sheet coherence lengths, and are thus more likely to exchange molecules and molecular clusters to build stable nanofibers. Furthermore, we speculate that nanofiber endcaps in metastable assemblies contain "defects" in the β-sheet structure, and are thus highly dynamic areas where PA molecules can more easily join the nanofiber or break off to join a longer nanofiber. When long annealed nanofibers are physically fractured, perhaps the newly created endcaps retain order in their hydrogen bonds and are thus less dynamic.

4.3.3 Flash Freezing Versus Slowly Freezing

To further explore how freezing affects PA assemblies, we performed experiments where we slowly froze annealed PA nanofibers, as opposed to flash freezing them in liquid nitrogen. A slower freezing process should result in larger ice crystals, as well as prolong the time that nanostructures in solution are exposed to cold temperatures and ice nucleation. Instead of flash freezing the PA solutions with liquid nitrogen, the solutions were allowed to equilibrate in a -20°C freezer. Slowly freezing PA solutions

decreases the viscosity (Figure 4-7a), similar to flash freezing PA (Figure 4-2b). However, we found that re-annealing slowly frozen PA solutions allows the solutions to recover, on average, their original viscosity (Figure 4-7a). To determine if exposure to cold temperature alone disrupted nanostructures, we equilibrated PA solutions in a 4°C refrigerator overnight. This refrigeration, after which no solid ice was observed, does not decrease the PA solution's viscosity (Figure 4-7b). Furthermore, cross-polarized microscopy shows smaller monodomains in slowly frozen PA solutions (Figure 4-7c), similar to flash frozen PA solutions (Figure 4-2e), and larger monodomains in refrigerated PA solutions (Figure 4-7d), similar to the original annealed PA (Figure 4-2d). In both slowly frozen (Figure 4-7e) and refrigerated (Figure 4-7f) samples, cryoTEM images show long nanofibers extending beyond the field of view, which must not be sufficiently large to capture fiber length differences at this scale. Interestingly, cryoTEM was able to capture the shorter length of flash frozen PA nanofibers (Figure 4-2g), which showed an approximate 75% decrease in viscosity (Figure 4-2b) relative to annealed PA, while slowly frozen PA nanofibers showed an approximate 53% decrease (Figure 4-7a). These data suggest that slowly frozen nanofibers are longer than their flash frozen counterparts, possibly because slower ice nucleation reduces the rate of nanofiber rupture, thus requiring less repair. Furthermore, slowly frozen nanofibers may have less cohesive β-sheets than flash frozen nanofibers, which allows them to rearrange more easily during subsequent annealing. While flash frozen nanofibers solidify long before their hydrogen bonds can be destabilized, PA nanofibers in the liquid portion of a partially frozen solution may adsorb to ice crystals, which may destabilize their hydrogen

bonds. For proteins, infrared spectroscopy has shown that, in partially frozen systems, adsorption to ice crystals can result in loss of secondary structure.[216]

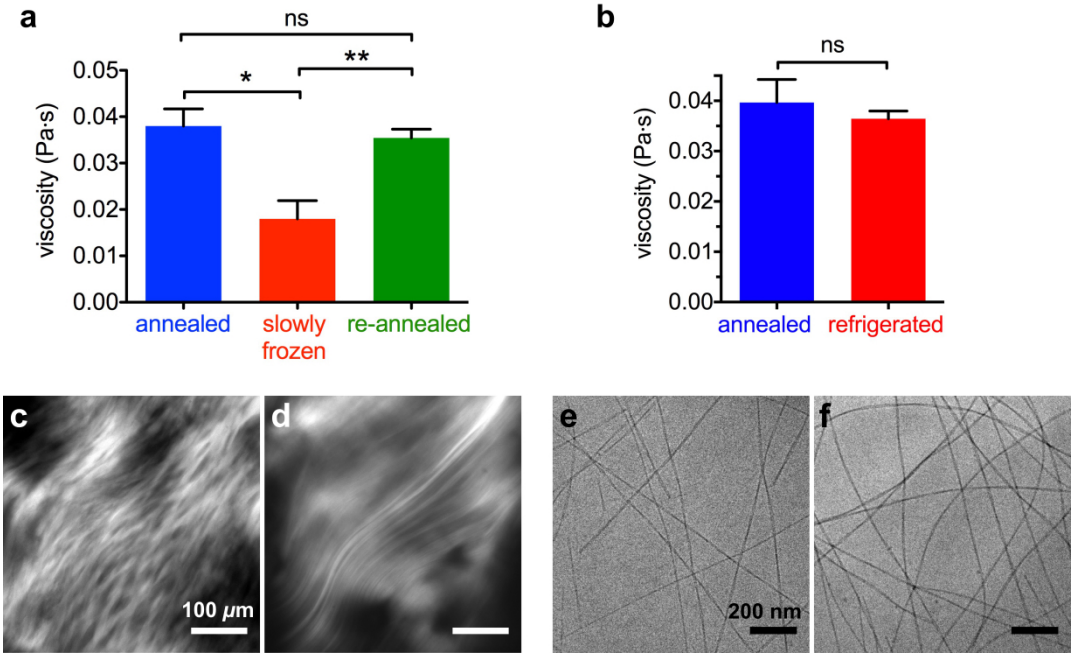

Figure 4-7: Slowly freezing and refrigerating PA. (a) Viscosity of annealed, slowly frozen, and re-annealed PA (*p = 0.0062 **p = 0.0053, two-tailed paired t-tests (error bars represent standard error of mean). (b) Viscosity of annealed PA and refrigerated PA (two-tailed paired t-test). (c, d) Cross-polarized micrographs of slowly frozen PA and refrigerated PA, respectively. (e, f) CryoTEM of slowly frozen PA and refrigerated PA, respectively.

4.3.4 Damage and Self-Repair after Freeze Drying

After characterizing the self-repair of PA nanofibers from freezing, both rapidly with liquid nitrogen and slowly within a freezer, we were motivated to explore the consequences on bioactivity after freeze drying. From a functional point of view, the nanostructures should be stored dried rather than frozen in the hydrated state before coming into contact with living tissues. Since flash freezing breaks long nanofibers into

shorter ones (Figure 4-2), we expected that freeze drying would have a similar effect. Also, since the volume of PA nanofibers contains water molecules that contribute to their self-assembly,[208] we expected that the added dehydration step would disrupt the nanofibers even further than freezing alone. Since the presence of water triggers self-assembly and directs hydrogen bonding of PA molecules as a result of hydrophobic collapse, we hypothesized that nanofibers would easily "re-assemble" after freeze drying as the nanostructured material is reconstituted as aqueous solutions. We freeze dried (flash freeze with liquid nitrogen followed by sublimation of water under vacuum) and reconstituted annealed PA solutions (Figure 4-8a, left pathway) and found that the viscosity decreases, similar to what we found in the case of the flash freezing pathway (Figure 4-8b). Re-annealing this reconstituted PA (Figure 4-8a, left pathway) increases the viscosity, but not to the original value (Figure 4-8b). Despite the lower viscosity, PA nanofibers "re-created" after freeze drying form large aligned monodomains (Figure 4-8c), appear long by cryoTEM (Figure 4-8d), and the gels they form are capable of supporting cell spreading and adhesion (Figure 4-8e) as well as retaining BSA protein (Figure 4-9). Thus these nanostructures remain bioactive, similar to those exposed to flash freezing and re-annealed.

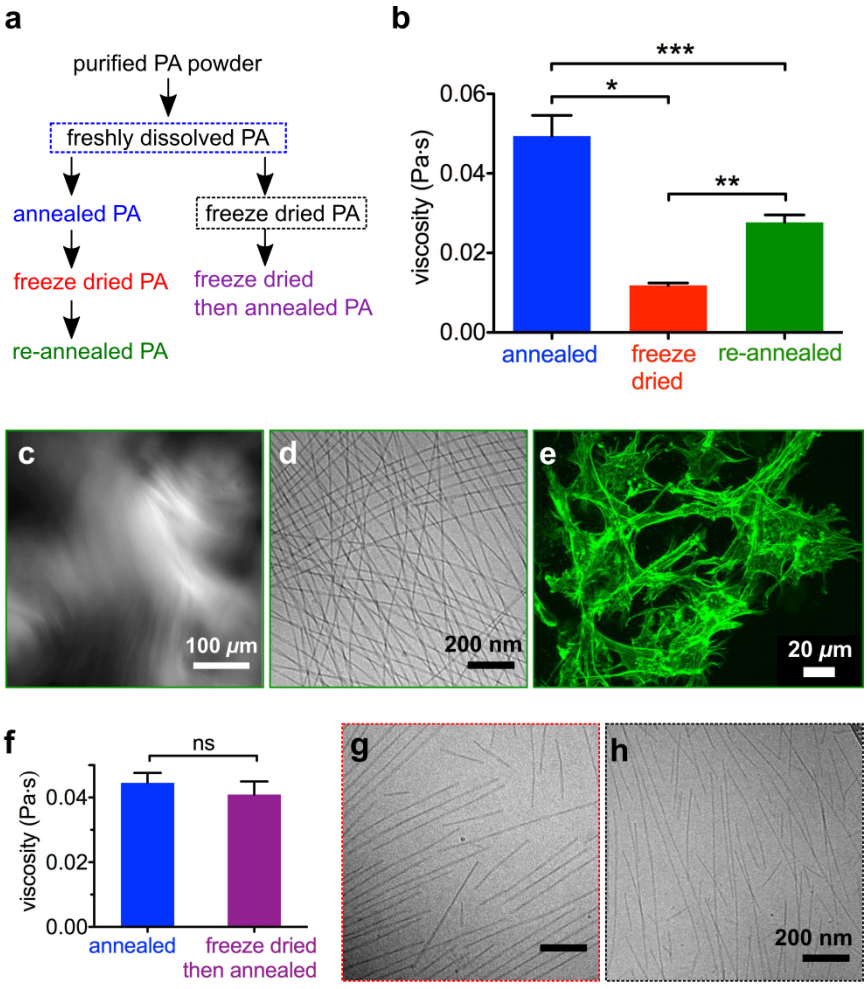

Figure 4-8: Self-repair after damage from freeze drying. (a) Two freeze drying pathways for PA, with (left) and without (right) annealing prior to freeze drying. (b) Viscosity of annealed, freeze dried, and re-annealed PA (*p = 0.0007 **p = 0.0007 ***p = 0.0102, two-tailed paired t-tests, error bars represent standard error of mean). (c) Cross-polarized light micrograph of freeze dried and re-annealed PA. (d) CryoTEM of freeze dried and re-annealed PA. (e) Confocal micrograph of MC3T3 mouse preosteoblast cells encapsulated inside freeze dried and re-annealed PA gel, visualized by actin staining. (f) Viscosity of PA after annealing freshly dissolved solution, and annealing freshly dissolved solution that has been freeze dried (not significant, two-tailed paired t-test, error bars represent standard error of mean). (g) CryoTEM of PA immediately after reconstitution of powder, freeze dried from an annealed PA solution (left pathway). (h) CryoTEM of PA immediately after reconstitution of powder, freeze dried from a freshly dissolved solution (right pathway).

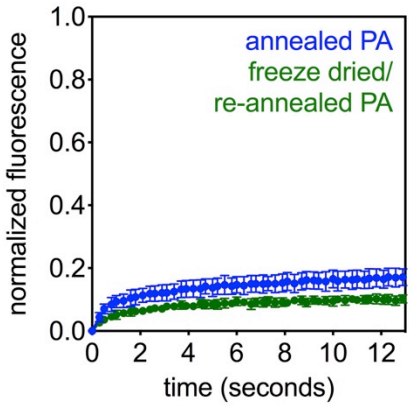

Figure 4-9: Effect of freeze drying on protein interactions with PA. Fluorescence recovery after photobleaching (FRAP) experiments on FITC-conjugated BSA, encapsulated within annealed and freeze dried/re-annealed PA solutions and gels (error bars are 95% confidence intervals).

We also note that small angle x-ray scattering (SAXS) of PA nanofibers show very minor changes during both flash freezing and freeze drying and subsequent re-annealing (Figure 4-10) demonstrating that the fibrous geometry is maintained, even as hydrogen bonds are rearranging and nanofiber length is changing.

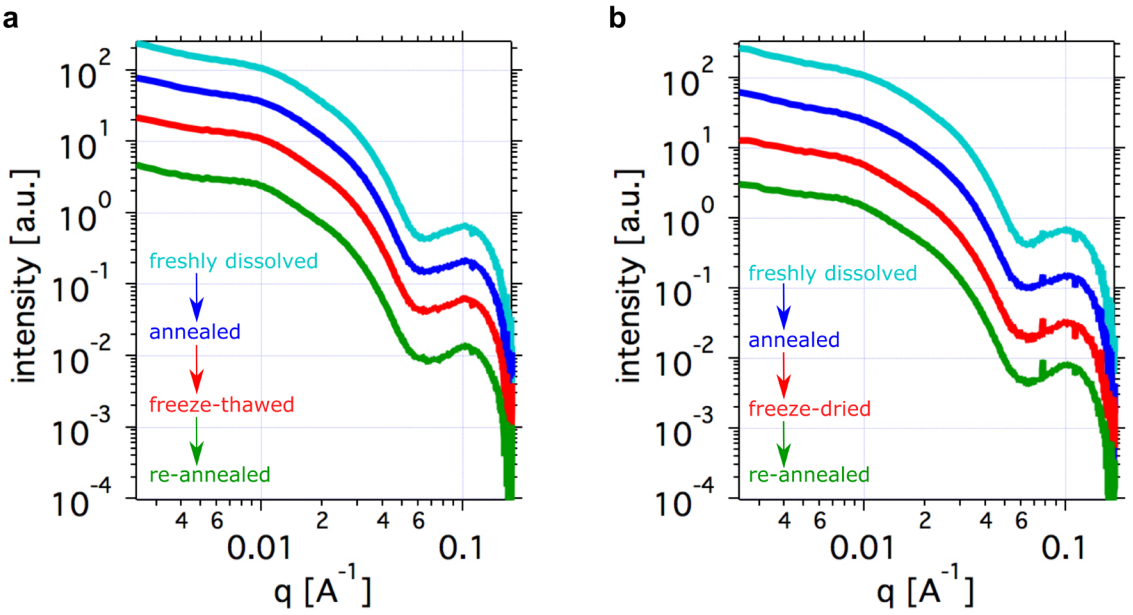

Figure 4-10: Small angle x-ray scattering of PA during freezing and freeze drying. (a) Small angle x-ray scattering (SAXS) profiles of freshly dissolved PA, and PA that is then annealed, flash frozen, and re-annealed. (b) SAXS profiles of freshly dissolved PA, and PA that is then annealed, freeze-dried, and re-annealed.

We then investigated whether omitting the annealing step before freeze drying would prevent the decrease in viscosity (Figure 4-8a, right pathway), similar to our experiment with flash freezing freshly dissolved PA before annealing (Figure 4-4a, right pathway). Bypassing annealing before freeze drying will generally prevent a decrease in viscosity (Figure 4-8f), similar to bypassing annealing before flash freezing (Figure 4-4f). However, this trend is not as consistent when freeze drying PA, with some experiments showing a decrease in viscosity and others showing an increase, and thus on average a change in viscosity is not observed (Figure 4-11).

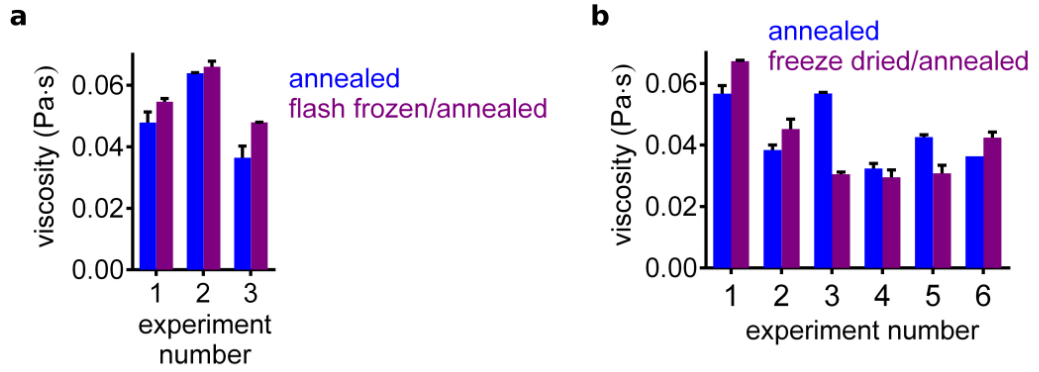

Figure 4-11: Variation in PA after freeze drying. (a) Variation between three experiments for annealing PA, with and without flash freezing before annealing. All three experiments show a small increase in viscosity if PA is flash frozen before annealing, and the average is reported in Figure 4-4f. (b) Variation between six experiments for annealing PA, with and without freeze drying before annealing. The first two experiments show an increase in viscosity if PA is freeze- dried before annealing, but the third experiment showed a decrease in viscosity. The experiment was repeated three more times, with varying results. On average, the viscosity does not change with freeze drying before annealing, which is reported in Figure 4-8f.

CryoTEM images of PA immediately after reconstitution, following freeze drying from annealed PA solution (Figure 4-8g) and freshly dissolved solution (Figure 4-8h), show no obvious differences, and both also appear similar to the original freshly dissolved PA (Figure 4-4g). While the cryoTEM micrographs appear very similar, we speculate that freezing annealed PA preserves the cohesive β-sheets of long nanofibers, which persist into the melted (flash frozen) or dried (freeze dried) states. Although nanostructures are disrupted during freeze drying, the preserved β-sheets diminish the system's ability to rearrange during subsequent annealing. These preserved β-sheets can be avoided if PA is not annealed before freeze drying, however, in contrast to the case of just freezing this processing pathway will not always prevent a decrease in viscosity

(Figure 4-11). We therefore suspected that the dehydration process was causing other changes to PA self-assembly in addition to those introduced by freezing alone, which do not appear to occur in a reproducible manner.

4.3.5 Effect of Freeze Drying Conditions on Self-Repair

To investigate how freeze drying affects self-assembly of the PAs investigated, we varied freeze drying conditions. We hypothesized that freeze drying could increase the electrostatic charge on headgroups of PA molecules by converting the glutamic acids into their conjugate salt form. The added negative charges would add repulsive forces among PA molecules, thus decreasing their propensity to self-assemble and changing their energy landscape.[103] Previous work on freeze drying of proteins has shown that their ionization states in solution persist into the dried state, leading to a phenomenon called "pH memory."[217, 218] Because the solution pH determines the ionization states, freeze dried proteins "remember" the pH of the aqueous solution from which they were dried.[217, 218] This "remembered" ionization state persists if the proteins are reconstituted into organic solvents, but is "erased" if proteins are reconstituted into aqueous media with a new pH value.[217] In the case of freeze drying PAs, the three headgroups are "remembered" as either protonated glutamic acids or deprotonated glutamate salts. Although these ionization states can change upon reconstitution with aqueous media, the relative amount of glutamic acids versus glutamate salts in the PA powder will be determined by the previous freeze drying step. If this powder is reconstituted with pure water, which has no buffering capacity, the amount of conjugate acid versus conjugate

base that was present can continue to exert an effect. During self-assembly, the three glutamic acid side chains interact with each other and with neighboring molecules, which can affect their ionization state. Under our specific stoichiometric conditions (15 mM NaOH to 8.66 mM PA, which contain 26 mM glutamic acids), we expect a wide range of possible ionization state configurations within the assembled nanostructures. When the PA is freshly dissolved and metastable, these configurations are likely to be highly dynamic, and perhaps highly variable from sample to sample. Upon drying in the presence of a non-volatile base like NaOH, we speculate that this variable configuration of ionization states gets kinetically trapped, with some Na^+ ions bound to the glutamate residues, maintaining them as glutamate salts, and others existing as phase separated NaOH powder. Thus, the large variation in possible ionization state configurations and NaOH powder amounts after freeze drying can lead to variations in energy landscapes upon reconstitution of PA.

To better control the ionization states of the PA's glutamic acids after freeze drying, we freeze dried PA from solutions containing a volatile base (NH_4OH instead of NaOH). Previous work has shown that the pH memory effect in proteins is suppressed when they are dried from solutions containing volatile buffers.[218] The drying process removes the volatile buffers, leaving behind uncharged residues, effectively removing any "memory" of the ionization state in buffered solution.[218] Unlike NaOH, NH_4OH cannot remain in the freeze dried powder as a solid, and NH_4^+ ions are not likely to remain bound to glutamate residues, as the removal of NH_3 gas under vacuum would deplete the NH_4^+ ions by Le Chatelier's principle ($NH_4^+COO^- \rightarrow NH_3 + COOH$). Thus, our strategy was to add excess volatile NH_4OH (1% volume/volume) to deprotonate PA

as much as possible *before* freeze drying, and to add a specific amount of NaCl (non-volatile salt) to control the number of glutamic acid residues that remain ionized *after* freeze drying. While PA powder freeze dried from NaOH dissolves easily when reconstituted in pure water, PA powder freeze dried from NH_4OH is not soluble (Figure 4-12a), suggesting that the glutamic acids are left non-ionized and the base has also been removed. However, when we add 15 mM NaCl to the solution before freeze drying, the resulting powder was found to be water-soluble (Figure 4-12a). In contrast, the PA powder is also not soluble if the NaCl is added later (by freeze drying without salt and reconstituting in 15 mM NaCl). This suggests that the positive Na^+ ions form sodium glutamate salts with the PA, increasing its solubility above that of PA with glutamic acids. We measured UV-visible absorbance of the supernatant in these samples to estimate the concentration of soluble peptide (Figure 4-12b), which confirmed our visual observations on the solubility.

a

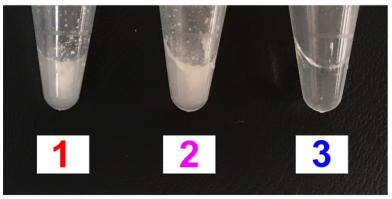

	1	2	3
freeze-dried in:	1% NH_4OH	1% NH_4OH	1% NH_4OH + 15mM NaCl
reconstituted with:	pure water	15mM NaCl	pure water
	cloudy	cloudy	clear

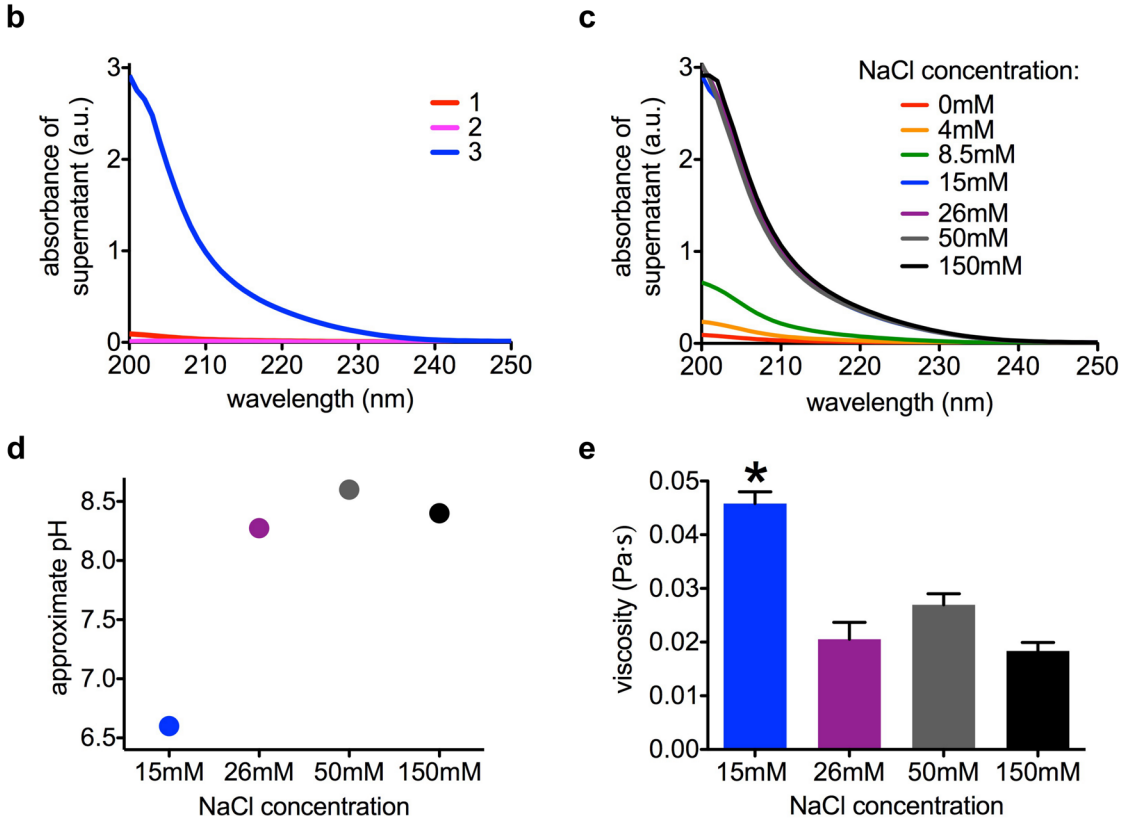

Figure 4-12: Freeze drying PA in a volatile solvent. (a) Photographs of PA solutions after freeze drying and reconstitution, using solvents indicated in chart. (b) UV-visible absorbance spectra of freeze dried PA solutions from panel *a*. (c) UV-visible absorbance spectra of freeze dried PA solutions immediately after reconstitution, with indicated concentrations of NaCl present during freeze drying. (d) Approximate pH values of freeze dried PA solutions after reconstitution and subsequent annealing, with indicated concentrations of NaCl present during freeze drying. (e) Viscosity of freeze dried PA solutions after annealing, with indicated concentrations of NaCl present during freeze drying (15mM NaCl sample is significantly different from all other samples, $p < 0.05$, two-tailed paired t-test; error bars represent standard error of mean).

We then varied the concentration of NaCl in solution before freeze drying to see if we could control the extent of ionization in the final dried PA. We dissolved 8.66 mM (1 wt%) PA with a fixed amount of NH_4OH (1% volume/volume), and varied the concentration of NaCl in the solution (4, 8.5, 15, 26, 50, 150 mM). These samples, containing a total of 26 mM ionizable carboxylic acids (8.66 mM PA, three glutamic acids per $V_3A_3E_3$ PA), were freeze dried and reconstituted with pure water. UV-visible spectroscopy shows that as low as 4 mM NaCl increases the PA solubility, and that PA solubility improves up to a maximum at 15 mM NaCl (Figure 4-12c). To further explore the idea that the NaCl controls the ionization state of the PA's glutamic acids, we then annealed the fully soluble PA solutions (those containing 15 – 150 mM NaCl) and measured the approximate pH. Since PA immediately after reconstitution is metastable and highly dynamic, we compared the annealed solutions, which should contain more stable nanostructures. The PA solution freeze dried from 15 mM NaCl is more acidic than PA freeze dried from higher NaCl concentrations (Figure 4-12d), suggesting that it contains fewer carboxylic acids in the deprotonated, ionized state than samples with more added NaCl. All samples had been exposed to the same amount of NH_4OH base and NaCl alone does not affect the pH of water (Figure 4-13).

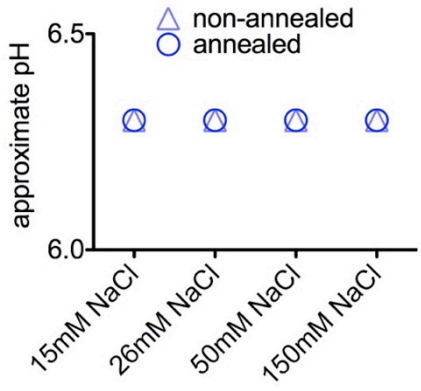

Figure 4-13: The pH of 1% NH_4OH + NaCl solutions, that were freeze-dried, reconstituted, and then annealed. These solutions contained no PA.

At 15 mM NaCl, there are enough Na^+ ions to maintain approximately two out of three carboxylate anions per PA molecule, while at least 26 mM of Na^+ ions is sufficient to stabilize all three carboxylate groups. Taken together, the solubility and pH data suggest that the presence of NaCl during freeze drying determines how many glutamate salt residues on the PA's headgroups will be maintained into the dried state, and thus the amount of negative charges on the PA nanostructures after reconstitution in pure water. In this specific case, PA freeze dried with 15 mM NaCl contains less negative charge than PA freeze dried with higher amounts of NaCl since this sample has less Na^+ ions to maintain negatively charged carboxylate groups during freeze drying.

Since increased charges on the PA are known to promote repulsive forces and change the energy landscape,[103] we expected that the change in the PA's charged state, induced by certain freeze drying conditions, would affect PA self-assembly. Indeed, PA freeze dried from 15 mM NaCl is significantly more viscous than PA samples with higher NaCl concentrations (Figure 4-12e), which is likely due to the lower negative charge on

the 15 mM NaCl sample, suggested by the solution's more acidic pH (Figure 4-12d). Previous work has shown that increased pH can increase the electrostatic charge on acidic PA molecules, which disrupts their self-assembly,[219] and our experiments show that simply adding more NaOH base to a PA solution will result in lower viscosity after annealing (Figure 4-14).

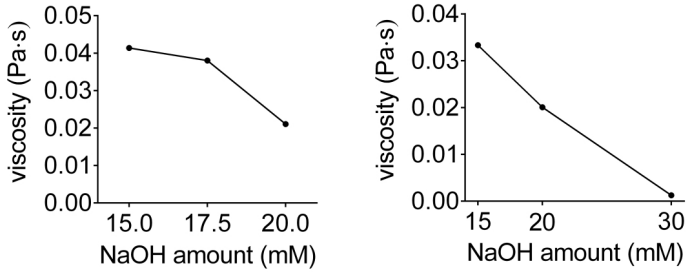

Figure 4-14: PA viscosity experiments with varying pH.

When approximately all three glutamic acids are deprotonated instead of two, the added charge frustrates self-assembly by introducing repulsion between PA molecules, shifting the thermodynamic minimum to relatively shorter, less cohesive nanofibers. The self-repair capacity of PA nanostructures relies on the "functional" long nanofibers existing at an energy minimum that can be accessed with equilibration through the use of thermal energy. The NH_4OH and NaCl experiments suggest that certain processing steps, particularly freeze drying, can shift this energy landscape minimum and thus complicate self-repair. When freeze drying freshly dissolved PA in NaOH, these energy landscape shifts varied from sample to sample, due to the wide range of possible ionization states within highly dynamic nanostructures and the ability of Na^+ ions to exist in either phase-

separated NaOH powder or sodium glutamate conjugates on the PA. Using NH_4OH and NaCl, we were able to better control the PA's ionization states and shed light on the possible mechanism through which freeze drying causes shifts in energy landscape. Taken together, the solubility, pH, and viscosity experiments (Figure 4-12) suggest that counterions present during freeze drying can increase the net charge on the PA by maintaining conjugate salt groups, which can change the energy minimum in the PA's energy landscape. In this specific case, Na^+ ions present during freeze drying of $V_3A_3E_3$ PA maintain the glutamic acid residues as negatively charged glutamate salts, which introduces charge repulsion and disrupts self-assembly, thus shifting the energy minimum to shorter nanofibers that produce a less viscous solution. When the source of these Na^+ ions is NaOH, these energy landscape shifts happen in a highly variable way because the amount of glutamate salts after freeze drying is not easily controlled. This variation is reduced when NaCl is the source of Na^+ ions, and this way the amount of glutamate salts after freeze drying can be controlled.

4.3.6 Ionic Reactions During Freeze Drying

At 1 wt% (8.66 mM) PA, and three carboxylic acids per PA molecules, there are a total of 26 mM carboxylic acids. As described above, we found that freeze drying 1 wt% PA dissolved in 1% NH_4OH results in a powder that is not soluble in pure water. Adding 4 mM and 8.5 mM NaCl to the 1% NH_4OH solution improves the freeze dried powder's solubility, but at least 15 mM NaCl is required to confer full solubility (Figure 4-12). We presume that 15 mM of Na^+ ions have bound to the carboxylate anions of the PA,

maintaining them in their sodium carboxylate salt form, which is more soluble than the acid form. Higher concentrations of NaCl (26, 50, 150 mM) also confer full solubility. This data suggests that slightly less than 2/3 (15/26 mM) carboxylic acids must be deprotonated to carboxylate salts to fully dissolve PA at 8.66 mM. This is consistent with the observation that around 15 mM NaOH is required to dissolve the PA to 8.66 mM, which is how all experiments described above (in this Chapter) were performed.

When the samples are freeze dried from aqueous NaOH, positive Na^+ ions that can stabilize carboxylate anions and hydroxide ions required to initially dissolve the PA originate from the same source. In the final freeze dried powder, some Na^+ ions may be associated with PA while others exist in NaOH powder, and the exact distribution is likely not reproducible due to the dynamic nature of freshly dissolved, metastable PA *before* freeze-drying. Freeze drying in a volatile base (NH_4OH) and non-volatile salt (NaCl) separates the source of hydroxide ions to initially dissolve PA and the source of non-volatile counterions that "fix" the PA's ionization state into the dried state. We speculate that the effect of freeze drying on the PA's ionization state can depend on complex equilibria between ionic reactions during freeze drying. During freeze drying, the equilibrium between NH_4^+ and NH_3 will be significantly shifted towards NH_3 as it is continuously removed under high vacuum, depleting the system of NH_4^+ ions that can stabilize carboxylate anions. When PA is freeze-dried in 15 mM NH_4Cl instead of 15 mM NaCl, along with the same concentration of 1% NH_4OH, the solubility after reconstitution is decreased but still above that of NH_4OH alone (Figure 4-15).

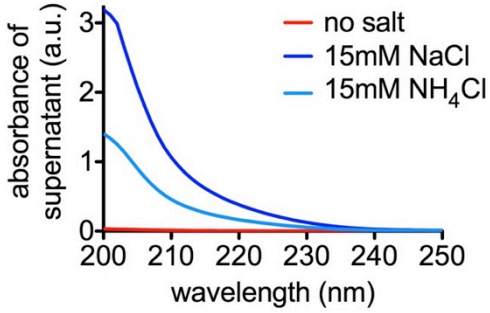

Figure 4-15: UV-visible absorbance of PA freeze-dried from 1% NH_4OH, without and with two different types of salts (NaCl and NH_4Cl).

This is consistent with a previous finding that "partial" pH memory was observed when freeze drying in buffers with one volatile component and one non-volatile component (i.e. $(NH_4)_2HPO_4$).[218] We speculate that this effect is due to complex ion equilibriums, and ions cannot be classified as simply "volatile" or "non-volatile." For example, we presume that NH_3 gas is volatile but NH_4^+ ions are not. When freeze drying PA in NH_4Cl and NH_4OH vs. NH_4OH *alone*, the equilibrium between NH_4^+ ions and NH_3 will still deplete the system of NH_4^+ ions that can stabilize carboxylate anions. However, the presence of Cl^- ions may help drive the equilibrium back towards NH_4^+ ions. Because HCl is a strong acid, H^+ ions will be inclined to fully dissociate from Cl^- ions, thus pushing the equilibrium towards NH_4^+ ions. In the absence of Cl^- ions, H^+ ions react with OH^- to form water that sublimes away. These reactions are illustrated below:

$$NH_4^+ + OH^- \leftrightarrow NH_3 + H_2O \quad (1)$$

$$NH_4^+ + Cl^- \leftrightarrow NH_3 + HCl \quad (2)$$

In equation 1, as NH_3 gas is removed and H_2O is sublimed under vacuum, by Le Chatelier's principle, the equilibrium will shift to the right and deplete the system of NH_4^+ ions. In equation 2, although NH_3 gas will also be removed, the propensity of HCl to remain dissociated will provide a driving force to push the equilibrium towards the left. We speculate that if the PA headgroups were sufficiently acidic, they would be capable of driving the equilibrium towards NH_4^+ ions and maintaining them into the dried state. Although supramolecular rearrangements likely do not occur in the frozen, solid state, we presume that ionic reactions may still occur. However, solution-state supramolecular configurations *before* freeze drying may affect the effective ionization potential (i.e. pK_a) of PA, which may affect ionic reactions *during* freeze drying. We also note the freeze drying process *itself* can have an affect on the ionic reactions. In all work presented here, the samples were freeze dried on a port-type freeze dryer, which does not provide temperature control of the sample. We hypothesize that the temperature during drying can have an effect on the rate of the ionic reactions described above. This work has focused mainly on the affect of the solvent the PA molecules are freeze dried in, but we speculate that different drying cycles could yield different results.

4.3.7 Kinetics of Self-Repair

Peptide amphiphile nanofiber elongation – either during initial annealing or re-annealing a damaged state – is limited by the kinetics of self-assembly. Even when long nanofibers are the clear thermodynamic minimum, the PA's intermolecular hydrogen bonds do not instantly arrange into this configuration, and instead must overcome an energy barrier to do so. We speculate that the exact kinetics to reach the thermodynamic

minimum is dependent on both the PA sequence and the solvent conditions. For the $V_3A_3E_3$ PA used in this work, we studied the affects of various heating times at 80°C (experiment schematic in Figure 4-16a), on freshly dissolved PA solutions containing 1 wt% PA dissolved in 15 mM NaOH. For these experiments, the PA solutions were not slow cooled overnight after heating, and were instead cooled immediately by submersion in water at room temperature. We speculate that the slow cooling step allows nanofibers to better equilibrate, but we skipped this step to better observe the effects of heating alone. This data shows that the viscosity increases gradually during 30 minutes of heating, the total amount of time used in the standard annealing procedure (80°C 30 minutes, slow cool overnight).[71, 103] Rapidly cooling the sample does not compromise the heat-induced increase in viscosity, suggesting that the majority of nanofiber elongation occurs during heating, which provides energy for hydrogen bonds to rearrange towards their thermodynamic minimum. However, we speculate that the slow cooling step allows for better equilibration of the hydrogen bonds.

To corroborate the viscosity data, we also performed dynamic light scattering (DLS) experiments. Because DLS assumes a spherical model, the measured sizes do not accurately reflect the length of nanofibers; however, trends between samples can still be observed. The DLS data shows the same trend as the viscosity data, with the measured size increasing gradually during the 30 minutes of heating. The correlation function shifts to longer lag times, indicating larger objects (Figure 4-16c). Cross-polarized light micrographs of PA show that the samples become birefringent upon with only 5 minutes of heating, indicating the formation of liquid crystalline structures after this short heating time.

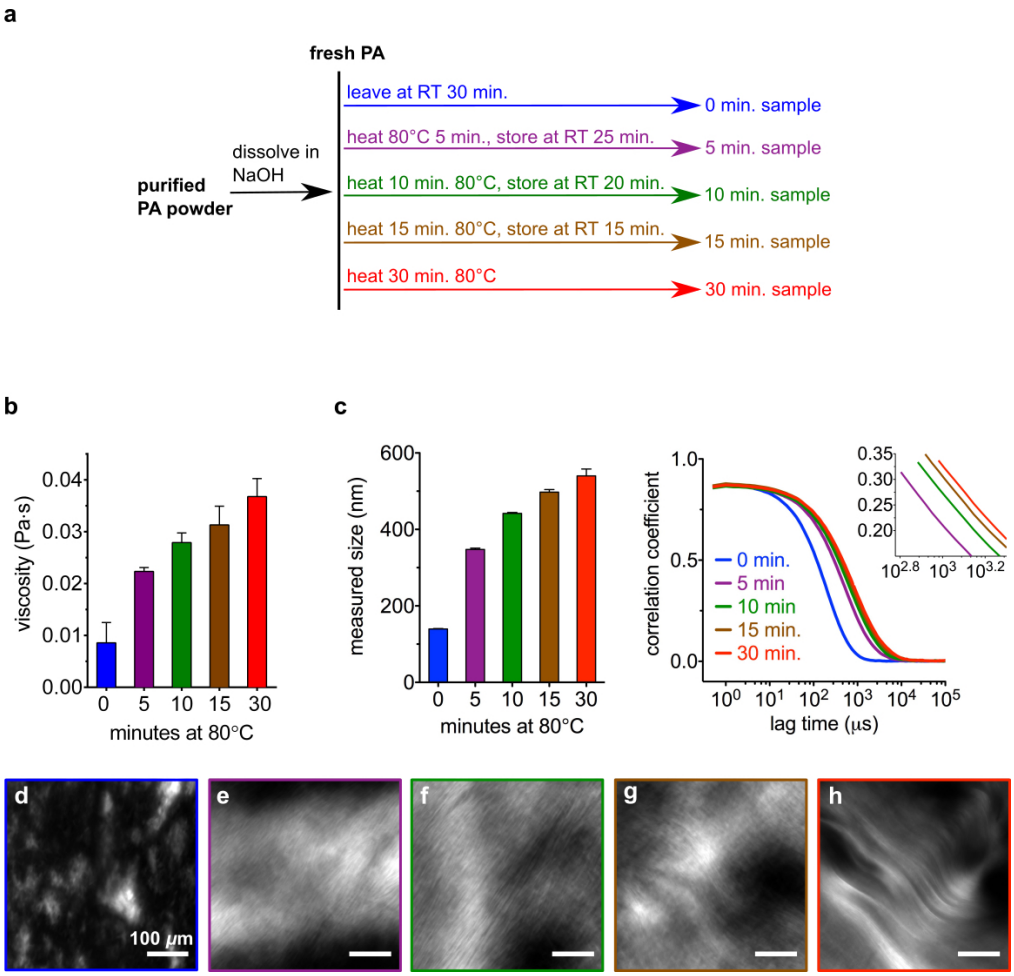

Figure 4-16: Heating PA for various times. (a) Schematic showing experimental set-up for heating freshly dissolved PA for various times. RT: Room temperature. (b) Viscosity of PA heated for various times as described in panel *a*. (c) Dynamic light scattering (DLS) data for PA heated for various times as described in panel *a*. The left graph shows the measured size, while the right graph shows the correlation function used to calculate this size. The inset shows a zoomed in portion of the graph. (d-h) Birefringence micrographs of PAs heated for various times as described in panel *a*.

The above data show that for freshly dissolved PA solutions, self-assembly into thermodynamically preferred long nanofibers does not occur instantly, and that the amount of thermal energy given to the system controls the kinetics of nanofiber

elongation. After freezing or freeze drying, which do not change the chemical identity of the PAs, we speculate that the kinetics to elongate towards a thermodynamic are similar to freshly dissolved PA. As described above, freeze drying can shift the thermodynamic minimum to shorter nanofibers by increasing the charge density on the PA's headgroups. In this case, the "original" long nanofibers cannot be recovered, because they are no longer the thermodynamic minimum. However, nanofiber elongation towards the new thermodynamic minimum is still dependent on thermal energy input, similar to PA that has not been freeze dried. We performed dynamic light scattering (DLS) experiments on 1 wt% PA that had been freeze dried in 1% NH_4OH and 15 mM NaCl, and then reconstituted in pure water. After reconstitution, the PA was first diluted to 1 mM with pure water (from 8.66 mM, 1 wt%), and then heated for 10 minutes at 65°C, 80°C, or 95°C. This solution was cooled by submersion in room temperature water, after which DLS measurements were taken. The DLS data show that higher temperatures lead to a larger measured size on the DLS, suggesting more elongation of nanofibers (Figure 4-17a). After freeze drying, the PAs do not instantly reach their thermodynamic minimum upon reconstitution, similar to freshly dissolved PA in NaOH (Figure 4-16). Instead, the elongation kinetics depend on the amount of thermal energy the system receives, in this case, controlled by varying temperature.

Annealed and flash frozen PA does not reach its original viscosity after re-annealing (Figure 4-4), which we hypothesized was due to kinetic traps hindering elongation. Unlike freeze drying, during which complex ionic reactions can occur (Figure 4-12), flash freezing should not alter the overall charged state of the PA's headgroups and thus the thermodynamic minimum should not have shifted. Thus, we

speculate that – in theory – the original viscosity can be recovered by re-annealing at a higher temperature or for a longer time period, which should remove the kinetic barrier to reach the thermodynamic minimum. Experimentally, these procedures carry the risk of solvent evaporation during heating. We have observed the formation of condensation on the sides and cap of the Eppendorf tubes, which changes the concentration of PA in the bulk solution. We performed an experiment where we annealed and flash froze PA, and then re-annealed for 30 minutes as well as 60 minutes. We measured the viscosity of the original annealed PA (orig.), PA that was flash frozen and re-annealed for 30 minutes (re30), and PA that was flash frozen and re-annealed for 60 minutes (re60). We obtained inconsistent results for samples that were re-annealed for 60 minutes (Figure 4-17b). Whereas the data on heating freshly dissolved PA up to 30 minutes shows a steady increase in viscosity with increased heating time (Figure 4-16), re-annealing flash frozen PA for 60 vs. 30 minutes shows no consistent trend. In one experiment it reaches the original viscosity, in another one it seems to be slightly lower than the sample re-annealed for only 30 minutes (Figure 4-17). We hypothesize that longer heating times can introduce more error due to solvent evaporation and increased condensation within the tube. Indeed, this may happen to a certain extent during the heating procedures used in this work (30 minute at 80°C). However, we note that while the data on re-annealing for 60 minutes is not consistent, re-annealing for 30 minutes consistently did not reach the original annealed viscosity. This is consistent with the data in Figure 4-4, and these are completely separate experiments from the ones shown in that Figure.

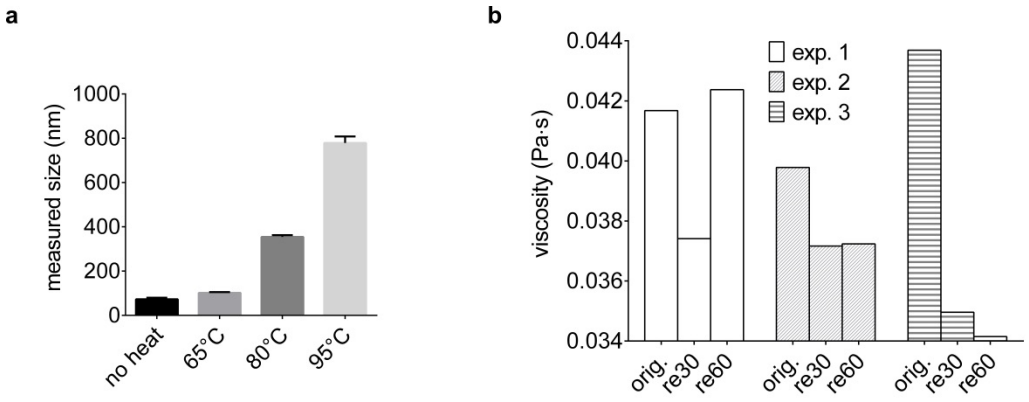

Figure 4-17: PA nanofiber elongation with temperature and time. (a) Dynamic light scattering experiment on freeze-dried PA (freeze-dried in 1% NH_4OH + 15 mM NaCl), heated for 10 minutes at various temperatures. (b) Viscosity of annealed, and flash frozen and re-annealed PA. "Orig." refers to the original annealed PA, "re30" refers to PA that was flash frozen and re-annealed for 30 minutes, and "re60" refers to PA that was flash frozen and re-annealed for 60 minutes.

4.4 CONCLUSIONS

We have described a thermally activated self-repair pathway for PA nanostructures, which can restore long nanofibers after they break into shorter ones. Long nanofibers are superior to shorter ones in supporting cell adhesion, and the repair pathway was able to recover this biological function. This self-repair pathway works by overcoming the activation barrier to return the system to the thermodynamically preferred long nanofibers. Some thermal histories will result in kinetic traps that impede this thermal repair process, specifically annealing prior to freezing or freeze drying will result in short nanofibers containing highly cohesive internal structures that suppress the ability of nanostructures to re-elongate. Since this self-repair pathway succeeds when thermal energy reconfigures the system towards an energy minimum containing the long nanofibers necessary for bioactivity, any pathway that shifts this minimum will

complicate the repair process. This was demonstrated by our freeze drying experiments, where the dehydration process can increase the electrostatic charges on PA nanostructures. In contrast, freezing alone should not change the PA's net charge and shift the energy minimum, so "incomplete" self-repair may be attributed purely to kinetic traps. In principle, longer heating times or higher temperatures should overcome the energy barrier to achieve "complete" self-heating, but can lead to solvent evaporation or precipitation, thus altering solution concentrations (Figure 4-17). Such kinetic traps should therefore be avoided through the design of processing pathways. The self-repair capacity of supramolecular nanostructures is highly possible, but must be optimized by careful selection of processing pathways, which no doubt are necessary in the actual use of the systems for biological applications. We hypothesize that the self-repair capacity of supramolecular nanostructures when their environment disrupts them should be broadly applicable to many chemical structures.

4.5 MATERIALS AND METHODS

Peptide Synthesis

Peptide amphiphiles molecules (C_{16}-$V_3A_3E_3$ PA) were synthesized using fluorenylmethyloxycarbonyl (Fmoc) solid phase peptide synthesis, by coupling Fmoc-protected amino acids (P3 BioSystems, Louiseville, KY, USA) from Rink amide MBHA resin (Novabiochem [EMD Millipore], Billerica, MA, USA). All amino acid couplings were performed in a CEM Liberty microwave-assisted peptide synthesizer (CEM, Matthews, NC, USA), using default microwave settings. Fmoc groups were deprotected

using 20% 4-methylpiperidine and 0.1 M hydroxybenzotriazole (HOBt) in dimethylformamide (DMF) at 75 °C for 3–4 min. Amino acids were coupled using 5 molar equivalents (equiv) of protected amino acid, 5 equiv *O*-benzotriazole-*N*, *N*, *N*′, *N*′-tetramethyluronium hexafluorophosphate (HBTU) and 10 equiv *N*,*N*-diisopropylethylamine (DIEA), at 75 °C for 5–10 min. Using this same procedure, palmitic acid (C_{16}) was conjugated to the N-terminus of the peptide ($V_3A_3E_3$). After each coupling, unreacted amines were capped using 0.5 M acetic anhydride, 0.125 M DIEA and 0.015 M HOBt in DMF, at 65 °C for 2 minutes.

Completed PA molecules were cleaved off the resin using a solution of 95:2.5:2.5 trifluoroacetic acid/triisopropylsilane/water for 2–3 h. Volatile solvents were removed with rotary evaporation, and the PA was precipitated with cold diethyl ether and dried using a fritted filter. The PA was then purified by preparatory scale reverse phase high-performance liquid chromatography (HPLC, Varian), using a Phenomenex Gemini column (C18 stationary phase, 5 μm, 100 Å pore size, either 30 × 150 mm or 50 x 250 mm). A mobile phase of acetonitrile and water was used, both containing 0.1% NH_4OH to aid solubility of acidic PA. Pure fractions were identified and collected, using electrospray ionization (ESI) mass spectroscopy. Excess acetonitrile was removed with rotary evaporation, freeze-dried, and the powders stored at -20°C until use. The purity of PA molecules was confirmed using liquid chromatograph-mass spectroscopy (LC-MS), which was performed using an Agilent 6520 QTOF-LCMS with a similar Phenomenex column.

Sample Preparation (PA Solutions in NaOH)

Purified PA powder was dissolved to 1 wt% (8.66 mM) in 15 mM NaOH. For pH variation experiments, different NaOH amounts were used as indicated. Immediately after dissolving the PA powder, the solution is the freshly dissolved PA solution. To create the annealed PA, this PA solution was submerged in an 80°C water bath for 30 minutes and slowly allowed to cool to room temperature overnight. For the 60-minute annealing procedure, the sample was heated for 60 minutes at 80°C before slowly cooling overnight. For all re-annealing procedures, this heating and cooling cycle was also used. Because evaporation and condensation of liquid around the tube can occur during heating at 80°C, all annealing procedures were performed with at least 50 μL of PA solution in a 1.7 mL Eppendorf tube. For experimental techniques requiring a dilution of the PA solution, the sample was always annealed at 1 wt% and diluted right before analysis. For experiments on the kinetics of PA self-assembly, PA solutions were heated at 80°C for the indicated times (5 – 30 minutes) and then cooled immediately by submersion in room temperature water.

Sample Preparation (PA Solutions NH_4OH)

The purified PA powder was first dissolved to 2 wt% (17.3 mM) with 2% NH_4OH (volume/volume), and the solution was divided into different samples. Pure water or a salt solution (NaCl or NH_4CL) was added in equal volume to this PA solution, such that the final concentrations were 1% NH_4OH, 1 wt% (8.66 mM) PA, and the desired concentration of NaCl or NH_4Cl. After freeze drying, these samples were reconstituted to 1 wt% PA in pure water or 15 mM NaCl as indicated. For experimental techniques

requiring a dilution of the PA solution, the sample was always annealed at 1 wt% and diluted right before analysis.

Flash Freezing Procedure

For flash freezing procedures, the PA solution was submerged in liquid nitrogen for approximately 30 seconds and allowed to thaw at room temperature. With <250 μL of PA solution in 1.7 mL Eppendorf tubes, complete freezing was always achieved in less than 30 seconds.

Slowly Freezing Procedure

For experiments where PA was slowly frozen, PA solutions were allowed to equilibrate in a standard freezer (-20°C) overnight, after which complete freezing was observed.

Refrigeration Procedure

PA solutions were allowed to equilibrate in a standard refrigerator (4°C) overnight, after which no solid ice was observed.

Freeze Drying Procedure

PA solutions were flash frozen as described in *Flash Freezing Procedures* above. While still frozen, the samples were transferred to a port-type freeze drier and allowed to dry overnight. With <250 μL of PA solution in 1.7 mL Eppendorf tube, complete drying was achieved overnight.

Viscosity Measurements

Viscosity measurements were performed on an MCR 302 rheometer (Anton Paar, Graz, Austria). The CP25-2 fixture (25 mm diameter cone-plate) was used to analyze 200 μL of PA, with the rheometer plate set to 23°C. In all experiments, the PA solution contained 1 wt% of PA. The shear rate was increased from 1–100 s^{-1} over 240 seconds, and the final viscosity at 100 s^{-1} is reported. To account for batch-to-batch variations of from PA synthesis, all samples for one experiment came from the same PA stock solution. For example, for the experiment where PA was annealed, flash frozen, and then re-annealed, one annealed PA solution was created for all the samples. Some of this solution was then used to measure the viscosity of annealed PA, while the rest was flash frozen. After flash freezing, some of the sample was taken to measure the viscosity of flash frozen PA, and some was re-annealed.

Nanoparticle Tracking Analysis (NTA)

PA solutions were diluted from 1 wt% to 0.00125 wt% with pure water immediately before analysis. Diluted samples were loaded into a NanoSight LM10-HS nanoparticle tracking analysis (NTA) system (Malvern Instruments, Malvern, UK) with a 405 nm laser light source, and a 60 second video of light scattered by PA was recorded at 30 frames/second. NTA only records *light scattered by* PA nanofibers, and does not produce a resolved image of the nanofibers themselves. However, the length of the PA nanofibers can be roughly estimated by the "apparent" fibers seen in NanoSight videos, where the view area is known to be 80 μm × 100 μm × 10 μm (depth). Images extracted from the video frames were used to quantify "apparent" nanofiber lengths in ImageJ.

Two frames from each video were chosen, from near the beginning and end of the frame sequence. This approach was chosen to maximize the chances of quantifying different nanofibers, which come in and out of view throughout the 60 seconds. Using 5-6 videos, at least 100 nanofibers were measured for each experimental condition.

Cross-Polarized Light Microscopy

PA solutions at 1 wt% (50 μL) were pipetted onto glass slides and observed between cross-polarizers.

Cryogenic Transmission Electron Microscopy (cryoTEM)

Before use, 300-mesh copper grids with lacey carbon film (Electron Microscopy Sciences, Hatfield, PA, USA) were glow discharged for 30 seconds in a PELCO easiGlow system (Ted Pella, Inc., Redding, CA, USA). PA solutions (4 μL) were pipetted onto grids, blotted, and plunged into liquid ethane with an FEI Vitrobot Mark IV (FEI, Hillsboro, OR, USA), maintained around 95% humidity. While submerged in liquid nitrogen, vitrified samples were transferred to a Gatan 626 cryo-holder (Gatan, Pleasanton, CA, USA) and imaged on a JEOL 1230 TEM operating at 100 kV. Liquid nitrogen temperatures were maintained during imaging, and micrographs were captured with a bottom-mounted Gatan 832 camera.

It was not possible to prepare all samples for cryoTEM at the same dilution, due to the differences in solution viscosity and nanostructure properties. More viscous solutions with more nanostructures required dilution for blotting. The following samples were diluted to 0.01 wt% in pure water immediately before plunging: 1) annealed, 2)

annealed/flash frozen, 3) annealed/flash frozen/re-annealed, 4) annealed/freeze-dried/re-annealed PA solutions, 4) slowy frozen PA, and 5) refrigerated PA. For refrigerated PA, the Vitrobot was set to 4°C. The following samples were plunged at 1 wt% without dilution: 1) freshly dissolved, 2) freshly dissolved/flash frozen, 3) annealed/freeze-dried, and 4) freshly dissolved/freeze-dried.

Scanning Electron Microscopy (SEM)

Immediately before gel formation, 1 wt% PA was diluted 9:1 in pure water to 0.9 wt%, to mimic experiments where proteins or cells were loaded into PA solutions before gelation (FRAP and cell encapsulation experiments). PA gels were created by pipetting 4 µL of 30mM $CaCl_2$ onto Parafilm, and then introducing 10 µL of 0.9 wt% PA solution into this $CaCl_2$ droplet. Next, PA gels underwent a gradual ethanol exchange, where they were submerged in ethanol-water solutions containing gradually increasing amounts of ethanol: 10 minutes at 30%, 40%, 50%, 60%, 70%, 80%, 90%, and 95% EtOH, and then 15-20 minutes at 100% EtOH. Using a Samdri-795 critical point dryer (Tousimis, Rockville, MD, USA), dehydrated gels were purged with supercritical CO_2 for 10 minutes and then dried through the critical point of CO_2. Dried samples were mounted onto carbon tape, with a small drop of carbon paste in between the tape and sample to improve adhesion. To enhance conductivity, samples were coated with 16 nm of osmium metal using an SPI Osmium Coater (SPI Supplies, West Chester, PA, USA). Coated samples were imaged with a Hitachi SU-8030 SEM (Hitachi, Tokyo, Japan) operating at 2.0 kV.

Rheological Analysis of Gels

Similar to viscosity experiments, annealed and flash frozen PA samples were obtained from the same PA solution, in order to account for PA batch-to-batch variation or errors in sample preparation. Thus, each annealed PA measurement is "paired" with a flash frozen PA measurement. Similar to viscosity measurements, we found that while the absolute values of rheology measurements differed from sample to sample, the same trend between annealed and flash frozen PA were repeatedly observed.

Rheological analysis of PA gels was performed using an MCR 302 rheometer (Anton Paar, Graz, Austria). PA solutions at 1 wt% were diluted to 0.9 wt% in pure water immediately before the experiment, to mimic experiments where proteins or cells were loaded into PA solutions before gelation (FRAP and cell encapsulation experiments). This 0.9 wt% PA solution (143 μL) was loaded onto the rheometer plate, set to 23°C. A total of 57 μL of 30 mM $CaCl_2$ was introduced to the CP25-2 fixture (25 mm diameter cone-plate) in small droplets, as evenly spread as possible, and gelation was initiated when the fixture contacted the sample. The gel was equilibrated for 25 minutes (1500 seconds) at constant strain (0.1%) and angular frequency (10 rad/sec), and the final storage modulus is reported.

Immediately following the 25-minute equilibration period, a frequency sweep experiment was conducted. The strain was fixed at 0.1%, and the frequency was logarithmically decreased from 100 to 1 radians/second. After the frequency sweep experiment, the frequency was held constant at 10 rad/sec, and the strain logarithmically increased from 0.1 – 100%.

Cell Encapsulation Experiments

MC3T3-E1 subclone 4 mouse preosteoblasts (ATCC, Manassas, VA, USA) were maintained using standard cell culture techniques, in Alpha Minimum Essential Medium (Catalog No. A1049001, GIBCO [Thermo Fisher] Waltham, MA, USA) supplemented with 10% fetal bovine serum (FBS, Denville Scientific, South Plainfield, NJ, USA), 100 U/mL penicillin, and 100 μg/mL streptomycin (Pen Strep, GIBCO). FBS was heat-inactivated before use. Cells were passaged using 0.25% trypsin (GIBCO), and used for experiments at passages 4-6. For experiments, cells were suspended to 70,000 cells/μL in media, and this cell solution was mixed with 1 wt% PA in a 1:9 ratio, resulting in final concentrations of 0.9 wt% PA and 7000 cells/μL. A 4 µL $CaCl_2$ droplet was deposited in a 14 mm glass-bottom dish (MatTek Corporation, Ashland, MA, USA), and 10 μL of the PA/cell mixture introduced into the droplet to form a gel containing 5000 cells/μL. The $CaCl_2$ droplet contained 30 mM $CaCl_2$, to initiate gelation of PA, as well as 400 mM NaCl, to adjust the ionic strength of the gels. The PA solution contains no physiological salts, so NaCl was added to the calcium to provide physiological ionic strength for cells.

Cells were allowed to equilibrate for 24 hours, and then samples were prepared for confocal or TEM imaging. For confocal microscopy, gels were fixed in 4% paraformaldehyde and then permeabilized with 0.4% Triton X and 2% bovine serum albumin, both for 30 minutes at room temperature. Cells were then stained by incubating gels with a 1:200 dilution of Alexa Fluor 488 phalloidin (Molecular Probes), overnight at 4°C. All these solutions were dissolved in PBS w/ $CaCl_2$, which was also used to rinse samples three times between all steps. After phalloidin staining, gels were mounted onto

glass slides with Immu-Mount and observed on a Nikon AIR confocal microscope. All images presented are the maximum intensity projections of 15 μm thick z-stacks.

Thin-Sectioning for Transmission Electron Microscopy (TEM)

PA gels containing encapsulated cells were fixed in 2% paraformaldehyde, 2.5% glutaraldehyde in PBS, and stored at 4°C in this solution until embedding. When samples were ready to be processed further, they were transferred to the primary fixative. Incubation steps for fixation were performed in a Pelco Biowave with a cold spot and vacuum chamber (Ted Pella, Inc., Redding, CA, USA), followed by agitation at room temperature. The protocol is detailed below:

Solution	**Time in Biowave**	**Time at (RT), with agitation**	**Number of times repeated**
1) Primary fixation: Modified Karnovsky's solution, with 2% paraformaldehyde, 1.5% glutaraldehyde in 0.05M sodium phosphate buffer, pH 7.4	4 minutes	5 minutes	2
2) Buffer wash: 0.05M sodium phosphate buffer, pH 7.4	1 minute	5 minutes	3
	4 minutes	5 minutes	1
3) Secondary fixation: 1.5% osmium tetroxide	4 minutes	5 minutes	1
4) DI water wash	1 minute	5 minutes	2
	1 minute	15 minutes	1

Following fixation, samples were gradually dehydrated in acetone. Samples were sequentially incubated in 30%, 50%, 70%, 90%, and twice in 100% acetone. Each incubation step was performed inside a Pelco Biowave, for 40 seconds followed by approximately 3 minutes of agitation at room temperature. After dehydration, samples were infiltrated in EMBed812 resin (Electron Microscopy Sciences, Hatfied, PA, USA) with acetone. The following protocol was used:

Solution (acetone / resin ratio)	**Time in Biowave**	**Time at (RT), with agitation**	**Number of times repeated**
1) 2:1	3 minutes	30 minutes	1
2) 1:1	3 minutes	1-4 hours	1
3) 1:2	3 minutes	overnight	1
4) 100% resin	3 minutes	1 hour	2

After resin embedding, samples were polymerized in an oven at 60°C for 24 hours. A Leica Ultracut S ultramicrotome (Leica Microsystems, Wetzlar, Germany) was used to cut 90 nm thick sections, which were collected onto copper grids and post-stained with 3% uranyl acetate and Reynold's lead citrate. Samples were imaged on a 1230 JEOL TEM operating at 100 kV, and micrographs captured with a Gatan 832 camera.

Fluorescence Recovery After Photobleaching (FRAP)

FRAP experiments were performed on bovine serum albumin (BSA), tagged with fluorescein isothiocyanate (FITC), in PA solutions and gels (Molecular Probes, Eugene, OR, USA). FITC-BSA stock (2 mg/mL) was prepared by dissolving BSA powder in

pure water, and stored at -20°C until use. Immediately before the experiment, 1 wt% PA solution was mixed with the FITC-BSA stock in a 9:1 ratio, resulting in 0.9 wt% PA and 0.2 mg/mL BSA. For *FRAP on PA solutions* with BSA, 50 μL of PA/BSA mixture was pipetted into glass-bottom dishes (MatTek Corporation, Ashland, MA, USA). For *FRAP on PA gels*, a 4 μL droplet of 30 mM $CaCl_2$ was deposited on Parafilm, and 10 μL of PA/BSA mixture introduced into the droplet to create a gel. Gels were placed in glass-bottom dishes.

PA solutions and gels were imaged on a Leica SP5 confocal microscope (Leica, Wetzler, Germany), which was used to perform FRAP experiments. Imaging and photobleaching were performed with the 488 nm laser line, with 17% power for imaging, and 50% power for photobleaching 10 μm-diameter circles. The microscope scanned a 512x512 pixel area at 1000 Hz, allowing an image to be captured approximately every 0.263 seconds. Fluorescence intensity in the region of interest (ROI, 10 μm-diameter circles) was monitored for approximately 13 seconds, including 10 pre-bleach frames, followed by 2 bleach frames, and finally 50 post-bleach frames. Each experimental condition was repeated with 3 different samples, with 5 ROIs examined per sample, resulting in a total of 15 measurements for each condition.

To account for photobleaching due to *imaging*, the ROI's fluorescence intensity ($I_{measured}$) was corrected using a different region of the sample, which was never intentionally photobleached ($I_{unbleached}$). The following equation was used to obtain corrected values for the ROI's fluorescence intensity ($I_{corrected}$). The value for $I^0_{unbleached}$ is the fluorescence intensity of region used for correction in the first pre-bleach frame, where photobleaching from imaging would be minimal.

$$I_{corrected} = I_{measured} * \frac{I^0_{unbleached}}{I_{unbleached}}$$

The corrected intensities ($I_{corrected}$) were then normalized ($I_{normalized}$) to a value between 0 and 1 (where 1 represents full recovery), and plotted over time. The pre-bleach fluorescence ($I_{prebleach}$) was obtained by averaging the ROI's fluorescence intensity in the 10 pre-bleach frames, while the post-bleach intensity ($I_{postbleach}$) was obtained by taking the ROI's fluorescence intensity immediately after photobleaching. The following equation was used to normalize fluorescence intensity in the ROI for all other time points ($I_{corrected}$):

$$I_{normalized} = \frac{I_{corrected} - I_{postbleach}}{I_{prebleach} - I_{postbleach}}$$

Circular Dichroism (CD)

PA solutions were diluted to 0.05 wt% from 1 wt%, immediately before loading into a 1mm path length quartz cuvette. CD spectra in the wavelength range 190–250 nm were captured on a JASCO J-815 spectrophotometer, at room temperature.

Small Angle X-Ray Scattering (SAXS)

SAXS measurements were performed using Beamline 5-ID-D of the DuPont-Northwestern-Dow Collaborative Access Team (DND-CAT), located at the Advanced Photon Source of Argonne National Laboratory. A double crystal monochromator was used to select a beam energy of 17 keV ($\lambda = 0.7293$), and the detector was positioned 8.5 cm behind the sample. PA solutions at 1 wt% were loaded into quartz capillaries, with 1.5 mm diameter with 0.1 mm wall thickness (Charles Supper, Natick, MA, USA).

Ultraviolet-Visible Spectroscopy (UV-Vis)

PA powders were reconstituted with pure water to obtain a 1 wt% solution (50 uL of pure water to reconstitute 0.5 mg was used in all experiments). Samples were briefly vortexed and centrifuged for 5 minutes at 14,000 rotations per minute, and the clear supernatant taken and transferred to another tube. Because PA powder does not settle to the bottom of the tube easily, this centrifugation step was repeated two more times to ensure that no precipitates interfered with UV-visible absorbance measurements. After three centrifugation steps, all for 5 minutes at 14,000 rpm, the clear supernatant was diluted 1:10 with pure water. This diluted sample was loaded into a 0.1 mm path length quartz cuvette, and UV-visible absorbance spectra in the range 200-400 nm were collected on a LAMBDA 1050 spectrophotometer (Perkin Elmer, Waltham, MA, USA). All UV-visible spectra were plotted from 200 - 250nm, because no signal was observed at the higher wavelengths. Because NH_4OH is volatile during freeze-drying, NaCl solutions at the appropriate concentration were used to perform solvent background

subtract (i.e. 15 mM NaCl was the background for PA freeze-dried from 1% NH_4OH and 15 mM NaCl).

Dynamic Light Scattering (DLS)

PA was first dissolved to 1 wt% (8.66 mM) and then immediately diluted to 1 mM PA with pure water, because 1 wt% is too concentrated for DLS experiments. These diluted PA solutions were then heated as described. DLS measurements were taken on a Zetasizer Nano ZSP (Malvern Instruments, Malvern, UK). Because DLS assumes a spherical model, the measured sizes do not accurately reflect the length of nanofibers; however, trends between samples can still be observed.

5 A PEPTIDE AMPHIPHILE BONE GRAFT FOR SPINAL FUSION

5.1 OBJECTIVES AND SIGNIFICANCE

Built from non-covalent interactions, supramolecular biomaterials are extremely versatile but can be highly sensitive to pathway selection. This presents challenges to clinical translation, where certain processing pathways may be necessary for large-scale manufacturing and clinical use. In this work, we address this challenge in a specific supramolecular biomaterial, a bone graft comprised of self-assembled peptide amphiphile (PA) nanofibers. For spinal fusion surgeries, PA bone grafts can reduce the therapeutic bone morphogenetic protein-2 (BMP-2) dose 100-fold in a small animal model. Currently, supraphysiological doses BMP-2 are used clinically, delivered through an absorbable type 1 collagen sponge. This PA's non-covalent structures are susceptible to change in solution, so the PA should freeze dried and stored as a dry powder to increase stability and shelf life. After rehydration, the PA must be immediately ready for use, because lengthy or complex preparation steps are not permitted in surgical settings. We identify here a freeze drying pathway that produces a functional PA material, despite causing noticeable disruptions to PA nanostructures. This freeze dried PA is capable of achieving a 100% fusion rate in a rat model, with 100-fold less BMP-2 than the established therapeutic dose. We also present a non-functional freeze drying pathway that achieves a lower fusion rate (17%), which surprisingly showed superior *in-vitro* results but was not effective *in-vivo.* Our results underscore the effect of pathway dependence on clinical translation of this PA, which we believe applies to other supramolecular biomaterials.

5.2 BACKGROUND

Supramolecular biomaterials are built from non-covalent interactions, which can be tuned to achieve specific mechanical or chemical properties.[9, 16, 65, 86, 220] Non-covalent bonds also enable the design of structures that are reversible and responsive to environmental cues, allowing the material to mimic the dynamic nature of biological systems.[9, 12, 16, 65] However, non-covalent self-assembly can also give rise to energy landscapes, which lead to complex pathway dependence behavior in supramolecular assemblies.[101-103, 135] Recent work has shown that some pathways can result in cytotoxic structures or structures with compromised ability to promote cell adhesion.[103, 135] Thus, high sensitivity to pathway selection has significant implications for biological function, which presents challenges to clinical translation. Unfortunately, stringent requirements for pathway selection may not be compatible with procedures necessary for clinical translation, such as large-scale manufacturing, long-term storage, transportation to end users, and material preparation by end users. Specifically, recent work has shown that freeze drying, a common procedure to preserve organic materials, can disrupt supramolecular structures and also cause complex shifts in energy landscape positions.[135]

Over the past two decades, our laboratory has developed a class of supramolecular biomaterials comprised of self-assembling peptide amphiphiles (PAs).[63, 65] In canonical form, PAs contain an alkyl tail to cause hydrophobic collapse, a β-sheet forming peptide sequence to induce self-assembly into one-dimensional nanostructures, and charged peptide residues to promote solubility in water.[31, 32] We have used this platform to develop supramolecular scaffolds for regenerating bone,[107-110] cartilage,[111] muscle,[87] blood vessels,[112] neurons,[89, 113] spinal cord,[114] and peripheral nerves,[115] which have shown

success in preclinical models. In one specific application, PAs are used as bone grafts for spinal fusion,[107, 108] a surgical procedure where two adjacent spinal vertebrae are permanently fused. Successful fusion requires the presence of an osteoinductive scaffold to induce bone formation, and insufficient bone growth will lead to non-union.[221] Bone morphogenetic protein-2 (BMP-2) is a growth factor that induces osteogenesis,[222] and recombinantly synthesized human BMP-2 can successfully promote vertebral fusion when delivered through an absorbable type I collagen sponge.[223] However, supraphysiological doses of BMP-2 are required to achieve sufficient bone growth, which can lead to side effects such as ectopic bone,[224-226] inflammation,[227-229] infection,[230, 231] neurological complications,[227, 232] and retrograde ejaculation.[233-235] Our laboratory has shown that PAs can reduce the therapeutic BMP-2 dose 10 - 100 times in a small animal model,[107, 108] demonstrating that PAs can potentially improve the safety of BMP-2 bone grafts used clinically.

Knowing that PA assemblies have complex energy landscapes and pathway dependence behavior, we wanted to identify pathways conducive to clinical translation, using the spinal fusion application as a case study. This specific case requires therapeutic materials to have shelf life on the order of years, and to be ready for use on demand with minimal preparation time. Unstable materials may be preserved as a freeze dried powder and rehydrated immediately prior to surgery, which is how protein-based drugs are generally supplied.[127] In this work, we explore the effects of freeze drying on the *in-vivo* efficacy of PA-based bone grafts, knowing that freeze drying can disrupt PA nanostructures.[135] By performing materials characterization and *in-vitro* experiments alongside the *in-vivo* studies, we again insight into how the structure of PA assemblies

affects their therapeutic efficacy, shedding light on design criteria for clinical translation pathways.

5.3 RESULTS AND DISCUSSION

5.3.1 Freeze Drying PA Disrupts Nanostructures and Bioactivity

We dissolved $V_3A_3E_3$ PA (Figure 5-1a) to 2 wt% (17.32 mM) in aqueous media, using 30 mM NaOH to deprotonate the glutamic acid residues and enable solubility. Immediately after the PA dissolved at 2 wt%, we diluted it to 1 wt% with pure water. We chose this procedure for consistency with experiments where we instead diluted PA with glycerol, to test its lyoprotective properties. We then thermally annealed the 1 wt% PA solutions (80°C 30 minutes, slow cool overnight), to equilibrate the PA assemblies to their thermodynamic minimum. For this PA molecule under these solvent conditions (high charge screening, low charge density on nanofibers), the thermodynamic minimum is infinitely long nanofibers.[71, 103, 135] To increase the stability and thus shelf life of this material, it is advantageous to store it in the dry state. The long-term storage of pre-annealed solutions is unfavorable, because the non-covalent nature of PA assemblies makes them susceptible to change over time. Thus, we freeze dried the annealed PA solutions (**pathway 1**) and rehydrated the powder (**pathway 2**), according to the processing pathway illustrated in Figure 5-1b. For clinical applications, the dry PA powder can be stored long-term and rehydrated immediately prior to use. Similar to previous work,[135] we found that freeze drying breaks long nanofibers into shorter ones by several characterization techniques. The viscosity of **pathway 2** PA is around 4x lower

than the viscosity of **pathway 1** PA (Figure 5-1c), suggesting disruption of the long nanofibers. Due to long nanofibers aligning into bundles, annealed PA solutions are known to be liquid crystalline and exhibit birefringence.[71] In the current work, we confirmed that **pathway 1** PA contains birefringent monodomains (Figure 5-1d), and then found that they are lost in **pathway 2** PA (Figure 5-1e). As long nanofibers break into shorter ones, they no longer possess the necessary length to form aligned domains, so the solution loses its liquid crystalline nature. As expected, cryogenic electron transmission micrographs (cryoTEM) show long nanofibers extending beyond the field of view in **pathway 1** PA (Figure 5-1f) and shorter nanofibers of more heterogeneous lengths in **pathway 2** PA (Figure 5-1g). Although dried materials are more stable than their hydrated counterparts, long nanofibers are known to be superior to shorter ones for supporting cell adhesion,[103, 135] so their breakage during freeze drying is concerning. For successful spinal fusion, cells must infiltrate the PA scaffold to form new bone, so compromising cell adhesion can potentially be detrimental. To further explore this, we created PA scaffolds using **pathway 1** and **pathway 2** PA, and examined their structure and bioactivity *in-vitro*.

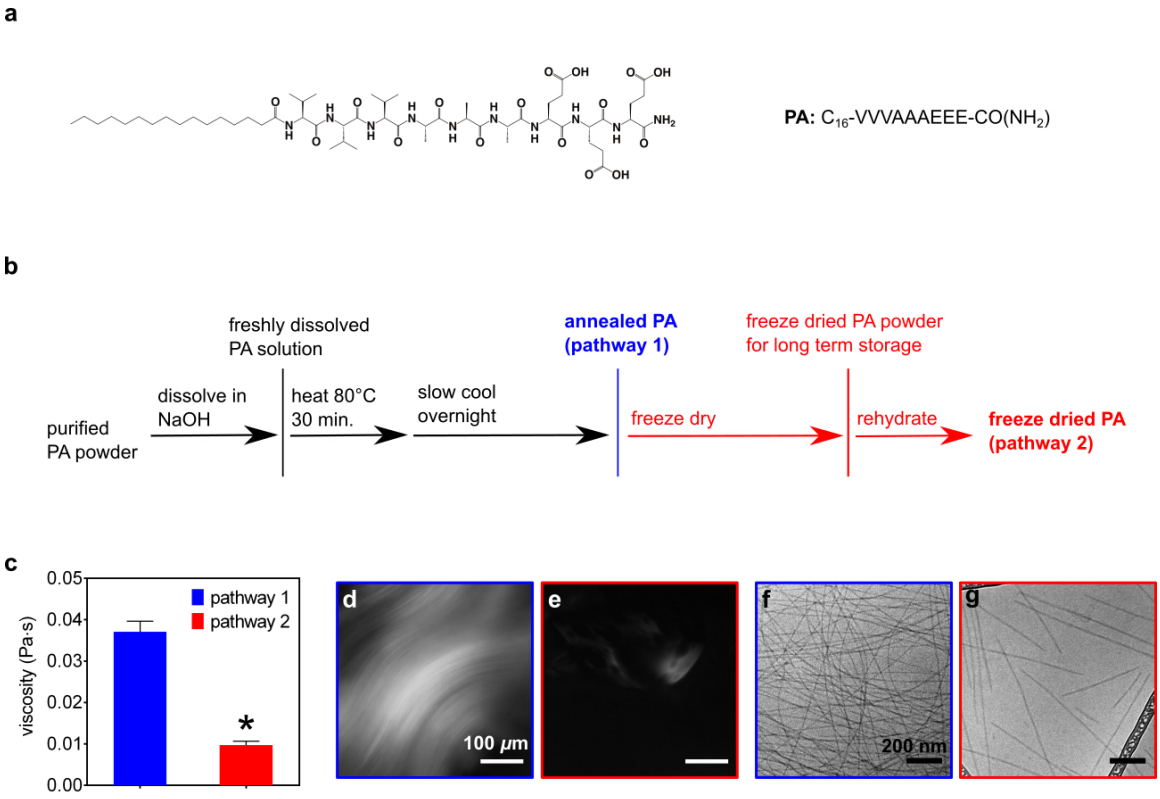

Figure 5-1: Freeze drying annealed PA solutions for long term storage. (a) Chemical structure of $V_3A_3E_3$ PA. (b) Diagram illustrating processing pathways for creating **pathway 1** and **pathway 2** PA solutions. (c) Viscosity of **pathway 1** and **pathway 2** PA solutions (t-test, *$p<0.0001$). Polarized light micrographs of (d) **pathway 1** and (e) **pathway 2** PA solutions. Cryogenic transmission electron micrographs of (f) **pathway 1** and (g) **pathway 2** PA solutions.

Clinically, BMP-2 is delivered on an absorbable collagen sponge (ACS), which we also use to deliver PA.[107, 108] The collagen sponge provides physical support for soft PA gels, and is a commercially available product that is currently used for spinal fusion. We applied **pathway 1** and **pathway 2** PA solutions to collagen sponges (ACS), and then induced gelation of PA nanofibers with $CaCl_2$ (Figure 5-2a). When loading BMP-2 onto the scaffolds, BMP-2 is mixed with the PA solution as illustrated (Figure 5-2a), but no BMP-2 was incorporated for experiments where BMP-2 was not relevant (i.e. imaging of

PA nanostructures). We examined the PA scaffolds' surface morphology using scanning electron microscopy (SEM), and found that **pathway 1** scaffolds are comprised of long nanofibers while **pathway 2** scaffolds are comprised of shorter ones (Figure 5-2b-c), which is consistent with our characterization of the two PA solutions (Figure 5-1). To examine cell adhesion to these PA scaffolds, we seeded MC3T3 preosteoblast cells onto their surfaces. After a 4-hour incubation, we fixed and stained the cytoskeleton of the cells, and found no drastic morphological differences between cells on the two scaffolds (Figure 5-2d-e). From this data, we believe that both scaffolds can support cell adhesion to some extent. However, when we performed an MTS assay to detect cell metabolic activity on the scaffolds, we found that there was less MTS signal from **pathway 2** scaffolds (Figure 5-2f). This suggests the **pathway 2** scaffolds, while they can support cell adhesion, are not as effective a **pathway 1** scaffolds in doing so. This is consistent with previous results from our laboratory, which showed that long nanofibers are superior to shorter ones for supporting cell adhesion, even if their chemical compositions are identical.[103, 135] Although these data all strongly suggests that the ideal PA bone graft should contain long nanofibers, the long preparation time needed to achieve them (80°C 30 minutes, slow cool overnight) is unsuitable for clinical translation. An off-the-shelf material containing pre-annealed long nanofibers is also not favorable, because their non-covalent nature makes them susceptible to change during transport and storage.

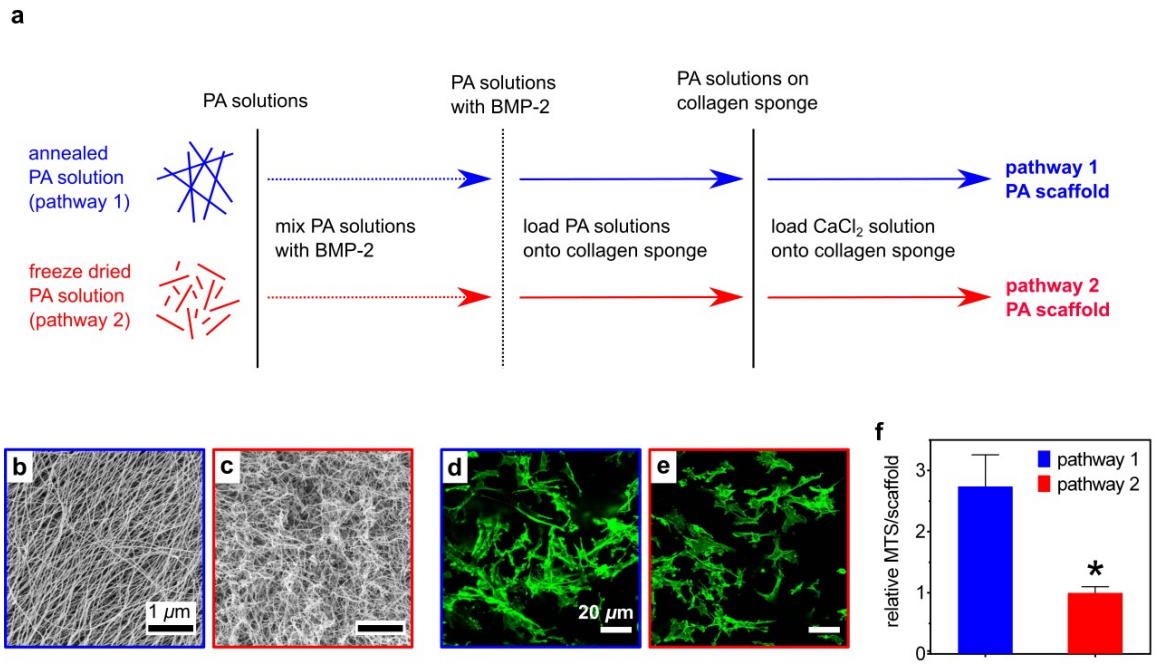

Figure 5-2: Cell adhesion to PA scaffolds. (a) Diagram illustrating the preparation of implantable scaffolds from PA. Scanning electron micrographs of scaffolds formed from (b) **pathway 1** PA and (c) **pathway 2** PA. Confocal micrographs of MC3T3 cells seeded onto scaffolds formed from (d) **pathway 1** PA and (e) **pathway 2** PA, visualized with actin staining. (f) MTS assay for MC3T3 cells seeded onto PA scaffolds (t-test, *p<0.01).

5.3.2 Addition of a Lyoprotectant to PA

We examined whether the addition of a cryo/lyo-protectant to PA solutions could preserve long nanofibers during freeze drying. In 1949, researchers discovered the cryoprotective properties of glycerol for storage of human sperm. They found that if the sperm was frozen in the presence of glycerol, the sperm remained viable after freezing and thawing.[236] We prepared annealed PA solutions containing 1 wt% PA and 5% glycerol, which have a similar viscosity compared to annealed PA solutions containing no glycerol (Figure 5-3a versus Figure 5-1c). When annealed PA solutions containing 5% glycerol are freeze dried and rehydrated, the viscosity decreased (~25% decrease,

Figure 5-3a), but not nearly as much as when PA is freeze dried without glycerol (~75% decrease, Figure 5-1c). In the presence of glycerol, annealed PA still exhibits birefringent monodomains (Figure 5-3b), which appear very similar to those found in annealed PA without glycerol (Figure 5-1d). When annealed PA with glycerol is freeze dried, the large monodomains are not lost (Figure 5-3c), in contrast to when PA is freeze dried without glycerol (Figure 5-1e). CryoTEM shows long nanofibers extending beyond the field of view in annealed PA containing glycerol, before (Figure 5-3d) and after freeze drying (Figure 5-3e). Both of these solutions can be loaded onto collagen sponges to form implantable scaffolds, and both scaffolds contain long nanofibers that appear similar to annealed PA without glycerol (Figure 5-3d-e, Figure 5-2b).

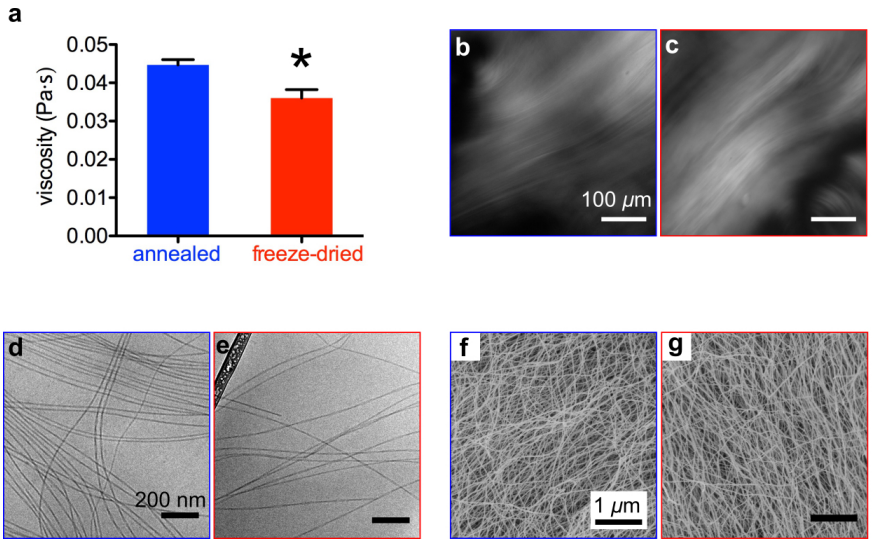

Figure 5-3: Freeze drying PA in 5% glycerol. (a) Viscosity of PA annealed in the presence of 5% glycerol, and the same solution after freeze drying and rehydration (t-test, *p<0.01). Polarized light micrographs of PA annealed in the presence of 5% glycerol (b), and the same solution after freezing and rehydration (c). CryoTEM of PA annealed in the presence of 5% glycerol (d), and the same solution after freezing and rehydration (e). SEM micrographs of PA annealed in the presence of 5% glycerol (f), and the

same solution after freeze drying and rehydration (g), both loaded onto absorbable collagen sponges.

These experiments with glycerol show that it has the ability to preserve long PA nanofibers during freeze drying (Figure 5-4). However, we note that freeze dried solid is not a powder that readily dissolves when rehydrated, and is instead a sticky substance that requires some time to dissolve (Figure 5-4). Indeed, the sticky nature of the solid may be the reason glycerol has lyoprotective properties, because long nanofibers stuck within this "gooey" substance may be protected from breakage. However, the long dissolution time is not favorable for clinical use, where materials should be prepared as quickly and as simply as possible. Therefore, we were motivated to look at other preparation pathways that were compatible with the surgical setting.

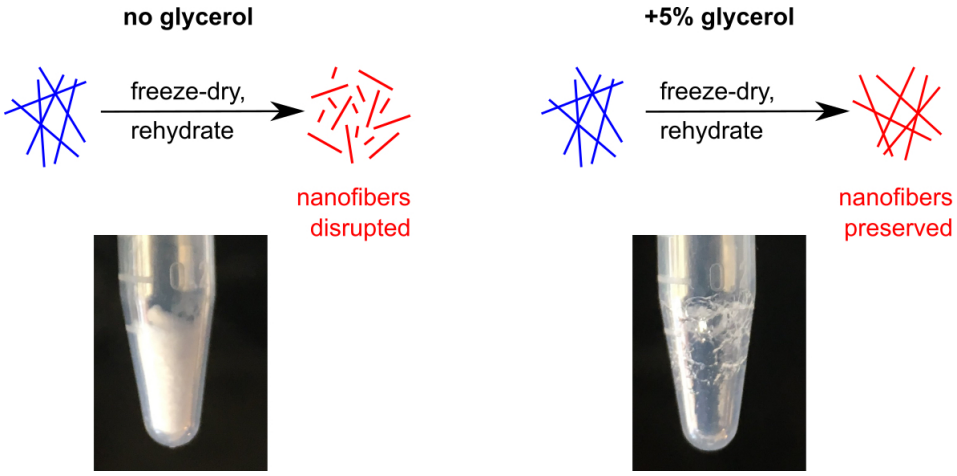

Figure 5-4: Schematic summarizing the effects of glycerol during freeze drying of long annealed PA nanofibers. Photographs of the freeze dried solid, without and with glycerol, are included.

5.3.3 A Shortened Heating and Cooling Cycle

The elongation of nanofibers is kinetically limited, requiring time and energy input for the reaction to proceed.[103, 135] Currently, our laboratory has ample evidence that heating PA solutions at 80°C for 30 minutes followed by slow cooling overnight will allow elongation to proceed and drive the system towards its global minimum.[71, 103, 135] For surgical applications such as spinal fusion, lengthy overnight preparation procedures are not feasible. Thus, we were motivated to study a shortened annealing cycle, which involves 10 minutes of heating at 80°C and then cooling the solution immediately. Also, because we know from previous work that freeze drying in NaOH without prior annealing can result in a variable material (Chapter 4),[135] we chose to solubilize the PA in a different solvent for freeze drying. The previous work (Chapter 4) also showed that freeze drying in NH_4OH and NaCl may improve the reproducibility,[135] which we use in the current work. In this method, acidic PA powders are solubilized for freeze drying with NH_4OH, which is volatile and will be removed under vacuum during freeze drying.[135] A non-volatile counterion, Na^+ from NaCl, is added to maintain glutamic acids as glutamate salts, so that a water soluble freeze dried powder is obtained.[135] As described in Figure 5-5a, we freeze dried PA in this solvent and rehydrated it (**pathway 3**), and then subjected the sample to a shortened heating and cooling cycle (**pathway 4**). We measured the viscosity of **pathway 3** and **pathway 4** PA, and found that the viscosity increases with only 10 minutes of heating at 80°C (Figure 5-5b). This suggests that the shortened heating and cooling cycle is sufficient to induce nanofiber elongation, and we proceeded to visualize the PA solutions using light and electron microscopy. Polarized

light micrographs show that **pathway 3** PA (Figure 5-5c) is largely isotropic while **pathway 4** PA (Figure 5-5d) contains liquid crystalline domains, which is associated with longer nanofibers that can align with each other.[71] Indeed, cryoTEM reveals short nanofibers that end within the field of view in **pathway 3** PA (Figure 5-5e) and longer nanofibers extending beyond the field of view in **pathway 4** PA (Figure 5-5f).

We then loaded **pathway 3** and **pathway 4** PA onto collagen sponges and induced gelation with $CaCl_2$ (Figure 5-2a), and then imaged the scaffolds using scanning electron microscopy. As expected, SEM micrographs show that **pathway 3** PA scaffolds are comprised of short nanofibers (Figure 5-5g) while **pathway 4** PA scaffolds are comprised of longer ones (Figure 5-5h). Unexpectedly, we noticed a difference between **pathway 2** and **pathway 3** PA scaffolds. We did not expect any differences because both are freeze dried PA solutions immediately after rehydration, containing metastable assemblies that have not had time to elongate into their thermodynamic state. When the SEM field of view was zoomed out to observe micron-scale features, we noticed that **pathway 3** PA scaffolds were considerably more porous than **pathway 2** PA scaffolds (Figure 5-5i-j). Since the critical point drying process for SEM imaging can introduce artifacts into the sample, we wanted to study **pathway 2** and **pathway 3** gels using a different technique. We measured the rheological properties of **pathway 2** and **pathway 3** gels alone, with no collagen sponge, using $CaCl_2$ to crosslink the PA solutions. We found that **pathway 3** PA forms significantly weaker gels than **pathway 2** PA, with a storage modulus nearly an order of magnitude lower (Figure 5-5k). Thus, it is reasonable that the weaker gels of **pathway 3** PA would leave a more porous collagen sponge.

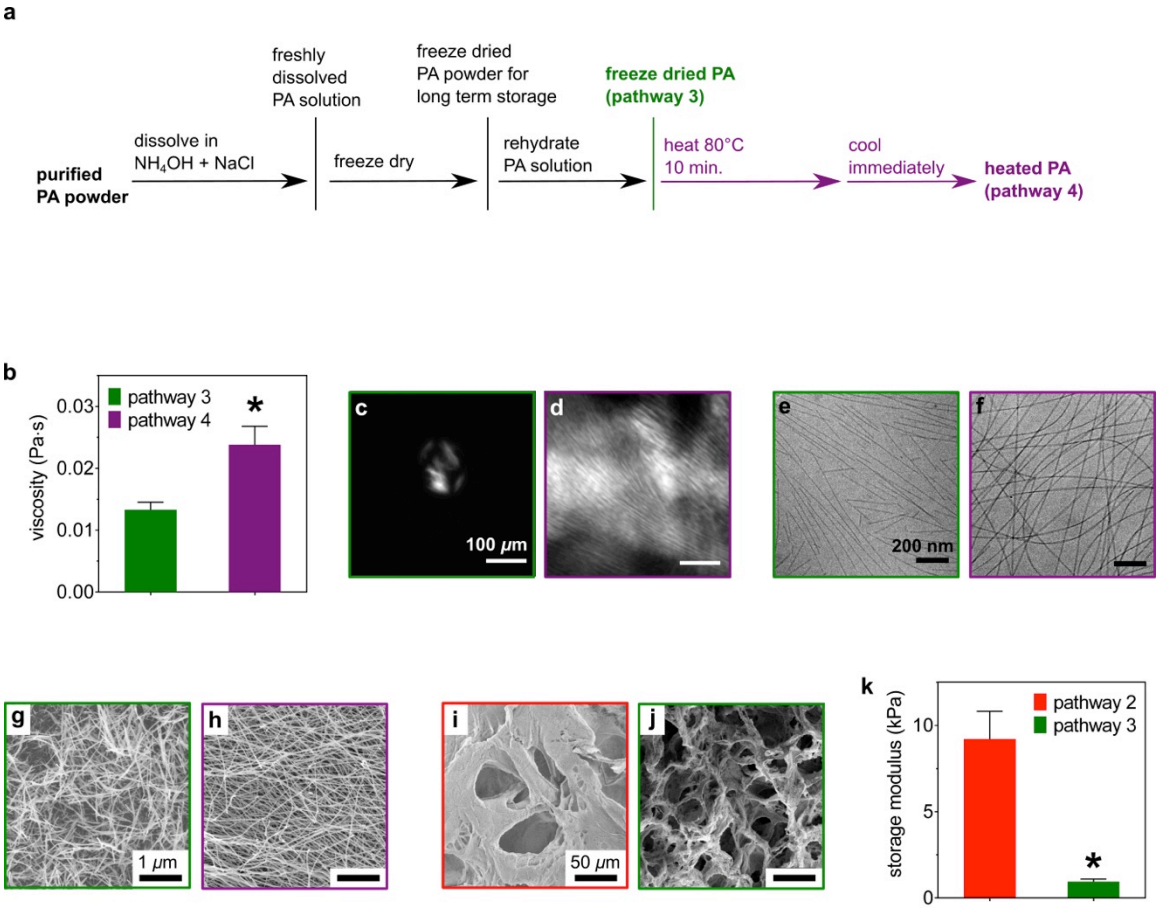

Figure 5-5: A shortened annealing cycle. (a) Diagram illustrating two additional processing pathways, creating **pathway 3** and **pathway 4** PA solutions. (b) Viscosity of **pathway 3** and **pathway 4** PA (t-test, *p<0.001). Polarized light micrographs of (c) **pathway 3** and (d) **pathway 4** PA. Cryogenic transmission electron micrographs of (e) **pathway 3** and (f) **pathway** 4 PA. SEMs of scaffolds formed from (g) **pathway 3** PA and (h) **pathway 4** PA. Zoomed out SEMs of scaffolds formed from **pathway 2** PA (i) and **pathway 3** PA (j). (k) Storage modulus of **pathway 2** PA and **pathway 3** PA gels, formed by gelation with $CaCl_2$ (t-test, *p<0.001).

5.3.4 In-Vitro Characterization of Peptide Amphiphile Scaffolds

Since these PA scaffolds are intended to act as spinal fusion bone grafts, we wanted to study their ability to promote osteogenic differentiation *in-vitro*. We used C2C12 mouse myoblasts as an *in-vitro* model, because this cell line is known to

differentiate into an osteoblastic lineage when exposed to ostoegenic cytokines like BMP-2. Our laboratory has previously used the C2C12 cell line to probe the osteogenic potential of PA nanostructures, although those experiments were 2D, with cells cultured on surfaces and PA dissolved in the cell media.[107, 108] In the current work, we performed a 3D experiment where we mixed C2C12 cells with PA solutions, loaded the cells and PA onto collagen sponges, and then induced gelation of PA using $CaCl_2$. In some experiments, BMP-2 was added to the PA solution and thus became encapsulated in the PA scaffolds, and in other experiments BMP-2 was added to the cell media surrounding the scaffolds (Figure 5-6a). The cells were incubated with BMP-2 for three days, after which we measured alkaline phosphate (ALP) activity, an early marker for osteogenic differentiation. Due to the interference of negatively charged PA with assays that detect DNA or protein, we could not normalize the ALP activity to the number of cells, and instead plotted the relative ALP activity detected per scaffold. We found that when BMP-2 is encapsulated within the scaffold, no ALP activity was detected above that of a negative control receiving no BMP-2 treatment (Figure 5-6b). We believe the reason no ALP activation occurs *in-vitro* is that BMP-2 is sequestered within the PA gels and therefore not available to cells. In fact, the ability to bind and slowly release BMP-2 is important to the success of PA as spinal fusion scaffolds,[108] so this result is not surprising. In the *in-vivo* system, degradation of the PA gel occurs over several weeks, which does not occur during a 3-day *in-vitro* experiment. Interestingly, when the BMP-2 is added to the cell media as opposed to encapsulated within the PA scaffolds, we get the same results *except* that ALP activation is detected in **pathway 3** scaffolds (Figure 5-6b). This result was also confirmed by staining the scaffolds for ALP activity, which revealed

ALP positive cells only at the surface of **pathway 3** scaffolds (Figure 5-6c). Since the materials characterization data suggests that **pathway 3** scaffolds are highly porous compared to the other PA scaffolds (Figure 5-5j-k), we hypothesize that its porous structure allows BMP-2 in the cell media to access the cells and induce ALP activity. In all other PA scaffolds, the BMP-2 in the media becomes sequestered by the PA gels and is therefore unavailable to cells. Since **pathway 2** and **pathway 3** PA are both freeze dried PA solutions immediately after rehydration, and thus both at a metastable state in their energy landscape,[103, 135] we were intrigued by the drastic differences between their scaffolds.

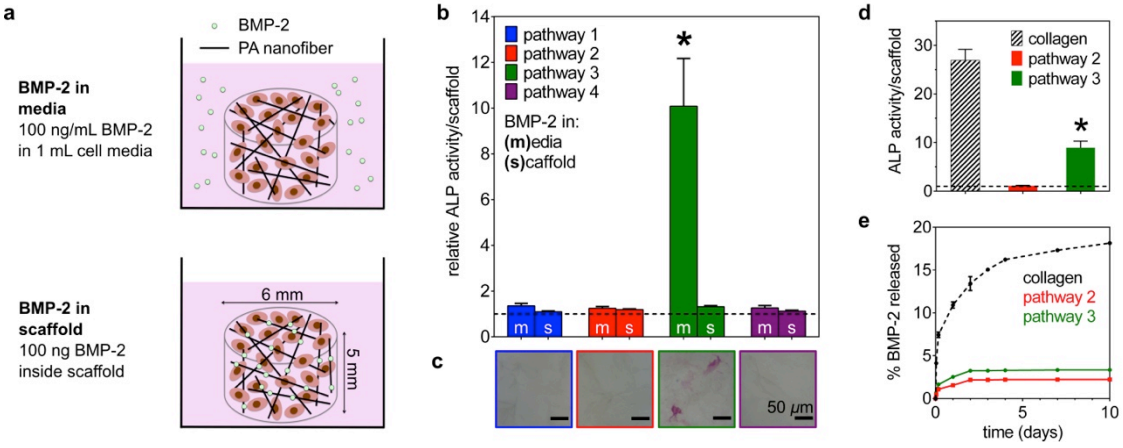

Figure 5-6: *In-vitro* characterization of PA scaffolds. (a) Schematic illustrating experimental set-up for *in-vitro* experiments. (b) Alkaline phosphatase (ALP) activity of C2C12 cells encapsulated within PA scaffolds, using the set-up described in panel *a* (one-way ANOVA, *p<0.05). Since the measured outcome is relative ALP, all PA conditions were analyzed in tandem. (c) Staining for ALP positive cells on PA scaffolds, when BMP-2 was added to the cell media. The color key in panel *b* applies. (d) ALP activity of C2C12 cells encapsulated within PA scaffolds, compared to a collagen scaffold with no PA. These are separate experiments from the ones shown in panel *b*, conducted in tandem with the collagen scaffold alone (one-way ANOVA, *p<0.05). (e) BMP-2 release from PA scaffolds and collagen scaffolds with no PA, measured using ELISA.

Moving forward, we decided to focus on **pathway 2** and **pathway 3** PA, which both require no additional preparation beyond rehydration of PA. The *in-vitro* experiments suggested that **pathway 3** PA may create more efficacious scaffolds than other freeze drying pathways such as **pathway 2**. We repeated the ALP activity assay with BMP-2 in the cell media, comparing **pathway 2** and **pathway 3** PA with a bare collagen sponge. As expected, cells seeded onto a collagen sponge showed 20-30 times more ALP activity when exposed to BMP-2, compared to their counterparts that received no growth factor (Figure 5-6d). Using the same point of comparison, BMP-2 fails to signal cells in **pathway 2** scaffolds but causes a 10-fold increase in ALP activity in **pathway 3** scaffolds (Figure 5-6d). In this experiment, the collagen sponge is the most porous scaffold, since there are no PA nanofibers "blocking" the pores. Therefore, the BMP-2 in the media is completely free to interact with the cells and induce ALP expression. **Pathway 3** scaffolds exhibit "intermediate" behavior because it contains PA that can bind and sequester rhBMP-2, but its porous microstructure allows some growth factor to still interact with cells. Although scaffold porosity should facilitate cell infiltration and nutrient diffusion, the inability of collagen to bind and slowly release BMP-2 diminishes its efficacy *in-vivo.* Clinically, collagen sponges must be loaded with supraphysiological doses to successfully promote fusion. Conversely, the ability of PA to bind and slowly release BMP-2 allows it to reduce the therapeutic BMP-2 dose *in-vivo*.[108] This would not be reflected in the *in-vitro* experiment, where BMP-2 is in the cell media and cannot "escape" the scaffolds. Therefore, we loaded BMP-2 into bare collagen sponges and **pathway 2** and **3** PA scaffolds, and studied BMP-2 release kinetics using an enzyme-linked immunosorbent assay (ELISA). Both **pathway 2** and **pathway 3** PA

scaffolds outperformed bare collagen sponges in retaining rhBMP-2 (Figure 5-6e), and we note that the higher porosity of **pathway 3** scaffolds does not significantly compromise its ability to retain BMP-2. From all this data, we hypothesized that **pathway 3** scaffolds might outperform **pathway 2** scaffolds *in-vivo.* Although **pathway 3** scaffolds do not contain the long nanofibers of **pathway 1** scaffolds (Figure 5-2), its higher porosity (Figure 5-5j) and weaker gels (Figure 5-5k) may ease cell infiltration and also allow cells better access to the underlying collagen, which is a natural extracellular matrix component of bone. Thus, we proceeded to test the therapeutic efficacy of **pathway 2** and **3** PA scaffolds *in-vivo*, using **pathway 1** scaffolds as a point of comparison.

5.3.5 In-Vivo Efficacy of Peptide Amphiphile Scaffolds

We tested the PA scaffolds using a well-established rat posterolateral lumbar intertransverse spinal fusion model, where therapeutic materials are implanted between the L4 and L5 transverse processes. After 8 weeks, L4-L5 fusion is accessed by blinded manual palpation of three independent scorers. A fusion score of 0 indicates that no fusion occurred, a score of 1 indicates successful unilateral fusion, and a score of 2 indicates successful bilateral fusion. An average score ≥1 indicates that the animal successfully fused, and fusion rate is the percentages of animals that fuse. In this model, it is established that 10 μg/animal of BMP-2 is required to achieve 100% fusion if the BMP-2 is applied to a bare collagen sponge.[107, 108] Our laboratory has demonstrated the ability of PA-based scaffolds to reduce the therapeutic BMP-2 up to 100 times in this rat

model.[107, 108] Indeed, we achieved this result with **pathway 1** PA, and were surprised to find that **pathway 2** PA also achieved 100% fusion (Figure 5-7). This result was unexpected because several techniques show the breakage of long nanofibers upon freeze-drying (Figure 5-1, Figure 5-2b-c), and previous work from our laboratory has shown that long nanofibers support cell adhesion better than shorter ones.[103, 135] Thus, we conclude that while nanofiber length is an important factor, decreased length will not completely suppress their bioactivity. Despite the better performance of **pathway 3** PA *in-vitro* (Figure 5-6), it only achieved a 17% fusion rate *in-vivo*, in contrast to the 100% fusion rate achieved by both **pathway 1** and **pathway 2** PA (Figure 5-7). Since **pathway 3** scaffolds were highly porous compared to the other PA scaffolds, the data suggests that porosity is not an important factor for PA efficacy in promoting fusion. Perhaps degradation of the PA gels allows cell infiltration, even if the collagen pores are initially "clogged." Since **pathway 2** and **pathway 3** PA both show the ability to retain BMP-2 (Figure 5-6e), the growth factor release data alone explain the differences *in-vivo*. However, it is possible that the weaker PA gels of **pathway 3** degrade faster, causing the BMP-2 to be released must earlier. Taken together, the **pathway 1, 2,** and **3** data suggest that short, freeze dried PA nanofibers can be efficacious bone grafts for spinal fusion, if the proper freeze drying pathway is selected. For further optimization of freeze drying pathways, we note that *in-vitro* experimental results may not predict how the material will behave *in-vivo.*

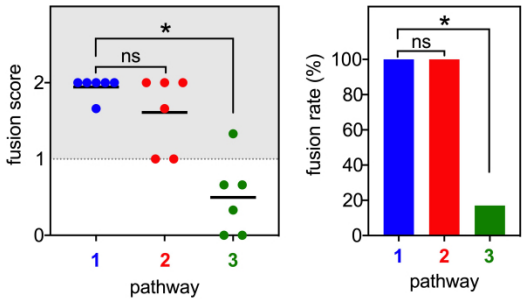

Figure 5-7: *In-vivo* efficacy of PA scaffolds. Fusion scores (one-way ANOVA, $p<0.0001$) and associated fusion rate (Fisher's exact test, $*p = 0.0152$) from a rat spinal fusion experiment, 8 weeks after treatment with 100 ng/rat BMP-2, delivered through indicated PA scaffolds.

5.3.6 Further Investigation of Freeze Drying Conditions

Since **pathway 2** and **pathway 3** PA differ in both solvent and processing steps (**pathway 2**: NaOH, annealed prior to freeze drying; **pathway 3**: NH_4OH, never annealed prior to freeze drying), we wanted to further examine the effects of these two variables. We dissolved PA to 1 wt% in either solvent, and processed them as indicated below.

1. NaOH, never annealed
2. NaOH, annealed prior to freeze drying - This is a slightly modified version of **pathway 2** PA, which was first dissolved to 2 wt% and immediately diluted to 1 wt% with pure water. This sample was instead simply dissolved to 1 wt%. The data in Figure 5-8a shows that this slight modification does not significantly change the PA gel's storage modulus. The trend between this "modified" pathway 2 PA and pathway 3 PA (Figure 5-8b) is similar to the trend between the original pathway 2 PA and pathway 3 PA (Figure 5-5k).
3. NH_4OH, never annealed - This is **pathway 3** PA.

4. NH_4OH, annealed prior to freeze drying

After dissolving the PA in the indicated solvent, and annealing if applicable, the PA solutions were freeze dried overnight. The PA powders were then rehydrated with pure water, and the 1 wt% PA solutions were analyzed by measuring their storage modulus (when gelled with $CaCl_2$). We chose to do rheology experiments because **pathway 2** and **pathway 3** PA showed drastically different storage moduli (Figure 5-5k).

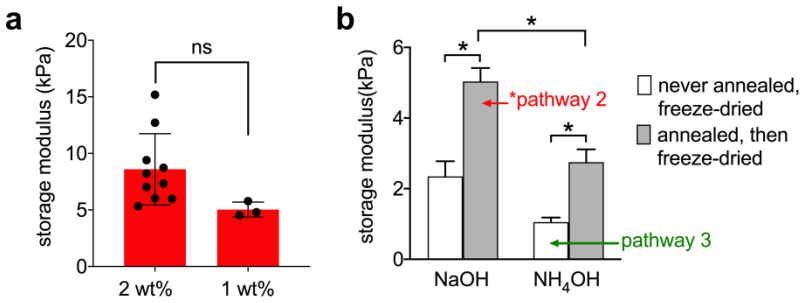

Figure 5-8: Effect of solvent and annealing prior to freeze drying. (a) Storage modulus of pathway 2 PA (dissolved to 2 wt% PA in NaOH, immediately diluted to 1 wt%, annealed, freeze-dried) compared to a slightly modified version of **pathway 2** PA (dissolved to 1 wt% PA in NaOH, annealed, freeze-dried). T-test, not significant. Error bars are standard deviation. (b) Storage modulus of PsA processed as indicated. The processing pathways that correspond to **pathway 2** and **pathway 3** are labeled. The asterisk indicates that this is a slight modification from **pathway 2**, as described in panel *a*. Two-way ANOVA, *p<0.05.

From Figure 5-8b, we see that both prior annealing and the choice of solvent affect the properties of the material. Even though freeze drying is known to break long nanofibers created by annealing (Figure 5-1), annealing prior to freeze drying results in stiffer PA gels regardless of solvent (Figure 5-8b). The solvent that the PA was dissolved in for freeze drying (all PAs are rehydrated with pure water to form a visually clear

solution) also has an effect, with NaOH resulting in stiffer PA gels (Figure 5-8b). The *in-vivo* studies showed that **pathway 2** PA, i.e. PA that had been dissolved in NaOH and annealed prior to freeze drying, achieves 100% fusion. This rheology data suggests that these exact processing conditions are necessary for this biological function, i.e. the PA must be dissolved in NaOH and annealed prior to freeze drying, even if freeze drying will break long nanofibers formed through annealing. It is possible that, although freeze drying breaks long nanofibers, the prior annealing step produces longer nanofibers than if the freeze dried sample had never been annealed. This may be due to some nanofibrous structures being preserved in the powder.

To further probe the effects of solvent and annealing on subsequently freeze dried samples, we performed Fourier-transform infrared spectroscopy (FTIR) on PA solutions. We prepared the following 1 wt% PA solutions, using deuterated solvents D_2O and NaOD to reduce solvent interference in the amide I/II region:

1. PA freshly dissolved in NaOD
2. PA freshly dissolved in NaOD, then freeze dried and rehydrated with D_2O
3. PA freshly dissolved in NaOD, then annealed (**pathway 1** PA, with minor modification: PA was dissolved directly to 1 wt% as opposed to 2 wt% and then diluted)
4. PA freshly dissolved in NaOD, then annealed, then freeze dried and rehydrated with D_2O (**pathway 2** PA, with minor modification: PA was dissolved directly to 1 wt% as opposed to 2 wt% and then diluted)
5. PA freshly dissolved in NH_4OH, then freeze dried and rehydrated with D_2O (**pathway 3** PA)

In the FTIR spectra of these samples (Figure 5-9), the peak around 1622 cm^{-1} likely corresponds to amides that are within a β-sheeted environment, whereas the peak around 1560 cm^{-1} likely corresponds to amides that are within a less ordered environment. As expected for $V_3A_3E_3$ PA, which is known to have high propensity for β-sheet formation due to the V_3A_3 peptide portion[75, 80], the peak at 1622 cm^{-1} is prominent in all solutions. Not surprisingly, the annealed sample (blue trace) qualitatively shows the largest peak, and it is known to contain long nanofibers with cohesive β-sheets.[103, 135]

However, the presence of the 1622 cm^{-1} peak in all samples suggests that, even as various processing steps may disrupt the self-assembled nanostructures formed by the PA, the ability of the PA molecules to form β-sheeted structure is not lost. This is consistent with previous work showing the self-repair capacity of PA nanofibers after disruption from freezing or freeze drying.[135] We note that the spectrum of the **freshly dissolved, freeze-dried NaOD** sample qualitatively similar to the spectrum of the **annealed, freeze-dried NaOD** sample, although these two samples had different storage moduli (Figure 5-8b). Thus, the FTIR data suggests that the difference in storage moduli (a bulk property) is not caused by differences at the molecular level, because both samples appear to be capable of β-sheet formation. Therefore, it is possible that annealing prior to freeze drying causes an increase in nanofiber length, compared to samples that have never been annealed. Although freeze drying will break the long nanofibers created by annealing, it is possible that they are still longer than if the PA had never been annealed. The *in-vivo* function (Figure 5-7) of each sample is labeled on the FTIR spectra, and it appears that the loss of some qualitative features upon freeze drying (i.e. the 1622 cm^{-1} peak becomes smaller) does not compromise bioactivity.

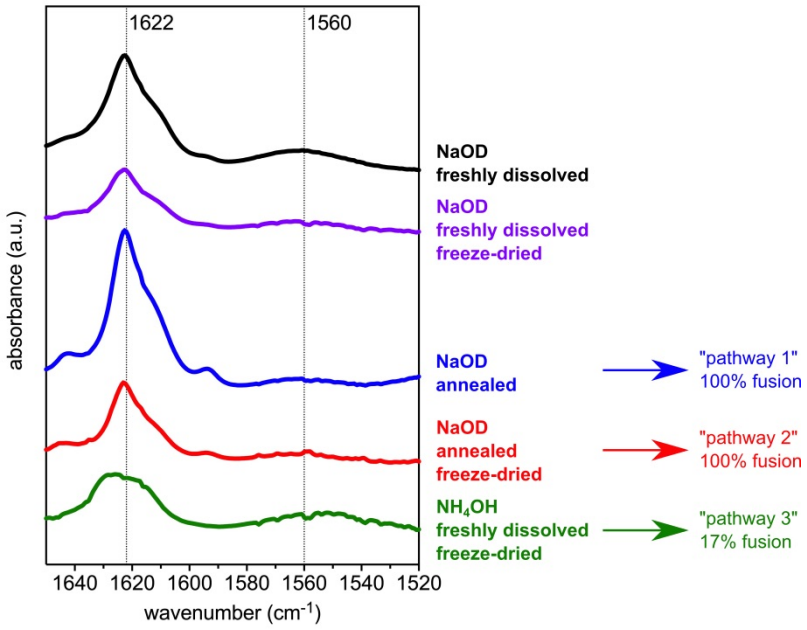

Figure 5-9: FTIR of 1 wt% PA solutions, processed as indicated.

5.4 CONCLUSIONS

We have identified a freeze drying pathway that does not compromise the PA's *in-vivo* efficacy in a rat spinal fusion model (**pathway 1** versus **2**), which was not obvious because freeze-drying drastically disrupts PA nanofibers. Specifically, both **pathways 1** and **2** produced PA that was capable of reducing the therapeutic BMP-2 dose 100 times *in-vivo*. Interestingly, not every freeze-drying pathway will result in PA assemblies with this desired biological function (**pathway 3**). Freeze dried PA immediately after rehydration can be considered a metastable state, where the system has not had time to equilibrate towards its thermodynamic minimum of long nanofibers. Indeed, both **pathway 2** and **pathway 3** PA contain shorter nanofibers than solutions that had been subjected to heat (**pathways 1, 4**) for equilibration. The *in-vivo* data suggests that not all

metastable positions in the energy landscape are equal, and that some can be significantly more bioactive than others (**pathway 2** versus **3)**. One possibility is that some nanofiber elongation occurs upon rehydration of PA powder, and under certain conditions and processing pathways (**pathway 2)**, this elongation is "enough" for biological function. This is encouraging for surgical applications such as spinal fusion, where materials must be ready to use with minimal preparation, so thermodynamic positions in the energy landscape will likely be inaccessible. In summary, this works suggests that, for certain clinical applications, PA assemblies should be designed for use in a metastable state. Kinetic barriers must be overcome to reach the global minimum, and the short preparation times allowed in surgical settings will not provide sufficient time or energy input. This concept is common in biology, where functional proteins are not necessarily the most thermodynamically stable configuration. We believe the ideas presented in this work can be applied to translating other supramolecular biomaterials with complex self-assembly energy landscapes.

5.5 MATERIALS AND METHODS

Peptide Synthesis

$V_3A_3E_3$ PA was synthesized using solid-phase peptide synthesis and purified using reverse high performance liquid chromatography, with the same procedure as described in Chapter 2.

Preparation of PA Solutions

Pathway 1 – $V_3A_3E_3$ PA was first dissolved to 2 wt% in 30 mM NaOH, and immediately diluted to 1 wt% with pure water. This PA solution, containing 1 wt% PA in 15 mM NaOH, was heated at 80°C for 30 minutes and then allowed to slow cool overnight.

Pathway 2 – Pathway 1 PA solutions were prepared as described above. These solutions were flash frozen in liquid nitrogen, and then transferred to a port-type freeze drier. This was always done in 1.7 mL Eppendorf tubes, where the volume of PA was always small enough to freeze completely after ≤ 30 seconds of submersion in liquid nitrogen, and to completely dry overnight. This powder was rehydrated with pure water to produce a 1 wt% PA solution.

Pathway 3 – $V_3A_3E_3$ PA was dissolved to 1 wt% in a solvent containing 1% NH_4OH and 15 mM NaCl. The 1% NH_4OH refers to the dilution of a concentrated NH_4OH solution (28 – 32%) to 1% volume/volume in water. This PA solution was freeze dried the same way as described for Pathway 2 PA. The resultant powder was rehydrated with pure water to produce a 1 wt% PA solution.

Pathway 4 – Pathway 3 PA solutions were prepared as described above. These solutions were heated at 80°C for 10 minutes and then cooled immediately by submersion in RT water.

Annealed PA with 5% Glycerol – $V_3A_3E_3$ PA was first dissolved to 2 wt% in 30 mM NaOH, and immediately diluted to 1 wt% with a 10% (v/v) glycerol solution. The glycerol solution was 10% volume glycerol in pure water. This PA solution, containing 1 wt% PA in 15 mM NaOH and 5% glycerol, was heated at 80°C for 30 minutes and then allowed to slow cool overnight.

Freeze Dried PA with 5% Glycerol – Annealed PA containing 5% glycerol was prepared as described above. These solutions were flash frozen in liquid nitrogen, and then transferred to a port-type freeze drier. This was always done in 1.7 mL Eppendorf tubes, where the volume of PA was always small enough to freeze completely after ≤ 30 seconds of submersion in liquid nitrogen, and to completely dry overnight. This solid - which is a sticky, "gooey" substance - was rehydrated with pure water to produce a 1 wt% PA solution.

Viscosity

Viscosity measurements were performed on an MCR 302 rheometer (Anton Paar, Graz, Austria). The CP25-2 fixture (25 mm diameter cone-plate) was used to analyze 200 μL of 1 wt% PA, with the rheometer plate set to 23°C. The shear rate was increased from 1–100 s^{-1} over 240 seconds, and the final viscosity at 100 s^{-1} is reported.

Polarized Light Microscopy

PA solutions at 1 wt% (50 μL) were pipetted onto glass slides and observed between cross-polarizers, set to 90°.

Cryogenic Transmission Electron Microscopy (CryoTEM)

Before use, 300-mesh copper grids with lacey carbon film (Electron Microscopy Sciences, Hatfield, PA, USA) were glow discharged for 30 seconds in a PELCO easiGlow system (Ted Pella, Inc., Redding, CA, USA). PA solutions (4 μL) were pipetted onto grids, blotted, and plunged into liquid ethane with an FEI Vitrobot Mark IV

(FEI, Hillsboro, OR, USA), maintained around 95% humidity. Pathway 1 PA, pathway 4 PA, annealed PA with 5% glycerol, and annealed/freeze dried PA with 5% glycerol were diluted 1:100 (volume:volume) in pure water before blotting, because highly viscous solutions cannot be blotted onto grids at 1 wt%. Pathway 2 and pathway 3 PA were blotted at 1 wt% with no dilutions, because they are less viscous. While submerged in liquid nitrogen, vitrified samples were transferred to a Gatan 626 cryo-holder (Gatan, Pleasanton, CA, USA) and imaged on a JEOL 1230 TEM operating at 100 kV. Liquid nitrogen temperatures were maintained during imaging, and micrographs were captured with a bottom-mounted Gatan 832 camera.

Creating PA Scaffolds on Collagen Spong

Before loading onto collagen sponges, 1 wt% PA was diluted 9:1 (volume:volume) in pure water to 0.9 wt%, to mimic experiments where BMP-2 is mixed with the PA and loaded onto the scaffolds. This PA solution (50 μL) was loaded onto cylindrical collagen scaffolds that measured 6 mm in diameter and 5 mm long. Helistat® collagen sponges (10 cm x 7.5 cm x 5 mm) were purchased from Integra LifeSciences (Plainsboro, NJ, USA), and a 6 mm biopsy punch was used to cut individual scaffolds for experiments. After the PA solutions were loaded onto collagen sponges, 50 μL of 30 mM $CaCl_2$ was added to the scaffold to induce gelation of PA. To maximize absorption of solutions into the collagen sponge, all loading steps were done with the collagen sponge on Parafilm®. The Parafilm® repels liquid, so it will not wick the solutions away from the porous sponge.

Scanning Electron Microscopy (SEM)

Collagen/PA scaffolds were created as described above. To prepare the scaffolds for SEM imaging, they were subject to a gradual ethanol exchange followed by critical point drying. They were submerged in ethanol-water solutions containing gradually increasing amounts of ethanol: 10 minutes at 30%, 40%, 50%, 60%, 70%, 80%, 90%, and 95% EtOH, and then 15-20 minutes at 100% EtOH. Using a Samdri-795 critical point dryer (Tousimis, Rockville, MD, USA), dehydrated gels were purged with supercritical CO_2 for 10 minutes and then dried through the critical point of CO_2. Dried samples were mounted onto carbon tape, with a small drop of carbon paste in between the tape and sample to improve adhesion. To enhance conductivity, samples were coated with either 16 nm of osmium metal using an SPI Osmium Coater (SPI Supplies, West Chester, PA, USA), or 15 nm of gold-palladium (Au-Pd) using a Denton III Desk Sputter Coater (Denton Vacuum, Moorestown, NJ, USA). Coated samples were imaged with a Hitachi SU-8030 SEM (Hitachi, Tokyo, Japan) operating at 2.0 kV.

MC3T3 Cell Culture

MC3T3-E1 subclone 4 mouse preosteoblasts (ATCC, Manassas, VA, USA) were maintained using standard cell culture techniques, in Alpha Minimum Essential Medium (αMEM, Catalog No. A1049001, GIBCO [Thermo Fisher] Waltham, MA, USA) supplemented with 10% fetal bovine serum (FBS, Denville Scientific, South Plainfield, NJ, USA), 100 U/mL penicillin, and 100 μg/mL streptomycin (Pen Strep, GIBCO). FBS was heat-inactivated before use. Cells were passaged using 0.25% trypsin (GIBCO), and used for experiments at passages 5-7.

Seeding MC3T3 Cells onto Collagen/PA Scaffolds

Collagen/PA scaffolds were created as described above, and transferred to a 96-well cell culture plate. MC3T3 cells were seeded onto the scaffolds, at 40,000 cells/scaffold, suspended in 30 μL of αMEM cell media. The cells (40,000 cells/30 μL) were allowed to physically settle onto the scaffolds for 5 minutes before 120 μL of αMEM media was added to the well (total 150 μL cell media/well). Cells were then incubated for 4 hours at 37°C. Before staining for actin or MTS assay analysis, the scaffolds were washed in 2x in PBS. After each PBS wash, the scaffolds were gently placed on a Kimwipe to remove liquid inside the scaffold.

Cytoskeleton Staining

After the 4-hour incubation, cells were fixed in 4% paraformaldehyde and then permeabilized with 0.4% Triton X and 2% bovine serum albumin, both for 30 minutes at room temperature. Cells were then stained by incubating gels with a 1:200 dilution of Alexa Fluor 488 phalloidin (Molecular Probes), overnight at 4°C. All solutions were dissolved in PBS w/ $CaCl_2$, which was also used to rinse samples three times between all steps. After phalloidin staining, the scaffold surfaces were imaged using the 20x objective of a Nikon AIR confocal microscope. The images shown are maximum intensity projections of 25 μm z-stacks.

MTS Assay

In this assay, MTS [3-(4,5-Dimethylthiazol-2-yl)-5-(3-carboxymethoxyphenyl)-2-(4-sulfophenyl)-2H-tetrazolium)] was used to detect the presence of cell metabolic

activity. MC3T3 cells were seeded onto collagen/PA scaffolds as described above. After the 4-hour incubation and PBS washes, the scaffolds with adhered cells were returned to 96-well plates and incubated with 150 μL of MTS working solution for 1 hour at 37°C. The MTS working solution was prepared and the incubation carried out according to the manufacturer's instructions (CellTiter 96® AQueous MTS Reagent Powder, Promega, Madison, WI, USA). After incubation, 100 μL of MTS working solution was harvested, centrifuged to remove PA that may have become dislodged from the scaffolds, and the absorbance at 490 nm read on a Cytation^{TM}3 (BioTek, Winooski, VT, USA). Blank scaffolds with PA on collagen but no cells were prepared in each PA condition, and the experiment was carried out the same way. The absorbance of these blanks was subjected from the absorbance of the samples.

Rheological Properties of PA Gels

Rheological analysis of PA gels was performed using an MCR 302 rheometer (Anton Paar, Graz, Austria), using a 25 mm cone-plate fixture (CP25-2). PA solutions (1 wt% PA, 150 μL) were loaded onto the rheometer plate, set to 23°C. To induce gelation of the PA, 50 μL of 30 mM $CaCl_2$ was pipetted onto the CP25-2 fixture in small droplets, as evenly spread as possible. Gelation was initiated when the fixture came into contact with the sample for the measurement. The gel was equilibrated for 25 minutes (1500 seconds) at constant strain (0.1%) and angular frequency (10 rad/sec), and the final storage modulus is reported.

C2C12 Cell Culture

C2C12 mouse myoblasts (ATCC, Manassas, VA, USA) were maintained using standard cell culture techniques, in Dulbecco's Modified Eagle's Medium (DMEM, Catalog No. 30-2002, ATCC, Manassas, VA, USA) supplemented with 10% fetal bovine serum (FBS, GIBCO [Thermo Fisher] Waltham, MA, USA), 100 U/mL penicillin, and 100 μg/mL streptomycin (Pen Strep, GIBCO). FBS was heat-inactivated before use. Cells were passaged using 0.05% trypsin (GIBCO), and used for experiments at passages 4-5.

Treat C2C12 Cells with BMP-2 in Scaffold

Since both cells and BMP-2 solution had to be mixed with PA, PA solutions were prepared at 1.1 wt% instead of 1 wt%. Otherwise, they were prepared as described above. A 20,000 ng/mL BMP-2 solution was created by diluting the 1.5 mg/mL BMP-2 stock (INFUSE™, Medtronic Sofamor Danek, Memphis, TN, USA) 75x with pure water. An 80,000 cells/μL C2C12 suspension in DMEM was also created. Next, the 1.1 wt% PA solution, BMP-2 solution, and cell suspension was mixed in a 10:1:1 volume ratio, such that the final PA concentration was 0.9166 wt%. For controls with no BMP-2, pure water was added instead of the BMP-2 solution.

Helistat® collagen sponges (10 cm x 7.5 cm x 5 mm) were purchased from Integra LifeSciences (Plainsboro, NJ, USA), and a 6 mm biopsy punch was used to cut individual scaffolds for experiments (6-mm diameter by 5 mm length). The solution containing PA, cells, and BMP-2 (60 μL) was loaded onto cylindrical collagen scaffolds that measured 6 mm in diameter and 5 mm long. To maximize absorption of solutions

into the collagen sponge, all loading steps were done with the collagen sponge on Parafilm®. The Parafilm® repels liquid, so the surface will not wick the solutions away from the porous sponge. To sterilize the Parafilm®, it was exposed to ultraviolet (UV) light within a tissue culture hood for 10 minutes. Thus, cells were encapsulated at 400,000 cells/scaffold and BMP-2 was encapsulated at 100 ng/scaffold. Next, a salt solution (40 μL) containing 37.5 mM $CaCl_2$ and 187.5 mM NaCl was applied to the scaffolds to induce gelation of PA and to adjust the scaffold to physiological ionic strength. These scaffolds with encapsulated cells and BMP-2 were placed into 48-well plates, and surrounded with 1 mL of DMEM media.

Treat C2C12 Cells with BMP-2 in Cell Media

PA solutions with 1 wt% PA were prepared as described above. An 80,000 cells/μL C2C12 cell suspension in DMEM was created. PA was mixed with cells in a 9:1 volume ratio, such that the final PA concentration was 0.9 wt%. Helistat® collagen sponges (10 cm x 7.5 cm x 5 mm) were purchased from Integra LifeSciences (Plainsboro, NJ, USA), and a 6 mm biopsy punch used to cut individual scaffolds for experiments (6-mm diameter by 5 mm length). The solution containing PA, cells, and BMP-2 (50 μL) was loaded onto cylindrical collagen scaffolds that measured 6 mm in diameter and 5 mm long. To maximize absorption of solutions into the collagen sponge, all loading steps were done with the collagen sponge on Parafilm®. The Parafilm® repels liquid, so the surface will not wick the solutions away from the porous sponge. To sterilize the Parafilm®, it was exposed to ultraviolet (UV) light within a tissue culture hood for 10 minutes. Thus, cells were encapsulated at 400,000 cells/scaffold. Next, a salt solution

(50 μL) containing 30 mM $CaCl_2$ and 150 mM NaCl was applied to the scaffolds to induce gelation of PA and to adjust the scaffold to physiological ionic strength. For samples containing no PA and only the collagen sponge, 400,000 C2C12 cells were suspended in 100 μL of DMEM, which was loaded onto the collagen sponge. These scaffolds with encapsulated cells and BMP-2 were placed into 48-well plates, and surrounded with 1 mL of DMEM media. The cells were allowed to equilibrate overnight before they were exposed to DMEM media containing BMP-2.

To make the BMP-2 treatment media, a 1.5 mg/mL BMP-2 stock (INFUSE™, Medtronic Sofamor Danek, Memphis, TN, USA) was diluted 100x in pure water to obtain a 15,000 ng/mL BMP-2 solution. This solution was further diluted in DMEM media containing 2.5% FBS, such that the final BMP-2 concentration was 100 ng/mL. The FBS content was reduced from the usual 10% to 2.5% because serum proteins can interfere with growth factor signaling. Scaffolds containing cells were then transferred to BMP-2 treatment media, in a 48-well dish surrounded by 1 mL of media.

ALP Colorimetric Assay

After 3 days of incubation with BMP-2, either in the scaffold of in the media, the ALP activity in cells was analyzed. Scaffolds were rinsed in PBS and then gently placed onto a Kimwipe to soak up excess liquid. This PBS wash followed by removing excess liquid was repeated twice. The scaffolds were then placed into Eppendorf tubes and subjected to two freeze-thaw cycles, where they were submerged in liquid nitrogen to freeze and then submerged in room temperature water to thaw. These freeze-thawing steps were done to rupture the cell membranes and disrupt the PA gel, to aid in extracting

the ALP. While the scaffold was thawing during the second freeze-thaw cycle, 100 μLof M-Per™ Buffer (Thermo Fisher, Waltham, MA, USA) containing Halt™ Protease Inhibitor (Thermo Fisher, Waltham, MA, USA) was added to the scaffold. The scaffolds were then horn sonicated to further disrupt the cell membranes and PA gel, to maximize extraction of ALP into M-Per™ buffer. Following horn sonication, forceps were used to squeeze the scaffolds against the sides of the Eppendorf tubes, in order to remove as much liquid as possible from the scaffolds. The scaffolds were then discarded. The M-Per™ buffer containing extracted proteins was centrifuged at 13.2 rpm for 2 minutes. The supernatant (50 μL) was then analyzed for ALP activity using a SensoLyte® pNPP Alkaline Phosphate Kit (AnaSpec, Fremont, CA, USA).

ALP Staining

C2C12 cells were encapsulated in PA/collagen scaffolds and treated with BMP-2 in the cell media, as described above. After a 3-day incubation with BMP-2, ALP-positive cells were visualized using a Stemgent® Alkaline Phosphatase Staining Kit II (Stemgent, Cambridge, MA, USA), following the manufacturer's instructions. Due to the 3D nature of the experiment, the color change took longer than the manufacturer-recommended 5–15 minutes, which was likely optimized for cells in 2D culture. Instead, the color change took around 1-2 hours to develop. Furthermore, we note that this experiment would only detect ALP-positive cells at the surface of the scaffolds, because collagen scaffolds are optically dense.

ELISA (Enzyme-Linked Immunosorbent Assay) for BMP-2 Releases

A 6-mm biopsy punch was used to cut individual scaffolds (6-mm diameter by 5 mm length) out of a Helistat® collagen sponge sheet (10 cm x 7.5 cm x 5 mm, Integra LifeSciences, Plainsboro, NJ, USA). PA solutions at 1 wt% were prepared, and a BMP-2 solution was prepared by diluting a 1.5 mg/mL stock (INFUSE™, Medtronic Sofamor Danek, Memphis, TN, USA) to 20,000 ng/mL in pure water. The PA and diluted BMP-2 solutions were mixed in a 9:1 volume ratio, such that the resultant solution contained 0.9 wt% PA and 2000 ng/mL BMP-2. This PA/BMP-2 mixture (50 μL) was added to the individual collagen scaffolds, so the scaffolds were loaded with 100 ng of BMP-2. The PA was then gelled by adding 50 μL of 30 mM $CaCl_2$ to the collagen scaffold. The addition of PA/BMP-2 and $CaCl_2$ solutions to the collagen scaffolds were done on Parafilm®, which has a hydrophobic surface that does not wick away liquid from the porous sponge. For samples with no PA, the 20,000 ng/mL BMP-2 solution was further diluted 20x to 1000 ng/mL with pure water. This solution (100 μL) containing BMP-2 and no PA was added to a collagen scaffold. All these scaffolds containing BMP-2 were allowed to equilibrate at room temperature for 15 minutes, after which they were placed into 2 mL Eppendorf tubes. Release media (0.1% BSA in PBS, 1 mL) was added to each tube. At each time point, 700 μL of the release media was extracted, and replaced with 700 μL of fresh release media. The extracted samples were stored at -80°C until analysis by ELISA. BMP-2 in the samples was detected using a Human BMP-2 DuoSet ELISA kit (Catalog No. DY355-05, R&D Systems) following the manufacturer's instructions.

Rat Posterolateral Lumbar Intertransverse Spinal Fusion

Helistat® collagen sponges (10 cm x 7.5 cm x 5 mm) were purchased from Integra LifeSciences (Plainsboro, NJ, USA), and 1.5 cm x 0.5 cm x 5 mm (original thickness) scaffolds were cut from these sponges using a sharp blade. PA solutions at 1 wt% were prepared, and a 1.5 mg/mL BMP-2 stock solution (INFUSE™, Medtronic Sofamor Danek, Memphis, TN, USA) was diluted 399x with pure water to 3759.4 ng/mL BMP-2 (2 μL BMP-2 + 796 μL water). The PA and diluted BMP-2 solutions were mixed in a 9:1 volume ratio, such that the final solution contained 0.9 wt% PA and 50 ng BMP/133 μL of solution. This volume (133 μL) will be loaded onto each scaffold, so with each rat receiving two scaffolds (one per side of spine), each rat receives 100 ng BMP-2 total. The scaffolds were placed onto Parafilm®, and 133 μL of PA/BMP-2 solution was added to the scaffold, followed by 133 μL of 30 mM $CaCl_2$ to induce gelation of PA. Adding 133 μL of PA/BMP-2 solution to 1.5 cm x 0.5 cm x 0.5 cm scaffolds achieves a similar PA:collagen ratio as the *in-vitro* experiments (50 μL PA on 6-mm diameter x 5 mm long cylindrical discs). The Parafilm® provided a hydrophobic surface that does not wick away liquid from the porous sponge. The experimental groups tested were: 1) Pathway 1 PA scaffolds + 100 ng BMP-2/rat; 2) Pathway 2 PA scaffolds + 100 ng BMP-2/rat; 3) Pathway 3 PA scaffolds + 100 ng BMP-2/rat.

This study was approved by the Institutional Animal Care and Use Committee (IACUC), and carried out within its policies. Scaffolds were implanted between the L4-L5 transverse processes of female Sprague-Dawley rats aged 12-16 weeks, using an established surgical technique.[107, 108] This study consisted of 18 rats, with 6 randomly assigned to each of the three experimental groups. During surgery, the rats were

maintained on heating pads and a continuous isoflurane inhalational anesthetic delivery system, and monitored for respiratory or cardiac difficulties. The L4-L5 transverse processes were exposed through a posterior midline incision, followed by two fascial incisions 4 mm from the midline on either side. A blunt instrument was used to dissect the muscle and expose the periosteum of the spine. After exposure, the L4-L5 transverse processes were irrigated with a sterile gentamicin/saline solution, and the cortical layer was decorticated using a high speed burr. The scaffolds were implanted bilaterally between L4-L5, within the paraspinal musculature. The fascial incisions were closed with closed using 3-0 Monocryl absorbable sutures, and the skin incision closed using wound clips. After surgery, the rats were housed in separate cages.

Eight weeks post-surgery, rats were euthanized and the spines were harvested. Harvested spines were placed into 10% Neutral Buffered Formalin for 7 - 10 days, followed by incubation in 50% EtOH for 2 hours, and then stored in 70% EtOH until analysis. Using an established method, spines were scored with manual palpitation by blinded observers, and the average score of three independent observers is reported. The scoring system is as follows: 0 = no bridging; 1 = unilateral bridging; and 2 = bilateral bridging. To calculate fusion rates, rats receiving a score $\geq$1 were considered fused. The fusion rate is the percentage of animals that are successfully fused.

Fourier-Transform Infrared Spectroscopy

PA solutions (40 μL) were placed between two CaF_2 windows with a 50 μm PTFE spacer. A Bruker Tensor 37 FTIR Spectrometer was used to collect IR spectra of these

samples from 400 – 4000 cm^{-1} at a resolution of 1 cm^{-1}, averaging 25 scans. The spectra from the region 1520 – 1650 cm^{-1} is plotted.

6 CONCLUSION

6.1 CH 2: SELF-SORTING IN SUPRAMOLECULAR ASSEMBLIES

One advantage of supramolecular biomaterials is the allowance for *modular* design.[2, 17-19] Supramolecular structures can be modulated by tuning the individual molecules participating in nanoscale self-assembly, enabling a "bottom-up" design approach. This is in contrast to the processing of existent materials into therapeutic products; for example, when collagen (Helistat®, Integra LifeSciences), alginate (Tegaderm™, 3M), or cellulose (Nanoderm™, Axcelon Biopolymers Corporation) are harvested and processed into wound dressings, their nanoscale features cannot be fine-tuned. One example of modular design is the creation of multicomponent supramolecular systems, where two or more rationally chosen molecules are allowed to self-assemble together, under rationally chosen molar ratios and conditions.[2, 17-19, 98, 99] While the use of multiple components allows greater diversity in material design, our knowledge of multicomponent self-assembly is incomplete. Specifically, the factors that drive different molecules to self-sort or co-assembly are not completely understood, although there is literature that offers some insights.[51, 129-133] In our specific PA platform, this is particularly relevant in materials where diluent PA molecules are combined with epitope-bearing PA molecules.[98, 99, 108, 111]

In Chapter 2, a multicomponent PA system was presented and a condition that promoted self-sorting was identified. FITC- and TAMRA-conjugated PA were mixed with diluent PA bearing no fluorophore, with the diluent PA in molar excess of the two fluorescent PAs. All three PAs contained negatively charged headgroups. FRET and

confocal imaging experiments showed that, in conditions of relatively low ionic strength, FITC-conjugated PA segregated from TAMRA-conjugated PA. This result was surprising because no molecular recognition motifs exist to promote self-sorting, since FITC- and TAMRA are attached to the same PA backbone, which is identical to the diluent PA except for a lysine linker to attach the fluorophore. FRAP experiments showed that FITC-conjugated PA was highly mobile while TAMRA-conjugated PA was immobile, when both PAs were surrounded by diluent PA nanostructures. This suggests that FITC-conjugated PA cannot associate strongly with the negatively charged diluent PA assemblies, which is likely due to the -2 charge of the FITC fluorophore. The FITC-conjugated PA remains in the solution around the diluent PA nanofibers, and are thus highly mobile by FRAP. Conversely, TAMRA is zwitterionic so TAMRA-conjugated PA can co-assemble with the diluent PA matrix. When the solution's ionic strength was increased with addition of NaCl, providing Na^+ ions to screen the PA's negative charges, self-sorting was suppressed. This was accompanied by lower mobility of FITC-conjugated PA, which can now associate with the diluent PA nanofibers and mix with the TAMRA-conjugated PA. In summary, the "self-sorting" is mediated by interactions with a supramolecular matrix, which the self-sorted species differentially associate with. Compared to the current literature that focuses on molecular recognition events, this work proposes a different mechanism for supramolecular self-sorting.

Multicomponent PA systems are often created when epitope-bearing PAs are mixed with diluent PAs. In this study, the "epitope-bearing" PAs contained pendant fluorophores (FITC or TAMRA), which were originally presumed to be much simpler than bioactive peptide chains. Although peptide-based epitopes will behave differently

than small molecule fluorophores, this work presents some insights for mixing epitope-bearing PAs with diluent PAs. Specifically, the charge of the epitope relative to the diluent PA should be considered, in the context of the specific solvent conditions.

6.2 CH 3: CELL DEATH MEDIATED BY ALKYL TAIL PLACEMENT

While Chapter 2 revealed complexity in multicomponent supramolecular systems, Chapter 3 focused on single component systems and demonstrated complexity in molecular design rules. Built from non-covalent interactions that can be modulated, supramolecular biomaterials have the advantage of being *highly tunable*.[8-11] Unlike the static covalent bonds in polymers, non-covalent interactions have a characteristic equilibrium association constant (K_{eq}), which is affected by the association (k_a) and dissociation (k_d) constants. These parameters can be fine-tuned to achieve desired material properties, if the link between molecular design and supramolecular interactions is thoroughly understood. Chapter 3 showed that miniscule alterations to cationic PA molecules had significant consequences for their cytotoxic properties.

Similar to previous reports,[75] cationic PAs with weak supramolecular cohesion were cytotoxic while similar PAs with strong supramolecular were not. Building from this result, experiments in Chapter 3 showed that alkyl tail placement and peptide polarity affected the cytotoxic properties of PA assemblies. As shown by time course experiments, cationic PAs with the alkyl tail at the N-terminus rapidly exerted cytotoxic effects, while cationic PAs with the alkyl tail at the C-terminus killed cells more slowly. The faster cell death is likely caused by immediate physical disruption of the cell membrane, but the slower cell death must occur through a slower process. Mechanistic

studies linked the slower cell death to an oncotic mechanism, where PA nanostructures sequester cholesterol from the plasma membrane, initiating signaling pathways that lead to programmed cell death. Interestingly, changing the polarity of the lysine linker between the alkyl tail and the peptide sequence suppressed cholesterol sequestration and rescued cell viability. In summary, these cationic PAs were tuned at the nanoscale with small alterations to molecular design, by changing the alkyl tail placement and thus peptide polarity, hydrogen bonding sequence, or lysine linker polarity. These nanoscale changes changed the internal structure of the PA assemblies, which then exerted differential effects on micron-scale cell membranes.

Interestingly, different cell membrane interactions (physical disruption versus cholesterol sequestration versus no interaction) were achieved with different supramolecular assemblies. This deviates from the conventional wisdom that cationic species disrupt negatively charged cell membrane solely through electrostatic interactions.[75-79] Similar phenomenon likely occurs in other supramolecular structures that interface with the supramolecular lipid bilayer of cell membranes.

6.3 CH 4: SELF-REPAIR OF SUPRAMOLECULAR NANOSTRUCTURES

The inherent *reversibility*[9, 16, 88] of non-covalent bonds is often touted as an advantage of supramolecular biomaterials, and can be used to design self-healing materials[58, 61, 62, 199-203, 237] or materials that can be altered to differentially induce biological behaviors.[73, 238, 239] While non-covalent reversibility has been exploited to mend mechanical defects[58, 61, 62, 199-203, 237], the possibility of repairing incorrectly self-

assembled structures has not been explored. One major cause for defective supramolecular structures is incorrect choice of self-assembly pathway,[101-103] leading to encounters with kinetic traps and non-functional energy landscape positions. While faulty self-assembly pathways should be avoided when possible, some processing steps may be necessary for large-scale applications such as clinical translation. In the case of PAs, they must be preserved with freezing or freeze drying for large-scale applications such as clinical use, because their self-assembled structures are highly dynamic in solution.

The results presented in Chapter 4 show that freezing and freeze drying can indeed cause structural and functional damage to supramolecular structures. Specifically, long nanofibers, known to be favorable for supporting cell adhesion,[103] break into shorter ones during freezing or freeze drying. This was confirmed by several techniques, including rheological, spectroscopic, and microscopy experiments. Importantly, cells encapsulated in short, freeze-damaged PA nanofiber gels did not spread as well as cells in longer PA nanofiber gels. The long nanofibers can be recovered, as well as their ability to support cell adhesion, by subjecting the PA to a previously reported annealing cycle. Long nanofibers are thermodynamically preferred, and annealing overcomes the energy barrier to reach the global minimum, although kinetic traps can impede the process. Certain processing steps (i.e. freeze drying) can shift the global minimum of the system by changing the charge density on the PA, which further complicates self-repair.

In conclusion, Chapter 4 offers the following insights for optimizing the self-repair capacity of supramolecular structures: The desired structures should be designed as a thermodynamic minimum, to which the system can return to after damage. The damaged

states are then kinetic traps, which are ideally not deep wells, and viable self-assembly pathways should exist between the "damaged" kinetic traps and "repaired" global minimum. Importantly, this work was conducted on a system with a single PA molecule, and these results are likely generalizable to other single component supramolecular systems. However, based on the work in Chapter 2, multicomponent systems may have more complicated energy landscapes that can complicate the repair process. For example, it is possible that multicomponent nanofibers will re-elongate after breakage, but the configuration of the different molecules may be different after "repair."

6.4 CH 5: A PEPTIDE AMPHIPHILE BONE GRAFT FOR SPINAL FUSION

Following from work in Chapter 4, Chapter 5 presented a freeze dried PA formulation for a specific clinical application. In preclinical models, PAs have shown promise to be effective bone grafts for spinal fusion surgeries, which can reduce the need for supraphysiological doses of recombinant BMP-2.[107, 108] The freeze dried PA formulation reduced the therapeutic BMP-2 dose 100x in a rat spinal fusion model, on par with PA that had not been freeze dried for preservation. Scientifically, this result was surprising because freeze drying noticeably broke long PA nanofibers into shorter ones, and longer nanofibers are known to be more effective at supporting cell adhesion.[103, 135] The short nanofibers in this freeze dried PA can be considered a functional metastable state in the PA's energy landscape. A non-functional metastable state, formed through another freeze drying pathway, was also identified.

Although Chapter 4 reported the self-repair capacity of PA nanofibers, it is a kinetically limited process, requiring an annealing cycle for nanofiber elongation to proceed. Long and cumbersome preparation procedures are not permitted in the operating room, so the PA must be ready to use immediately after rehydration of the freeze dried powder. Supplying pre-prepared PA nanofibers in solution is not ideal, because their non-covalent nature makes them dynamic and susceptible to change over time. Comparable surgical products have a shelf-life on the order of a few years. Therefore, the ability to freeze dry PA without compromising its bioactivity significantly improves its potential for clinical translation.

Thus, despite the challenges posed by dynamic non-covalent bonds, particularly in causing pathway dependence, a PA formulation compatible with surgical procedures was generated. Indeed, this formulation was of a well-studied PA molecule in a single component system, but more complex materials may be developed if their non-covalent interactions are thoroughly understood and controlled. The same non-covalent interactions that enable the advantages of supramolecular biomaterials (i.e. highly tunable, reversible, responsive, modular) are the same non-covalent interactions that give rise to complex pathway dependence behavior and energy landscapes, which are currently much easier to manage in single component systems. Looking beyond the PA platform described in this work, this thesis suggests that supramolecular biomaterials have the capacity to become clinical therapies, and the capacity to precisely tune their non-covalent interactions is vital to realizing this potential.

REFERENCES

1. Langer, R.; Tirrell, D. A. Designing materials for biology and medicine. *Nature.* **2004** 428(6982), 487-492.

2. Webber, M. J.; Appel, E. A.; Meijer, E.; Langer, R. Supramolecular biomaterials. *Nature Materials.* **2016** 15(1), 13-26.

3. Huebsch, N.; Mooney, D. J. Inspiration and application in the evolution of biomaterials. *Nature.* **2009** 462(7272), 426-432.

4. Jokinen, J.; Dadu, E.; Nykvist, P.; Käpylä, J.; White, D. J.; Ivaska, J.; Vehviläinen, P.; Reunanen, H.; Larjava, H.; Häkkinen, L. Integrin-mediated cell adhesion to type I collagen fibrils. *Journal of Biological Chemistry.* **2004** 279(30), 31956-31963.

5. Harburger, D. S.; Calderwood, D. A. Integrin signalling at a glance. *Journal of Cell Science.* **2009** 122(2), 159-163.

6. Zeltz, C.; Gullberg, D. The integrin–collagen connection–a glue for tissue repair? *Journal of Cell Science.* **2016** 129(4), 653-664.

7. Desiraju, G. R. Chemistry beyond the molecule. *Nature.* **2001** 412(6845), 397.

8. Appel, E. A.; Forster, R. A.; Koutsioubas, A.; Toprakcioglu, C.; Scherman, O. A. Activation energies control the macroscopic properties of physically cross-linked materials. *Angewandte Chemie International Edition.* **2014** 53(38), 10038-10043.

9. Wojtecki, R. J.; Meador, M. A.; Rowan, S. J. Using the dynamic bond to access macroscopically responsive structurally dynamic polymers. *Nature Materials.* **2011** 10(1), 14-27.

10. Yount, W. C.; Loveless, D. M.; Craig, S. L. Small-molecule dynamics and mechanisms underlying the macroscopic mechanical properties of coordinatively cross-linked polymer networks. *Journal of the American Chemical Society.* **2005** 127(41), 14488-14496.

11. Yount, W. C.; Loveless, D. M.; Craig, S. L. Strong means slow: Dynamic contributions to the bulk mechanical properties of supramolecular networks. *Angewandte Chemie International Edition.* **2005** 44(18), 2746-2748.

12. Aggeli, A.; Bell, M.; Boden, N.; Keen, J.; Knowles, P.; McLeish, T.; Pitkeathly, M.; Radford, S. Responsive gels formed by the spontaneous self-assembly of peptides into polymeric β-sheet tapes. *Nature.* **1997** 386(6622), 259-262.

13. Banwell, E. F.; Abelardo, E. S.; Adams, D. J.; Birchall, M. A.; Corrigan, A.; Donald, A. M.; Kirkland, M.; Serpell, L. C.; Butler, M. F.; Woolfson, D. N. Rational design and application of responsive α-helical peptide hydrogels. *Nature Materials.* **2009** 8(7), 596-600.

14. Beck, J. B.; Rowan, S. J. Multistimuli, multiresponsive metallo-supramolecular polymers. *Journal of the American Chemical Society.* **2003** 125(46), 13922-13923.

15. Schneider, J. P.; Pochan, D. J.; Ozbas, B.; Rajagopal, K.; Pakstis, L.; Kretsinger, J. Responsive hydrogels from the intramolecular folding and self-assembly of a designed peptide. *Journal of the American Chemical Society.* **2002** 124(50), 15030-15037.

16. Sijbesma, R. P.; Beijer, F. H.; Brunsveld, L.; Folmer, B. J.; Hirschberg, J. K.; Lange, R. F.; Lowe, J. K.; Meijer, E. Reversible polymers formed from self-complementary monomers using quadruple hydrogen bonding. *Science.* **1997** 278(5343), 1601-1604.

17. Hudalla, G. A.; Sun, T.; Gasiorowski, J. Z.; Han, H.; Tian, Y. F.; Chong, A. S.; Collier, J. H. Gradated assembly of multiple proteins into supramolecular nanomaterials. *Nature Materials.* **2014** 13(8), 829-836.

18. Mollet, B. B.; Comellas-Aragonès, M.; Spiering, A. J. H.; Söntjens, S. H. M.; Meijer, E. W.; Dankers, P. Y. W. A modular approach to easily processable supramolecular bilayered scaffolds with tailorable properties. *Journal of Materials Chemistry B.* **2014** 2(17), 2483-2493.

19. Wisse, E.; Spiering, A. J. H.; Dankers, P. Y. W.; Mezari, B.; Magusin, P. C. M. M.; Meijer, E. W. Multicomponent supramolecular thermoplastic elastomer with peptide-modified nanofibers. *Journal of Polymer Science Part A: Polymer Chemistry.* **2011** 49(8), 1764-1771.

20. Bangham, A. D.; Horne, R. W. Negative staining of phospholipids and their structural modification by surface-active agents as observed in the electron microscope. *Journal of Molecular Biology.* **1964** 8(5), 660-668.

21. Bangham, A. D.; Standish, M. M.; Watkins, J. C. Diffusion of univalent ions across the lamellae of swollen phospholipids. *Journal of Molecular Biology.* **1965** 13(1), 238-252.

22. Bangham, A. D.; Horne, R. W.; Glauert, A. M.; Dingle, J. T.; Lucy, J. A. Action of saponin on biological cell membranes. *Nature.* **1962** 196, 953-955.

23. Barenholz, Y. Doxil(R)--the first FDA-approved nano-drug: lessons learned. *Journal of Controlled Release.* **2012** 160(2), 117-134.

24. Henry, B. D.; Neill, D. R.; Becker, K. A.; Gore, S.; Bricio-Moreno, L.; Ziobro, R.; Edwards, M. J.; Mühlemann, K.; Steinmann, J.; Kleuser, B.; Japtok, L.; Luginbühl, M.; Wolfmeier, H.; Scherag, A.; Gulbins, E.; Kadioglu, A.; Draeger, A.; Babiychuk, E. B. Engineered liposomes sequester bacterial exotoxins and protect from severe invasive infections in mice. *Nature Biotechnology.* **2014** 33(1), 81-88.

25. Lasic, D. D.; Needham, D. The “stealth" liposome: A prototypical biomaterial. *Chemical Reviews.* **1995** 95(8), 2601-2628.

26. Sekine, Y.; Moritani, Y.; Ikeda-Fukazawa, T.; Sasaki, Y.; Akiyoshi, K. A hybrid hydrogel biomaterial by nanogel engineering: Bottom-up design with nanogel and liposome building blocks to develop a multidrug delivery system. *Advanced Healthcare Materials.* **2012** 1(6), 722-728.

27. Yatvin, M. B.; Weinstein, J. N.; Dennis, W. H.; Blumenthal, R. Design of liposomes for enhanced local release of drugs by hyperthermia. *Science.* **1978** 202(4374), 1290-1293.

28. Aggeli, A.; Bell, M.; Boden, N.; Keen, J. N.; Knowles, P. F.; McLeish, T. C. B.; Pitkeathly, M.; Radford, S. E. Responsive gels formed by the spontaneous self-assembly of peptides into polymeric β-sheet tapes. *Nature.* **1997** 386(6622), 259-262.

29. Aggeli, A.; Nyrkova, I. A.; Bell, M.; Harding, R.; Carrick, L.; McLeish, T. C. B.; Semenov, A. N.; Boden, N. Hierarchical self-assembly of chiral rod-like molecules as a model for peptide β-sheet tapes, ribbons, fibrils, and fibers. *Proceedings of the National Academy of Sciences.* **2001** 98(21), 11857-11862.

30. Haines-Butterick, L.; Rajagopal, K.; Branco, M.; Salick, D.; Rughani, R.; Pilarz, M.; Lamm, M. S.; Pochan, D. J.; Schneider, J. P. Controlling hydrogelation kinetics by peptide design for three-dimensional encapsulation and injectable delivery of cells. *Proceedings of the National Academy of Sciences.* **2007** 104(19), 7791-7796.

31. Hartgerink, J. D.; Beniash, E.; Stupp, S. I. Self-assembly and mineralization of peptide-amphiphile nanofibers. *Science.* **2001** 294(5547), 1684-1688.

32. Hartgerink, J. D.; Beniash, E.; Stupp, S. I. Peptide-amphiphile nanofibers: a versatile scaffold for the preparation of self-assembling materials. *Proceedings of the National Academy of Sciences.* **2002** 99(8), 5133-5138.

33. Hauser, C. A. E.; Deng, R.; Mishra, A.; Loo, Y.; Khoe, U.; Zhuang, F.; Cheong, D. W.; Accardo, A.; Sullivan, M. B.; Riekel, C.; Ying, J. Y.; Hauser, U. A. Natural tri- to hexapeptides self-assemble in water to amyloid β-type fiber aggregates by unexpected α-helical intermediate structures. *Proceedings of the National Academy of Sciences.* **2011** 108(4), 1361-1366.

34. Zhang, S.; Holmes, T. C.; DiPersio, C. M.; Hynes, R. O.; Su, X.; Rich, A. Self-complementary oligopeptide matrices support mammalian cell attachment. *Biomaterials.* **1995** 16(18), 1385-1393.

35. Fletcher, J. M.; Harniman, R. L.; Barnes, F. R. H.; Boyle, A. L.; Collins, A.; Mantell, J.; Sharp, T. H.; Antognozzi, M.; Booth, P. J.; Linden, N.; Miles, M. J.; Sessions, R. B.; Verkade, P.; Woolfson, D. N. Self-assembling cages from coiled-coil peptide modules. *Science.* **2013** 340(6132), 595-599.

36. Gradišar, H.; Božič, S.; Doles, T.; Vengust, D.; Hafner-Bratkovič, I.; Mertelj, A.; Webb, B.; Šali, A.; Klavžar, S.; Jerala, R. Design of a single-chain polypeptide tetrahedron assembled from coiled-coil segments. *Nature Chemical Biology.* **2013** 9(6), 362-366.

37. Ryadnov, M. G.; Woolfson, D. N. Engineering the morphology of a self-assembling protein fibre. *Nature Materials.* **2003** 2(5), 329-332.

38. Berndt, P.; Fields, G. B.; Tirrell, M. Synthetic lipidation of peptides and amino acids: monolayer structure and properties. *Journal of the American Chemical Society.* **1995** 117(37), 9515-9522.

39. Mozhdehi, D.; Luginbuhl, K. M.; Simon, J. R.; Dzuricky, M.; Berger, R.; Varol, H. S.; Huang, F. C.; Buehne, K. L.; Mayne, N. R.; Weitzhandler, I.; Bonn, M.; Parekh, S. H.; Chilkoti, A. Genetically encoded lipid–polypeptide hybrid biomaterials that exhibit temperature-triggered hierarchical self-assembly. *Nature Chemistry.* **2018** 10(5), 496-505.

40. Chen, L.; Morris, K.; Laybourn, A.; Elias, D.; Hicks, M. R.; Rodger, A.; Serpell, L.; Adams, D. J. Self-assembly mechanism for a naphthalene−dipeptide leading to hydrogelation. *Langmuir.* **2010** 26(7), 5232-5242.

41. Fleming, S.; Ulijn, R. V. Design of nanostructures based on aromatic peptide amphiphiles. *Chemical Society Reviews.* **2014** 43(23), 8150-8177.

42. Jayawarna, V.; Ali, M.; Jowitt, T. A.; Miller, A. F.; Saiani, A.; Gough, J. E.; Ulijn, R. V. Nanostructured hydrogels for three-dimensional cell culture through self-assembly of fluorenylmethoxycarbonyl–dipeptides. *Advanced Materials.* **2006** 18(5), 611-614.

43. Yang, Z.; Gu, H.; Fu, D.; Gao, P.; Lam, J. K.; Xu, B. Enzymatic formation of supramolecular hydrogels. *Advanced Materials.* **2004** 16(16), 1440-1444.

44. Petka, W. A.; Harden, J. L.; McGrath, K. P.; Wirtz, D.; Tirrell, D. A. Reversible hydrogels from self-assembling artificial proteins. *Science.* **1998** 281(5375), 389-392.

45. Shen, W.; Zhang, K.; Kornfield, J. A.; Tirrell, D. A. Tuning the erosion rate of artificial protein hydrogels through control of network topology. *Nature Materials.* **2006** 5(2), 153-158.

46. Wong Po Foo, C. T. S.; Lee, J. S.; Mulyasasmita, W.; Parisi-Amon, A.; Heilshorn, S. C. Two-component protein-engineered physical hydrogels for cell encapsulation. *Proceedings of the National Academy of Sciences.* **2009** 106(52), 22067-22072.

47. Buerkle, L. E.; von Recum, H. A.; Rowan, S. J. Toward potential supramolecular tissue engineering scaffolds based on guanosine derivatives. *Chemical Science.* **2012** 3(2), 564-572.

48. Dankers, P. Y. W.; Harmsen, M. C.; Brouwer, L. A.; Van Luyn, M. J. A.; Meijer, E. W. A modular and supramolecular approach to bioactive scaffolds for tissue engineering. *Nature Materials.* **2005** 4(7), 568-574.

49. Fukushima, K.; Liu, S.; Wu, H.; Engler, A. C.; Coady, D. J.; Maune, H.; Pitera, J.; Nelson, A.; Wiradharma, N.; Venkataraman, S.; Huang, Y.; Fan, W.; Ying, J. Y.; Yang, Y. Y.; Hedrick, J. L. Supramolecular high-aspect ratio assemblies with strong antifungal activity. *Nature Communications.* **2013** 4, 2861(article number).

50. Fukushima, K.; Tan, J. P. K.; Korevaar, P. A.; Yang, Y. Y.; Pitera, J.; Nelson, A.; Maune, H.; Coady, D. J.; Frommer, J. E.; Engler, A. C.; Huang, Y.; Xu, K.; Ji, Z.; Qiao, Y.; Fan, W.; Li, L.; Wiradharma, N.; Meijer, E. W.; Hedrick, J. L. Broad-spectrum antimicrobial supramolecular assemblies with distinctive size and shape. *ACS Nano.* **2012** 6(10), 9191-9199.

51. Onogi, S.; Shigemitsu, H.; Yoshii, T.; Tanida, T.; Ikeda, M.; Kubota, R.; Hamachi, I. In situ real-time imaging of self-sorted supramolecular nanofibres. *Nature Chemistry.* **2016** 8(8), 743-752.

52. Roosma, J.; Mes, T.; Leclère, P.; Palmans, A. R. A.; Meijer, E. W. Supramolecular materials from benzene-1,3,5-tricarboxamide-based nanorods. *Journal of the American Chemical Society.* **2008** 130(4), 1120-1121.

53. Kim, S. H.; Nederberg, F.; Jakobs, R.; Tan, J. P. K.; Fukushima, K.; Nelson, A.; Meijer, E. W.; Yang, Y. Y.; Hedrick, J. L. A supramolecularly assisted transformation of block-copolymer micelles into nanotubes. *Angewandte Chemie International Edition.* **2009** 48(25), 4508-4512.

54. Appel, E. A.; Biedermann, F.; Rauwald, U.; Jones, S. T.; Zayed, J. M.; Scherman, O. A. Supramolecular cross-linked networks via host−guest complexation with cucurbit[8]uril. *Journal of the American Chemical Society.* **2010** 132(40), 14251-14260.

55. Appel, E. A.; Loh, X. J.; Jones, S. T.; Biedermann, F.; Dreiss, C. A.; Scherman, O. A. Ultrahigh-water-content supramolecular hydrogels exhibiting multistimuli responsiveness. *Journal of the American Chemical Society.* **2012** 134(28), 11767-11773.

56. Boekhoven, J.; Rubert Pérez, C. M.; Sur, S.; Worthy, A.; Stupp, S. I. Dynamic display of bioactivity through host–guest chemistry. *Angewandte Chemie International Edition.* **2013** 52(46), 12077-12080.

57. Harada, A.; Kobayashi, R.; Takashima, Y.; Hashidzume, A.; Yamaguchi, H. Macroscopic self-assembly through molecular recognition. *Nature Chemistry.* **2010** 3(1), 34-37.

58. Kakuta, T.; Takashima, Y.; Nakahata, M.; Otsubo, M.; Yamaguchi, H.; Harada, A. Preorganized hydrogel: Self-healing properties of supramolecular hydrogels formed by polymerization of host–guest-monomers that contain cyclodextrins and hydrophobic guest groups. *Advanced Materials.* **2013** 25(20), 2849-2853.

59. Rodell, C. B.; Kaminski, A. L.; Burdick, J. A. Rational design of network properties in guest–host assembled and shear-thinning hyaluronic acid hydrogels. *Biomacromolecules.* **2013** 14(11), 4125-4134.

60. Fullenkamp, D. E.; He, L.; Barrett, D. G.; Burghardt, W. R.; Messersmith, P. B. Mussel-inspired histidine-based transient network metal coordination hydrogels. *Macromolecules.* **2013** 46(3), 1167-1174.

61. Holten-Andersen, N.; Harrington, M. J.; Birkedal, H.; Lee, B. P.; Messersmith, P. B.; Lee, K. Y. C.; Waite, J. H. pH-induced metal-ligand cross-links inspired by mussel yield self-healing polymer networks with near-covalent elastic moduli. *Proceedings of the National Academy of Sciences.* **2011** 108(7), 2651-2655.

62. Mozhdehi, D.; Ayala, S.; Cromwell, O. R.; Guan, Z. Self-healing multiphase polymers via dynamic metal–ligand interactions. *Journal of the American Chemical Society.* **2014** 136(46), 16128-16131.

63. Hendricks, M. P.; Sato, K.; Palmer, L. C.; Stupp, S. I. Supramolecular assembly of peptide amphiphiles. *Accounts of Chemical Research.* **2017** 50(10), 2440-2448.

64. Cui, H.; Webber, M. J.; Stupp, S. I. Self‐assembly of peptide amphiphiles: From molecules to nanostructures to biomaterials. *Biopolymers.* **2010** 94(1), 1-18.

65. Matson, J. B.; Stupp, S. I. Self-assembling peptide scaffolds for regenerative medicine. *Chemical Communications.* **2012** 48(1), 26-33.

66. Abagnale, G.; Steger, M.; Nguyen, V. H.; Hersch, N.; Sechi, A.; Joussen, S.; Denecke, B.; Merkel, R.; Hoffmann, B.; Dreser, A. Surface topography enhances

differentiation of mesenchymal stem cells towards osteogenic and adipogenic lineages. *Biomaterials.* **2015** 61, 316-326.

67. McMurray, R. J.; Gadegaard, N.; Tsimbouri, P. M.; Burgess, K. V.; McNamara, L. E.; Tare, R.; Murawski, K.; Kingham, E.; Oreffo, R. O.; Dalby, M. J. Nanoscale surfaces for the long-term maintenance of mesenchymal stem cell phenotype and multipotency. *Nature Materials.* **2011** 10(8), 637-644.

68. Park, J.; Kim, D.-H.; Kim, H.-N.; Wang, C. J.; Kwak, M. K.; Hur, E.; Suh, K.-Y.; An, S. S.; Levchenko, A. Directed migration of cancer cells by the graded texture of the underlying matrix. *Nature Materials.* **2016** 15(7), 792-801.

69. Kim, D.-H.; Lipke, E. A.; Kim, P.; Cheong, R.; Thompson, S.; Delannoy, M.; Suh, K.-Y.; Tung, L.; Levchenko, A. Nanoscale cues regulate the structure and function of macroscopic cardiac tissue constructs. *Proceedings of the National Academy of Sciences.* **2010** 107(2), 565-570.

70. Capito, R. M.; Azevedo, H. S.; Velichko, Y. S.; Mata, A.; Stupp, S. I. Self-assembly of large and small molecules into hierarchically ordered sacs and membranes. *Science.* **2008** 319(5871), 1812-1816.

71. Zhang, S.; Greenfield, M. A.; Mata, A.; Palmer, L. C.; Bitton, R.; Mantei, J. R.; Aparicio, C.; Olvera de la Cruz, M.; Stupp, S. I. A self-assembly pathway to aligned monodomain gels. *Nature Materials.* **2010** 9(7), 594-601.

72. Cui, H.; Pashuck, E. T.; Velichko, Y. S.; Weigand, S. J.; Cheetham, A. G.; Newcomb, C. J.; Stupp, S. I. Spontaneous and x-ray–triggered crystallization at long range in self-assembling filament networks. *Science.* **2010** 327(5965), 555-559.

73. Freeman, R.; Han, M.; Álvarez, Z.; Lewis, J. A.; Wester, J. R.; Stephanopoulos, N.; McClendon, M. T.; Lynsky, C.; Godbe, J. M.; Sangji, H. Reversible self-assembly of superstructured networks. *Science.* **2018** 362(6416), 808-813.

74. Ortony, J. H.; Newcomb, C. J.; Matson, J. B.; Palmer, L. C.; Doan, P. E.; Hoffman, B. M.; Stupp, S. I. Internal dynamics of a supramolecular nanofibre. *Nature Materials.* **2014** 13(8), 812-816.

75. Newcomb, C. J.; Sur, S.; Ortony, J. H.; Lee, O.-S.; Matson, J. B.; Boekhoven, J.; Yu, J. M.; Schatz, G. C.; Stupp, S. I. Cell death versus cell survival instructed by supramolecular cohesion of nanostructures. *Nature Communications.* **2014** 5, 3321(article number).

76. Chen, J.; Hessler, J. A.; Putchakayala, K.; Panama, B. K.; Khan, D. P.; Hong, S.; Mullen, D. G.; DiMaggio, S. C.; Som, A.; Tew, G. N. Cationic nanoparticles induce

nanoscale disruption in living cell plasma membranes. *Journal of Physical Chemistry B.* **2009** 113(32), 11179-11185.

77. Fröhlich, E. The role of surface charge in cellular uptake and cytotoxicity of medical nanoparticles. *International Journal of Nanomedicine.* **2012** 7, 5577-5591.

78. Huang, Y.-W.; Cambre, M.; Lee, H.-J. The toxicity of nanoparticles depends on multiple molecular and physicochemical mechanisms. *International Journal of Molecular Sciences.* **2017** 18(12), 2702(article number).

79. Lin, J.; Alexander-Katz, A. Cell membranes open "doors" for cationic nanoparticles/biomolecules: insights into uptake kinetics. *ACS Nano.* **2013** 7(12), 10799-10808.

80. Newcomb, C. J.; Sur, S.; Lee, S. S.; Yu, J. M.; Zhou, Y.; Snead, M. L.; Stupp, S. I. Supramolecular nanofibers enhance growth factor signaling by increasing lipid raft mobility. *Nano Letters.* **2016** 16(5), 3042-3050.

81. da Silva, R. M.; van der Zwaag, D.; Albertazzi, L.; Lee, S. S.; Meijer, E.; Stupp, S. I. Super-resolution microscopy reveals structural diversity in molecular exchange among peptide amphiphile nanofibres. *Nature Communications.* **2016** 7, 11561(article number).

82. Choquet, D.; Felsenfeld Dp Fau - Sheetz, M. P.; Sheetz, M. P. Extracellular matrix rigidity causes strengthening of integrin-cytoskeleton linkages. *Cell.* **1997** 88(1), 39-48.

83. Gilbert, P. M.; Havenstrite, K. L.; Magnusson, K. E.; Sacco, A.; Leonardi, N. A.; Kraft, P.; Nguyen, N. K.; Thrun, S.; Lutolf, M. P.; Blau, H. M. Substrate elasticity regulates skeletal muscle stem cell self-renewal in culture. *Science.* **2010** 329(5995), 1078-1081.

84. Yang, C.; Tibbitt, M. W.; Basta, L.; Anseth, K. S. Mechanical memory and dosing influence stem cell fate. *Nature Materials.* **2014** 13(6), 645-652.

85. Yusko, E. C.; Asbury, C. L. Force is a signal that cells cannot ignore. *Molecular Biology of the Cell.* **2017** 25(23), 3717-3833.

86. Pashuck, E. T.; Cui, H.; Stupp, S. I. Tuning supramolecular rigidity of peptide fibers through molecular structure. *Journal of the American Chemical Society.* **2010** 132(17), 6041-6046.

87. Sleep, E.; Cosgrove, B. D.; McClendon, M. T.; Preslar, A. T.; Chen, C. H.; Sangji, M. H.; Pérez, C. M. R.; Haynes, R. D.; Meade, T. J.; Blau, H. M. Injectable biomimetic liquid crystalline scaffolds enhance muscle stem cell transplantation. *Proceedings of the National Academy of Sciences.* **2017** 114(38), E7919-E7928.

88. Yu, Z.; Tantakitti, F.; Yu, T.; Palmer, L. C.; Schatz, G. C.; Stupp, S. I. Simultaneous covalent and noncovalent hybrid polymerizations. *Science.* **2016** 351(6272), 497-502.

89. Silva, G. A.; Czeisler, C.; Niece, K. L.; Beniash, E.; Harrington, D. A.; Kessler, J. A.; Stupp, S. I. Selective differentiation of neural progenitor cells by high-epitope density nanofibers. *Science.* **2004** 303(5662), 1352-1355.

90. Arnold, M.; Cavalcanti‐Adam, E. A.; Glass, R.; Blümmel, J.; Eck, W.; Kantlehner, M.; Kessler, H.; Spatz, J. P. Activation of integrin function by nanopatterned adhesive interfaces. *ChemPhysChem.* **2004** 5(3), 383-388.

91. Berg, M. C.; Yang, S. Y.; Hammond, P. T.; Rubner, M. F. Controlling mammalian cell interactions on patterned polyelectrolyte multilayer surfaces. *Langmuir.* **2004** 20(4), 1362-1368.

92. Cavalcanti-Adam, E. A.; Micoulet, A.; Blümmel, J.; Auernheimer, J.; Kessler, H.; Spatz, J. P. Lateral spacing of integrin ligands influences cell spreading and focal adhesion assembly. *European Journal of Cell Biology.* **2006** 85(3-4), 219-224.

93. Mann, B. K.; Tsai, A. T.; Scott-Burden, T.; West, J. L. Modification of surfaces with cell adhesion peptides alters extracellular matrix deposition. *Biomaterials.* **1999** 20(23-24), 2281-2286.

94. Massia, S. P.; Hubbell, J. A. An RGD spacing of 440 nm is sufficient for integrin alpha V beta 3-mediated fibroblast spreading and 140 nm for focal contact and stress fiber formation. *The Journal of Cell Biology.* **1991** 114(5), 1089-1100.

95. Rezania, A.; Healy, K. E. The effect of peptide surface density on mineralization of a matrix deposited by osteogenic cells. *Journal of Biomedical Materials Research.* **2000** 52(4), 595-600.

96. Rowley, J. A.; Mooney, D. J. Alginate type and RGD density control myoblast phenotype. *Journal of Biomedical Materials Research.* **2002** 60(2), 217-223.

97. Wang, X.; Yan C Fau - Ye, K.; Ye K Fau - He, Y.; He Y Fau - Li, Z.; Li Z Fau - Ding, J.; Ding, J. Effect of RGD nanospacing on differentiation of stem cells. *Biomaterials.* **2013** 34(12), 2865-2874.

98. Sur, S.; Tantakitti, F.; Matson, J. B.; Stupp, S. I. Epitope topography controls bioactivity in supramolecular nanofibers. *Biomaterials Science.* **2015** 3(3), 520-532.

99. Storrie, H.; Guler Mo Fau - Abu-Amara, S. N.; Abu-Amara Sn Fau - Volberg, T.; Volberg T Fau - Rao, M.; Rao M Fau - Geiger, B.; Geiger B Fau - Stupp, S. I.; Stupp, S. I. Supramolecular crafting of cell adhesion. *Biomaterials.* **2007** 28(31), 4608-4618.

100. Webber, M. J.; Tongers J Fau - Renault, M.-A.; Renault Ma Fau - Roncalli, J. G.; Roncalli Jg Fau - Losordo, D. W.; Losordo Dw Fau - Stupp, S. I.; Stupp, S. I. Development of bioactive peptide amphiphiles for therapeutic cell delivery. *Acta Biomaterialia.* **2010** 6(1), 3-11.

101. Korevaar, P. A.; George, S. J.; Markvoort, A. J.; Smulders, M. M.; Hilbers, P. A.; Schenning, A. P.; De Greef, T. F.; Meijer, E. Pathway complexity in supramolecular polymerization. *Nature.* **2012** 481(7382), 492-496.

102. Korevaar, P. A.; Newcomb, C. J.; Meijer, E.; Stupp, S. I. Pathway selection in peptide amphiphile assembly. *Journal of the American Chemical Society.* **2014** 136(24), 8540-8543.

103. Tantakitti, F.; Boekhoven, J.; Wang, X.; Kazantsev, R. V.; Yu, T.; Li, J.; Zhuang, E.; Zandi, R.; Ortony, J. H.; Newcomb, C. J.; Palmer, L. C.; Shekhawat, G. S.; Olvera de la Cruz, M.; Schatz, G. C.; Stupp, S. I. Energy landscapes and functions of supramolecular systems. *Nature Materials.* **2016** 15(4), 469-476.

104. Noé, F.; Schütte, C.; Vanden-Eijnden, E.; Reich, L.; Weikl, T. R. Constructing the equilibrium ensemble of folding pathways from short off-equilibrium simulations. *Proceedings of the National Academy of Sciences.* **2009** 106(45), 19011-19016.

105. Hartl, F. U. Molecular chaperones in cellular protein folding. *Nature.* **1996** 381(6583), 571-580.

106. Hartl, F. U.; Bracher, A.; Hayer-Hartl, M. Molecular chaperones in protein folding and proteostasis. *Nature.* **2011** 475(7356), 324-332.

107. Lee, S. S.; Fyrner, T.; Chen, F.; Álvarez, Z.; Sleep, E.; Chun, D. S.; Weiner, J. A.; Cook, R. W.; Freshman, R. D.; Schallmo, M. S. Sulfated glycopeptide nanostructures for multipotent protein activation. *Nature Nanotechnology.* **2017** 12(8), 821-829.

108. Lee, S. S.; Hsu, E. L.; Mendoza, M.; Ghodasra, J.; Nickoli, M. S.; Ashtekar, A.; Polavarapu, M.; Babu, J.; Riaz, R. M.; Nicolas, J. D. Gel scaffolds of BMP‐2‐binding peptide amphiphile nanofibers for spinal arthrodesis. *Advanced Healthcare Materials.* **2015** 4(1), 131-141.

109. Lee, S. S.; Huang, B. J.; Kaltz, S. R.; Sur, S.; Newcomb, C. J.; Stock, S. R.; Shah, R. N.; Stupp, S. I. Bone regeneration with low dose BMP-2 amplified by biomimetic supramolecular nanofibers within collagen scaffolds. *Biomaterials.* **2013** 34(2), 452-459.

110. Mata, A.; Geng, Y.; Henrikson, K. J.; Aparicio, C.; Stock, S. R.; Satcher, R. L.; Stupp, S. I. Bone regeneration mediated by biomimetic mineralization of a nanofiber matrix. *Biomaterials.* **2010** 31(23), 6004-6012.

111. Shah, R. N.; Shah, N. A.; Lim, M. M. D. R.; Hsieh, C.; Nuber, G.; Stupp, S. I. Supramolecular design of self-assembling nanofibers for cartilage regeneration. *Proceedings of the National Academy of Sciences.* **2010** 107(8), 3293-3298.

112. Webber, M. J.; Tongers, J.; Newcomb, C. J.; Marquardt, K.-T.; Bauersachs, J.; Losordo, D. W.; Stupp, S. I. Supramolecular nanostructures that mimic VEGF as a strategy for ischemic tissue repair (vol 108, pg 13438, 2011). *Proceedings of the National Academy of Sciences* **2012** 109(23), 9220-9220.

113. Edelbrock, A. N.; Àlvarez, Z.; Simkin, D.; Fyrner, T.; Chin, S. M.; Sato, K.; Kiskinis, E.; Stupp, S. I. Supramolecular nanostructure activates TrkB receptor signaling of neuronal cells by mimicking brain-derived neurotrophic factor. *Nano Letters.* **2018** 18(10), 6237-6247.

114. Pan, L.; North, H. A.; Sahni, V.; Jeong, S. J.; Mcguire, T. L.; Berns, E. J.; Stupp, S. I.; Kessler, J. A. β1-Integrin and integrin linked kinase regulate astrocytic differentiation of neural stem cells. *PLoS One.* **2014** 9(8), e104335.

115. Li, A.; Hokugo, A.; Yalom, A.; Berns, E. J.; Stephanopoulos, N.; McClendon, M. T.; Segovia, L. A.; Spigelman, I.; Stupp, S. I.; Jarrahy, R. A bioengineered peripheral nerve construct using aligned peptide amphiphile nanofibers. *Biomaterials.* **2014** 35(31), 8780-8790.

116. Conda-Sheridan, M.; Lee, S. S.; Preslar, A. T.; Stupp, S. I. Esterase-activated release of naproxen from supramolecular nanofibres. *Chemical Communications.* **2014** 50(89), 13757-13760.

117. Moyer, T. J.; Kassam, H. A.; Bahnson, E. S.; Morgan, C. E.; Tantakitti, F.; Chew, T. L.; Kibbe, M. R.; Stupp, S. I. Shape‐dependent targeting of injured blood vessels by peptide amphiphile supramolecular nanostructures. *Small.* **2015** 11(23), 2750-2755.

118. Soukasene, S.; Toft, D. J.; Moyer, T. J.; Lu, H.; Lee, H.-K.; Standley, S. M.; Cryns, V. L.; Stupp, S. I. Antitumor activity of peptide amphiphile nanofiber-encapsulated camptothecin. *ACS Nano.* **2011** 5(11), 9113-9121.

119. So, M. M.; Mansukhani, N. A.; Peters, E. B.; Albaghdadi, M. S.; Wang, Z.; Rubert Pérez, C. M.; Kibbe, M. R.; Stupp, S. I. Peptide amphiphile nanostructures for targeting of atherosclerotic plaque and drug delivery. *Advanced Biosystems.* **2018** 2(3), 1700123.

120. Zha, R. H.; Sur, S.; Boekhoven, J.; Shi, H. Y.; Zhang, M.; Stupp, S. I. Supramolecular assembly of multifunctional maspin-mimetic nanostructures as a potent peptide-based angiogenesis inhibitor. *Acta Biomaterialia.* **2015** 12, 1-10.

121. Zha, R. H.; Sur, S.; Stupp, S. I. Self‐assembly of cytotoxic peptide amphiphiles into supramolecular membranes for cancer therapy. *Advanced Healthcare Materials.* **2013** 2(1), 126-133.

122. Morgan, C. E.; Dombrowski, A. W.; Rubert Pérez, C. M.; Bahnson, E. S.; Tsihlis, N. D.; Jiang, W.; Jiang, Q.; Vercammen, J. M.; Prakash, V. S.; Pritts, T. A. Tissue-factor targeted peptide amphiphile nanofibers as an injectable therapy to control hemorrhage. *ACS Nano.* **2015** 10(1), 899-909.

123. Bhatnagar, B. S.; Bogner, R. H.; Pikal, M. J. Protein stability during freezing: separation of stresses and mechanisms of protein stabilization. *Pharmaceutical Development and Technology.* **2007** 12(5), 505-523.

124. Fonte, P.; Soares, S.; Costa, A.; Andrade, J. C.; Seabra, V.; Reis, S.; Sarmento, B. Effect of cryoprotectants on the porosity and stability of insulin-loaded PLGA nanoparticles after freeze-drying. *Biomatter.* **2012** 2(4), 329-339.

125. van Winden, E. C.; Zhang, W.; Crommelin, D. J. Effect of freezing rate on the stability of liposomes during freeze-drying and rehydration. *Pharmaceutical Research.* **1997** 14(9), 1151-1160.

126. Mazur, P. Cryobiology: The freezing of biological systems. *Science.* **1970** 168(3934), 939-949.

127. Tang, X. C.; Pikal, M. J. Design of freeze-drying processes for pharmaceuticals: practical advice. *Pharmaceutical Research.* **2004** 21(2), 191-200.

128. Versluis, F.; van Esch, J. H.; Eelkema, R. Synthetic self‐assembled materials in biological environments. *Advanced Materials.* **2016** 28(23), 4576-4592.

129. Ligthart, G.; Ohkawa, H.; Sijbesma, R. P.; Meijer, E. Complementary quadruple hydrogen bonding in supramolecular copolymers. *Journal of the American Chemical Society.* **2005** 127(3), 810-811.

130. Ishida, Y.; Aida, T. Homochiral supramolecular polymerization of an “S”-shaped chiral monomer: translation of optical purity into molecular weight distribution. *Journal of the American Chemical Society.* **2002** 124(47), 14017-14019.

131. Ma, Y.; Kolotuchin, S. V.; Zimmerman, S. C. Supramolecular polymer chemistry: self-assembling dendrimers Using the DDA·AAD (GC-like) Hydrogen Bonding Motif. *Journal of the American Chemical Society.* **2002** 124(46), 13757-13769.

132. Morris, K. L.; Chen, L.; Raeburn, J.; Sellick, O. R.; Cotanda, P.; Paul, A.; Griffiths, P. C.; King, S. M.; O’Reilly, R. K.; Serpell, L. C. Chemically programmed self-sorting of gelator networks. *Nature Communications.* **2013** 4, 1480(article number).

133. Ardoña, H. A. M.; Draper, E. R.; Citossi, F.; Wallace, M.; Serpell, L. C.; Adams, D. J.; Tovar, J. D. Kinetically-controlled coassembly of multichromophoric peptide hydrogelators and the impacts on energy transport. *Journal of the American Chemical Society.* **2017** 139(25), 8685-8692.

134. Hendrikse, S. I.; Wijnands, S. P.; Lafleur, R. P.; Pouderoijen, M. J.; Janssen, H. M.; Dankers, P. Y.; Meijer, E. Controlling and tuning the dynamic nature of supramolecular polymers in aqueous solutions. *Chemical Communications.* **2017** 53(14), 2279-2282.

135. Chen, C. H.; Palmer, L. C.; Stupp, S. I. Self-repair of structure and bioactivity in a supramolecular nanostructure. *Nano Letters.* **2018** 18(11), 6832-6841.

136. Deka, C.; Lehnert, B.; Lehnert, N.; Jones, G.; Sklar, L.; Steinkamp, J. Analysis of fluorescence lifetime and quenching of FITC‐conjugated antibodies on cells by phase‐sensitive flow cytometry. *Cytometry Part A.* **1996** 25(3), 271-279.

137. Iqbal, A.; Arslan, S.; Okumus, B.; Wilson, T. J.; Giraud, G.; Norman, D. G.; Ha, T.; Lilley, D. M. Orientation dependence in fluorescent energy transfer between Cy3 and Cy5 terminally attached to double-stranded nucleic acids. *Proceedings of the National Academy of Sciences.* **2008** 105(32), 11176-11181.

138. Creutz, S.; van Stam, J.; Antoun, S.; De Schryver, F. C.; Jérôme, R. Exchange of polymer molecules between block copolymer micelles studied by emission spectroscopy. A method for the quantification of unimer exchange rates. *Macromolecules.* **1997** 30(14), 4078-4083.

139. van Stam, J.; Creutz, S.; De Schryver, F. C.; Jérôme, R. Tuning of the cxchange dynamics of unimers between block copolymer micelles with temperature, cosolvents, and cosurfactants. *Macromolecules.* **2000** 33(17), 6388-6395.

140. Soumpasis, D. M. Theoretical analysis of fluorescence photobleaching recovery experiments. *Biophysical Journal.* **1983** 41(1), 95-97.

141. Motulsky, H. J.; Brown, R. E. Detecting outliers when fitting data with nonlinear regression - a new method based on robust nonlinear regression and the false discovery rate. *BMC Bioinformatics.* **2006** 7(123).

142. Kerr, J. F.; Wyllie, A. H.; Currie, A. R. Apoptosis: a basic biological phenomenon with wide-ranging implications in tissue kinetics. *British Journal of Cancer.* **1972** 26(4), 239-257.

143. Meier, P.; Finch, A.; Evan, G. Apoptosis in development. *Nature.* **2000** 407(6805), 796-801.

144. Qu, X.; Zou Z Fau - Sun, Q.; Sun Q Fau - Luby-Phelps, K.; Luby-Phelps K Fau - Cheng, P.; Cheng P Fau - Hogan, R. N.; Hogan Rn Fau - Gilpin, C.; Gilpin C Fau - Levine, B.; Levine, B. Autophagy gene-dependent clearance of apoptotic cells during embryonic development. *Cell.* **2007** 128(5), 931-946.

145. Jacobson, M. D.; Weil M Fau - Raff, M. C.; Raff, M. C. Programmed cell death in animal development. *Cell.* **1997** 88(3), 347-354.

146. Nagata, S.; Tanaka, M. Programmed cell death and the immune system. *Nature Reviews Immunology.* **2017** 17(5), 333-340.

147. Opferman, J. T.; Korsmeyer, S. J. Apoptosis in the development and maintenance of the immune system. *Nature Immunology.* **2003** 4(5), 410-415.

148. Hartley, S. B.; Crosbie, J.; Brink, R.; Kantor, A. B.; Basten, A.; Goodnow, C. C. Elimination from peripheral lymphoid tissues of self-reactive B lymphocytes recognizing membrane-bound antigens. *Nature.* **1991** 353(6346), 765-769.

149. MacDonald, H. R.; Schneider, R.; Lees, R. K.; Howe, R. C.; Acha-Orbea, H.; Festenstein, H.; Zinkernagel, R. M.; Hengartner, H. T-cell receptor Vβ use predicts reactivity and tolerance to Mlsa- encoded antigens. *Nature.* **1988** 332(6159), 40-45.

150. Nemazee, D. A.; Bürki, K. Clonal deletion of B lymphocytes in a transgenic mouse bearing anti-MHC class I antibody genes. *Nature.* **1989** 337(6207), 562-566.

151. Teh, H. S.; Kisielow, P.; Scott, B.; Kishi, H.; Uematsu, Y.; Blüthmann, H.; von Boehmer, H. Thymic major histocompatibility complex antigens and the αβ T-cell receptor determine the CD4/CD8 phenotype of T cells. *Nature.* **1988** 335(6187), 229-233.

152. Desmoulière, A.; Redard, M.; Darby, I.; Gabbiani, G. Apoptosis mediates the decrease in cellularity during the transition between granulation tissue and scar. *The American Journal of Pathology.* **1995** 146(1), 56-66.

153. Greenhalgh, D. G. The role of apoptosis in wound healing. *International Journal Of Biochemistry & Cell Biology.* **1998** 30(9), 1019-1030.

154. Ambrosini, G.; Adida, C.; Altieri, D. C. A novel anti-apoptosis gene, survivin, expressed in cancer and lymphoma. *Nature Medicine.* **1997** 3(8), 917-921.

155. Evan, G. I.; Vousden, K. H. Proliferation, cell cycle and apoptosis in cancer. *Nature.* **2001** 411(6835), 342.

156. Hengartner, M. O.; Horvitz, H. R. C. elegans cell survival gene ced-9 encodes a functional homolog of the mammalian proto-oncogene bcl-2. *Cell.* **1994** 76(4), 665-676.

157. Itoh, N.; Yonehara, S.; Ishii, A.; Yonehara, M.; Mizushima, S.-I.; Sameshima, M.; Hase, A.; Seto, Y.; Nagata, S. The polypeptide encoded by the cDNA for human cell surface antigen Fas can mediate apoptosis. *Cell.* **1991** 66(2), 233-243.

158. Suda, T.; Takahashi, T.; Golstein, P.; Nagata, S. Molecular cloning and expression of the fas ligand, a novel member of the tumor necrosis factor family. *Cell.* **1993** 75(6), 1169-1178.

159. Yuan, J.; Shaham, S.; Ledoux, S.; Ellis, H. M.; Horvitz, H. R. The C. elegans cell death gene ced-3 encodes a protein similar to mammalian interleukin-1β-converting enzyme. *Cell.* **1993** 75(4), 641-652.

160. Liu, X.; Kim, C. N.; Yang, J.; Jemmerson, R.; Wang, X. Induction of Apoptotic Program in Cell-Free Extracts: Requirement for dATP and Cytochrome c. *Cell.* **1996** 86(1), 147-157.

161. Miura, M.; Zhu, H.; Rotello, R.; Hartwieg, E. A.; Yuan, J. Induction of apoptosis in fibroblasts by IL-1β-converting enzyme, a mammalian homolog of the C. elegans cell death gene ced-3. *Cell.* **1993** 75(4), 653-660.

162. Zou, H.; Henzel, W. J.; Liu, X.; Lutschg, A.; Wang, X. Apaf-1, a Human Protein Homologous to C. elegans CED-4, Participates in Cytochrome c–Dependent Activation of Caspase-3. *Cell.* **1997** 90(3), 405-413.

163. Majno, G.; Joris, I. Apoptosis, oncosis, and necrosis. An overview of cell death. *The American Journal of Pathology.* **1995** 146(1), 3-15.

164. Trump, B. F.; Berezesky Ik Fau - Chang, S. H.; Chang Sh Fau - Phelps, P. C.; Phelps, P. C. The pathways of cell death: oncosis, apoptosis, and necrosis. *Toxicologic Pathology.* **1997** 25(1), 82-88.

165. Weerasinghe, P.; Buja, L. M. Oncosis: an important non-apoptotic mode of cell death. *Experimental and Molecular Pathology.* **2012** 93(3), 302-308.

166. Balvan, J.; Krizova, A.; Gumulec, J.; Raudenska, M.; Sladek, Z.; Sedlackova, M.; Babula, P.; Sztalmachova, M.; Kizek, R.; Chmelik, R.; Masarik, M. Multimodal holographic microscopy: distinction between apoptosis and oncosis. *PLoS One.* **2015** 10(3), e0121674.

167. Mills, E. M.; Xu D Fau - Fergusson, M. M.; Fergusson Mm Fau - Combs, C. A.; Combs Ca Fau - Xu, Y.; Xu Y Fau - Finkel, T.; Finkel, T. Regulation of cellular oncosis by uncoupling protein 2. *Journal of Biological Chemistry.* **2002** 277(30), 27385-27392.

168. Napierska, D.; Thomassen, L. C. J.; Rabolli, V.; Lison, D.; Gonzalez, L.; Kirsch-Volders, M.; Martens, J. A.; Hoet, P. H. Size-dependent cytotoxicity of

monodisperse silica nanoparticles in human endothelial cells. *Small.* **2009** 5(7), 846-853.

169. Park, M. V. D. Z.; Neigh, A. M.; Vermeulen, J. P.; de la Fonteyne, L. J. J.; Verharen, H. W.; Briedé, J. J.; van Loveren, H.; de Jong, W. H. The effect of particle size on the cytotoxicity, inflammation, developmental toxicity and genotoxicity of silver nanoparticles. *Biomaterials.* **2011** 32(36), 9810-9817.

170. Zhang, L.; Wu, L.; Si, Y.; Shu, K. Size-dependent cytotoxicity of silver nanoparticles to Azotobacter vinelandii: Growth inhibition, cell injury, oxidative stress and internalization. *PloS One.* **2018** 13(12), e0209020.

171. Arvizo, R. R.; Miranda, O. R.; Thompson, M. A.; Pabelick, C. M.; Bhattacharya, R.; Robertson, J. D.; Rotello, V. M.; Prakash, Y. S.; Mukherjee, P. Effect of nanoparticle surface charge at the plasma membrane and beyond. *Nano Letters.* **2010** 10(7), 2543-2548.

172. Jing, B.; Zhu, Y. Disruption of Supported Lipid Bilayers by Semihydrophobic Nanoparticles. *Journal of the American Chemical Society.* **2011** 133(28), 10983-10989.

173. Kim, S. T.; Saha, K.; Kim, C.; Rotello, V. M. The role of surface functionality in determining nanoparticle cytotoxicity. *Accounts of Chemical Research.* **2013** 46(3), 681-691.

174. Leroueil, P. R.; Berry, S. A.; Duthie, K.; Han, G.; Rotello, V. M.; McNerny, D. Q.; Baker, J. R.; Orr, B. G.; Banaszak Holl, M. M. Wide varieties of cationic nanoparticles induce defects in supported lipid bilayers. *Nano Letters.* **2008** 8(2), 420-424.

175. Favi, P. M.; Gao, M.; Johana Sepulveda Arango, L.; Ospina, S. P.; Morales, M.; Pavon, J. J.; Webster, T. J. Shape and surface effects on the cytotoxicity of nanoparticles: Gold nanospheres versus gold nanostars. *Journal of Biomedical Materials Research Part A.* **2015** 103(11), 3449-3462.

176. Zhang, B.; Sai Lung, P.; Zhao, S.; Chu, Z.; Chrzanowski, W.; Li, Q. Shape dependent cytotoxicity of PLGA-PEG nanoparticles on human cells. *Scientific Reports.* **2017** 7(1), 7315(article number).

177. Zhao, X.; Ng S Fau - Heng, B. C.; Heng Bc Fau - Guo, J.; Guo J Fau - Ma, L.; Ma L Fau - Tan, T. T. Y.; Tan Tt Fau - Ng, K. W.; Ng Kw Fau - Loo, S. C. J.; Loo, S. C. Cytotoxicity of hydroxyapatite nanoparticles is shape and cell dependent. *Archives of Toxicology.* 87(6), 1037-1052.

178. Yeagle, P. Modulation of membrane function by cholesterol. *Biochimie.* **1991** 73(10), 1303-1310.

179. Yeagle, P. L. Cholesterol and the cell membrane. *Biochimica et Biophysica Acta* **1985** 822(3-4), 267-287.

180. Yeagle, P. L. Lipid regulation of cell membrane structure and function. *The FASEB Journal.* **1989** 3(7), 1833-1842.

181. Kwik, J.; Boyle, S.; Fooksman, D.; Margolis, L.; Sheetz, M. P.; Edidin, M. Membrane cholesterol, lateral mobility, and the phosphatidylinositol 4, 5-bisphosphate-dependent organization of cell actin. *Proceedings of the National Academy of Sciences.* **2003** 100(24), 13964-13969.

182. Ohvo-Rekilä, H.; Ramstedt, B.; Leppimäki, P.; Slotte, J. P. Cholesterol interactions with phospholipids in membranes. *Progress in Lipid Research.* **2002** 41(1), 66-97.

183. Bolotina, V.; Omelyanenko, V.; Heyes, B.; Ryan, U.; Bregestovski, P. Variations of membrane cholesterol alter the kinetics of Ca 2+-dependent K+ channels and membrane fluidity in vascular smooth muscle cells. *Pflügers Archiv.* **1989** 415(3), 262-268.

184. Chen, Q.; Amaral, J.; Biancani, P.; Behar, J. Excess membrane cholesterol alters human gallbladder muscle contractility and membrane fluidity. *Gastroenterology.* **1999** 116(3), 678-685.

185. Cooper, R. A. Influence of increased membrane cholesterol on membrane fluidity and cell function in human red blood cells. *Journal of Supramolecular Structure.* **1978** 8(4), 413-430.

186. Gleason, M. M.; Medow, M. S.; Tulenko, T. N. Excess membrane cholesterol alters calcium movements, cytosolic calcium levels, and membrane fluidity in arterial smooth muscle cells. *Circulation Research.* **1991** 69(1), 216-227.

187. Gniadecki, R. Depletion of membrane cholesterol causes ligand-independent activation of Fas and apoptosis. *Biochemical and Biophysical Research Communications.* **2004** 320(1), 165-169.

188. Zhang, L.; Kim, S. B.; Luitel, K.; Shay, J. W. Cholesterol depletion by TASIN-1 induces apoptotic cell eeath through the ER stress/ROS/JNK signaling in colon cancer cells. *Molecular Cancer Therapeutics.* **2018** 17(5), 943-951.

189. Newmeyer, D. D.; Ferguson-Miller, S. Mitochondria: Releasing Power for Life and Unleashing the Machineries of Death. *Cell.* **2003** 112(4), 481-490.

190. Marchetti, P.; Castedo M Fau - Susin, S. A.; Susin Sa Fau - Zamzami, N.; Zamzami N Fau - Hirsch, T.; Hirsch T Fau - Macho, A.; Macho A Fau - Haeffner, A.; Haeffner A Fau - Hirsch, F.; Hirsch F Fau - Geuskens, M.; Geuskens M Fau - Kroemer, G.; Kroemer, G. Mitochondrial permeability transition is a central

coordinating event of apoptosis. *Journal of Experimental Medicine.* 184(3), 1155-1160.

191. Newmeyer, D. D.; Farschon Dm Fau - Reed, J. C.; Reed, J. C. Cell-free apoptosis in Xenopus egg extracts: inhibition by Bcl-2 and requirement for an organelle fraction enriched in mitochondria. *Cell.* **1994** 79(2), 353-364.

192. Petit, P. X.; Lecoeur H Fau - Zorn, E.; Zorn E Fau - Dauguet, C.; Dauguet C Fau - Mignotte, B.; Mignotte B Fau - Gougeon, M. L.; Gougeon, M. L. Alterations in mitochondrial structure and function are early events of dexamethasone-induced thymocyte apoptosis. *Journal of Cell Biology.* **1995** 130(1), 157-167.

193. Zamzami, N.; Marchetti P Fau - Castedo, M.; Castedo M Fau - Decaudin, D.; Decaudin D Fau - Macho, A.; Macho A Fau - Hirsch, T.; Hirsch T Fau - Susin, S. A.; Susin Sa Fau - Petit, P. X.; Petit Px Fau - Mignotte, B.; Mignotte B Fau - Kroemer, G.; Kroemer, G. Sequential reduction of mitochondrial transmembrane potential and generation of reactive oxygen species in early programmed cell death. *Journal of Experimental Medicine.* **1995** 182(2), 367-377.

194. Deng, H.; Mondal, S.; Sur, S.; Woodworth, C. D. Establishment and optimization of epithelial cell cultures from human ectocervix, transformation zone, and endocervix optimization of epithelial cell cultures. *Journal of Cellular Physiology.* **2019** 234(6), 7683-7694.

195. Zhang, P.; Cheetham, A. G.; Lin, Y.-a.; Cui, H. Self-assembled Tat nanofibers as effective drug carrier and transporter. *ACS Nano.* **2013** 7(7), 5965-5977.

196. Kuang, Y.; Du, X.; Zhou, J.; Xu, B. Supramolecular nanofibrils inhibit cancer progression in vitro and in vivo. *Advanced Healthcare Materials.* **2014** 3(8), 1217-1221.

197. Rudra, J. S.; Tian, Y. F.; Jung, J. P.; Collier, J. H. A self-assembling peptide acting as an immune adjuvant. *Proceedings of the National Academy of Sciences.* **2010** 107(2), 622-627.

198. Kaitz, J. A.; Possanza, C. M.; Song, Y.; Diesendruck, C. E.; Spiering, A. J. H.; Meijer, E.; Moore, J. S. Depolymerizable, adaptive supramolecular polymer nanoparticles and networks. *Polymer Chemistry.* **2014** 5(12), 3788-3794.

199. Cordier, P.; Tournilhac, F.; Soulié-Ziakovic, C.; Leibler, L. Self-healing and thermoreversible rubber from supramolecular assembly. *Nature.* **2008** 451(7181), 977-980.

200. Chen, Y.; Kushner, A. M.; Williams, G. A.; Guan, Z. Multiphase design of autonomic self-healing thermoplastic elastomers. *Nature Chemistry.* **2012** 4(6), 467-472.

201. Burattini, S.; Colquhoun, H. M.; Fox, J. D.; Friedmann, D.; Greenland, B. W.; Harris, P. J.; Hayes, W.; Mackay, M. E.; Rowan, S. J. A self-repairing, supramolecular polymer system: healability as a consequence of donor–acceptor π–π stacking interactions. *Chemical Communications.* **2009** (44), 6717-6719.

202. Burattini, S.; Greenland, B. W.; Merino, D. H.; Weng, W.; Seppala, J.; Colquhoun, H. M.; Hayes, W.; Mackay, M. E.; Hamley, I. W.; Rowan, S. J. A healable supramolecular polymer blend based on aromatic π− π stacking and hydrogen-bonding interactions. *Journal of the American Chemical Society.* **2010** 132(34), 12051-12058.

203. Burnworth, M.; Tang, L.; Kumpfer, J. R.; Duncan, A. J.; Beyer, F. L.; Fiore, G. L.; Rowan, S. J.; Weder, C. Optically healable supramolecular polymers. *Nature.* **2011** 472(7343), 334-337.

204. Janovick, J. A.; Stewart, M. D.; Jacob, D.; Martin, L. D.; Deng, J. M.; Stewart, C. A.; Wang, Y.; Cornea, A.; Chavali, L.; Lopez, S. Restoration of testis function in hypogonadotropic hypogonadal mice harboring a misfolded GnRHR mutant by pharmacoperone drug therapy. *Proceedings of the National Academy of Sciences.* **2013** 110(52), 21030-21035.

205. Simola, M.; Hänninen, A. L.; Stranius, S. M.; Makarow, M. Trehalose is required for conformational repair of heat‐denatured proteins in the yeast endoplasmic reticulum but not for maintenance of membrane traffic functions after severe heat stress. *Molecular Microbiology.* **2000** 37(1), 42-53.

206. Marques, C.; Guo, W.; Pereira, P.; Taylor, A.; Patterson, C.; Evans, P. C.; Shang, F. The triage of damaged proteins: degradation by the ubiquitin-proteasome pathway or repair by molecular chaperones. *The FASEB Journal.* **2006** 20(6), 741-743.

207. Greenfield, M. A.; Hoffman, J. R.; Olvera de la Cruz, M.; Stupp, S. I. Tunable mechanics of peptide nanofiber gels. *Langmuir.* **2009** 26(5), 3641-3647.

208. Ortony, J. H.; Qiao, B.; Newcomb, C. J.; Keller, T. J.; Palmer, L. C.; Deiss-Yehiely, E.; Olvera de la Cruz, M.; Han, S.; Stupp, S. I. Water dynamics from the surface to the interior of a supramolecular nanostructure. *Journal of the American Chemical Society.* **2017** 139(26), 8915-8921.

209. Domigan, L. J.; Healy, J. P.; Meade, S. J.; Blaikie, R. J.; Gerrard, J. A. Controlling the dimensions of amyloid fibrils: Toward homogenous components for bionanotechnology. *Biopolymers.* **2012** 97(2), 123-133.

210. Zhao, J.; Bolisetty, S.; Adamcik, J.; Han, J.; Fernández-Ronco, M. P.; Mezzenga, R. Freeze–thaw cycling induced isotropic–nematic coexistence of amyloid fibrils suspensions. *Langmuir.* **2016** 32(10), 2492-2499.

211. Berns, E. J.; Sur, S.; Pan, L.; Goldberger, J. E.; Suresh, S.; Zhang, S.; Kessler, J. A.; Stupp, S. I. Aligned neurite outgrowth and directed cell migration in self-assembled monodomain gels. *Biomaterials.* **2014** 35(1), 185-195.

212. Erickson, C.; Trinkaus, J. Microvilli and blebs as sources of reserve surface membrane during cell spreading. *Experimental Cell Research.* **1976** 99(2), 375-384.

213. Bereiter-Hahn, J.; Luck, M.; Miebach, T.; Stelzer, H.; Voth, M. Spreading of trypsinized cells: cytoskeletal dynamics and energy requirements. *Journal of Cell Science.* **1990** 96(1), 171-188.

214. Charras, G.; Paluch, E. Blebs lead the way: how to migrate without lamellipodia. *Nature Reviews Molecular Cell biology.* **2008** 9(9), 730-736.

215. Phan, H. T.; Bartelt-Hunt, S.; Rodenhausen, K. B.; Schubert, M.; Bartz, J. C. Investigation of bovine serum albumin (BSA) attachment onto self-assembled monolayers (SAMs) using combinatorial quartz crystal microbalance with dissipation (QCM-D) and spectroscopic ellipsometry (SE). *PloS One.* **2015** 10(10), e0141282.

216. Schwegman, J. J.; Carpenter, J. F.; Nail, S. L. Evidence of partial unfolding of proteins at the ice/freeze‐concentrate interface by infrared microscopy. *Journal of Pharmaceutical Sciences.* **2009** 98(9), 3239-3246.

217. Costantino, H. R.; Griebenow, K.; Langer, R.; Klibanov, A. M. On the pH memory of lyophilized compounds containing protein functional groups. *Biotechnology and Bioengineering.* **1997** 53(3), 345-348.

218. Zacharis, E.; Halling, P. J.; Rees, D. G. Volatile buffers can override the "pH memory" of subtilisin catalysis in organic media. *Proceedings of the National Academy of Sciences.* **1999** 96(4), 1201-1205.

219. Cote, Y.; Fu, I. W.; Dobson, E. T.; Goldberger, J. E.; Nguyen, H. D.; Shen, J. K. Mechanism of the pH-controlled self-assembly of nanofibers from peptide amphiphiles. *Journal of Physical Chemistry C.* **2014** 118(29), 16272-16278.

220. Aida, T.; Meijer, E.; Stupp, S. Functional Supramolecular Polymers. *Science.* **2012** 335(6070), 813-817.

221. Boden, S. D. Biology of lumbar spine fusion and use of bone graft substitutes: present, future, and next generation. *Tissue Engineering.* **2004** 6(4), 383-399.

222. Reddi, A. H. Role of morphogenetic proteins in skeletal tissue engineering and regeneration. *Nature Biotechnology.* **1998** 16(3), 247-252.

223. McKay, B.; Sandhu, H. S. Use of recombinant human bone morphogenetic protein-2 in spinal fusion applications. *Spine.* **2002** 27(16S), S66-S85.

224. Chen, N.-F.; Smith, Z. A.; Stiner, E.; Armin, S.; Sheikh, H.; Khoo, L. T. Symptomatic ectopic bone formation after off-label use of recombinant human bone morphogenetic protein-2 in transforaminal lumbar interbody fusion: Report of 4 cases. *Journal of Neurosurgery: Spine.* **2010** 12(1), 40-46.

225. Deutsch, H. High-dose bone morphogenetic protein–induced ectopic abdomen bone growth. *The Spine Journal.* **2010** 10(2), e1-e4.

226. Rihn, J. A.; Patel, R.; Makda, J.; Hong, J.; Anderson, D. G.; Vaccaro, A. R.; Hilibrand, A. S.; Albert, T. J. Complications associated with single-level transforaminal lumbar interbody fusion. *The Spine Journal.* **2009** 9(8), 623-629.

227. Muchow, R. D.; Hsu, W. K.; Anderson, P. A. Histopathologic inflammatory response induced by recombinant bone morphogenetic protein-2 causing radiculopathy after transforaminal lumbar interbody fusion. *The Spine Journal.* **2010** 10(9), e1-e6.

228. Perri, B.; Cooper, M.; Lauryssen, C.; Anand, N. Adverse swelling associated with use of rh-BMP-2 in anterior cervical discectomy and fusion: a case study. *The Spine Journal.* **2007** 7(2), 235-239.

229. Shahlaie, K.; Kim, K. D. Occipitocervical fusion using recombinant human bone morphogenetic protein-2: adverse effects due to tissue swelling and seroma. *Spine.* **2008** 33(21), 2361-2366.

230. Cahill, K. S.; Chi, J. H.; Day, A.; Claus, E. B. Prevalence, complications, and hospital charges associated with use of bone-morphogenetic proteins in spinal fusion procedures. *Journal of the American Medical Association.* **2009** 302(1), 58-66.

231. Williams, B. J.; Smith, J. S.; Fu, K.-M. G.; Hamilton, D. K.; Polly Jr, D. W.; Ames, C. P.; Berven, S. H.; Perra, J. H.; Knapp Jr, D. R.; McCarthy, R. E. Does bone morphogenetic protein increasethe incidence of perioperative complicationsin spinal fusion?: A comparison of 55,862 cases of spinal fusion with and without bone morphogenetic protein. *Spine.* **2011** 36(20), 1685-1691.

232. Choudhry, O. J.; Christiano, L. D.; Singh, R.; Golden, B. M.; Liu, J. K. Bone morphogenetic protein–induced inflammatory cyst formation after lumbar fusion causing nerve root compression: Case report. *Journal of Neurosurgery: Spine.* **2012** 16(3), 296-301.

233. Burkus, J. K.; Dryer, R. F.; Peloza, J. H. Retrograde ejaculation following single-level anterior lumbar surgery with or without recombinant human bone

morphogenetic protein–2 in 5 randomized controlled trials. *Journal of Neurosurgery: Spine.* **2013** 18(2), 112-121.

234. Carragee, E. J.; Mitsunaga, K. A.; Hurwitz, E. L.; Scuderi, G. J. Retrograde ejaculation after anterior lumbar interbody fusion using rhBMP-2: a cohort controlled study. *The Spine Journal.* **2011** 11(6), 511-516.

235. Comer, G. C.; Smith, M. W.; Hurwitz, E. L.; Mitsunaga, K. A.; Kessler, R.; Carragee, E. J. Retrograde ejaculation after anterior lumbar interbody fusion with and without bone morphogenetic protein-2 augmentation: a 10-year cohort controlled study. *The Spine Journal.* **2012** 12(10), 881-890.

236. Polge, C.; Smith, A. U.; Parkes, A. S. Revival of spermatozoa after vitrification and dehydration at low temperatures. *Nature.* **1949** 164(4172), 666.

237. Bastings, M. M. C.; Koudstaal, S.; Kieltyka, R. E.; Nakano, Y.; Pape, A. C. H.; Feyen, D. A. M.; van Slochteren, F. J.; Doevendans, P. A.; Sluijter, J. P. G.; Meijer, E. W.; Chamuleau, S. A. J.; Dankers, P. Y. W. A fast pH-switchable and self-healing supramolecular hydrogel carrier for guided, local catheter injection in the infarcted myocardium. *Advanced Healthcare Materials.* **2014** 3(1), 70-78.

238. Pires, R. A.; Abul-Haija, Y. M.; Costa, D. S.; Novoa-Carballal, R.; Reis, R. L.; Ulijn, R. V.; Pashkuleva, I. Controlling cancer cell fate using localized biocatalytic self-assembly of an aromatic carbohydrate amphiphile. *Journal of the American Chemical Society.* **2015** 137(2), 576-579.

239. Webber, M. J.; Newcomb, C. J.; Bitton, R.; Stupp, S. I. Switching of self-assembly in a peptide nanostructure with a specific enzyme. *Soft Matter.* **2011** 7(20), 9665-9672.

VITA

Charlotte Hui Chen was born on March 12, 1987 in Beijing, China, and later grew up in New Orleans, Louisiana and Houston, Texas. She is the daughter of Hua Chen and Qian Zhang. She first got involved with scientific research the summer following her sophomore year of high school, at MD Anderson Cancer Center in Houston, Texas. In the laboratory of Prof. Isaiah "Josh" Fidler, she did cancer biology research that is quite different from the materials science work she does now, 15 years later. The common theme is that she has always been passionate about research for medical applications.

Charlotte received her Bachelors in Biomedical Engineering from Johns Hopkins University (Baltimore, MD) in 2009, and her Masters in Bioengineering from Stanford University (Stanford, CA) in 2010. Following graduation, she journeyed across the Pacific Ocean to Sydney, Australia, where she worked at a small but vibrant startup called Endoluminal Sciences. Eventually she came back home to the United States, where she worked at Relypsa, a pharmaceutical startup based in Santa Clara, California. Her industry experience taught her the importance of basic science knowledge to successful clinical translation, which motivated her return to school for PhD studies.

Charlotte joined Prof. Samuel Stupp's laboratory in 2013, where she has worked on peptide amphiphile-based supramolecular biomaterials. In the future, she hopes to apply basic science knowledge to support the clinical translation of biomaterials.

INDUSTRY EXPERIENCE

Research Associate | 04/2012 – 12/2012
Relypsa | Santa Clara, CA, USA

- *Scale-up manufacturing of a polymer-based hyperkalemia drug, performed assays to validate In-Process Controls (IPC)*
- *Supported Chemistry, Manufacturing, and Controls (CMC) for New Drug Application (NDA)*

Research Fellow/Biomedical Engineer | 09/2010 – 11/2011
The Heart Research Institute/Endoluminal Sciences | Sydney, NSW, Australia

- *Developed biomaterials for endovascular drug delivery and transcatheter aortic valve replacement devices*
- *Analyzed relevant market, intellectual property, and regulatory pathways*
- *Mentored undergraduate interns*

LECTURES

Rising Stars of SQI Lectures: Pathway Complexity in Supramolecular Biomaterials Affects Therapeutic Efficacy: Considerations for Clinical Translation
April 5, 2019 | Simpson Querrey Institute, Northwestern University | Chicago, IL, USA

Invited Talk: Peptide Amphiphiles as Biomaterials: A Self-Assembling Journey From Monomors to Medicine
March 1, 2019 | Clarkson University, School of Arts and Sciences | Potsdam, NY, US

CONFERENCE PRESENTATIONS

Materials Research Society | Fall Meeting & Exhibit
November 25 - 30, 2018 | Boston, MA, USA
Oral Presentation: *Large-scale self-sorting in supramolecular assemblies*

Gordon Research Conferences | Biomaterials and Tissue Engineering
June 23 - 28, 2017 | Holderness, NH, USA
Poster: *Self-repair of structure and bioactivity in a supramolecular nanofiber*

Cardiovascular Research Foundation | Transcatheter Cardiovascular Therapeutics
November 7 - 11, 2011 | San Francisco, CA, USA
Poster: *A low-profile highly conformable sealing technology for transcatheter heart valves.*

AWARDS

T32 Training Grant | 10/2017 - present
National Institutes of Health | Two-year pre-doctoral training grant

National Defense Science and Engineering Graduate Fellowship | 09/2014 – 08/2017
US Department of Defense | Three-year PhD fellowship

Cabell Fellowship | 09/2013 – 06/2014
Northwestern McCormick School of Engineering | One-year PhD fellowship

Whitaker International Fellowship | 09/2010 – 11/2011
Whitaker Foundation | One-year international research fellowship

Vredenburg Scholar | 05/2007 – 08/2007
Johns Hopkins Whiting School of Engineering | Summer international research funding

PUBLICATIONS

1. Chen CH, Palmer L, Stupp SI. Self-Repair of Structure and Bioactivity in a Supramolecular Nanostructure. *Nano Letters.* 2018, 18(11): 6832-41.
2. Chen CH, Palmer L, Stupp SI. Self-Sorting Mediated by Interactions with a Supramolecular Matrix. *In Preparation*
3. Chen CH et al, Stupp SI. A Shelf-Stable Supramolecular Bone Graft for Spinal Fusion Surgeriess. *In Preparation*
4. Sipes D*, Chen CH*, Avolio L, Stoian A, Ranslow M, Liebich S, Stupp SI, Sur S. Programmed Cell Death Instructed by Membrane Interacting Supramolecular Assemblies. *In Preparation.* *Equal Contribution
5. Yun C, Katchko KM, Schallmo MS, Jeong S, Yun J, Chen CH, Weiner JA, Park C, George A, Stupp SI, Hsu WK, Hsu EL. Aryl Hydrocarbon Receptor Antagonists Mitigate the Effects of Dioxin on Critical Cellular Functions in Differentiating Human

Osteoblast-Like Cells. *International Journal of Molecular Sciences.* 19(1): E225, 2018. PMID: 29324662

6. Sleep E, Cosgrove BD, McClendon MT, Preslar AT, Chen CH, Sangji MH, Rubert Pérez CM, Haynes RD, Meade TJ, Blau HM, Stupp SI. Injectable biomimetic liquid crystalline scaffolds enhance muscle stem cell transplantation. *Proceedings of the National Academy of Sciences USA*. 2017 114 (38) E7919-E7928
7. Lee S, Sur S, Jouët-Pastré H, Chen CH, McClendon M, Stupp SI. Divalent counterions dictate pH-sensitivity of peptide amphiphile self-assembly. *In Preparation*

CONFERENCE PAPERS

1. M Ng, V Wong, B Bobillier, B Endersbee, M Le Hellaye, C Chen, J Murdoch, M Skalsky, A Mitra. TCT-792: A low-profile highly conformable sealing technology for transcatheter heart valves. *Journal of the American College of Cardiology 2011; 58(20 Supplement): B211.*
2. J Hsu, C Chen, S Huang, S Kim, A Lee, D Li, A Liu, T Tsai, J Wang, B Yoon. Automated Control of Blood Glucose in the OR and Surgical ICU. *Engineering in Medicine and Biology Society 2009, Annual International Conference of the IEEE;* p. 1286-9.
3. C Kut, C Chen, J Wong, R Taylor. Improving the utility of in-room video camera systems for continuous surveillance of patient motion during radiation treatment. *Journal of Applied Clinical Medical Physics 2008; 9(3).*

TEACHING EXPERIENCE

Teaching Assistant: MSE 336 Chemical Synthesis of Materials | 03/2017 – 06/2017
Northwestern University | Evanston, IL, USA

Teaching Assistant: MSE 332 Mechanical Behavior of Solids | 09/2016 – 12/2016
Northwestern University | Evanston, IL, USA

Teaching Assistant: CSCI 600.107 Introduction to Java | 09/2008 – 05/2009
Johns Hopkins University | Baltimore, MD, USA